PULSE PROPAGATION ALONG CONDUCTORS IN LOW–DENSITY, COLD PLASMAS AS APPLIED TO ELECTRODYNAMIC TETHERS IN THE IONOSPHERE

by

Sven Gunnar Bilén

A dissertation submitted in partial fulfillment
of the requirements for the degree of
Doctor of Philosophy
(Electrical Engineering)
in The University of Michigan
1998

Doctoral Committee:

Associate Professor Brian E. Gilchrist, Chairperson
Professor Ronald M. Gilgenbach
Research Scientist Valdis V. Liepa
Associate Professor Kamal Sarabandi

UMI Number: 9909852

UMI
300 North Zeeb Road
Ann Arbor, MI 48103

There is a time for everything,
and a season for every activity under heaven....
—Ecclesiastes 3:1 NIV

To my wife, Carmen, for her love and support
and to my parents for nurturing my God-given talents.

ACKNOWLEDGEMENTS

No effort this large can be successful without assistance, discussions, and advice from many different people. For most of these people I have been able to recognize their important inputs and will do my best to thank them here; however, I am aware that there may be others whose inputs were needed but I may have somehow missed noticing them. For those who fall in this category, please accept my heartfelt thank-you.

During the course of my studies, I have had the privilege of being a member of the Shuttle Electrodynamic Tether System (SETS) cadre on two Shuttle missions: STS-46 and STS-75. On the SETS experiment* team were many people whose efforts helped obtain two unique datasets under very adverse conditions. Members of the SETS team whom I wish to specifically thank include Victor Agüero, Peter Banks, Paul Cobb, Linda Habash-Krause, Pete Hansen, Rohini Indiresan, Dave Lauben, Laura Liebler, Dave Morris, John Murray, John Raitt, Don Thompson (Thank you Don), Vip Tolat, Nestor Voronka, Brent White, and Scott Williams. In addition to the SETS team, I would like to extend a general thank-you to the cadres of the many other experiments that were part of the Tethered Satellite System (TSS).

For three-and-a-half years of my Ph.D. candidacy, I was fortunate to have a fellowship through the NASA Graduate Student Researchers Program.† I wish to

*NASA contract NAS8-938391

†NASA contract NGT-51166

thank my NASA Marshall Space Flight Center contact and mentor, Nobie Stone, who was extremely helpful by showing me around the center and talking with me during my several visits to MSFC and during the TSS missions.

From the Plasmadynamics and Electric Propulsion Laboratory I would like to acknowledge Prof. Alec Gallimore's gracious donation of chamber time throughout the years in exchange for my electrical–engineering advice (VIRTUAL SVEN: "Have you checked your grounding?"). I would like to specifically thank Matt Domonkos for help setting up and operating the hollow cathode assembly and the rest of the PEPL group (some of whom have graduated and moved on by now) for their various discussions and suggestions: Colleen Marrese, Brad King, Frank Gulzcinski, John Foster, Sang–Wook Kim, James Haas, and George Williams.

I would also like to thank the many other researchers, engineers, technicians, and students I have been privileged to work with during my Ph.D. efforts. In particular: Hide Usui, Torsten Neubert, and John Luginsland for general help with PIC codes; Keith Cartwright for help with XOOPIC; Craig Garvin for stimulating conversations on nonlinear sheaths and modeling of them; Preston Powell, an 1997 Summer REU student, for help with the Langmuir probe analyses; Mark Huetteman for advice on sample preparation for the experiments; and Nelly deMaldonado, Debi Batey, and Michele Maurer for secretarial support.

As a member of the RadLab, I've had access to many fine facilities and people. A few of the RadLab students I'd particularly like to thank are Shawn Ohler, Mike Nurnberger, and Rick Searcy.

I would like to specifically thank my thesis committee for the effort they've put into seeing that I actually finish: Ron Gilgenbach, Val Liepa, and Kamal Sarabandi. To my advisor and committee chairman, Brian Gilchrist, a very special thanks. It's hard to believe that we came to Michigan at the same time, you striving for tenure, me for the Ph.D. degree. I think our work together has been very fruitful and I look forward to collaboration in the future.

I would also like to thank Chen–To Tai for encouraging me to use his mathematically correct notations for vector calculus operations—gradient, divergence, and curl—in this thesis. Because of the novelty of this new notation, I have included a summary description of it in Appendix F.

And lastly, on the personal side I would like to thank the many people who have supported me all these years (and, yes, pestered me, too). To my parents, Lennart and Sigrid, you never could have known the troubles caused by that screwdriver you gave me when I was only a year old. Those shocks from the electrical outlets are probably what sent me down the path I'm on today—Electromagnetics (using high–voltages, no less). To my wife, Carmen, thanks for putting up with the many nights without me. To Tom and Ruth, thanks for the constant encouragement; you know what a huge effort the Ph.D. can be. To my brother, Lars, and sister, Anna, thanks.

One never notices what has been done;
one can only see what remains to be done.
—Marie Curie

TABLE OF CONTENTS

LIST OF FIGURES

Figure

LIST OF TABLES

Table

LIST OF APPENDICES

Appendix

CHAPTER I

Introduction

It has been estimated that over 99% of the matter in the universe exists in the plasma state. Indeed, the Earth exists as but a "bubble" of lower energy matter traveling in the vast plasma background of the solar system. Here on Earth, however, we can create small, localized "pockets" of plasma. Generated in vacuum chambers and other devices, plasmas perform a multitude of useful tasks, such as semiconductor processing and metal hardening, and plasmas are an inherent part of the so–far–elusive goal of sustainable energy: fusion. We can also use these pockets of plasma to test the designs of spacecraft and sensors that we launch above our atmosphere. Properly testing their designs ensures that the spacecraft will survive and operate correctly as they leave the confines of the Earth's atmosphere and encounter the vast plasma media surrounding the Earth: the ionosphere, the Van Allen radiation belts, and the solar wind.

In recent years, the spacecraft we design for sending into space are becoming very large. This increase in size presents new challenges to and opportunities for spacecraft design; the concept of length must now be accounted for when designing and flying these larger spacecraft. For example, long conductors—on the order of 100–20,000 m and longer—are now being used and proposed for scientific research and engineering applications as long antennas and in electrodynamic–tether systems. As another example, the power systems on large orbiting platforms, such as the soon–to–be–constructed *International Space Station* (ISS), will utilize long conductors to channel power from distant (> tens of meters) solar arrays. These solar arrays will themselves be mounted on large metallic support structures which will be about 100 m long and exposed to the plasma environment.

Since these long conductors and structures are surrounded by a plasma medium, the plasma–conductor interaction must be taken into account. Not doing so can result in dire consequences to the spacecraft and its operation, including spacecraft failure. Plasma interaction with short conductors has been an area of research interest for many years. This research has produced a fairly good understanding of the plasma–probe interaction for both steady–state and transient small signals, *i.e.*, small applied voltages on the order of the plasma potential. In recent years, there has also been a research interest in the plasma's response to high–voltages applied to short, plasma–immersed conductors, *e.g.*, plasma–processing systems. There is, however, little current understanding of the physical processes involved as the conductor lengths increase, especially for high–voltage excitation. That is, the plasma–conductor interaction as a distributed phenomenon (*i.e.*, along the conductor's length) for large applied voltages is not well understood.

1.1 Research Motivation

There are three primary motivations for this work. The first is to characterize the general propagation behavior of electromagnetic (EM) pulses along conductors in cold, low–density plasmas. The second is to aid in understanding the scientific and engineering data collected during past and future electrodynamic–tether missions. Examples of such missions are the two Tethered Satellite System missions which flew in 1992 (TSS–1) and in 1996 (TSS–1R), and a proposed mission called Propulsive Small Expendable Deployer System (ProSEDS), scheduled to fly early in the next century [*Johnson*, 1997]. The third motivation is to determine the mechanism(s) behind the interaction between widely separated points on spacecraft in an ionized atmosphere. In many cases, this interaction is an adverse coupling causing undesirable interference. For example, how might a source such as an antenna located at one point on a large ionospheric structure (*e.g.*, ISS) affect sensitive systems located at some distance from the first?

1.1.1 General Electromagnetic Signal Propagation

One motivation of this research is to develop an understanding of the general propagation behavior of EM pulses and signals along conductors in plasmas. While cold, low–density plasmas are the focus here, the techniques employed—such as determining nonlinear sheath characteristics and developing circuit models—also lend themselves to other types of geometries and densities, which are found in such devices as plasma processing facilities and fusion reactors. Hence, while the plasmas generated in these facilities are not cold, low–density plasmas, the concept of a nonlinear transmission–line is valid.

For example, some plasma–processing facilities, currently only in the research phase, have become quite large with the hope that they can be used to process many semiconductor wafers at a time. Figure 1.1a shows a hexode plasma–processing chamber with a center electrode of length $\sim$ 65 cm and faces $\sim$ 17.5 cm wide. The applied RF voltages have been generally assumed constant along the length of the conductor. However, *Savas and Donohoe* [1989a] measured the variation in the RF–

potential amplitude along the electrode's length and found a 10–15% variation in the potential of the fundamental mode (f_{rf} = 13.56 MHz, $\lambda \sim 22$ m) from the top of the electrode to the bottom. More importantly, they found a 30–40% variation in the second harmonic and a 70–80% variation in the third and fourth harmonics. This was attributed to the decrease in wavelength with increasing harmonic number and also to increased inductive impedance, ωL. This voltage nonuniformity can adversely affect implantation energies and dosage levels which can lead to poorly fabricated semiconductors.

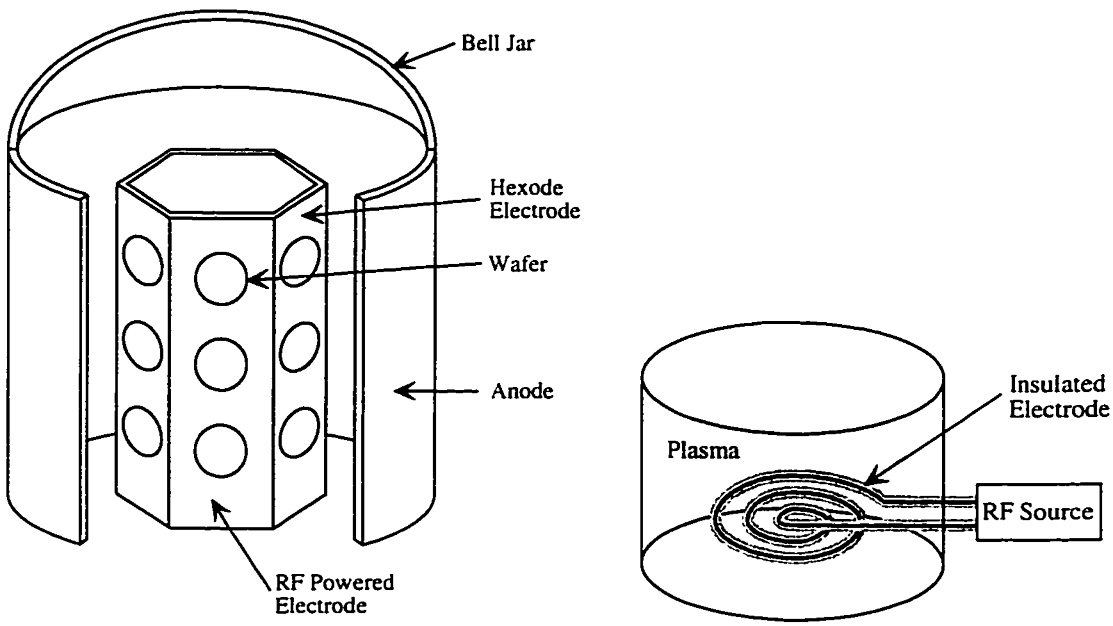

(a) (b)

Figure 1.1: Long conductors in plasma chambers for plasma processing: (a) cut-away view of a large plasma etch chamber with a long, hexode, RF-powered electrode (adapted from *Savas and Donohoe* [1989a]), (b) ICRF plasma chamber with immersed electrode (adapted from *Sugai et al.* [1994]).

Inductively coupled RF plasma (ICRF or ICP) systems generate a plasma via current–flowing antennas of helical or spiral shape which are typically placed on the outside of the vacuum vessel containing the plasma. Recently, however, some ICRF systems (Figure 1.1b) have been developed which utilize conductors immersed in the plasma [*Denisov et al.*, 1984; *Shirakawa et al.*, 1990; *Sugai et al.*, 1994]. Since these conductors make contact with the plasma, the signals on them are affected by and interact with the plasma. In addition, the lengths of these conductors may be long enough in many systems such that length is no longer negligible when compared to the wavelength of the excitation frequency or its harmonics.

In fusion reactors, the region between the wall and the plasma can support two possible surface waves, one of which is analogous to the TEM mode that propagates in a coaxial cable [*Lawson*, 1992]. The potential existence of these waves localized to the plasma surface or "scrape–off" layer is important since, if excited, the waves would not propagate into the plasma. Instead, their energy would be dissipated at the plasma edge, which may cause undesirable side effects. Hence, proper modeling of the waves is needed to determine effective methods for ensuring that they are not excited.

1.1.2 Electrodynamic Tethers

Electrodynamic tethers are conducting wires—which may be uninsulated or fully to partially insulated—that typically join two separated spacecraft as they orbit the Earth or other planetary body having a magnetic field. Electrodynamically tethered, orbiting systems have become a reality with the first flights of the Tethered Satellite System (Figure 1.2) in August 1992 (TSS–1) and February 1996 (TSS–1R) and the Plasma Motor Generator (PMG) in June 1993. In addition, there have been several electrodynamically tethered, suborbital sounding rockets flown in the past several years, including MAIMIK in November 1985, CHARGE–2 (Cooperative High–Altitude Rocket Gun Experiment) in December 1985, OEDIPUS–A (Observations of Electric–Field Distributions in the Ionospheric Plasma—A Unique Strategy) in January 1989, and CHARGE–2B in March 1992. Table 1.1 provides a list of known tether flights to date, both electrodynamic and not. In addition to these flown systems, many future applications of orbiting, electrodynamically tethered systems include:

- power and thrust generation for orbiting systems [*Penzo and Ammann*, 1989; *Johnson*, 1997], including possibly the *International Space Station* [*Crouch et al.*, 1995; *Johnson and Herrmann*, 1998] and at Jupiter [*Gallagher et al.*, 1998];
- large orbiting ULF/ELF/VLF communication antennas [*Grossi et al.*, 1984; *Lorenzini et al.*, 1992];
- extremely–long–baseline double probes for measurement of ionospheric electric–field structure [*Gilchrist et al.*, 1995];
- remote sensing of planetary geologies from orbit;
- stimulation of artificial aurorae and associated effects [*Martínez–Sanchez and Sanmartín*, 1997]; and
- radio astronomy [*Linscott*, 1992].

Before electrodynamic–tether systems can be fully exploited, a complete understanding of their electrical response is needed, which requires an understanding of both their steady–state and their transient response. Also, in order to analyze the data returned from tethered missions such as TSS–1 and TSS–1R, an understanding of the physical interaction of the tethered system with the surrounding ionospheric

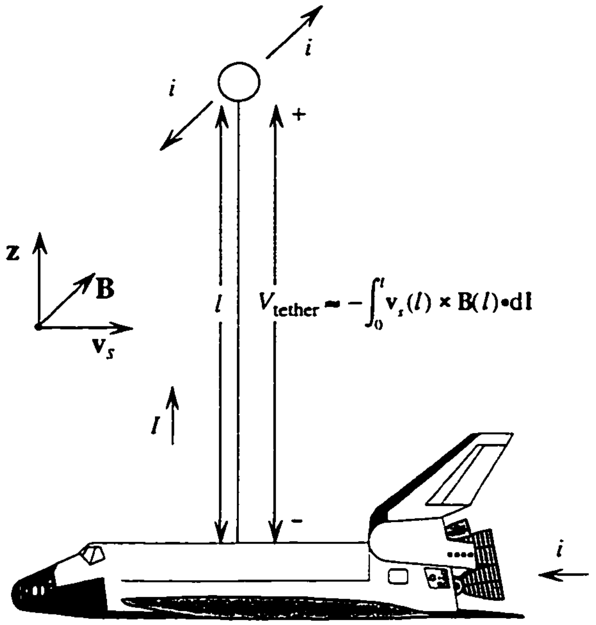

Figure 1.2: Schematic of the Tethered Satellite System.

plasma is needed. Current models of the interaction are based on low–voltage and/or static–sheath assumptions. Thus, an improved tether model is needed to account for high induced voltages and dynamic sheaths. With an improved tether model, it will be possible to determine the importance of the tether–plasma interaction to the overall transient response of electrodynamically tethered systems with long deployed lengths.

1.1.3 Interactions Between Separated Points and Adverse Coupling

Electromagnetic compatibility and interference (EMC/EMI) issues must be considered in the design of spacecraft and spacecraft structures if mission success is to be ensured. Improper elimination and/or containment of EMI can result in data–product loss or service reduction, at best, to complete mission failure, at worst. When examining the EMC environment of a spacecraft, the assumption is often made of

Table 1.1: Listing of known tether flights to date on both orbital and suborbital platforms (electrodynamic-mission names are *italicized*). Adapted from *Johnson* [1997].

Mission Name	Year	Orbit	Length	Comments
Gemini 11	1967	LEO	30 m	spin stabilized at 0.15 rpm
Gemini 12	1967	LEO	30 m	local vertical, stable swing
H-9M-69	1980	suborbital	500 m	partial deployment
S-520-2	1981	suborbital	500 m	partial deployment
CHARGE-1	1983	suborbital	500 m	full deployment
CHARGE-2	1984	suborbital	500 m	full deployment
MAIMIK	1985	suborbital	$\sim$ 400 m	8-keV electron generator
ECHO-7	1988	suborbital	unknown	magnetic field aligned
OEDIPUS-A	1989	suborbital	958 m	spin stabilized at 0.7 rpm
CHARGE-2B	1992	suborbital	500 m	full deployment
TSS-1	1992	LEO	267 m	partial deployment, retrieved
SEDS-1	1993	LEO	20 km	downward deploy, swing and cut
PMG	1993	LEO	500 m	upward deploy
SEDS-2	1994	LEO	20 km	local vert. stabilized, downward deploy
OEDIPUS-C	1995	suborbital	1174 m	magnetic field aligned
TSS-1R	1996	LEO	19.6 km	severed during deploy
TiPS	1996	LEO	4 km	long-life-tether mission

free-space propagation of EMI signals since present models and test procedures are generally based on this assumption. However, several spacecraft experiments have shown that transient or continuous-wave (CW) electromagnetic signals (interference) can propagate over even long distances—a particular case in which free-space modeling would probably not indicate an EMC issue—due to the plasma-sheath regions which surround the spacecraft.

As an example of adverse EMC, *Osbourne et al.* [1967] describe a mechanism for adverse signal coupling on *Aluette I*[1] whereby, under certain circumstances, its VLF receiver observed an interference signal originating with its electrical converter system. They conclude that:

[1]The primary experiment on *Aluette I*, which flew in 1963–64, was an ionospheric sounder with a 150-ft (45.7-m) dipole antenna.

> "[The reported] observations suggest a mechanism based on a coupling of the converter signal to the solar cells through the $\mathbf{v} \times \mathbf{B}$ induced sheath phenomena, resulting in an asymmetric distribution of electron collection over the spacecraft and thus coupling to the v.l.f. receiver. This mechanism is purely a charged–particle collection phenomenon and does not require capacitive effects of electromagnetic coupling, although they can contribute to asymmetry in the observed signals."

Balmain et al. [1990] indicate that EMI signals might also propagate along large space structures as "sheath waves". These sheath waves might cause interference signal levels to be much higher than they would be without the presence of the plasma. Their suggestion is based on results from the OEDIPUS–A tethered sounding rocket experiment (described in Section 2.5.2), which showed quantitative evidence of sheath waves excited along its insulated tether surrounded by the ionospheric plasma. The excited sheath waves had sharply defined passbands and stopbands. Within the lowest passband, OEDIPUS–A detected resonance fringes which could be scaled to determine the phase and group refractive indices of the observed sheath–waves [*James and Whalen*, 1991; *Godard et al.*, 1991].

1.2 Situation of Research

Except in some research on antennas and sheath waves, conductor length generally has not been accounted for when describing the plasma–conductor interaction. Specifically, research to date has generally concentrated on the one–dimensional aspects of the transient plasma sheath, that is, expansion away from a conductor surface. The research presented here examines the two–dimensional aspects of the transient sheath: expansion not only away from a surface, but along it as well. Since long conductors such as electrodynamic tethers will have, in many cases, hundreds and even thousands of volts applied to or induced across them, this research concentrates on large applied voltages. In addition, the applied voltages are negative since, along most of its length, the tether is biased negatively with respect to the local plasma (this will be shown in Section 2.3.2). Under negative high–voltage excitation the sheath is dynamic and nonlinear—unlike the assumptions generally used for low excitation voltages, those being static sheath size or linearized sheath characteristics. The existence of a dynamic and nonlinear sheath fundamentally changes the nature of EM propagation along electrodynamic tethers.

As implied in the discussion above, high–voltage pulse propagation along a plasma–immersed conductor cannot be analyzed in the same manner as it is along other transmission lines, such as along coaxial cables or parallel–wire lines. This is due primarily to the fact that, unlike these other transmission lines, the geometry of the plasma–conductor system is not rigid because the plasma effectively forms the outer conductor. *James et al.* [1995] state that the tether, sheath, and surrounding plasma can form an approximation to a coaxial RF transmission line to the degree that the surrounding plasma can be regarded as the outer conductor. These coaxial modes are known as sheath waves and are a concept described under the assumption of static sheaths.

Present tether transmission–line models [*e.g.*, *Arnold and Dobrowolny*, 1980; *Osmolovsky et al.*, 1992] assume, as a first–order approximation, that the plasma–sheathed tether can be modeled as a simple rigid coaxial cable (Figure 1.3a). While this has proven acceptable for short tethers [*e.g.*, *Bilén et al.*, 1995], an improved model is needed for longer deployed tether lengths, primarily to account for the higher induced voltages and the dynamic sheath. That is, in the transient case of a pulse propagating along the tether, the approximate coaxial geometry is dynamic since the surrounding plasma is affected by the pulse's passage (Figure 1.3b), unlike the case of typical coaxial cable which has a rigid–metal sheathing.

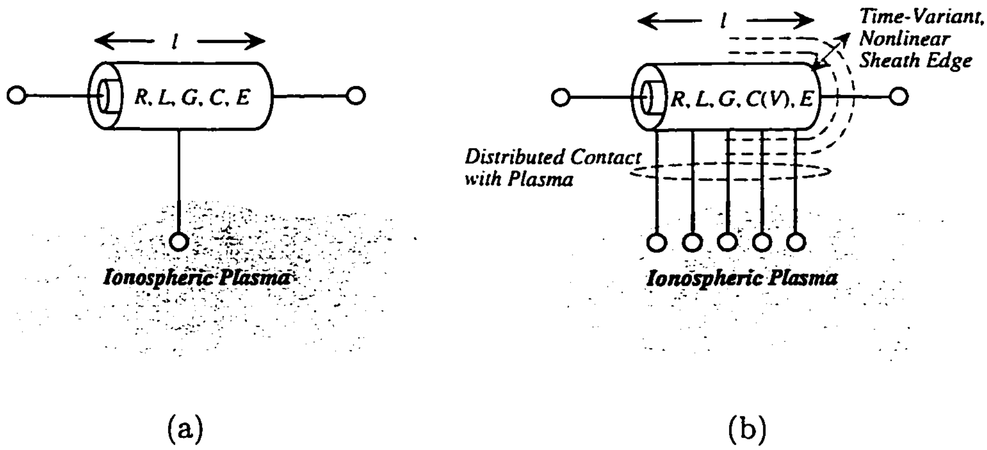

Figure 1.3: Electrodynamic–tether transmission–line models: (a) static–sheath model and (b) dynamic–sheath model.

1.3 Contributions of Research and Scope of Study

The primary contributions of this work are two. The first is the development of a voltage–dependent sheath model valid in the frequency regime between the electron and ion plasma frequencies and for negative high voltages. This model is developed analytically and verified via plasma–chamber experiments and particle–in–cell computer simulations.

The second contribution is a circuit model for electrodynamic–tether transmission lines that incorporates the high–voltage sheath dynamics. The transmission–line circuit model, which can be applied to insulated and uninsulated plasma–immersed cylinders, is implemented with the standard SPICE circuit–simulation program. The SPICE implementation allows complete tether systems to be modeled by including circuit–models of the endpoints (which produce perturbations on the tether) with the tether model itself. A range of excitation methods can be analyzed. Implementation in SPICE also requires closed–form (*i.e.*, non–transcendental and non–iterative) solutions for the parameters. This is in contrast with the complicated dispersion relations often derived for waves on plasma–immersed conductors.

There are two other contributions of this work that are included in the appendices. The first is an analysis of the far–field plasma environment of the hollow–cathode assembly (HCA). This experimental characterization shows that the HCA can be used to provide a plasma environment which closely resembles that found in the ionosphere. The remaining contribution is a transient circuit model of the Tethered Satellite System that was developed. This model was used to analyze TSS–1 mission data and used a rigid coaxial model of the TSS tether which is valid under the low–voltage conditions of the TSS–1 mission.

Throughout this work we assume a tether transmission line with TSS geometry. The models can be extended to other tether geometries, in addition to other plasma–(insulator)–conductor geometries for which the conductor diameter is on the order of or smaller than the Debye length or, alternately, much smaller than the sheath distance.

In developing the transmission–line model, we first developed a model of the sheath response for a section of the transmission line. Then, certain assumptions were made to allow the model to become distributed along the length of the line. Direct distributed results were not possible for three reasons. First, no Earth–bound experimental system was large enough to contain even a few tens of meters of tether transmission line. This is certainly the case for the low–density plasmas and high voltages needed to simulate propagation along the tethered system in the ionosphere since the dynamic sheath can be large and magnetic fields can penetrate a long distance from the line.[2] Second, particle–in–cell simulations of such a system are not possible due to the computational costs of simulating even a few tens of meters. In addition, since the scope of this work was not PIC–code development, we relied on an available code which does not simulate propagation delay along a conductor.[3] Third, the TSS system might have been able to provide some info on propagation velocities, but the unfortunate break before achieving full deployment made moot the scheduled experiments.

1.4 Dissertation Overview

The six chapters of this dissertation are structured as follows:

Chapter I gives an introduction to the research, the contributions made by it, the scope of the study, and an outline of the dissertation.

Chapter II provides background information relevant to this work as well as a literature survey on previous work in the field.

Chapter III develops a voltage–dependent sheath model valid in the frequency regime between the electron and ion plasma frequencies. This model is developed analytically and verified via plasma–chamber experiments and particle–in–cell simulations.

Chapter IV develops a circuit model of the tether transmission line with parameters based on the dynamic, voltage–dependent sheath.

---

[2]For low voltages (*i.e.*, static sheaths) and/or higher plasma densities, the technique of spiraling a long conductor, similar to that of *Morin and Balmain* [1993], could be employed.

[3]The extensibility of the XOOPIC code, however, does allow the possibility of including such features [*Verboncoeur et al.*, 1995].

Chapter V implements the tether–transmission–line circuit model in SPICE and employs the model to examine several different excitations along the tether.

Chapter VI presents the conclusions of this dissertation and provides suggestions for future research.

In addition, this dissertation contains six appendices which are structured as follows:

Appendix A summarizes the ionospheric plasma parameters used in this work.

Appendix B presents the results of a study on the far–field plasma environment of a hollow–cathode assembly and its application to ionospheric plasma research.

Appendix C presents Langmuir–probe measurement theory for plasma measurements in the orbital–motion–limited regime.

Appendix D includes the description of a transient circuit model of the Tethered Satellite System which was developed and analyses of TSS mission data performed with the model.

Appendix E contains listings of the simulation input files for the numerical simulations performed in the dissertation.

Appendix F presents a table of the nomenclature used in the dissertation.

CHAPTER II

Background and Previous Work

This chapter provides background information of importance to the present work as well as a literature survey of previous work in the field. The chapter begins with a general description of plasmas, plasma resonance frequencies, and the ionospheric plasma environment. Plasma–object interactions are then described, which include plasma sheaths, current collection, and pulsed–voltages to surfaces in plasmas. The next section describes electrodynamic tethers and tether potential structures. Following that is a review of research regarding antennas in plasmas and sheath waves along conductors in plasmas. Finally, an overview of various nonlinear transmission lines is presented.

2.1 Cold, Low–Density Plasmas

2.1.1 Definition of a Plasma

The word *plasma* comes from a Greek word meaning "something molded or formed." The term was first applied by I. Langmuir to the ionized gas of an electric discharge and is now applied to a wide variety of macroscopically neutral substances that contain many free electrons and ionized atoms or molecules exhibiting a collective behavior. To be labeled accurately as a plasma, a candidate substance must satisfy the *plasma criteria*, which are described below.

First, a plasma must be macroscopically neutral, sometimes also known as "quasi–neutral". What this means is that, in the absence of disturbances (in equilibrium with no external forces present), the net charge in a given volume of plasma must be zero. Thus, the microscopic space–charge fields in the plasma's interior cancel each other and no net space charge exists over a macroscopic region. That is, the direction of the internal electric forces tends to reduce the space–charge density. Hence, plasma electrons and ions are bound to each other collectively by the space–charge forces. This condition can be written mathematically as

$$|n_e - \sum_k Z_{ik} n_{ik}| \ll n_e, \tag{2.1}$$

where n_e is the electron density, Z_{ik} is the ionization level of the kth ion species, and n_{ik} is the density of the kth ion species. However, in most analytic work on plasmas, except when using Poisson's equation, Equation (2.1) is written as $n_e = \sum_k Z_{ik} n_{ik}$.

Second, the dimensions of the plasma must be larger than a Debye length, denoted λ_D, which is the most fundamental unit of length in a plasma. The Debye length, which is developed in Section 2.2.1, is independent of particle mass and makes no assumptions about the absence of neutral particles. Hence, a plasma does not depend on the degree of ionization. Mathematically, this criterion is written

$$L_p \gg \lambda_D = \sqrt{\frac{\varepsilon_0 k T_e}{q^2 n_e}}, \tag{2.2}$$

where L_p represents the characteristic scale–length or size of the plasma, ε_0 is the permittivity of free space, k is Boltzmann's constant, T_e is the electron temperature in Kelvin, and q is the elementary charge.

Third, the number of electrons inside a Debye sphere, N_D, must be very large, *i.e.*,

$$N_D = \frac{4\pi}{3} n_e \lambda_D^3 \gg 1. \tag{2.3}$$

This criterion is due to the shielding effects of plasmas that result from the collective particle behavior inside a Debye sphere. Thus, this criterion also means that the average distance between electrons must be very small when compared to λ_D.

2.1.2 Cold–Plasma Approximation

It is often desirable to make certain simplifying approximations about the plasma medium such that a solution to a given problem can be found. One such approximation is called the *cold-plasma* approximation. This approximation is made by forcing the electron and ion temperatures to zero, or alternatively, by ignoring thermal particle motions [*Hutchinson*, 1987]. Electrons (and ions) are taken to be at rest except for motions induced by external forces such as wave fields. The cold–plasma approximation implies that the thermal speed of the particles is so low that they do not move a "wavelength" in one wave period [*Krall and Trivelpiece*, 1986]. In addition, in the cold–plasma approximation, all particles move alike, *i.e.*, there is no thermal spreading.

A cold plasma, however, is a purely analytical tool since, in reality, most plasmas have at least one thermal velocity component. The cold plasma approximation is also singular since $\lambda_D \to 0$ as $T_e \to 0$. Despite these caveats, the cold plasma approximation allows us to learn by using simple initial conditions and easily understood diagnostics.

2.1.3 Plasma Resonance Frequencies

Knowledge of several plasma resonance frequencies is important since objects immersed in plasmas generally exhibit resonances when excited at these frequencies.

Table 2.1: Summary of plasma resonance frequencies, with typical values for ionospheric plasma ($B_0 = 0.35$ G $= 3.5 \times 10^{-5}$ T, $n_e = n_i = 10^{12}$ m^{-3}, O$^+$ ions).

Resonance Frequency	Nomenclature	Equation	Typical Value
electron plasma	$\omega_{pe} = \omega_p$	$\sqrt{\frac{n_e q^2}{\varepsilon_0 m_e}}$	56.4 Mrad/s (8.98 MHz)
ion plasma	ω_{pi}	$\sqrt{\frac{n_i Z_i^2 q^2}{\varepsilon_0 m_i}}$	329 krad/s (52.3 kHz)
electron cyclotron	ω_{ce}	$\frac{qB_0}{m_e}$	6.16 Mrad/s (908 kHz)
ion cyclotron	ω_{ci}	$\frac{Z_i q B_0}{m_i}$	209 rad/s (33.3 Hz)
upper hybrid	ω_{uh}	$\sqrt{\omega_{pe}^2 + \omega_{ce}^2}$	56.7 Mrad/s (9.03 MHz)
lower hybrid	ω_{lh}	$\frac{1}{\omega_{lh}^2} = \frac{1}{\omega_{ce}\omega_{ci}} + \frac{1}{\omega_{pe}^2}$ $\approx \sqrt{\omega_{ce}\omega_{ci}}$	35.9 krad/s (5.71 kHz)

For example, the input impedance of an antenna exhibits resonance at the plasma frequency. In this section, a qualitative description of these plasma resonance frequencies is given and also equations for their calculation. Table 2.1 summarizes and presents typical values of each for a typical low–Earth–orbit (LEO) ionospheric plasma. More detailed descriptions of these frequencies and their derivation may be found in *Stix* [1992] and *Chen* [1984].

We begin by looking at two important plasma resonance frequencies: the electron plasma frequency and the ion plasma frequency. In a plasma, if the electrons are displaced from a uniform background of ions, then an electric field is established in the direction which restores the neutrality of the plasma by restoring the electrons to their original positions. As the electrons are being restored to their original (equilibrium) positions, they overshoot because of their inertia and oscillate around their equilibrium positions at a characteristic frequency known as the electron plasma frequency, ω_{pe}. This frequency is also known simply as the plasma frequency, ω_p, and is given by

$$\omega_p = \omega_{pe} = \sqrt{\frac{n_e q^2}{\varepsilon_0 m_e}}, \tag{2.4}$$

where m_e is the electron mass. Since the ions are much heavier than the electrons, the electron oscillations occur on a timescale much shorter than the ion response time. Hence, in the above description, the ion locations were considered fixed. However, if the electrons could be held fixed and the ions displaced, then an ion plasma frequency, ω_{pi}, could be similarly derived. This frequency is defined by

$$\omega_{pi} = \sqrt{\frac{n_i Z_i^2 q^2}{\varepsilon_0 m_i}}, \tag{2.5}$$

where m_i is the ion mass and Z_i is the ionization level; *e.g.*, for O^+, $Z_i = +1$.

In a magnetized plasma, the electrons and ions have characteristic cyclotron frequencies since the particles tend to circle around the magnetic field lines due to the Lorentz force. The electron cyclotron frequency, ω_{ce}, is given by

$$\omega_{ce} = \frac{q|\mathbf{B}_0|}{m_e} = \frac{qB_0}{m_e}. \tag{2.6}$$

where $\mathbf{B}_0$ is an external (*i.e.*, not caused by the plasma itself) magnetic field. Similarly, the ion cyclotron frequency, ω_{ci}, is given by

$$\omega_{ci} = \frac{Z_i q|\mathbf{B}_0|}{m_i} = \frac{Z_i q B_0}{m_i}. \tag{2.7}$$

There are two additional characteristic plasma resonances which are important when dealing with wave propagation in magnetized plasma: the upper hybrid and lower hybrid frequencies. The upper hybrid frequency, ω_{uh}, which is defined by

$$\omega_{uh} = \sqrt{\omega_{pe}^2 + \omega_{ce}^2}, \tag{2.8}$$

is the frequency of electrostatic waves across $\mathbf{B}_0$, whereas waves along $\mathbf{B}_0$ are the usual plasma oscillations with $\omega = \omega_{pe}$. As in the description of the electron plasma frequency, ions are considered to be stationary and electrons in the plane wave form regions of compression and rarefaction. However, the electron trajectories become ellipses due to the Lorentz force since $\mathbf{B}_0$ is perpendicular to electron movement. The two restoring forces, the electrostatic field (which gives ω_{pe}) and the Lorentz force (which gives ω_{ce}), make the upper hybrid frequency larger than that of only the plasma frequency.

The lower hybrid frequency, ω_{lh}, results from allowing ion motion in the description above and examining propagation perpendicular to $\mathbf{B}_0$. The frequency is given by

$$\frac{1}{\omega_{lh}^2} = \frac{1}{\omega_{ce}\omega_{ci}} + \frac{1}{\omega_{pe}^2} \tag{2.9}$$

or approximately as

$$\omega_{lh} \approx \sqrt{\omega_{ce}\omega_{ci}} \tag{2.10}$$

when $\omega_{ce}\omega_{ci} \ll \omega_{pe}^2$. At the lower hybrid frequency, the displacement of the massive ions by the E–field is equal to the electron displacement due to the polarization drift.

2.1.4 Ionospheric Plasma Environment

An important example of a low-density plasma region is the Earth's ionosphere. This section gives some background information on the ionosphere at approximately 300–km altitude since one important application of this work is ionospheric electrodynamic tethers. Additionally, since this work is applied to tether systems primarily in low Earth orbit (LEO)—approximately 300–km altitude—we will concentrate on typical ionospheric plasma parameters at this altitude.

The ionosphere, in practice, has a lower limit of about 50 to 70 km and has no distinct upper limit, although an arbitrary limit of about 2000 km is set for most application purposes. The ionosphere tends to vary greatly with geomagnetic latitude and can be divided into three distinct regions: high–latitude, mid–latitude, and low–latitude [*Tascione*, 1988]. The high–latitude ionosphere is coupled to the magnetospheric tail by the stretched auroral magnetic–field lines which yields important consequences for this region. The low–latitude region is sensitive to plasma instabilities and changes to the magnetospheric ring current. The mid–latitude is easiest to understand since it most closely follows classical ionospheric models.

Experimental data on the neutral and ion composition of the Earth's atmosphere from 100 to 1000 km is shown in Figure 2.1. The 150–500 km altitude range is called the F–region and the altitude of maximum plasma density is termed the F–peak. In this region, nearly all of the ions are O^+ ions, which is to be expected since there is a high concentration of atomic oxygen in the neutral gas. It can also be seen that the plasma is quasi–neutral, that is, the electron and ion densities are equal. Typical plasma densities around 300–km altitude are in the range of 10^5 to 10^7 cm^{-3}, and vary due to day/night conditions, solar activity, latitude and longitude, and local perturbations.

Another aspect of ionospheric plasma is that it is magnetized by the geomagnetic field and as such is anisotropic. To first order, the geomagnetic field is that of a dipole tilted 11°, with respect to the Earth's spin axis, towards the North American continent. In the northern hemisphere, the **B**–field points toward the Earth's surface, whereas it points away in the southern hemisphere. That is, the Earth's magnetic field points from south to north. Approximate values of $\mathbf{B}_E$ (without tilt) can be determined from the following equation [*Kelly*, 1989]

$$\mathbf{B}_E = \frac{-0.6R_E^3}{R_c^3}\sin\theta_m\,\hat{r} + \frac{0.3R_E^3}{R_c^3}\cos\theta\,\hat{\theta}\ (\mathrm{G}), \tag{2.11}$$

where $R_E = 6371$ km is the Earth's radius, θ_m is magnetic latitude, and R_c is the

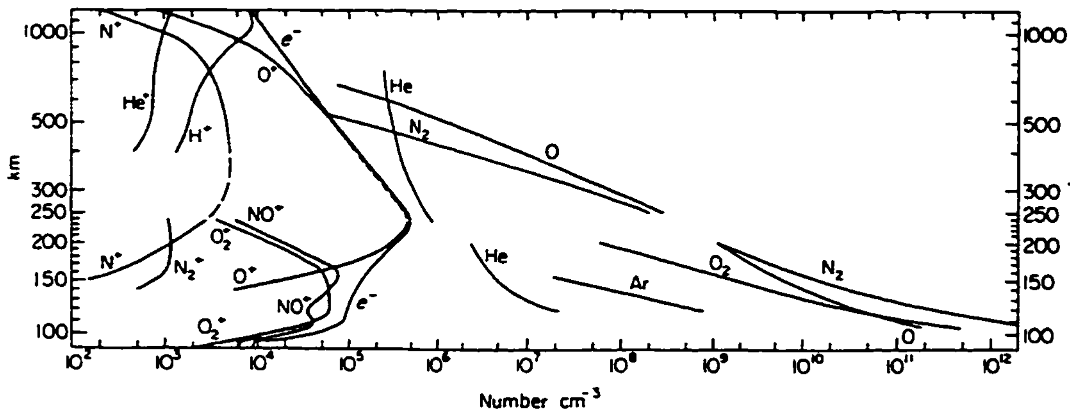

Figure 2.1: International Quiet Solar Year (IQSY) daytime atmospheric composition over White Sands, NM (32°N, 106°W). Helium measurements taken at nighttime. [Reprinted from *Johnson* [1969] by permission of the MIT Press, Cambridge, MA, USA. ©1969 MIT.]

distance from the Earth's center. The magnitude of $\mathbf{B}_E$ is given by

$$B_E = |\mathbf{B}_E(R_c, \theta_m)| = \frac{0.3 R_E^3}{R_c^3}\sqrt{1 + 3\sin^2\theta_m}\ (\mathrm{G}). \tag{2.12}$$

The magnitude of $\mathbf{B}_E$ varies from about 0.25 G at the magnetic equator to about 0.6 G near the poles on the Earth's surface. B_E decreases as $1/R_c^3$, so that at 300-km altitude it is approximately 0.9 times that on the surface.

2.2 Plasma–Object Interactions

2.2.1 Plasma Sheaths and Debye Length

When an object is immersed in a plasma, a contact-potential region, or plasma sheath, is formed between the object and the plasma in order to maintain the plasma's quasi-neutrality. The plasma sheath serves to shield the object's electric potential from the bulk of the plasma. Across the sheath region there is a voltage drop which is similar in form to the contact potential appearing at a p–n semiconductor junction. In this space–charge region, the electric potential of the object transitions to the undisturbed plasma potential.

The existence of the space–charge region is shown via the following physical argument. If we assume that the average thermal energies of the ions and electrons are equal,[1] *i.e.*, $\frac{1}{2}m_i v_{ti}^2 = \frac{1}{2}m_e v_{te}^2$, then because electrons have much less mass than ions, the velocity of electrons must be much greater than that of the ions, *i.e.*, $v_{te} \gg v_{ti}$.[2] Therefore, the random–particle current density must be much greater for electrons than for ions, $j_e \gg j_i$. Thus, the electron current to the body is initially greater than the ion current when the body is brought into contact with the plasma, and the body charges negatively until its potential is sufficiently lowered so that the net current to the body is zero. For the body to be in equilibrium, an equal number of positive and negative charges must arrive at the body per unit of time. Therefore, there must be a potential difference, or contact potential, between the plasma and the body to repel electrons and attract ions so that the currents are equal. This also means that the positive and negative charge densities within the region are unequal.

The transitioning space–charge region can be divided into two subregions: the *sheath* and the *presheath* (Figure 2.2). The sheath region has a strong potential gradient starting at the object wall and is not quasi–neutral at first since it is dominated by attracted species. Further away from the object, the potential transitions from object potential, V_a, to plasma potential, V_p, and the region becomes more quasi–neutral. The scale–length of this region, r_s, marks the sheath "edge". The presheath has a much longer scale–length than the sheath region. It is in this region that the transition from sheath–edge potential, V_e, to plasma potential occurs.

The sheath thickness is generally several times the Debye length, λ_D, which

[1]The electron average thermal energy, however, is often somewhat greater.
[2]Electron and ion thermal velocities are described in more depth at the end of this section.

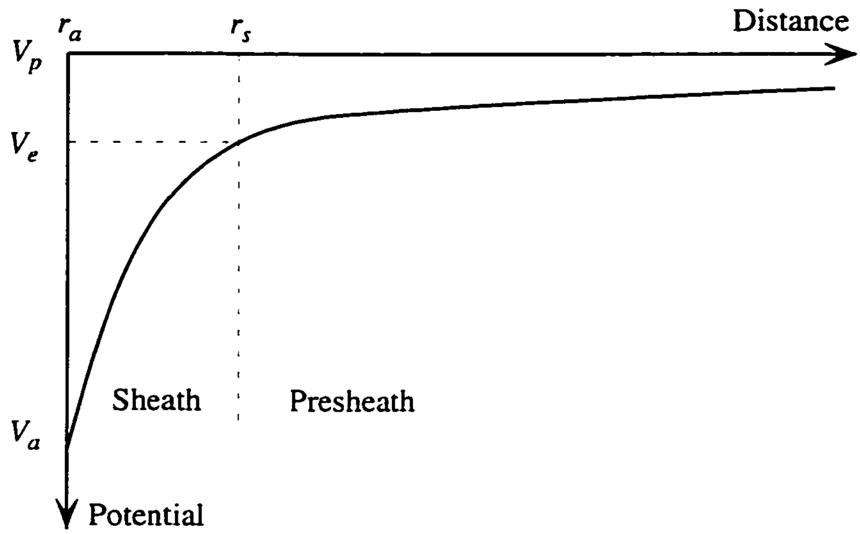

Figure 2.2: Plasma sheath geometry for negative object potential.

is a scale–length defined as the distance required to drop the potential to e^{-1} of the difference between the object potential and the plasma potential. The Debye length—which can also be considered the shielding distance around a test charge and the scale–length inside of which particle–particle effects occur most strongly and outside of which collective effects dominate [*Birdsall and Langdon*, 1985]—is given by

$$\lambda_D = \sqrt{\frac{\varepsilon_0 k T_e}{q^2 n_e}}, \tag{2.13}$$

where the electron temperature, T_e, is given in Kelvin. Another physical understanding of the Debye length [*Birdsall and Langdon*, 1985] is that it is the distance traveled by a particle at its thermal speed in $1/2\pi$ of the plasma cycle (valid for both electrons and ions[3]), *i.e.*,

$$\lambda_D = \frac{v_{te}}{\omega_{pe}} = \frac{v_{ti}}{\omega_{pi}}, \tag{2.14}$$

[3]Strictly speaking, the Debye length is typically not defined in terms of ion parameters such as T_i and n_i; however, for the qualitative definition given here, these parameters work.

where v_{te} and v_{ti} are the electron and ion thermal speeds, respectively. From Equation (2.4) for ω_{pe} and Equations (2.13) and (2.14) for λ_D, v_{te} is easily determined to be $v_{te} = \sqrt{\frac{kT_e}{m_e}}$. The ion thermal velocity is similarly defined as $v_{ti} = \sqrt{\frac{kT_i}{m_i}}$.[4] A sheath is referred to as "thin" or "thick" depending on the size of λ_D as compared to a characteristic object length, L_o, such as the radius, r_a, of a cylinder or a sphere. For a thin sheath, $L_o \gg \lambda_D$, whereas for a thick sheath, $L_o \ll \lambda_D$.

2.2.2 Current Collection to Probes in Plasmas

Two different theories exist that describe current collection to metallic probes in plasmas. These two theories, in effect, represent the limiting cases for current collection and which is used depends on whether a thin or thick sheath exists around the probe. For the thin-sheath case ($L_o \gg \lambda_D$) the Child–Langmuir (CL) theory applies, whereas for the thick-sheath case ($L_o \ll \lambda_D$) the orbital-motion-limited (OML) theory applies. This section will not explore the many nuances of each theory, but will merely provide a brief overview of each. In addition, the detailed derivations of each theory will not be presented, rather only the final results. For more detailed explanations, the reader is referred to the many review articles and books on electrical probes in plasmas [*e.g.*, *Schott*, 1995; *Swift and Schwar*, 1969, and others]. In this section, emphasis will be placed on OML theory since, as we shall see, the application of electrodynamic tethers generally falls in this regime.

[4] While some authors [*e.g.*, *Tanenbaum*, 1967] define the thermal speed in this manner, it should be noted that other authors [*e.g.*, *Chen*, 1984] define the thermal speed as $v_t = \sqrt{2kT/m}$. This brings up an interesting point about the various speeds derived from a Maxwellian distribution. The most-probable speed—also called the "most-probable thermal speed" [*Calder et al.*, 1993]—is given by $v_{\text{prob}} = \sqrt{2kT/m}$, the average speed $v_{\text{avg}} = \langle v \rangle = \sqrt{8kT/(\pi m)}$, and the root-mean-square (RMS) speed $v_{\text{rms}} = \sqrt{\langle v^2 \rangle} = \sqrt{3kT/m}$. The relation between these speeds is

$$v_{\text{prob}} = \frac{\sqrt{\pi}}{2} v_{\text{avg}} = \sqrt{\frac{2}{3}} v_{\text{rms}}.$$

For the derivation of these speeds see §5.4 of *Holt and Haskell* [1965].

2.2.2.1 Child–Langmuir Current Collection

The Child–Langmuir theory of current collection (also called "space–charge–limited" current collection) applies when the sheath is thin compared to the object size. In the CL case, a space–charge region surrounds the object preventing the perturbing fields from penetrating any significant distance into the plasma. Hence, the sheath's space charge limits the collection of current to the probe; the current is limited to that of the attracted–species' thermal currents by preventing acceleration to the probe of plasma particles outside of the sheath region. Figure 2.3 shows a schematic of the particle trajectories in a CL sheath.

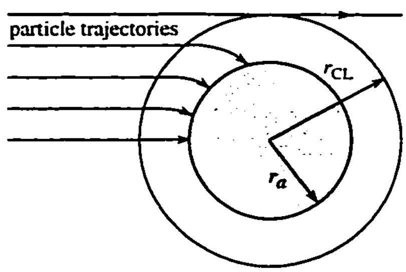

Figure 2.3: Child–Langmuir (space–charge–limited) sheath schematic.

The Child–Langmuir law [*Child*, 1911; *Langmuir*, 1913] is an expression for the current collected by a planar surface held at a potential of V_a with respect to the plasma and having a sheath of thickness $r_s = r_{\mathrm{CL}}$ and is written

$$j_{\mathrm{CL}} = \frac{4}{9} q_k \varepsilon_0 \sqrt{\frac{2}{q m_k}} \frac{|V_a|^{3/2}}{r_{\mathrm{CL}}^2}, \tag{2.15}$$

where the subscript $k = i, e$ depending on the attracted species. The CL law can be applied to many non–planar geometries since curved surfaces can be approximated as planes for sheaths that are thin enough. However, the law assumes $T_k \sim 0$.

Langmuir and Blodgett [1924] extended the CL law to planar, cylindrical, and spherical geometries with the assumptions of no collisions, no magnetic field, and Maxwell–Boltzmann velocity distribution. In this extension, Equation (2.15) becomes

$$j_{\mathrm{LB}} = \frac{4}{9} q_k \varepsilon_0 \sqrt{\frac{2}{q m_k}} \frac{|V_a - V_m|^{3/2}}{\alpha_{\mathrm{LB}}^2} \left(1 + \frac{2.66}{\sqrt{|\tilde{V}_a|}}\right), \tag{2.16}$$

where V_m is the potential minimum in the sheath,

$$\tilde{V}_a = \frac{q(V_a - V_m)}{kT_k},$$

and α_{LB} has the meaning of modified sheath factor in the three geometries:

- planar

$$\alpha_{\mathrm{LB}}^2 = r_s^2,$$

- cylindrical

$$\alpha_{\mathrm{LB}}^2 = r_a^2(\gamma - 0.4\gamma^2 + 0.09167\gamma^3 + \cdots)^2,$$

- spherical

$$\alpha_{\mathrm{LB}}^2 = r_a^2(\gamma^2 - 0.6\gamma^3 + 0.24\gamma^4 + \cdots),$$

where $\gamma = \ln(r_s/r_a)$ and T_k is the temperature of the attracted species. In most cases, V_m is small enough to be neglected. For large V_a, the value of $2.66/\sqrt{\tilde{V}_a} \to 0$ and thus can be neglected, whereby it is apparent that Equation (2.16) approximates Equation (2.15). The use of Equation (2.16) for large sheath thicknesses ($r_s \gg r_a$) or low densities ($r_a \ll \lambda_D$) is not recommended since the formula is derived on the assumption of radial motion. For these regimes, we must use the OML theory described in Section 2.2.2.2 below.

Equation (2.16) assumes zero velocity with respect to the plasma and cannot be directly applied to a rapidly moving body [*Garrett*, 1981]. Several researchers

[*Godard*, 1975; *Godard and Laframboise*, 1983; *Godard et al.*, 1991] have developed theories for current flow to cylindrical and spherical collectors in a collisionless plasma flow under the assumptions of thermal electrons and mesothermal ion flow $\theta_{ir} \gg \theta_i$. *Laframboise and Sonmor* [1993] review the probe theories for current collection in magnetoplasmas.

2.2.2.2 Orbital–Motion–Limited Current Collection

An OML sheath exists around the conductor for the case of a thin cylindrical conductor ($r_a \ll \lambda_D$) or if $r_a \ll r_s$, which occurs for large applied voltages. Unlike the CL–sheath derivation, which holds in the regime $r_a \gg \lambda_D$, not all particles which enter the OML sheath are collected, only those with trajectories that can be bent to the cylinder or sphere radius while still conserving angular momentum.[5] This situation is shown in Figure 2.4.

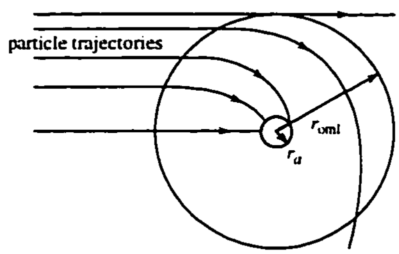

Figure 2.4: Orbital–motion–limited sheath schematic.

For an attracted species, $k = e, i$, *Laframboise* [1966] states that the orbital–motion–limited current density is given by

$$j_{\mathrm{oml}} = q_k n_{k0} v_{tk} \sqrt{\frac{2}{\pi}} \times \begin{cases} \dfrac{2}{\sqrt{\pi}} \left[\sqrt{\tilde{V}_a} + g\left(\sqrt{\tilde{V}_a}\right) \right], & \text{for a cylinder} \\ 1 + \tilde{V}_a, & \text{for a sphere,} \end{cases} \tag{2.17}$$

[5]Note that it does not make sense to talk about an orbital–motion limit for the planar case since $r_a \ll \lambda_D$ can never be satisfied.

where the function $g(x)$ is defined as

$$g(x) = \frac{\sqrt{\pi}}{2} \exp(x^2)[1 - \mathrm{erf}(x)].$$

The collected OML current is simply $i_{\mathrm{oml}} = j_{\mathrm{oml}} A$, which for a cylinder is per–unit–length collection. For large values of x, $\mathrm{erf}(x) \to 1$, hence $g(x) \to 0$ and can be ignored. For a cylinder radius of r_a, the OML current collected per unit length is thus given by the following equation

$$j_{\mathrm{oml}} \simeq 2\sqrt{2} r_a n_{k0} q_k v_{tk} \sqrt{\frac{q|V_a|}{kT_k}}. \tag{2.18}$$

It is interesting to note from Equation (2.18) that j_{oml} does not depend on the sheath radius, r_s. At first, this may seem strange since in the Child–Langmuir case, j_{CL} does depend on the sheath distance. However, unlike the CL case in which all attracted particles within the sheath are collected, for the OML case it is particles within an "impact radius" that are collected [*Laframboise*, 1966; *Allen*, 1992]. This impact radius is defined as $r_m(\theta_{k0}) = r_a(1 + V_a/\theta_{k0})^{1/2}$, where the initial energy of the attracted particle ($k = e, i$) is θ_{k0}. Hence, attracted particles which come in at the critical trajectory that just grazes r_m define the impact radius (or "absorption boundary"). The impact radius cannot be used to obtain easily the collected current since, in general, each particle will have a different energy and hence defines a different absorption boundary [*Whipple*, 1990]. Thus, the total current for the OML case is developed from a statistical integration of the particle energies as defined by a Maxwellian distribution, masking any well–defined sheath radius.

2.2.3 Plasma–Immersion Ion Implantation

The plasma–immersion ion implantation (PIII) technique[6] is a relatively new research area which involves application of large negative potentials to conductors in plasmas [*Chu*, 1996][7]. PIII is a non–line–of–sight process for injecting ions into primarily metallic and semiconductor objects in order to change their surface properties. PIII works by immersing a target in a plasma and applying a highly negative voltage pulse to it. This forms a sheath which accelerates ions into the target [*Emmert and Henry*, 1992]. Typical parameters for PIII are $n_e \sim 10^{15}$ to 10^{18} m^{-3}, $T_e \sim 1$ to 5 eV, applied voltage $V_a \sim -5$ to -50 kV, and pulse width $\tau_{ap} \sim 1$ to 10 μs [*Shamim et al.*, 1991]. The interest in transient sheath development for the PIII researchers is in predicting how many ions are implanted in the material per high–voltage pulse. Since sheath size and dynamics affect current and dosage levels, these researchers need to know how the sheath develops away from the substrate. While interest in sheath morphology has been revived recently due to its application in PIII, some of the earlier work on expanding sheaths was performed in the early 1970s [*e.g.*, *Chester*, 1970; *Andrews*, 1970; *Andrews and Varey*, 1971]. In addition, there is a fair amount of work in the literature (not necessarily related to PIII) dealing with the quick application of large negative potentials to spherical and cylindrical conductors [*e.g.*, *Ma and Shunk*, 1992; *Laframboise and Sonmor*, 1993; *Collins and Tendys*, 1994].

Let us begin with a qualitative description of what happens to the plasma surrounding the target during PIII. Initially, a high–voltage pulse is applied to the

[6]The PIII technique is also called the plasma–source ion implantation (PSII) technique. PIII appears to have become be the preferred name in order to differentiate it from conventional beamline implantation encompassing other plasma ion sources.

[7]This is an excellent review article on PIII which summaries theory, experiment, and applications.

target and electrons are driven away from the surface on the timescale of the inverse electron plasma frequency ($\sim \tau_{pe} = 2\pi/\omega_{pe}$, typically on the order of nanoseconds). After the electrons have been expelled, a uniform density "ion–matrix" sheath is left behind.[8] The ions within this sheath are then accelerated into the target on the timescale of the inverse ion plasma frequency ($\sim \tau_{pi} = 2\pi/\omega_{pi}$, typically on the order of microseconds). The sheath–edge is then driven further away from the target exposing new ions for extraction; this expansion speed is usually faster than the ion–acoustic speed, but gradually slows down. Finally, a steady–state Child–Langmuir–law sheath evolves on a much longer timescale ($t \gg 2\pi/\omega_{pi}$) around the target. In PIII, the voltage is fairly quickly returned to zero before the CL sheath fully develops since the CL sheath thickness generally exceed the plasma size [*Lieberman*, 1989]. It is the ion–matrix sheath and its temporal evolution which determine the current and the energy distribution of implanted ions.

Lieberman [1989] and others [*e.g.*, *Scheuer, et al.*, 1990] have developed a model of sheath evolution during PIII, which is based on several assumptions:

- The ion flow is collisionless.
- Electron motion is inertia–less. This assumption follows from the fact that the characteristic implantation timescale is much larger than τ_{pe}.
- The electron temperature, $\theta_e = kT_e/q$, is much smaller than the applied voltage, V_a. This means that Debye length is much smaller than the initial sheath size, $\lambda_D \ll r_{\rm sh}$, and the sheath edge is abrupt.
- The quasi–static CL–law sheath forms during and after matrix–sheath implan-

[8]The electrons will tend to oscillate as they are expelled before they settle at the ion–matrix sheath distance if $\tau_{ar} \ll \tau_{pe}$. This situation is discussed in Section 3.2.4, but for most PIII implementations $\tau_{ar} \gtrsim \tau_{pe}$.

tation. This means that the current demanded by the sheath is provided by the ions that are uncovered at the moving sheath edge as well as ions drifting to the target at the Bohm (ion–sound) speed, $u_B = \sqrt{kT_e/m_i}$.

- The electric field across the sheath is frozen at its initial value during the motion of an ion across the sheath.

The sheath size as a function of time is derived in the following manner. We begin with the Child–Langmuir law [Equation (2.15)], which provides the current density $j_{\rm CL}$ for a voltage V_s across a space–charge–limited sheath of thickness r_s:

$$j_{\rm CL} = \frac{4\varepsilon_0}{9}\sqrt{\frac{2q}{m_i}}\frac{|V_s|^{3/2}}{r_s^2}. \tag{2.19}$$

The charge per unit time crossing the sheath boundary is also another way to determine the current density, that is

$$j = q_e n_0 \left(\frac{dr_s}{dt} + u_B\right). \tag{2.20}$$

If equations (2.19) and (2.20) are equated, then we find an equation for the sheath velocity

$$\frac{dr_s}{dt} = \frac{2}{9}\frac{r_{\rm sh}^2 u_0}{r_s^2} - u_B, \tag{2.21}$$

where

$$r_{\rm sh} = \sqrt{\frac{2\varepsilon_0 V_s}{q_e n_0}} \tag{2.22}$$

is the ion–matrix sheath thickness (which will be derived in Section 3.2.1) and

$$u_0 = \sqrt{\frac{2q_e V_s}{m_i}} \tag{2.23}$$

is the characteristic ion velocity. When (2.21) is integrated, the following equation for sheath–edge position as a function of time is obtained,

$$\tanh^{-1}\left(\frac{r_s}{r_{\rm CL}}\right) - \frac{r_s}{r_{\rm CL}} = \frac{u_B t}{r_{\rm CL}} + \tanh^{-1}\left(\frac{r_{\rm sh}}{r_{\rm CL}}\right) - \frac{r_{\rm sh}}{r_{\rm CL}}, \tag{2.24}$$

where the steady–state CL–law sheath thickness, $r_{\rm CL}$, is obtained from (2.19) by setting $j_{\rm CL} = q_e n_0 u_B$:

$$r_{\rm CL} = r_{\rm sh}\sqrt{\frac{2}{9}\frac{u_0}{u_B}}. \tag{2.25}$$

In the limit of $r_s \ll r_{\rm CL}$ and since $r_{\rm sh} \ll r_{\rm CL}$, we find that

$$r_s = r_{\rm sh}[(2/3)\omega_{pi}t + 1]^{1/3}. \tag{2.26}$$

The timescale for establishing the steady–state CL sheath, $\tau_{\rm CL}$, can be found by substituting Equation (2.25) into Equation (2.26) and solving for t, which yields $\tau_{\rm CL} \sim (\sqrt{2}/9)\tau_{pi}(2q_eV_s/kT_e)^{3/4}$. In PIII, it is generally assumed that the applied–voltage pulse width, τ_{ap}, is much less than this time, *i.e.*, $\tau_{ap} \ll \tau_{\rm CL}$.

Qin et al. [1995] state that there is still some controversy as to whether to include u_B in the dynamic–sheath model. They believe that the dynamic–sheath model without the u_B term is a good approximation for most applications where heavier ions are implanted, ion density is relatively low, and the pulse potential is relatively high. The u_B term cannot be neglected, however, when the sheath–expansion speed is not higher than the ion–acoustic speed.

Other models for PIII have been proposed to alleviate some of the shortcomings of the model presented above that result from the initial assumptions. For example:

- The high–voltage–pulse risetime in the above derivation was assumed to be almost instantaneous. *Stewart and Lieberman* [1991] rederive sheath–expansion velocities for realistic pulses in which the voltage risetimes and falltimes constitute a significant fraction of the total pulse width.

- *Vahedi et al.* [1991] derive a general one–dimensional model in which the pressure of the neutrals is high enough such that the ion motion through the sheath is assumed to be highly collisional.

- *Scheuer, et al.* [1990] and other researchers have worked on extending the PIII model to cylindrical and spherical geometries. Other researchers have looked at non–symmetrical geometries such as square bars [*Sheridan*, 1994], trenches [*Sheridan*, 1996], and small bore holes [*Sheridan*, 1997].

One of the more effective methods for simulating PIII is via particle–in–cell (PIC) plasma simulation codes. (More detailed information on PIC may be found in Section 3.4.) For example, *Hong and Emmert* [1994, 1995] used a PIC code to develop a two–dimensional (2–d) fluid model of the PIII time–dependent sheath. Their code uses fluid equations for the cold, collisionless ions and couples that with Poisson's equation and with a Boltzmann relationship for the electrons. Their assumption of a Boltzmann relationship for the electrons allows their computation to jump over the electron timescale ($\sim 1/\omega_{pe}$) and solve the equations on the ion timescale ($\sim 1/\omega_{pi}$), which is the relevant timescale for sheath expansion. *Hahn and Lee* [1992] used a kinetic–PIC–simulation method for a bounded plasma system, which allowed them to include an external circuit as in laboratory experiments. This kinetic–PIC approach allowed them to predict kinetic properties which cannot be examined by the fluid approach. *Faehl et al.* [1994] used 2–d PIC simulations to examine the time–dependent formation of a sheath in PIII, including the depletion of the initial ion matrix and the expansion of the sheath into the plasma. They also looked at the role of insulating magnetic fields and secondary–electron production.

Measurements of the PIII sheath expansion have been made by many researchers including *Brutscher et al.* [1996] and *Shamim et al.* [1991].

2.2.4 Sheath Expansion and Collapse at Dielectric Surfaces

Emmert [1994] developed a model for the expanding sheath at dielectric surfaces in PIII that has some significant differences between it and the conductive–target solution assumed in the description of Section 2.2.3 above. These differences are due to the finite dielectric constant of the material and the accumulation of collected charge on its surface. This change in target material means that, on the timescale of the applied pulse, the charge implanted in the dielectric accumulates and cannot dissipate.

Similar to the case of a bare conductor, when a voltage V_a is applied to an insulated conductor, a negative voltage appears at the interface between the insulator and the plasma. This produces an ion–matrix sheath which expands into the plasma and ions are then accelerated toward the dielectric surface. These ions accumulate on the surface due to the low electrical conductivity of the dielectric and form a surface–charge layer with a charge density ρ_{sa}. Gauss' law allows us to determine the voltage across the sheath, V_s, as a function of time at the planar dielectric–plasma interface [*Emmert*, 1994]

$$V_s(t) = V_a(t) - \frac{E_s(t)r_d}{\varepsilon_d} + \frac{\rho_{sa}(t)r_d}{\varepsilon_d\varepsilon_0}, \tag{2.27}$$

where ε_d is the relative permittivity of the dielectric, E_s is the electric field in the plasma at the surface of the dielectric, and r_d is the thickness of the dielectric. Thus, the conductor voltage V_a is shielded, at least partly, by the presence of the surface charge.

Qin et al. [1995] perform a different analysis to arrive at the effect of dielectric charging on the ion current. During the high–voltage pulse, charge accumulates on the surface of the insulator. This charge builds up an opposing electric field which acts to partially cancel the exterior field that exists in the sheath. Thus, the ion current to the insulator will be reduced because of this reduced effective sheath potential. The charge which accumulates on the dielectric surface, Q_d, is given by

$$Q_d(t) = \int_0^t j_i(t)dt, \tag{2.28}$$

where $j_i(t)$ is a modified form of Equation (2.19) which includes the addition of a displacement–current term that results from the ion–matrix sheath and the ion–profile change during the pulse [*Qin et al.*, 1995; *Wood*, 1993], so that

$$j_i(t) = \frac{4\varepsilon_0}{9}\sqrt{\frac{2q}{m_i}}|V_s(t)|^{3/2}\left(\frac{1}{r_s^2(t)} + \frac{r_{\text{sh}}^2}{r_s^4(t)}\right). \tag{2.29}$$

The sheath voltage, V_s, in Equation (2.29) above is no longer a constant and becomes

$$V_s(t) = V_a - \frac{1}{C_d}\int_0^t j_i(t)dt, \tag{2.30}$$

where $V_s(t)$ is the effective sheath potential and C_d is the capacitance per unit area of the dielectric layer. Substituting the relation for j found in Equation (2.20) into Equation (2.30) we obtain

$$V_s(t) = V_a - \frac{n_0 q_e}{C_d}\left[\int_0^t dr_s + u_B\int_0^t dt\right], \tag{2.31}$$

and integrating, yields

$$V_s(t) = V_a - \frac{n_0 q_e}{C_d}[r_s(t) - r_{\text{sh}} + u_B t]. \tag{2.32}$$

An analytical model of oxide charging in PIII has been developed and implemented using SPICE. The use of a circuit simulation program such as SPICE allowed the plasma to be implemented as a nonlinear, time–dependent circuit element in which the sheath thickness is solved and ion current calculated [*En and Chung*, 1994]. This model was able to replicate measured quantities for sheath–quiescent, –expansion, and –collapse stages, as well as ion implant currents for a wide variety of voltage pulses and plasma conditions [*En and Chung*, 1994; *En et al.*, 1995].

In this model, the displacement current density, j_d, caused by the changing sheath capacitance was incorporated explicitly via the following relation

$$j_d = C_s \frac{dV_s}{dt} + V_s \frac{dC_s}{dt}, \tag{2.33}$$

where C_s is the sheath capacitance. In addition, their SPICE implementation facilitated the analysis of oxide–charging effects [*En et al.*, 1996] and charging at other dielectrics such as glass [*Linder and Cheung*, 1996].

2.3 Electrodynamic Tethers

Electrodynamic tethers are conducting wires—which may be fully or partially insulated—that join two separated spacecraft as they orbit the Earth or another planetary body having a magnetic field. The simplified, general geometry of a section of electrodynamic tether immersed in a magnetized plasma can be seen in Figure 2.5. The tether is represented by a cylindrical center conductor sheathed in a uniform dielectric. In reality, using the example of the Tethered Satellite System (TSS) tether, it may be constructed of stranded wire wrapped around a non–conducting core and covered with a dielectric sheathing made of several different materials (see Section 5.1.1 for a detailed description of the TSS tether). Not shown in this figure is the plasma sheath which forms around the tether and the effect of the magnetic field, which makes the plasma anisotropic. In the general geometry, the magnetic field may be arbitrarily oriented with respect to the tether, with different physics expected as that orientation changes. Propagation is along the z–axis and the cylinder is of arbitrary length.

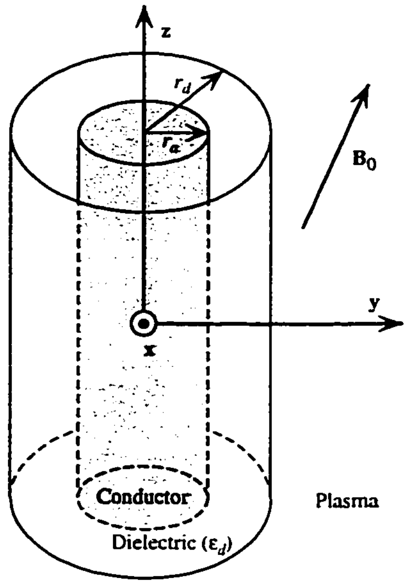

Figure 2.5: General cylindrical geometry for an electrodynamic tether.

2.3.1 Basic Principles of Electrodynamic Tethers

The principles behind the operation of an orbiting electrodynamic tether are fairly straightforward. In general, electrodynamic tethers possess three significant properties [*Banks*, 1989]: 1) due to the orbital motion of the tether, the wire has an intrinsic electromotive force (*emf*) generated along it, 2) the wire provides a low–resistance path connecting different regions of the ionosphere, and 3) access to external electron and ion currents is confined to specific locations, such as the endpoints, when the conductor is insulated. There are many papers that outline these principles in more detail, *e.g.*, *Banks* [1989] and *Banks et al.* [1981]. This section briefly describes the principles of electrodynamic tether systems using TSS as an example.

The first principle listed above, *emf* generation across the tether, results from the Lorentz force on the electrons in the tether as the system travels through the geomagnetic field. To determine the magnitude of this *emf*, we start with the Lorentz force equation for charged particles:

$$\mathbf{F} = q(\mathbf{E} + \mathbf{v}_s \times \mathbf{B}), \tag{2.34}$$

where $\mathbf{E}$ represents the ambient electric field and $\mathbf{v}_s \times \mathbf{B}$ represents the motional electric field. Since both terms in Equation (2.34) represent electric fields it can be rewritten as

$$\mathbf{F} = q\mathbf{E}_{\text{tot}}, \tag{2.35}$$

where $\mathbf{E}_{\text{tot}}$ is the total electric field and

$$\mathbf{E}_{\text{tot}} = \mathbf{E} + \mathbf{v}_s \times \mathbf{B}. \tag{2.36}$$

In order to get the total *emf* generated across the tether, we must integrate $\mathbf{E}_{\text{tot}}$ along the entire length of the tether, l. That is, the total tether potential, φ_{tether}, is

$$\varphi_{\text{tether}} = -\int_0^l \mathbf{E}_{\text{tot}}(l) \cdot d\mathbf{l} = -\int_0^l [\mathbf{E}(l) + \mathbf{v}_s(l) \times \mathbf{B}(l)] \cdot d\mathbf{l}, \tag{2.37}$$

which is negative since electrons in the tether are acted upon by the Lorentz force. The tether potential, φ_{tether}, is path–independent assuming a conservative resultant electric field and steady–state conditions. Thus, φ_{tether} can be calculated knowing only the relative locations of the endpoints (separation distance and orientation) and does not depend on the position of the tether between the endpoints.

Equation (2.37) is often written in a simplified form by making use of the following simplifying assumption. Since the ionospheric plasma surrounding TSS is generally a good conductor, the ambient electrostatic field $\mathbf{E}$ is small and is usually ignored. Thus, Equation (2.37) is often written as

$$\varphi_{\text{tether}} = -\int_0^l \mathbf{v}_s(l) \times \mathbf{B}(l) \cdot d\mathbf{l}. \tag{2.38}$$

The second and third principles are related to current flow through the tether. In order to have current flow through the tether, a connection must be made between the tether endpoints and the surrounding ionospheric plasma. In the case of TSS, this is done in one of two ways: either a SETS load resistor is connected between the tether and the Orbiter, or the DCORE electron gun assembly (EGA) is connected similarly[9]. When either of these is done, current flows through the tether with the conventions given in Figure 1.2 (Section 1.1). That is, current flows up the tether. This is because the resultant force on the electrons is toward the Orbiter. After electrons are collected at the satellite, they are conducted through the tether to the Orbiter where they are ejected via either passive or active means. Current closure occurs in the ionosphere, thus making the overall circuit complete.[10] The equation for this overall circuit can then be written as

$$-\varphi_{\text{tether}} = V_{\text{sat}} + I_{\text{tether}}R_{\text{tether}} + I_{\text{tether}}R_{\text{load}} + V_{\text{orb}} + I_{\text{tether}}Z_{\text{iono}} \tag{2.39}$$

where

φ_{tether} tether potential,

V_{sat} potential of the satellite with respect to the local plasma,

I_{tether} current through the tether,

R_{tether} tether resistance (approximately 2 kΩ),

R_{load} load resistance (approximately 15 Ω, 25 kΩ, 250 kΩ, or 2.5 MΩ),

V_{orb} potential of the Orbiter with respect to the local plasma,

Z_{iono} ionospheric effective impedance ($\sim$ 10's of ohms).

Let us consider the TSS system as an example of an upwardly deployed, electro-

[9]See *Agüero et al.* [1994] for a detailed description of the Shuttle Electrodynamic Tether System (SETS) and *Bonifazi et al.* [1994] for a description of the Deployer Core (DCORE) experiment.

[10]There is some controversy as to how current closure occurs in the ionospheric plasma. Investigation of the method of current closure was to be one of the primary objectives of and TSS–1 and TSS–1R.

dynamically tethered system in LEO. That is, the tether is vertically oriented, the Shuttle's orbital velocity, $v_{\rm orb}$, is 7.7 km/s in an eastward direction with respect to a stationary Earth ($v_{\rm rot} \approx 0.4$ km/s), and the geomagnetic field is oriented south to north. Since the ionospheric plasma and geomagnetic field co–rotate with the Earth, the orbital velocity should actually be in the reference frame of the Earth's rotation which yields $v_s \simeq 7.3$ km/s, where v_s is the spacecraft velocity relative to the Earth's rotation. Due to the 28.5° orbital inclination, the included angle between the velocity and magnetic vectors varies in a roughly sinusoidal fashion causing the tether potential to vary. With these effects, TSS–1 achieved a peak potential just under −60 V at the 267–m tether length [*Agüero et al.*, 1994]. At the longer 19.7–km deployment of TSS–1R, this potential was close to −3500 V [*Williams et al.*, 1998]. There were also variations due to tether libration and strength of the magnetic field, which varied depending on the orbital position of TSS.

2.3.2 Potential Structures Along the Tether

In an electrodynamic–tether system such as TSS, there are two DC steady–states: an open–circuited state called the *voltage mode* in which no current flows and a closed–circuited state called the *current mode* in which current flows along the tether from one end to the other. These two steady–states, or modes, cause two different potential structures to exist along the tether. The two states are the initial and final conditions, *i.e.*, the boundary conditions, of the transient case which occurs when a load impedance is connected or disconnected from the system. *Osmolovsky et al.* [1992] summarize this response by stating that "a change of the current in one of the [tether circuit] elements will lead to a redistribution of potential along the whole E–TSS [tether system] and a change in the potential of the collector or emitter relative to the ionospheric plasma in its turn will bring about a current change in the element and thus in the whole Collector–Tether–Emitter system." In this section, the potential structures of the two states will be examined.

The first potential structure occurs when the tether system is in the voltage mode. In this configuration a high–impedance load ($\simeq$ 35 MΩ in the case of TSS) is connected between the tether and the orbiter end of the system, as shown in Figure 2.6a. (It should be noted that the load occupies negligible length in the overall system, but has been enlarged in the figure for clarity.) Figure 2.6b is a diagram—similar to that found in *Martínez–Sanchez and Hastings* [1987]—showing the magnitude of the potentials with respect to the overall tether *emf*. Figure 2.6c is a diagram of the polarity with respect to the plasma potential and is similar to that found in *Savich* [1988]. The diagrams in Figure 2.6b and 2.6c complement each other. That is, the magnitude diagram shows that with no current flowing, there is no potential drop along the tether. The polarity diagram shows that, with respect to the plasma, the tether is biased more and more negatively along its length as one moves from the satellite to the Orbiter. (The tether potential is negative with respect to the plasma because the load is at the orbiter end of the system. If the load were at the satellite, the reverse would be true; that is, the tether potential would be positive with respect to the plasma.)

In the voltage mode, the tether *emf* is divided among the various sections of the system: load, tether, plasma, satellite, and Orbiter. Almost the entire voltage drop in the system occurs across the high–impedance load since negligible current flows along the tether. Indeed, this is how an accurate measurement of φ_{tether} is made, since the high–impedance load is simply the internal resistance of the voltage monitors. As mentioned above, little voltage drop occurs along the tether. At the

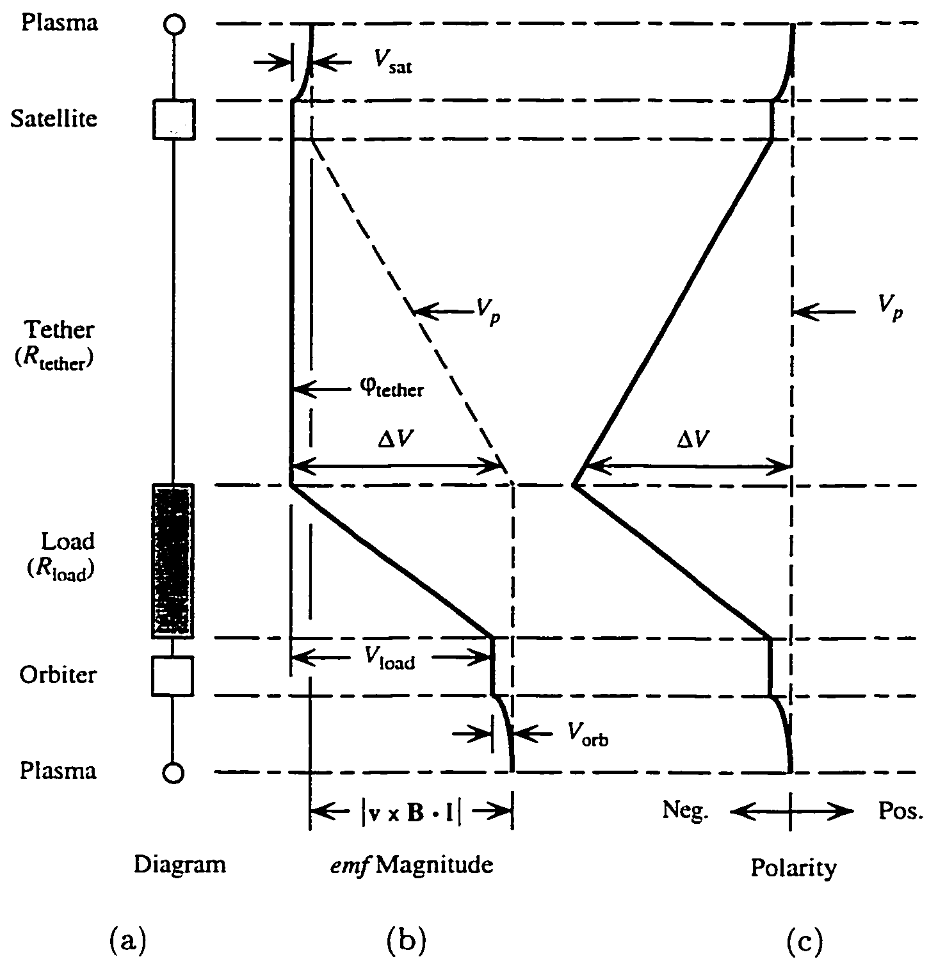

Figure 2.6: Potential diagram for tether system with high-impedance load (voltage-measuring mode): (a) placement of system components, (b) magnitude of system potentials, (c) polarity of system potentials. Note: the load occupies a negligible length in the overall system, but has been enlarged in the figure for clarity.

satellite and Orbiter ends of the tether, there is some potential drop with respect to the local plasma, labeled V_{sat} and V_{orb}, respectively. These drops are due to the spacecraft charging negative in the absence of current collection such that nearly zero current is collected at their surfaces (see Section 2.2.1). The ionospheric voltage drop, $I_{\text{tether}}Z_{\text{iono}}$, is not included in the figure since its effect is negligible.

The second potential structure occurs when the tether system is in the current mode. In this mode, a low-impedance load is placed between the tether end and the Orbiter, as shown in Figure 2.7, and measurable current flows. No longer does almost the entire voltage drop occur across the load impedance, but a significant fraction of the drop occurs across the tether due to the tether's internal resistance, R_{tether}. With the current flowing in the tether, the upper part of the tether is positively biased with respect to the plasma, whereas the lower part is negatively biased. In addition, V_{sat} and V_{orb} are established to collect electron and ion currents, respectively. Thus, the satellite tends to be positively biased, whereas the Orbiter is negatively biased. The maximum possible tether current is simply $I_{\text{tether}} = \varphi_{\text{tether}}/(R_{\text{tether}} + R_{\text{load}})$, and if this maximum level is achieved, then I_{tether} is said to be *tether-impedance limited.* If the ionospheric plasma cannot provide this level of current—which is often the case, especially in lower-density regions—I_{tether} is said to be *ionospheric limited* [*Thompson et al.*, 1993].

Another way of interpreting Figures 2.6 and 2.7 is through the concept of reference frame. For example, the solid black line in Figure 2.6b represents the tether voltage in the reference frame of the tether itself. Thus, it is seen that as one travels down the tether, there is no voltage drop along its length. However, in the reference frame of the plasma, *i.e.*, Figure 2.6c, the tether is biased more and more negatively as one travels down its length. Similar reference-frame interpretations can be made for the

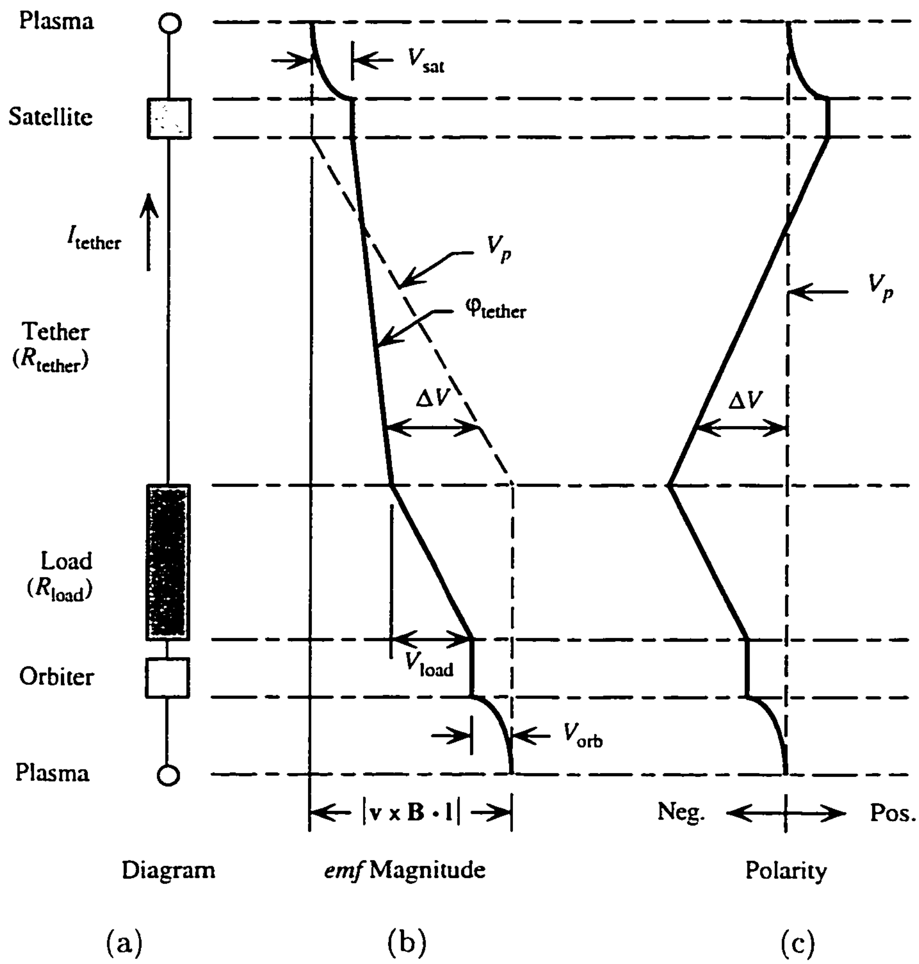

Figure 2.7: Potential diagram for tether system with low-impedance load (current-measuring mode): (a) placement of system components, (b) magnitude of system potentials, (c) polarity of system potentials. Note: the load occupies a negligible length in the overall system, but has been enlarged in the figure for clarity.

current-mode diagrams of Figure 2.7.

2.4 Antennas in Plasmas

Extensive research has been performed on the subject of antennas in both magnetized and unmagnetized plasmas. Most of this work has application to antennas placed on Earth-orbiting satellites and interplanetary probes as well as those placed in laboratory and tokamak plasmas. The focus of the research has been on short (less than a few wavelengths in length), uninsulated, wire antennas; relatively little work has been performed on long and/or insulated wire antennas. The research results have yielded an understanding of input and radiation impedances, current distribution along the antennas, radiation patterns, and effects of coupling to the plasma. Both experimental and theoretical work has been done. The remainder of this section gives an overview of some of the relevant work, much of which was performed in the 1960s and 70s. It should be noted that this review is not meant to be comprehensive, but rather a representative sampling since there is a large volume of work in this area.

Chen [1964] examined the radiation resistance of Hertzian- and cylindrical-dipole sources with a homogeneous plasma by considering the electro-acoustic wave that can be excited in addition to the usual EM wave. *Ament et al.* [1964] derived the input impedance of a cylindrical dipole in a homogeneous, anisotropic ionosphere with arbitrary orientation of the dipole to the Earth's magnetic field. They assumed a sinusoidal current distribution and low excitation value. *Mittra* [1965] developed a model of the radiation resistance of antennas in anisotropic media.

There have been many papers written on the input impedance of short dipoles in warm anisotropic plasma. *Balmain* [1964] derived a formula for the impedance of a short (compared to the wavelength) cylindrical dipole in a magnetoplasma which is valid for any orientation with respect to the magnetic field. A short dipole is used to avoid problems of theoretically determining the current distribution. Instead, a linear (triangular) current distribution that is maximum at the center feed point and zero at the ends is assumed. Good qualitative agreement is found between measured and theoretical results. *Lu and Mei* [1971] formulated the problem of a finite cylindrical dipole antenna arbitrarily oriented in a gyrotropic medium as an integral equation and found their results agreed closely with those of *Balmain* [1964] at low frequencies. In their case, they were able to obtain a convergence on the dipole current distribution.

Galejs [1966a] developed a variational formulation of the impedance of a finite cylindrical dipole antenna (where antenna length $L_a < 0.5\lambda$) embedded in a dielectric cylinder which is surrounded by a magneto–ionic medium (cold electron plasma) with a magnetic field parallel to the antenna axis. In a related work [*Galejs*, 1966b], a similar derivation is made for a perpendicular magnetic field. The dielectric region near the antenna is intended to approximate the effects of an ion sheath formed around the antenna immersed in the ionosphere. Impedance calculations are presented and plotted over the complete frequency range, showing the impedance resonances.

Ishizone et al. [1969a] experimentally examined how the sheath affects the current distribution along a cylindrical antenna in an unmagnetized plasma. They examined the current distribution of the antenna in the region of $\omega > \omega_{pe}$ when the DC bias voltage was varied. They found the current distribution was essentially determined by the phase constant $k_e = k_0(1 - \omega_{pe}^2/\omega^2)^{1/2}$, where k_0 is the phase constant in free space. They found that the wavelength became shorter as the sheath thickness increased. They also observed a slow–wave mode along the antenna in the region of

$\omega < \omega_{pe}/\sqrt{2}$. They interpreted this mode as a slow surface–wave mode propagating along the ion–sheathed conductor. This mode approaches the TEM coaxial mode when ω_{pe} approaches infinity.

In a subsequent paper, *Ishizone et al.* [1969b] examined the current distribution along a cylindrical antenna in an anisotropic plasma which was magnetized parallel to the antenna axis. They found that when the plasma frequency is relatively low, a traveling type of current exists in the region $\omega < \omega_{ce}$ and an attenuating type of current exists in the regions $\omega > \omega_{ce}$. One to a few resonance peaks were observed in the vicinity of the electron gyrofrequency, ω_{ce}. They also found that when the plasma frequency was relatively high, the gyroresonance disappeared and the standing wavelength was considerably shorter than in free space and decreased with increasing plasma frequency. They also state that the antenna current distribution in an anisotropic plasma differs little from that in an isotropic plasma if $\omega^2 \gg \omega_{ce}^2$.

About a year later, the theoretical analysis [*Ishizone et al.*, 1970a] and experimental verification [*Ishizone et al.*, 1970b] of EM–wave propagation along conducting wires in general magnetoplasmas was described. For the theoretical analysis, the wire was assumed to be infinitely long and very thin, and could be oriented at an arbitrary angle with respect to the magnetic field. An approximate propagation constant, k, was obtained:

$$k^2 = j\varepsilon_1(-\varepsilon_2/\varepsilon_1)^{1/2}k_0^2, \tag{2.40}$$

where

$$\varepsilon_1 = 1 - \frac{L}{1 - M^2} \quad \text{and} \quad \varepsilon_2 = 1 - L\frac{1 - M^2\sin^2\theta}{1 - M^2}$$

with

$$L = \frac{\omega_{pe}^2}{\omega(\omega - j\nu)} \quad \text{and} \quad M = \frac{\omega_{ce}}{\omega - j\nu}.$$

Angle θ subtends $\mathbf{B}_0$ and the wire and the sign of $(-\varepsilon_2/\varepsilon_1)^{1/2}$ is chosen such that $\mathrm{Im}[(-\varepsilon_2/\varepsilon_1)^{1/2}] \leq 0$. Their approximate propagation constant expressed by Equation (2.40) is the same as derived by *Ament et al.* [1964] except for the sign–choice condition. They found that the wave is always a propagating mode if $\omega > \omega_{uh}$ and its dispersion curve varies very little with the inclination angle, θ. The cutoff frequency of this mode is always ω_{uh} regardless of θ. In the frequency range $\omega < \omega_{uh}$, it was found that the dispersion curves for the propagating and complex modes are fairly sensitive to the inclination angle. By measuring the standing wave along a cylindrical monopole, *Ishizone et al.* [1970b] were able to experimentally verify their theoretical results. They found fairly good agreement between theory and measured results when the effect of the surrounding ion sheath was taken into account. That is, when $\omega > \omega_{uh}$, the results agreed to within several percent since the ion sheath did not effect this region as much as when $\omega < \omega_{uh}$, where they found the effects of the ion sheath to be quite considerable.

Rubinstein and Laframboise [1970] examined the disturbance of ionospheric plasma by a high power, metallic dipole antenna. They found that if the RF emission is powerful enough, it drives the DC potential of the antenna strongly positive which modifies the ion and electron distributions surrounding the antenna. For excitation frequencies $\omega \gg \omega_{pe}$, both electrons and ions will experience small oscillations and will drift away from the antenna because the RF amplitude is not constant in space. This force is the same for electrons and ions, but since electrons have lower mass, it affects electrons more than ions. If the antenna absorbs all charges reaching it, the electron repulsion will produce a net positive current to the antenna with the RF field applied which raises its DC potential. However, if the RF field varies slowly enough ($\omega \ll \omega_{pe}$), the plasma will have enough time to accommodate itself to the instantaneous probe potential and the effect will not occur. In this case, static I–V characteristics of a Langmuir probe can be used.

Basu and Maiti [1974] and *Biswas and Basu* [1990] examined small-signal propagation along dielectric–coated cylinders immersed in unmagnetized and magnetized plasma, respectively. More specifically, they performed theoretical analyses of the dispersion relation for propagation of axisymmetric transverse–magnetic modes (TM_{0m}) and plotted their results for different geometries. In both cases, they considered a conducting cylinder of radius r_a coated with a material of dielectric constant ε_d that extends from r_a to r_d. In the second case, a strong magnetic field is placed parallel to the axis of the cylinder which allows them to assume that the electrons are constrained to move in the z direction. They state that the plasma sheath surrounding a metallic cylinder in a plasma may be approximated by a vacuum sheath which occurs in the limiting case where $\varepsilon_d \rightarrow 1$. For both cases, however, they assume the plasma is flush with the dielectric coating.

Adachi [1977] examined the impedance of an antenna in a cold magnetoplasma via transmission–line theory. The theory is applicable to antennas which are not necessarily small with respect to the wavelength measured along the antenna. Via an electrostatic analysis, *Adachi* obtains values for distributed inductance and capacitance of the antenna, which leads to the characteristic impedance and propagation constant of the equivalent transmission–line circuit. Plots are presented of the propagation constant of the current along the antenna as well as plots of the antenna input impedance versus antenna angle with respect to $\mathbf{B}_0$, showing considerable effect at several resonance frequencies. The effect of the sheath was not considered in his work although it is stated that the effect of the sheath is important for determining some resonance frequencies.

Sawaya [1978] measured the impedance of a monopole antenna in a magnetoplasma. The antenna length was comparable to the free–space wavelength and was oriented at various directions with respect to the magnetic field. They observed interesting resonance phenomena of the antenna input impedance which depended on the antenna length and orientation. To compare their results with theory, they use a cold–plasma model and assume that the ion–sheath effect is negligible and assume that the current distribution along the antenna is sinusoidal.

Linh and Nachman [1990] examined the nonlinear resonance of a cylindrical monopole antenna immersed in an unmagnetized, collisionless plasma. They found that the half–frequency of the input signal is spontaneously excited when two conditions are met: 1) the driving frequency is twice the system's natural resonance frequency; and 2) the input power level is above some threshold value. The natural resonance frequency of the system is related to sheath waves propagating along the antenna, and they correspond to the standing–wave pattern which occurs when

$$(2N+1)\lambda/4 = L_a, \tag{2.41}$$

where N is a nonnegative integer, λ in the wavelength of the sheath waves, and L_a is the antenna length. The resonance frequencies depend on the sheath thickness, r_s, which is given by *Nachman et al.* [1988]

$$r_s = 2.15\lambda_D[q(V_p - V_a)/kT_e]^{1/2} \tag{2.42}$$

where V_p is the plasma potential, and V_a is the antenna DC bias level ($V_p > V_a$). When r_s is increased by increasing ($V_p - V_a$), the sheath–wave resonance frequencies increase as well. When the plasma frequency increases, so does the resonance frequency. There is a power threshold of the driving signal above which the subharmonic is excited. This threshold value increases with increasing negative DC bias, but is only weakly dependent on the plasma frequency. When the sheath was collapsed by biasing the antenna positively with respect to the plasma, the subharmonic disappeared. In addition, when the antenna was insulated by a solid Kapton®coating ($\varepsilon_r = 2.55$), no subharmonics were detected, even when the system was driven at high applied–power levels. This establishes as crucial the role of the ion sheath for the existence of the nonlinear process. The mechanism responsible for the nonlinear effect is the modulation of the sheath thickness, and hence the sheath capacitance, by the applied RF signal.

Morin and Balmain [1991] developed a warm–plasma, hydrodynamic, radio–frequency model of the ion sheath around a spherical conductor in a plasma. This model comprises contiguous layers of uniform, homogeneous plasma. The boundary conditions are applied at the conductor surface and at each of the plasma–plasma interfaces. The limit of the model is a single step discontinuity joining a uniform ambient plasma to a lower–density, uniform plasma extending to the conductor surface. It was established that the single–step model produces results similar to a smooth–profile model, as long as the sheath thickness is chosen appropriately. They found the sheath thickness to be $1.55\lambda_D$.

To summarize some of the major findings of researchers in this field:

- The ion–sheath region is very important as sheath–wave modes may propagate in it. The ion–sheath region tended to be ignored by early researchers.
- Resonance conditions can be established along the antennas and wires due to the presence of the sheath.
- Modulation of the sheath size by the applied RF voltages can cause nonlinear sheath responses to occur leading to higher–order harmonics. This nonlinearity

can also lead to wave rectification in some cases.

- The size of the sheath region falls in the range $r_s \sim 1$–$3\lambda_D$ for conductors (antennas) and can be larger or smaller depending on bias voltage and conductor radius.

2.5 Sheath Waves

The low–electron–density sheath surrounding a conductor when it is immersed in a plasma can act as a waveguide for the propagation of electromagnetic waves. In this metal–sheath–plasma region—analogous to a waveguide—waves satisfying the resonance conditions may propagate over long distances. These waves, called "sheath waves", become significant when the length of the conductor is not small compared to the wavelength. Sheath waves are slow waves which can propagate from zero frequency up to $\omega_{uh}/\sqrt{2}$ in anisotropic plasma [*Laurin et al.*, 1989]. Thus, waves can still propagate along a plasma–immersed wire even at low frequencies when the plasma is cut off for wave propagation. Recently, strong experimental evidence for sheath–wave propagation along an electrodynamic tether in the ionosphere was obtained during the OEDIPUS–A mission described later in Section 2.5.2 and in *James et al.* [1995].

Although there has been some work done on the problem of sheath waves along cylindrical conductors in anisotropic plasmas, the problem is quite difficult to solve analytically for the general case. Indeed, *James et al.* [1995] state that "no dispersion relation is known for sheath waves in a cylindrical magnetoplasma geometry." Some work, however, has examined isotropic plasmas and planar conductors in magnetoplasmas. In the planar case, the orientation of the surface with respect to the magnetic field is constant. However, for a cylinder, the angle between the surface normal and $\mathbf{B}_0$ is not constant. There are two cases in cylindrical geometry for which this can be avoided. The first is for a cylinder oriented along the **B**–field, with propagation in that direction, and the second has the same cylinder orientation, but with propagation in the azimuthal direction (around the cylinder)—of little interest when $r_a \ll \lambda$. The next section presents sheath–wave dispersion relations for planar magnetoplasma geometry and also for isotropic plasmas.

2.5.1 Sheath–Wave Dispersion Relations

2.5.1.1 Planar Magnetoplasma Geometry

Dispersion relations for sheath waves along planar conductors have been developed by *Laurin et al.* [1989], *Baker* [1991], and *Lüttgen and Balmain* [1995, 1996] for the three orthogonal directions of applied magnetic field. This section will examine these three orthogonal cases in summary form; the reader is referred to the referenced papers for details. Figure 2.8 shows the general planar geometry with the conductor and sheath in the yz–plane and wave propagation in the $+z$–direction. The three orthogonal cases for the magnetic field are along the x–, y–, and z–axis.

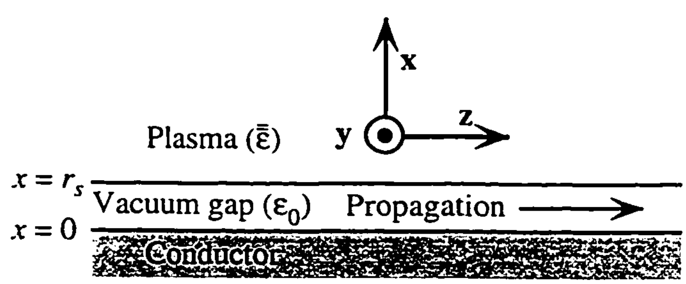

Figure 2.8: General planar geometry for sheath–wave derivations

The dispersion relationships for each of the three cases is found in a similar manner. Assuming e^{jwt} harmonic time dependence, we begin by writing Maxwell's equations for the sheath region[11]

$$
\begin{aligned}
\nabla\times\mathbf{E} &= -j\omega\mu_0\mathbf{H}, && (2.43a)\\
\nabla\times\mathbf{H} &= j\omega\varepsilon_0\mathbf{E}, && (2.43b)\\
\nabla\cdot\mathbf{E} &= 0, && (2.43c)\\
\nabla\cdot\mathbf{H} &= 0, && (2.43d)
\end{aligned}
$$

and for the plasma region

$$
\begin{aligned}
\nabla\times\mathbf{E} &= -j\omega\mu_0\mathbf{H}, && (2.44a)\\
\nabla\times\mathbf{H} &= j\omega\bar{\bar{\varepsilon}}\mathbf{E}, && (2.44b)\\
\nabla\cdot\bar{\bar{\varepsilon}}\mathbf{E} &= 0, && (2.44c)\\
\nabla\cdot\mathbf{H} &= 0. && (2.44d)
\end{aligned}
$$

Equations (2.44b) and (2.44c) reveal that, in the magnetized plasma region, the electric–flux density, $\mathbf{D}$, is related to the electric field, $\mathbf{E}$, by a permittivity tensor, $\bar{\bar{\varepsilon}}$. That is, $\mathbf{D} = \bar{\bar{\varepsilon}}\mathbf{E}$, where

$$
\bar{\bar{\varepsilon}} = \begin{bmatrix} \varepsilon_{xx} & \varepsilon_{xy} & \varepsilon_{xz} \\ \varepsilon_{yx} & \varepsilon_{yy} & \varepsilon_{yz} \\ \varepsilon_{zx} & \varepsilon_{zy} & \varepsilon_{zz} \end{bmatrix}. \qquad (2.45)
$$

The components of $\bar{\bar{\varepsilon}}$ depend on the orientation of the magnetic field. It is assumed that the plasma responds linearly to the EM disturbances, *i.e.*, that the properties of the plasma can be adequately characterized by the constant relative–permittivity tensor $\bar{\bar{\varepsilon}}$ at a given frequency.

The next step is to satisfy the boundary conditions at the conductor and at the sheath edge. Here, the superscript "sh" refers to the sheath region and superscript

[11]We have adopted Chen–To Tai's novel vector notation in this work. Please see Appendix F, Section F.2 for a description of the notation.

"p" the plasma region. At the conductor the tangential electric field is zero ($E_y^{sh} = E_z^{sh} = 0$). At the sheath edge, the tangential electric field is continuous ($E_y^p = E_y^{sh}$, $E_z^p = E_z^{sh}$); since there are no surface currents, the tangential magnetic field is continuous ($H_y^p = H_y^{sh}$, $H_z^p = H_z^{sh}$); the normal magnetic flux is continuous ($H_x^p = H_x^{sh}$); and since there is no charge density at the sheath edge, the normal electric flux density is continuous ($D_x^p = D_x^{sh}$).

$\mathbf{B}_0$ in the z–direction *Laurin et al.* [1989] present theoretical and experimental results of sheath–wave propagation in a plasma magnetized in the direction of wave propagation (z–direction). In this case the dielectric tensor can be written as

$$\bar{\bar{\varepsilon}} = \varepsilon_0 \begin{bmatrix} K' & jK'' & 0 \\ -jK'' & K' & 0 \\ 0 & 0 & K_0 \end{bmatrix}, \tag{2.46}$$

where

$$K' = 1 - \frac{UX}{U^2 - Y^2},\ K'' = \frac{-XY}{U^2 - Y^2},\ \text{and}\ K_0 = 1 - \frac{X}{U}$$

with

$$U = 1 - j\nu/\omega,\ X = \omega_{pe}^2/\omega^2,\ \text{and}\ Y = \omega_{ce}/\omega,$$

in which ω is the excitation frequency and ν is the plasma collision frequency. They found the dispersion relation for this case to be

$$\tanh^2(k_s r_s)(\theta\alpha_2 - \varphi\alpha_1) + \frac{\theta\alpha_1 - \varphi\alpha_2}{K_0} + \tanh(k_s r_s)(\varphi - \theta)\left(\frac{\alpha_1\alpha_2}{k_s K_0} + k_s\right) = 0 \tag{2.47}$$

where

$$\begin{aligned} \varphi &= K_0(k^2 - \beta_0^2 K') - K'\alpha_1^2, \\ \theta &= K_0(k^2 - \beta_0^2 K') - K'\alpha_2^2. \end{aligned}$$

The values for α_1^2 and α_2^2 are solutions of the biquadratic equation,

$$a\alpha^4 + b\alpha^2 + c = 0 \tag{2.48a}$$

where

$$a = K', \tag{2.48b}$$

$$b = \beta_0^2(K'^2 - K''^2 + K'K_0) - k^2(K_0 + K'), \tag{2.48c}$$

$$c = \beta_0^4 K_0(K'^2 - K''^2) - 2\beta_0^2 k^2 K_0 K' + k^4 K_0. \tag{2.48d}$$

The sheath edge is located at $x = r_s$, $k_s^2 = k^2 - \beta_0^2$ with $\beta_0^2 = \omega^2\varepsilon_0\mu_0$, and the TE and TM modes are coupled as a result of the boundary conditions at the sheath edge.

If we have an isotropic plasma instead of a magnetized plasma, then $\omega_{ce} = 0$ and $K' = K_0$ and $K'' = 0$. In this case, Equations (2.48a)–(2.48d) combine to form

$$(\alpha^2 + \beta_0^2 K_0 - k)^2 = 0 \tag{2.49}$$

or

$$\alpha_1^2 = \alpha_2^2 = \alpha^2 = k^2 - \beta_0^2 K_0 = k_0^2, \tag{2.50}$$

which leads to $\varphi = \theta = 0$. Hence, in the isotropic case the dispersion relation reduces to

$$\tanh(k_s r_s) = \frac{k_0}{K_0 k_s}. \tag{2.51}$$

B_0 in the x–direction *Baker* [1991] presents theoretical and experimental results of sheath–wave propagation in a plasma magnetized in the x–direction. In this case, the dielectric tensor is

$$\bar{\bar{\varepsilon}} = \varepsilon_0 \begin{bmatrix} K_0 & 0 & 0 \\ 0 & K' & jK'' \\ 0 & -jK'' & K' \end{bmatrix}, \tag{2.52}$$

where K_0, K', and K'' are defined as above. For this case, *Baker* found the dispersion relation to be

$$\begin{aligned} &\frac{K_0 k_s}{k_0^2}(\alpha_1+\alpha_2)\cosh^2(k_s r_s) \\ &+\left\{\frac{1}{k_0^2}\left[K' k_0^2 - K_0\left(\alpha_1^2+\alpha_1\alpha_2+\alpha_2^2\right)\right] - \frac{K_0^2 k_s}{k_0^4}\left(K' k_0^2 + K_0\alpha_1\alpha_2\right)\right\} \\ &\times\cosh(k_s r_s)\sinh(k_s r_s) + \frac{K_0 k_s^2}{k_0^4}\alpha_1\alpha_2(\alpha_1+\alpha_2)\sinh^2(k_s r_s) = 0. \end{aligned} \tag{2.53}$$

The values for α_1^2 and α_2^2 are again solutions of the biquadratic equation,

$$a\alpha^4 + b\alpha^2 + c = 0, \tag{2.54a}$$

except in this case:

$$a = K_0, \tag{2.54b}$$

$$b = \beta_0^2 K' K_0 - k^2 K_0 - K' k_0^2, \tag{2.54c}$$

$$c = k_0^2(\beta_0^2 K''^2 + k^2 K' - \beta_0^2 K'^2). \tag{2.54d}$$

There are several different solutions to the dispersion relation; however, most are highly attenuated. There is a passband bounded by ω_{ce} and $\omega_{uh}/\sqrt{2}$ which has relatively low attenuation and slow propagation velocity.

$\mathbf{B}_0$ in the y–direction *Lüttgen and Balmain* [1995, 1996] present theoretical and experimental results of sheath-wave propagation in a plasma magnetized in a direction perpendicular to the direction of propagation and the normal to the plane, that is, in the y–direction. In this case, the dielectric tensor is

$$\bar{\bar{\varepsilon}} = \varepsilon_0 \begin{bmatrix} K' & 0 & jK'' \\ 0 & K_0 & 0 \\ -jK'' & 0 & K' \end{bmatrix}, \tag{2.55}$$

where K_0, K', and K'' are again defined as above. For this case, they found the dispersion relation for the TE mode to be

$$\tanh(k_s r_s) = \frac{k_s}{k_0} = \sqrt{\frac{k^2 - \beta_0^2}{k^2 - \beta_0^2 K_0}}, \tag{2.56}$$

where, again, $k_0^2 = k^2 - \beta_0^2 K_0$ and for the TM mode

$$(kK'' - \alpha K') \tanh(k_s r_s) = \frac{k_1^2}{k_s}, \tag{2.57}$$

where

$$\begin{aligned} \alpha^2 &= k^2 - \beta_0^2 \frac{K'^2 - K''^2}{K'}, \\ k_1^2 &= k^2 - \beta_0^2 K'. \end{aligned}$$

However, Equation (2.56) was found to have no solution, *i.e.*, there is no propagating TE mode, which also has been found for the isotropic–plasma case [*Lüttgen and Balmain*, 1996].

There are two solutions to the TM dispersion relation [Equation (2.57)] for propagation in opposite directions along the conductor. These solutions have different propagation constants and the difference between them increases with increased magnetic–field strength. The solutions also have different cutoff frequencies with the difference between them always equal to the electron cyclotron frequency. What this means is that propagation along the conductor is nonreciprocal with an applied magnetic field in the y–direction.

2.5.1.2 Isotropic Plasmas

One of the first references to sheath waves is the work by *Marec and Mourier* [1970] in which they report experimental evidence for the existence of sheath waves and associated resonances. *Lassudri–Duchesne et al.* [1973] measured the current distribution along a cylindrical probe in an isotropic plasma. Their measurements indicated the presence of standing waves on the probe at frequencies below ω_{pe}. Both papers give an equation for sheath–wave resonance, stating that it can occur when the following condition is satisfied:

$$kL_a = \left(N + \frac{1}{2}\right)\pi \qquad (N = 0, 1, 2, \ldots), \tag{2.58}$$

where k is the propagation constant and L_a is the antenna length. This equation assumes an equivalent open at the antenna end, and hence the factor of 1/2 must be included. If this is not the case, then Equation (2.58) can be modified slightly by adding a $\Delta\varphi$ instead to account for the sum of phase changes experienced by the sheath waves as they reflect at both ends of the conductor [*Balmain et al.*, 1990], *i.e.*,

$$2kL_a + \Delta\varphi = 2N\pi \qquad (N = 0, 1, 2, \ldots). \tag{2.59}$$

The sheath–wave dispersion relation for planar geometry and isotropic plasma was also given in the previous section as the limiting case of the anisotropic plasma as $\mathbf{B}_0 \to 0$ [Equation (2.51)].

2.5.2 OEDIPUS Missions

The OEDIPUS–A (Observations of Electric Field Distributions in the Ionospheric Plasma—A Unique Strategy) tethered sounding–rocket experiment was designed to address the science of large double probes in the ionospheric plasma [*James and Whalen*, 1991; *Godard et al.*, 1991]. One of its important features was the ability to directly excite and detect electromagnetic waves along its insulated conductor. Of particular importance to the present work is their quantitative evidence of sheath waves excited along their ionospheric tether, with sharply defined passbands and stopbands. Within the lowest passband, OEDIPUS–A detected resonance fringes which could be scaled to determine the phase and group refractive indices of the observed sheath waves.

The OEDIPUS–A sounding rocket payload was launched from Andøya, Norway on 30 January 1989. It reached an apogee of 512 km and recorded 560 s of prime data. A little past apogee, the two halves of the payload (the "mother" and "daughter") were separated by a 958–m tether. The tether itself was a 24–AWG (0.51–mm) wire of 18 copper strands covered with an insulating Teflon®coating 0.4 mm thick [*James et al.*, 1995]. The tether was approximately aligned with $\mathbf{B}_E$, but did experience a misalignment of 8° right after separation which decreased smoothly to 7° at the end of the flight. Another cause of the misalignment could have been the residual helical shape in the deployed wire resulting from the wire being wound on a reel. For example, they found that the helical nature of their tether could add up to 3° of further misalignment [*James et al.*, 1995].

The OEDIPUS–A tether was long enough to test the sheath–wave concept of resonant length. They found that sheath waves were efficiently excited and guided by the tether. They also observed fringes in their data with spacing that varied inversely with the tether length and were interpreted as a demonstration of the resonant condition given in Equation (2.59).

2.6 Dynamic, Nonlinear Transmission Lines

In this section we discuss some of the theoretical treatments and models developed to describe dynamic, nonlinear transmission lines. Examples of such transmission lines include lightning and soliton lines.

2.6.1 Transmission–Line Models of Lightning

The lighting stroke is a very transient, highly nonlinear phenomenon. Initial dart leaders and return strokes have been modeled as guided waves propagating along a pre–ionized, conducting channel [*Borovsky*, 1995]. These guided waves can describe the propagation of the dart leader, which occurs when current is injected onto a conducting channel, and the return–stroke breakdown, which occurs when charge on the channel drains to Earth. Solving the full set of Maxwell's equations has shown such a model to be useful for describing pulse velocity and how charge and energy move along the lightning channel. *Borovsky* [1995] developed an electrodynamic model of dart–leader and return–stroke lightning phenomena from first principles, assuming a straight, uniform, cylindrical channel and harmonic propagating fields. The model ignores photon preheating and wave heating of the channel and was based on chosen (*i.e.*, not derived) values for a static channel size, uniform conductivity in the corona region, and pulse risetime (which set the highest harmonic of interest).

Nonlinear, coaxial–transmission–line models of lightning dart leaders and return strokes have also been developed. These models are based on the usual transmission–line parameters but have nonlinear parameters for per–unit–length resistance [*e.g.*, *Mattos*, 1988] and capacitance [*e.g.*, *Baum*, 1990; *Baum and Baker*, 1990]. *Baum* [1990] used a nonlinear relation for capacitance between the corona region and an "equivalent outer conductor" (a construction allowing termination of the model region). As the lightning current pulse propagates down the center conducting channel, a corona region forms. This corona region is also highly conducting, hence, the equivalent center conductor experiences an apparent size increase which increases the capacitance of the equivalent transmission line. *Baum* presents a nonlinear wave equation for this transmission line:

$$\frac{1}{L}\frac{\partial^2}{\partial z^2}\left[\frac{Q}{C(Q)}\right]-\frac{\partial^2 Q}{\partial t^2}=0. \tag{2.60}$$

The equation is nonlinear for Q since, by hypothesis, C is a function of Q only. The pulse propagation velocity on this line is given as [*Baum and Baker*, 1990]

$$v_p=\sqrt{\frac{1}{L}\frac{d}{dQ}\left[\frac{Q}{C(Q)}\right]}, \tag{2.61}$$

and depends on coronal charge and radius [via $C(Q)$], which leads to the pulse–front steepening and an electromagnetic shock front in a finite amount of time.

2.6.2 Solitary–Wave Transmission Lines

Solitary waves are pulses or wave packets which propagate in nonlinear dispersive media. Due to a dynamic balance between nonlinear and dispersive effects, these solitary waves can maintain their stable waveform over long distances. Solitons are special solitary waves which have interesting characteristics such as the ability to maintain their waveforms even after "overtaking" and "head–on" collisions with other solitons. They were first reported in the field of hydrodynamics in 1844 by Scott–Russell.[12]

One implementation of a nonlinear transmission–line structure consists of linear inductances, L, and nonlinear, voltage–dependent capacitances, $C(V)$.[13] Physical realizations of these nonlinear capacitances may be reverse–biased diodes [*e.g.*, *Nagashima and Amagishi*, 1978; *Jäger*, 1985]. On these nonlinear transmission lines, solitons can be created by feeding voltage pulses at the input of the line. For this

[12]See the article by *Scott* [1973] for some of the history of these waves and their observations, as well as an excellent review of the research through 1973. Two other review articles that deal with nonlinear transmission–line implementations are *Lonngren* [1978] and *Kuusela* [1995].

[13]There are many other implementations, including the use of nonlinear inductances.

line, the network equations are:

$$L\frac{\partial}{\partial t}I_N(t) = V_{N-1}(t) - V_N(t), \tag{2.62}$$

$$\frac{\partial}{\partial t}Q_N(t) = I_N(t) - I_{N+1}(t), \tag{2.63}$$

where $I_N(t)$ is the AC current through the inductor and $V_N(t)$ is the AC voltage across the capacitance as shown in Figure 2.9. The accumulated charge on the Nth nonlinear capacitor can be determined via

$$Q_N(t) = \int_{V_0}^{V_0+V_N(t)} C_N(V)dV, \tag{2.64}$$

where V_0 is an initial voltage, *e.g.*, the bias voltage of the capacitor. The functional form of the capacitance can be very different depending on the physical device or mathematical construct chosen. This capacitance value is substituted into Equation (2.64), which is solved and subsequently substituted into Equations (2.62) and (2.63) from which a nonlinear wave equation is then derived. Generally, this equation can be manipulated into the form of a Korteweg–deVries (KdV) equation or one of its variations, *e.g.*, the modified KdV (MKdV) and the negative modified KdV (nMKdV) equations [*Jäger*, 1985]. The solutions of these KdV equations are solitons.

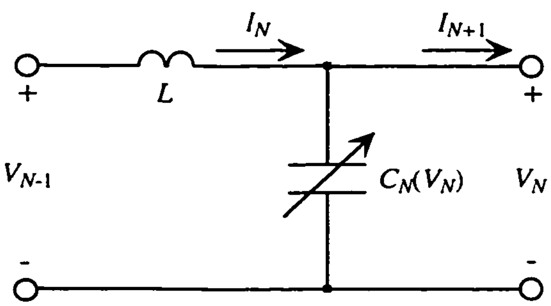

Figure 2.9: Nonlinear transmission–line segment.

One of the features of a nonlinear transmission line that supports soliton propagation is that an arbitrary input pulse breaks up into a prescribed number of solitons and a low–amplitude oscillatory tail [*Lonngren*, 1978]. The number of solitons number is determined by the duration and amplitude of the pulse [*Kuusela*, 1995; *Carter et al.*, 1995] in order that the following conservation laws are satisfied

$$\sum_{N=-\infty}^{\infty} I_N = \text{constant}, \tag{2.65a}$$

$$\sum_{N=-\infty}^{\infty} Q_N = \text{constant}. \tag{2.65b}$$

Figure 2.10 shows an input rectangular pulse breaking apart, in this case, into two solitons: a taller, faster one and a smaller, slower one. Larger–amplitude solitons travel faster than smaller–amplitude solitons.

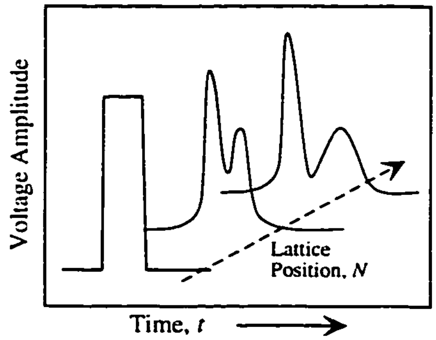

Figure 2.10: Pulse breaking apart into solitons.

2.6.3 Other Nonlinear Transmission Lines

Some other applications of nonlinear transmission lines are as harmonic generators [*Benson*, 1965] and as shock–wave producers [*Landauer*, 1960]. The process involved in these applications is illustrated in Figure 2.11, where the progressive steepening of the waveform is due to the phenomenon that larger voltages travel faster than smaller voltages on these lines. This steepening produces harmonics that can ultimately lead to the formation of a shock–wave front if the waveform steepens to a critical point.

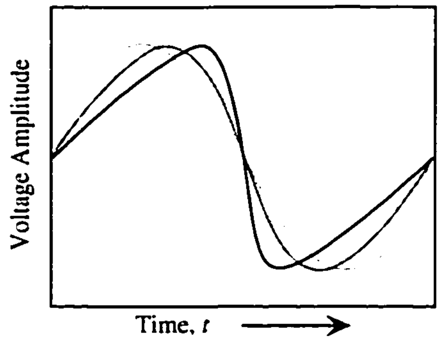

Figure 2.11: Propagation effects on nonlinear transmission lines: the formation of a harmonic waveform and ultimately a shock wave via progressive distortion of a waveform.

Savas [1989b] wrote the Telegrapher's equations with nonconstant shunt capacitance and admittance to describe sheath–electrode physics in a large hexode plasma–processing chamber (see Figure 1.1a). They state that the solution of these nonlinear equations yielded approximate agreement with observed harmonic magnitudes.

There is also a curious paper by *Kuźniar* [1987] that gives a theoretical treatment of electrical waves along long transmission lines with general time–varying parameters. The formulation is quite rigorous, but it only accounts for external changes to the line's parameters, *i.e.*, transmission–line parameters can change due to external stimuli but not due to the voltage wave itself.

CHAPTER III

Transient Plasma Sheath Model

An understanding of the temporal and voltage dependencies of the plasma sheath is the first step towards a transmission–line model for negative–HV–signal propagation along the plasma–immersed cylinder. In this chapter we develop a voltage–dependent model of the sheath valid in the frequency regime between the electron and ion plasma frequencies. We also discuss qualitatively the sheath response for frequencies higher and lower than this regime, although this information will not be used in developing the transmission–line model.

This chapter begins with an introduction to the derivation of the model and the assumptions used. The subsequent sections describe the temporal, voltage–dependent sheath analytically, through experiment, and via particle–in–cell computer simulations. The final section states the conclusions from these three descriptions and recaps the model as derived in this chapter.

3.1 Introduction

We begin with a qualitative description of the temporal evolution of the sheath around the conductor when excited by a negative HV pulse. We are interested in negative high voltages because tether potentials are generally negative with respect to the local plasma (see Section 2.3.2). From Fourier theory we know that a pulse can be described by an infinite series of sinusoidal waveforms, and as such contains a spectrum of frequencies that depends on the risetime, duration, and falltime of the pulse. The highest frequency of interest is related to the temporal excitation of the conductor, *e.g.*, $f_{\max} = 1/\tau_{ar}$, where τ_{ar} is the risetime of the pulse (here the voltage V_a on the conductor). There are four timescales (corresponding to four ranges of excitation frequencies or frequency components) for the plasma response; these four timescales are described below.

- The first timescale is linked to the initial application of potential on the conductor. The E–field from the biased conductor propagates outward at nearly the speed of light, and if $\tau_{ar} \ll \tau_{pe}$, then the plasma is not able to respond significantly on this timescale. This means that the sheath remains fairly static and the E–field penetrates into the plasma without being affected by it.

- The second timescale is linked to the response of the plasma electrons, which occurs on the order of the electron plasma period ($\tau_{pe} \sim 2\pi/\omega_{pe}$). Because of their low mass, the electrons are quickly repelled away from the conductor's surface as the negative voltage is established. After the electrons have been expelled from the region surrounding the conductor, an "ion–matrix" sheath is left behind.

- The third timescale, is linked to the ion response time, which is on the order of the ion plasma period ($\tau_{pi} \sim 2\pi/\omega_{pi}$). On this timescale, the ions begin to respond to the voltage disturbance on the conductor and to collect at the conductor surface, which causes the steady–state sheath distribution to begin developing.

- The fourth timescale is the time required to establish the steady–state–sheath structure around the conductor. For an insulated conductor this timescale depends on the time required for the sheath to collapse after charging of the insulation and for the bare conductor, depends on the time required to establish a steady–state sheath appropriate to the geometry. The geometry and size of the conductor determine whether the steady–state sheath is space–charge–limited (also known as Child–Langmuir) or orbital–motion–limited (OML).

In the derivations in this chapter, the following assumptions are made unless otherwise noted:

- Since we will be primarily interested in the range of excitation frequencies between the electron and ion plasma frequencies, the electrons are assumed to respond to stimuli (*i.e.*, the electrons are driven), but the ions are motionless.

- Cylindrical geometry is assumed. In addition, we assume that $r_a \lesssim \lambda_D$. At times, results for planar and spherical geometries will be shown (if they were obtained) to put the cylindrical results in context, to provide completeness, and to indicate how the results might be applied to other conductor/plasma geometries.

- The conductor radius is much less than the sheath radius ($r_a \ll r_{\rm sh}$). This is generally satisfied under the corollaries that the plasma density is low enough for $r_a \lesssim \lambda_D$ to apply (see the previous assumption) and the applied voltage $|V_a| \gg kT_e/q$.

- The sheath boundary is effectively a "wall"—or very steep—and no electrons exist within the sheath. That is, at the sheath edge, $r_{\rm sh}$, the electron density can be described by a step function which transitions from $n_e = 0$ to $n_e = n_0$. We can also state this as the spatial extent of the transition from $n_e = 0$ to $n_e = n_0$ at the sheath–edge is very much smaller than the total sheath size. This is in contrast to the generalized sheath radius, r_s, discussed in Section 2.2.1 and shown in Figure 2.2, which does not have a sharp edge.[1]

- A non–flowing plasma is assumed. Generally, for a spacecraft in the ionosphere, the spacecraft velocity falls between the electron and ion thermal velocities (*i.e.*, $v_{te} \gg v_s \gg v_{ti}$), which means that the ions are typically treated as a directed beam with uniform energy.

- The plasma is cold and collisionless.[2]

3.2 Analytical Description of Voltage–Dependent Sheath

The analytical description of the voltage–dependent sheath is developed using two complementary approaches: shielding of applied voltage and neutralization of applied charge. The approaches are complementary in that they are two methods of addressing the same problem. The applied–voltage approach works well when a reference point for voltage is available or can be assumed. Where such a reference is not available or cannot be assumed, the problem may still be addressed through the applied–charge approach.

In this section we begin by examining the applied–voltage approach, which allows us to use Poisson's equation to find a solution. The applied–charge approach is then presented. Another section on electron ringing due to rapid biasing is also included

[1]The nomenclature r_{sh} refers to the voltage–dependent ("driven") sheath, whereas r_s refers to a steady–state–sheath distance.
[2]See Section 2.1.2 for caveats with this approximation.

to show how the electrons respond when the conductor is biased faster than the electron plasma frequency. Finally, we briefly discuss sheath evolution and collapse.

3.2.1 Applied–Voltage Approach: The Ion–Matrix–Sheath Radius

The derivation of the ion-matrix-sheath radius from the standpoint of applied voltage on the conductor begins with Poisson's equation, which defines the potential structure, V, surrounding a conductor:

$$\nabla\nabla V = -\frac{\rho_v}{\varepsilon_0}, \tag{3.1}$$

where ρ_v is a volume charge density. If we assume symmetrical potential distributions—*i.e.*, infinite planar and cylindrical geometries or spherical symmetry—then Equation (3.1) reduces to

$$\frac{d^2V}{dr^2} + \frac{\alpha_P}{r}\frac{dV}{dr} = -\frac{q}{\varepsilon_0}(n_i - n_e), \tag{3.2}$$

where V is the conductor potential, n_i and n_e are the ion and electron plasma densities, and $\alpha_P = 0$, 1, or 2 for planar, cylindrical, or spherical geometries, respectively. The spatial variable r is measured from the surface of the conductor for planar geometry and is measured from the center of the conductor in cylindrical and spherical geometries. The plasma is assumed to have uniform density, *i.e.*, $n_i = n_e = n_0$, before voltage is applied to the conductor.[3]

For ease of analysis, it is convenient to introduce dimensionless (normalized) variables as follows: $\tilde{V} = q_eV/kT_e$ for potential, $\tilde{r} = r/\lambda_D$ for radius, $\tilde{n}_e = n_e/n_0$ for electron density, $\tilde{n}_i = n_i/n_0$ for ion density. Substituting these dimensionless quantities into Equation (3.2) yields the dimensionless Poisson's equation

$$\frac{d^2\tilde{V}}{d\tilde{r}^2} + \frac{\alpha_P}{\tilde{r}}\frac{d\tilde{V}}{d\tilde{r}} = -(\tilde{n}_i - \tilde{n}_e). \tag{3.3}$$

[3]The derivations of this section follow closely those given by *Conrad* [1987].

We have assumed that during the ion–matrix phase of sheath evolution, the electron density in the sheath is zero (*i.e.*, $n_e = 0$) and the ion density remains unchanged from before the voltage was applied and is uniform (*i.e.*, $n_i = n_0$). Equation (3.3) then becomes

$$\frac{d^2\tilde{V}}{d\tilde{r}^2} + \frac{\alpha_P}{\tilde{r}}\frac{d\tilde{V}}{d\tilde{r}} = -1, \tag{3.4}$$

which can be solved subject to the following boundary conditions: 1) the potential at the conductor, V, must equal the applied potential, V_a, *i.e.*, $\tilde{V} = \tilde{V}_a \equiv q_e V_a/kT_e$ at $\tilde{r} = \tilde{r}_a \equiv r_a/\lambda_D$, and 2) the electric field must vanish at the ion–matrix sheath–edge position, r_{sh}, *i.e.*, $\frac{d\tilde{V}}{d\tilde{r}} = 0$ at $\tilde{r} = \tilde{r}_{\text{sh}} \equiv r_{\text{sh}}/\lambda_D$. The solutions of Equation (3.4) subject to the above boundary conditions for the three geometries are [*Conrad*, 1987]:

- planar geometry

$$\tilde{V}(\tilde{r}) = -\tilde{V}_a + \tilde{r}_{\text{sh}}(\tilde{r} - \tilde{r}_a) + (\tilde{r}_a^2 - \tilde{r}^2)/2, \tag{3.5}$$

- cylindrical geometry

$$\tilde{V}(\tilde{r}) = -\tilde{V}_a + (\tilde{r}_{\text{sh}}^2/2)\ln(\tilde{r}/\tilde{r}_a) + (\tilde{r}_a^2 - \tilde{r}^2)/4, \tag{3.6}$$

- spherical geometry

$$\tilde{V}(\tilde{r}) = -\tilde{V}_a + (\tilde{r}_{\text{sh}}^3/3)(1/\tilde{r}_a - 1/\tilde{r}) + (\tilde{r}_a^2 - \tilde{r}^2)/6. \tag{3.7}$$

The expression for sheath position is then simply obtained by setting the potential $\tilde{V}(\tilde{r})$ at $\tilde{r} = \tilde{r}_{\text{sh}}$ to zero in Equations (3.5)–(3.7). Doing this yields:

- planar geometry

$$(\tilde{r}_{\text{sh}}/\tilde{r}_a - 1)^2 = 2\tilde{V}_a/\tilde{r}_a^2, \tag{3.8}$$

- cylindrical geometry

$$2(\tilde{r}_{\text{sh}}/\tilde{r}_a)^2 \ln(\tilde{r}_{\text{sh}}/\tilde{r}_a) - (\tilde{r}_{\text{sh}}/\tilde{r}_a)^2 + 1 = 4\tilde{V}_a/\tilde{r}_a^2, \tag{3.9}$$

- spherical geometry

$$2(\tilde{r}_{\text{sh}}/\tilde{r}_a)^3 - 3(\tilde{r}_{\text{sh}}/\tilde{r}_a)^2 + 1 = 6\tilde{V}_a/\tilde{r}_a^2. \tag{3.10}$$

In Figure 3.1, the parameter $\tilde{r}_{\text{sh}}/\tilde{r}_a$ is plotted against $\tilde{V}_a/\tilde{r}_a^2$ for each of the Equations (3.8)-(3.10).

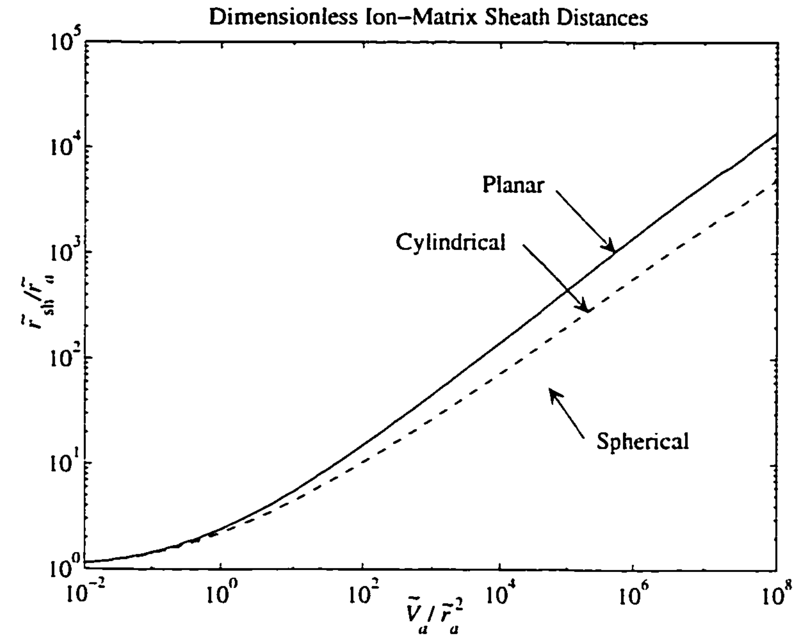

Figure 3.1: Dimensionless ion–matrix–sheath distances, $\tilde{r}_{\text{sh}}/\tilde{r}_a$, in planar, cylindrical, and spherical geometries as a function of the parameter $\tilde{V}_a/\tilde{r}_a^2$.

As a final step, we attempt to isolate the $\tilde{r}_{\text{sh}}$ term in Equations (3.8)-(3.10). For the planar case of Equation (3.8), this is relatively simple, and we obtain

$$\tilde{r}_{\text{sh}} = \tilde{r}_a + \sqrt{2\tilde{V}_a}.$$

However, since the potential in the planar case is translationally invariant, $\tilde{r}_a$ can be set to zero yielding

$$\tilde{r}_{\text{sh}} = \sqrt{2\tilde{V}_a}. \tag{3.11}$$

For the moment, we will skip over solving the cylindrical case since the logarithmic dependence in the equation does not allow isolation of $\tilde{r}_{\text{sh}}$. For the spherical case, in the thick–sheath limit (*i.e.*, $\tilde{r}_{\text{sh}} \gg \tilde{r}_a$), Equation (3.10) reduces to

$$\tilde{r}_{\text{sh}} \simeq (3\tilde{V}_a\tilde{r}_a)^{1/3} \text{ for } \tilde{r}_{\text{sh}} \gg \tilde{r}_a. \tag{3.12}$$

Returning to the cylindrical case, *Conrad* [1987] states that a reasonable approximation in the thick–sheath limit—within 20% for $10 < \tilde{V}_a/\tilde{r}_a^2 < 10^6$—may be obtained by taking the geometric mean of the planar and spherical thicknesses, yielding

$$\tilde{r}_{\text{sh}} \simeq 2^{1/4}3^{1/6}\tilde{V}_a^{5/12}\tilde{r}_a^{1/6}.$$

Since $2^{1/4}3^{1/6} \approx \sqrt{2}$, we can then write

$$\tilde{r}_{\text{sh}} \simeq \sqrt{2}\tilde{V}_a^{5/12}\tilde{r}_a^{1/6}.$$

However, comparison of this equation with the exact relation of Equation (3.9) results in noticeable discrepancy for the plasma parameters used in this research. A constant of $\sqrt{3}$, however, yields much better agreement, as is shown in Figure 3.2. Hence, we can write

$$\tilde{r}_{\text{sh}} \simeq \sqrt{3}\tilde{V}_a^{5/12}\tilde{r}_a^{1/6} \text{ for } \tilde{r}_{\text{sh}} \gg \tilde{r}_a. \tag{3.13}$$

In terms of physical quantities, the dimensionless equations for the ion–matrix–sheath position become

- planar geometry

$$r_{\text{sh}} = \sqrt{\frac{2V_a\varepsilon_0}{q_e n_0}}, \tag{3.14}$$

- cylindrical geometry

$$r_{\text{sh}} \simeq \sqrt{3}\left(\frac{V_a \varepsilon_0}{q_e n_0}\right)^{5/12} r_a^{1/6} \text{ for } r_{\text{sh}} \gg r_a, \tag{3.15}$$

- spherical geometry

$$r_{\text{sh}} \simeq \left(\frac{3V_a \varepsilon_a r_a}{q_e n_0}\right)^{1/3} \quad \text{for } r_{\text{sh}} \gg r_a. \tag{3.16}$$

Two items should be noted about the above equations and their derivation. First, the planar equation depends only on potential and plasma density, whereas the cylindrical and spherical equations also depend weekly on conductor radius. Second, it can be shown that in the thin–sheath limit ($r_{\text{sh}} \lesssim r_a$), the cylindrical and spherical equations reduce to the form of the planar equation (see Figure 3.1). All three solutions [Equations (3.14)–(3.16)] are plotted as a function of absolute applied voltage in Figure 3.2 for $r_a = 0.65$ mm (radius of wire used in experiments, see Table 3.2) and $n_e = 10^{12}$ m^{-3}. For the cylindrical case, the exact solution from Equation (3.9) is also plotted, showing that the approximation has good agreement for the chosen parameters.

3.2.2 Applied–Charge Approach: The Equal–Charge Radius

The derivation of the ion–matrix–sheath distance in Section 3.2.1 above yielded the scale–length for perturbation containment in the case where the voltage applied to the conductor is known. When the applied voltage is not known, but the applied charge is, then the equal–charge approach provides the appropriate scale–length: the equal–charge radius, r_{ch}. This radius can be thought of as the thickness of the slab that contains the charged conductor as well as the volume of charge from the plasma equal to that on the conductor [*Borovsky*, 1988]. The equal–charge radii for various geometries are:

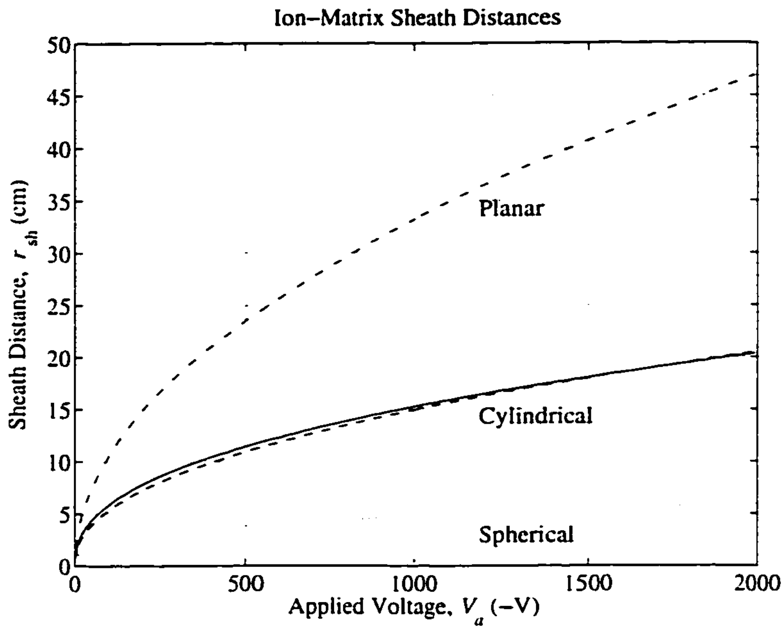

Figure 3.2: Ion–matrix sheath distances in planar, cylindrical [solid line is approximation from Equation (3.15), dashed line is exact solution from Equation (3.9)], and spherical geometries as a function of applied voltage for the following conditions: $r_a = 0.65$ mm, $n_0 = 1.0 \times 10^{12}$ m^{-3}.

- planar geometry

$$r_{\text{ch}} = \frac{\rho_{sa}}{n_0 q_e} = \frac{Q_a}{An_0 q_e} \text{ since } \rho_{sa} = Q_a/A, \tag{3.17}$$

- cylindrical geometry

$$r_{\text{ch}} = \left[\frac{2\rho_{sa} r_a}{n_0 q_e} + r_a^2\right]^{1/2} = \left[\frac{Q_a}{\pi n_0 q_e l} + r_a^2\right]^{1/2} \text{ since } \rho_{sa} = \frac{Q_a}{2\pi r_a l}, \tag{3.18}$$

- spherical geometry

$$r_{\text{ch}} = \left[\frac{3\rho_{sa} r_a^2}{n_0 q_e} + r_a^3\right]^{1/3} = \left[\frac{3Q_a}{4\pi n_0 q_e} + r_a^3\right]^{1/3} \text{ since } \rho_{sa} = \frac{Q_a}{4\pi r_a^2}, \tag{3.19}$$

where ρ_{sa} is the surface charge density, A is the planar surface area, Q_a is the total applied charge on the conductor, l is the length of the cylinder, and r_a is the radius of the cylinder or sphere.

Discharging of a charged object immersed in a plasma occurs via collecting charge of opposite polarity from the surrounding plasma. When objects are weakly charged, the resulting electric fields are also weak and the plasma is not strongly perturbed. In this case, the discharging is governed by the thermal flux of particles to the object. Thus, for a positively charged object the rate of discharge is determined by the thermal electron flux. Similarly, for a negatively charged object the rate of discharge is determined by the thermal ion flux. (For an object moving at orbital velocity, however, the discharge time is related to the ion ram current density.) For the case of weakly charged object, the thermal flux is sufficient to discharge the object on the order of the electron or ion plasma period, depending on whether the object is charged positive or negative [*Borovsky*, 1988].

For strongly charged objects, however, the resulting electric fields are strong enough to accelerate the nearby particles to velocities greatly exceeding their thermal velocity. The fastest possible discharge time would occur if an equal–charge–radius worth of charge were accelerated inward. This time provides a lower limit to the discharge time.

3.2.3 Comparison of Applied–Voltage and Applied–Charge Approaches

In Section 3.2.1 the ion–matrix radius, r_{sh}, was derived using the applied–voltage approach and in Section 3.2.2 the equal–charge radius, r_{ch}, was derived using the applied–charge approach. Since the claim was made that these two approaches are complementary, then r_{sh} should equal r_{ch}. In this section we show that this claim is indeed true by deriving the well–known expression between voltage and charge for a capacitor.

We begin the derivation with the equations for r_{sh} and r_{ch} in planar geometry

[Equations (3.14) and (3.17), respectively]:

$$r_{\rm sh} = \sqrt{\frac{2V_a\varepsilon_0}{q_e n_0}} \qquad \text{and} \qquad r_{\rm ch} = \frac{\rho_{sa}}{n_0 q_e} = \frac{Q_a}{An_0 q_e}.$$

If we set these two equations equal to each other and solve for V_a we obtain

$$V_a = \frac{\rho_{sa}^2}{2\varepsilon_0 n_0 q_e}. \tag{3.20}$$

We note that this voltage appears across a distance $d = r_{\rm ch} = r_{\rm sh}$, so with this equivalence and Equation (3.17) we can replace $\frac{\rho_{sa}}{n_0 q_e}$ with d to obtain

$$V_a = \frac{\rho_{sa} d}{2\varepsilon_0}.$$

Since $Q = \rho_s A$, we can substitute Q into the above equation to yield

$$V_a = \frac{Qd}{2A\varepsilon_0}.$$

Wood [1993] states that the capacitance of the planar ion–matrix sheath is $C = \frac{2\varepsilon_0 A}{d}$, which is twice the normal parallel–plate capacitance due to the presence of the space charge. Substituting this relation into the above equation, we obtain

$$V_a = \frac{Q}{C}.$$

We recognize this equation as the relationship between Q, C, and V for a capacitor. Hence, having obtained a recognizable, physical relationship indicates that the claim $r_{\rm sh} = r_{\rm ch}$ is indeed true. This brief derivation is a precursor to the more rigorous derivation of sheath capacitance that is performed in Section 4.2.1 for cylindrical geometry.

3.2.4 Electron Response for Rapid Biasing

The rapid application ($\tau_{ar} < \tau_{pe}$) of a large negative bias to a conductor in a plasma (Figure 3.3a) produces the following qualitative response. Initially, due to their lighter mass, the electrons surrounding the object are rapidly repelled from it, leaving behind a region of heavier ions (Figure 3.3b). This region of positive charge, known as the ion–matrix sheath or equal-charge volume, acts to shield the negative potential of the object from the ambient plasma. However, due to their inertia, the outward-bound electrons will overshoot this radius causing a net positive charge to exist around the object (Figure 3.3c). This additional charge attracts the electrons back towards the object, whereupon they overshoot the equilibrium radius and are again repelled outwards. Hence, an oscillation about this equilibrium position is set up. This bulk "sloshing" of the electrons sets up a temporal electric field which, depending on geometry, "rings" at or near the electron plasma frequency.

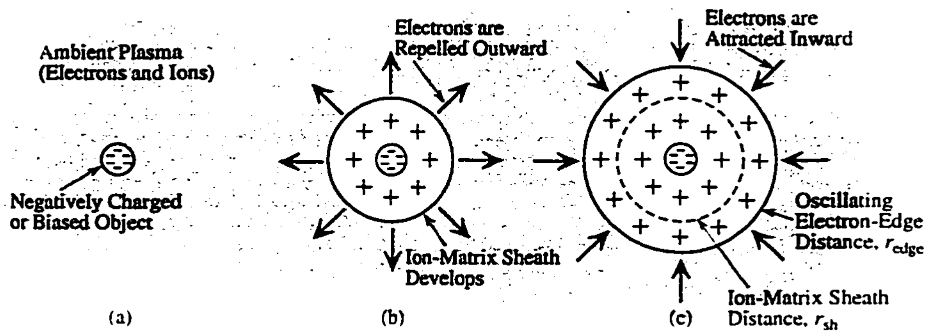

Figure 3.3: Electron–plasma–frequency ringing excited by rapidly biasing a conductor negative (or, alternately, rapidly charging the conductor): (a) initial charging, plasma undisturbed; (b) formation of ion–matrix sheath; (c) overshoot and subsequent attraction of electrons excites $\sim \omega_{pe}$ ringing.

The electric field of the high–frequency sheath due to the electron sloshing is composed of two regions [*Borovsky*, 1988]: a strong–electric–field "core" region established by the negatively charged object and a weaker, oscillating–electric–field region surrounding this core caused by the motion of the electrons about their equilibrium position, r_{sh} (Figure 3.3c).

The dynamic spatial edge of the electron distribution, denoted as r_{edge}, can be considered as the boundary between the core and the outer portion of the sheath (Figure 3.3c). To determine the charge density and hence the electric field inside the sheath, only the motion of this electron edge needs to be calculated [*Borovsky*, 1988]. Assuming a cold-plasma approximation, electrons move according to $\frac{\partial \mathbf{v}}{\partial t} = -\frac{q}{m_e}\mathbf{E}$ and, where the charge density is zero, the electron flow must be divergenceless, *i.e.*, $\nabla \mathbf{v} = 0$. These facts allow us to solve for the oscillatory motion of the electrons even though it is complicated by the radial dependence of the electric field.

We begin our derivation by assuming a planar geometry. In this case, the electric-field seen at r_{edge} is $E_{\text{edge}} = \frac{\rho_{sa}}{\varepsilon_0} + \frac{\rho_v}{\varepsilon_0} r_{\text{edge}}$ (from Gauss' Law), where ρ_{sa} is the surface charge density on the object surface and $\rho_v = qn_0$ is the volume charge density exposed in the ion–matrix sheath. The equation of motion for an electron at r_{edge} is $\frac{\partial^2 r_{\text{edge}}}{\partial t^2} = -\frac{q}{m_e} E_{\text{edge}}$. Substituting the relations for E_{edge} and ρ_v into the electron equation of motion, and noting that $r_{\text{ch}} = \frac{\rho_{sa}}{n_0 q_e}$ (where $q_e = -q$) yields

$$\frac{\partial^2 r_{\text{edge}}}{\partial t^2} = -\frac{q}{m_e}\left(-\frac{n_0 q}{\varepsilon_0} r_{\text{ch}} + \frac{n_0 q}{\varepsilon_0} r_{\text{edge}}\right). \tag{3.21}$$

We recall that $\omega_{pe} = \sqrt{\frac{n_0 q^2}{m_e \varepsilon_0}}$ and define $\tilde{r}_{\text{edge}} = \frac{r_{\text{edge}}}{r_{\text{ch}}}$, which allows us to rewrite Equation (3.21) as

$$\frac{\partial^2 \tilde{r}_{\text{edge}}}{\partial t^2} = \omega_{pe}^2 (1 - \tilde{r}_{\text{edge}}). \tag{3.22}$$

Similar equations of motion can be derived for the electron oscillation of the cold plasma in cylindrical and spherical geometries. All three equations are summarized below [*Borovsky*, 1988]:

- planar geometry

$$\frac{\partial^2 \tilde{r}_{\text{edge}}}{\partial t^2} = \omega_{pe}^2 (1 - \tilde{r}_{\text{edge}}), \tag{3.23}$$

- cylindrical geometry

$$\frac{\partial^2 \tilde{r}_{\text{edge}}}{\partial t^2} = \frac{\omega_{pe}^2}{2} \left(\frac{1}{\tilde{r}_{\text{edge}}} - \tilde{r}_{\text{edge}} \right), \tag{3.24}$$

- spherical geometry

$$\frac{\partial^2 \tilde{r}_{\text{edge}}}{\partial t^2} = \frac{\omega_{pe}^2}{3} \left(\frac{1}{\tilde{r}_{\text{edge}}^2} - \tilde{r}_{\text{edge}} \right). \tag{3.25}$$

The equation for planar geometry is a linear differential equation of ω_{pe} which means that the electron ringing frequency $\omega_{\text{ring}} = \omega_{pe}$ independent of amplitude. The equations for cylindrical and spherical geometries, however, are nonlinear differential equations. The nonlinear nature of these equations results in $\omega_{\text{ring}} \geq \omega_{pe}$. For small perturbations, though, Equations (3.24) and (3.25) are approximately linear as $\tilde{r}_{\text{edge}} = \frac{r_{\text{edge}}}{r_{\text{ch}}} \rightarrow 1$, which means $\omega_{\text{ring}} \sim \omega_{pe}$. For extremely large perturbations, *i.e.*, when $\tilde{r}_{\text{edge,min}} \rightarrow 0$, then $\omega_{\text{ring}} \rightarrow \sqrt{2}\omega_{pe}$ for cylindrical geometry and $\omega_{\text{ring}} \rightarrow \frac{2}{\sqrt{3}}\omega_{pe}$ for spherical geometry.

Borovsky [1988] employed particle–in–cell simulations to investigate this ringing. Listed here are several interesting results from his investigation into the ringing:

- The electron ringing frequency, ω_{ring}, remains fairly constant in cylindrical and spherical geometries even with large perturbations. This is surprising since the maximum and minimum excursions during the oscillations are not symmetric about $\tilde{r}_{\text{edge}}$. It is also surprising since a deep density cavity forms around the object during ringing which means that the local value of ω_{pe} can be much lower than ω_{pe0}.

- The amplitude of ringing $V_{\text{ring}} \approx |V_a|$ for large values of applied voltage, $|V_a|$, in both planar and cylindrical geometries except that V_{ring} more closely equals $|V_a|$ in planar geometry.

- The amplitude of the ω_{pe} ringing was found to be sensitive to the ratio of the object radius to the equal–charge radius, r_a/r_{ch}. For increasing values of r_a/r_{ch}, the system appears more planar and the coupling of the voltage spike to the plasma becomes stronger.

- The potential of the object in nonequilibrium plasma (plasma with regions of nonzero charge density) is not determined by the charge on it. In addition, the ringing does not cease when the object is discharged.

This last observation is quite intriguing, but it may have to do with the fact that in his simulations, *Borovsky* applied a charge or voltage to an object and then let it float to examine the ringing. This is in contrast with PIC simulations by *Calder et al.* [1993], where the conductors were clamped to an applied voltage. For an $r_a = 1\lambda_D$ conductor, *Calder et al.* found via PIC simulations an expression for the sheath resonance frequency

$$\omega_{\text{ring}} = \omega_{pe}(0.38 + 0.12 \log |\tilde{V}_a|), \tag{3.26}$$

which is smaller than the electron plasma frequency, not larger as in the work of *Borovsky*. However, since Equation (3.26) is empirically derived from PIC simulation results, it most likely accounts for the lowered local plasma density. This lowered local plasma density, in turn, lowers the local plasma frequency and also the sheath resonance frequency.

The energy associated with the ω_{pe} ringing energizes the electrons and launches large–amplitude Langmuir and ion–acoustic waves [*Borovsky*, 1988; *Calder et al.*, 1993]. The ringing also produces cavitation within the plasma via the oscillating two–stream instability and the ω_{pe} ringing may give rise to ω_{pe} electromagnetic radiation, which effectively means a rapidly biased object can be detected remotely [*Borovsky*, 1988].

The mechanisms which damp the oscillations may be the transfer of energy to shorter wavelength Langmuir waves and energetic electrons. The Langmuir condensate instability (oscillating two–stream instability) may also play a role in the ring decay [*Borovsky*, 1988].

3.2.5 Sheath Evolution

In the timescale on the order of the ion plasma period, τ_{pi}, the ions begin to move and a steady–state sheath begins to evolve. In planar geometry or when $r_a \gg \lambda_D$, a Child–Langmuir sheath evolves; that is, the sheath distance grows from $r_s = r_{\mathrm{sh}}$ initially to $r_s = r_{\mathrm{CL}}$. A brief description of the Child–Langmuir sheath is given in Section 2.2.2.1. As is shown in Section 2.2.3, how this sheath develops is an active area of research, especially for plasma–immersion ion implantation devices.

Since we are dealing with low–density plasmas and thin cylinders, the condition $r_a \gg \lambda_D$ does not hold. Instead, $r_a \lesssim \lambda_D$ holds and an orbital–motion–limited sheath evolves. An examination of OML–sheath evolution is beyond the scope of this work, but such a description would augment the model developed here by extending it into the frequency regime $\omega \lesssim \omega_{pi}$. In this work we limit ourselves to the frequency regime $\omega_{pe} \gg \omega \gg \omega_{pi}$ so that we do not have to take into account sheath evolution past the ion–matrix sheath.

3.2.6 Sheath Collapse

For the case of the negatively biased insulated cylinder, the applied voltage becomes shielded from the plasma as ions are collected to the surface of the insulation, and the sheath will begin to collapse. (See Section 2.2.4 for a brief discussion of this phenomenon.) The time required for sheath collapse depends on the density of the current flowing to the insulator and can be on the order of several milliseconds or more for typical tether geometries and ionospheric plasma densities. For the case of a bare cylinder, the sheath does not collapse, but rather evolves into the OML sheath as discussed in the previous section. The reason for this is that the applied voltage is not shielded by the collected charge since they move along the conductor as a current.

It should be mentioned that this description assumes that the conductor has been "clamped" to V_a with an ideal voltage source such that any amount of flowing current can be sourced or sunk. When this is not the case and the conductor is instead "floated", then the collected current eventually neutralizes all of the applied charge such that the object potential approaches the plasma floating potential. This floating case was the premise assumed in most of the PIC simulations performed by *Borovsky* [1988] but not the PIC simulations of *Calder et al.* [1993] who clamped the potential. In this work, we assume that any current collected along the conductor can be effectively sourced or sunk at the end; that is, the conductor potential is clamped to V_a. In reality, V_a from the source may change due to biasing conditions needed to source or sink the current on the line, but this is treated and modeled separately.[4] In our model, the conductor section (*i.e.*, a given section of tether) is connected to a source some distance away which acts as a reference point.[5]

[4]Appropriate models for the conductor's endpoints must be implemented since these endpoints might not be able to sink or source all current levels. See *Bilén et al.* [1995] and Appendix D, Section D.1 for an analysis of what effect this had on TSS-1-mission transient data during which the Orbiter was not always able to source needed current levels.

[5]See *Agüero* [1996] for using a tethered system as a remote plasma reference.

3.3 Plasma Chamber Experiments

The purpose of this set of experiments was to characterize the voltage dependence and the temporal response of the plasma sheath surrounding bare and insulated conductors as a pulsed, negative high–voltage was applied to each individually. The geometries of the conductor samples were chosen to closely match that of an electrodynamic tether, and in particular, the TSS tether. The plasma densities and temperatures were very similar to those of the ionosphere. The results of these experiments are used to corroborate the analytic sheath model developed in Section 3.2 and the results of the particle–in–cell simulations of Section 3.4. Hence, the experimental results can be applied to the problem of pulse propagation along electrodynamic tethers for the case where the pulsed voltage is large enough to significantly affect the surrounding plasma medium.

The concept of the experiment is as follows (see Figure 3.4). A sample is placed in a plasma where a steady–state sheath forms around it (at the floating potential). When a negative HV step is applied to the sample, the sheath responds by expanding to shield this new disturbance. Since the sample is now negatively biased, the sheath region is primarily devoid of electrons. Placed some distance away, a probe is biased positive such that it collects primarily an electron current. This probe is called a biased probe (BP). As the sheath expands past the BP, the number of electrons available to be collected decreases significantly, and hence the current collected by the probe falls as well. The time history of this BP current, which is measured across a resistor, yields the time history of the electrons in the region surrounding the BP, allowing a characterization of the temporal response of the sheath to the negative HV disturbance. The dependence of the sheath distance to the applied voltage is determined by positioning the probe at various distances from the sample under test. Comparison of the collected current waveforms then shows the location of the sheath edge for different applied voltages.

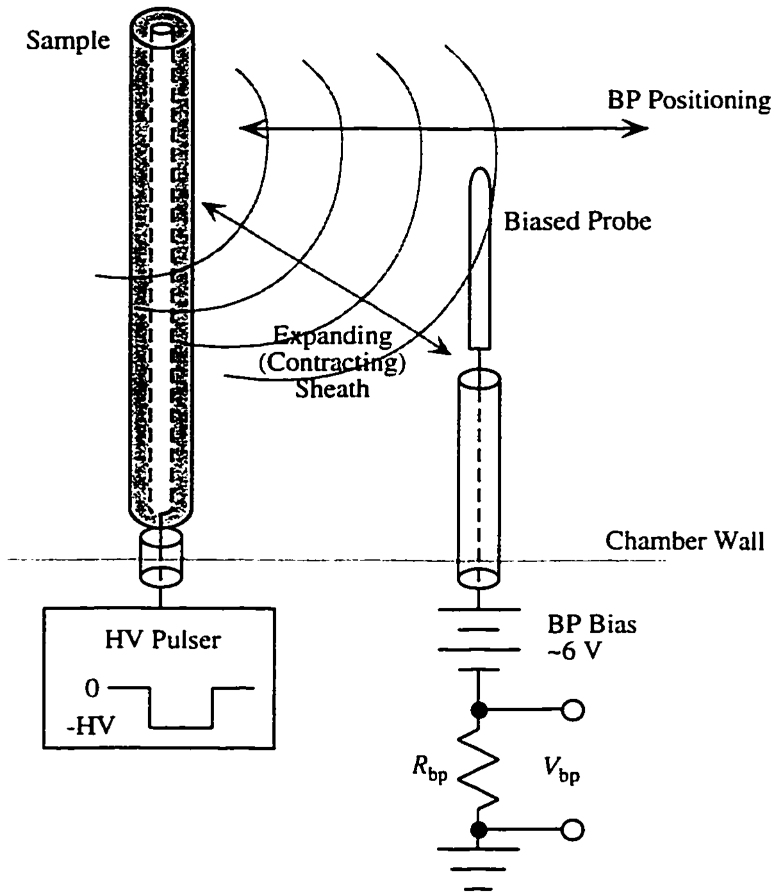

Figure 3.4: Diagram of the biased–probe system.

The experiments discussed here are similar to those performed by other researchers. However, the geometries of the sample and the plasma environment were chosen such that they matched as closely as possible the tether geometry and the surrounding ionosphere. These choices are in contrast with those of previous works which were chosen to match planar geometries (or the assumption of approximately planar sheaths, *i.e.*, CL sheaths) and higher plasma densities suitable for plasma processing.

3.3.1 Chamber Setup and Plasma Environment

The experiments were performed in the 6×9–m Michigan Large Chamber Plasma Facility (MLCPF) at the Plasmadynamics and Electric Propulsion Laboratory (PEPL) at the University of Michigan. Using a hollow cathode assembly (HCA) in this large chamber provided a plasma environment which closely simulates that of the ionosphere. The HCA provides a low–temperature, low–density, fairly uniform plasma in its far–field, and the MLCPF allows ample room such that the effects of plasma confinement—*i.e.*, interaction with the walls and support structures—can be reduced to a minimum. Appendix B provides a more detailed description of this chamber and the HCA plasma environment. Figure 3.5 is a diagram of the MLCPF as it was set up for these experiments.

During these tests, three different gases were used at different flowrates and discharge voltages in order to obtain different n_e's and T_e's. The plasma density and temperature throughout the measurement region was determined via the Langmuir–probe method as outlined in Appendix C. Contour plots of n_e for the entire sampling region can be found in Section B.2.1 of Appendix B. Table 3.1 lists the n_e values nearest the sample locations for each of the nine operating conditions and shows that the plasma density varies very little from side to side for each condition.

3.3.2 Sample Preparation

Four samples were used in these experiments: a bare plate, an insulated plate, an insulated wire, and a bare wire. The wire samples were designed to closely match the geometry of an electrodynamic tether (such as the TSS tether described in Section

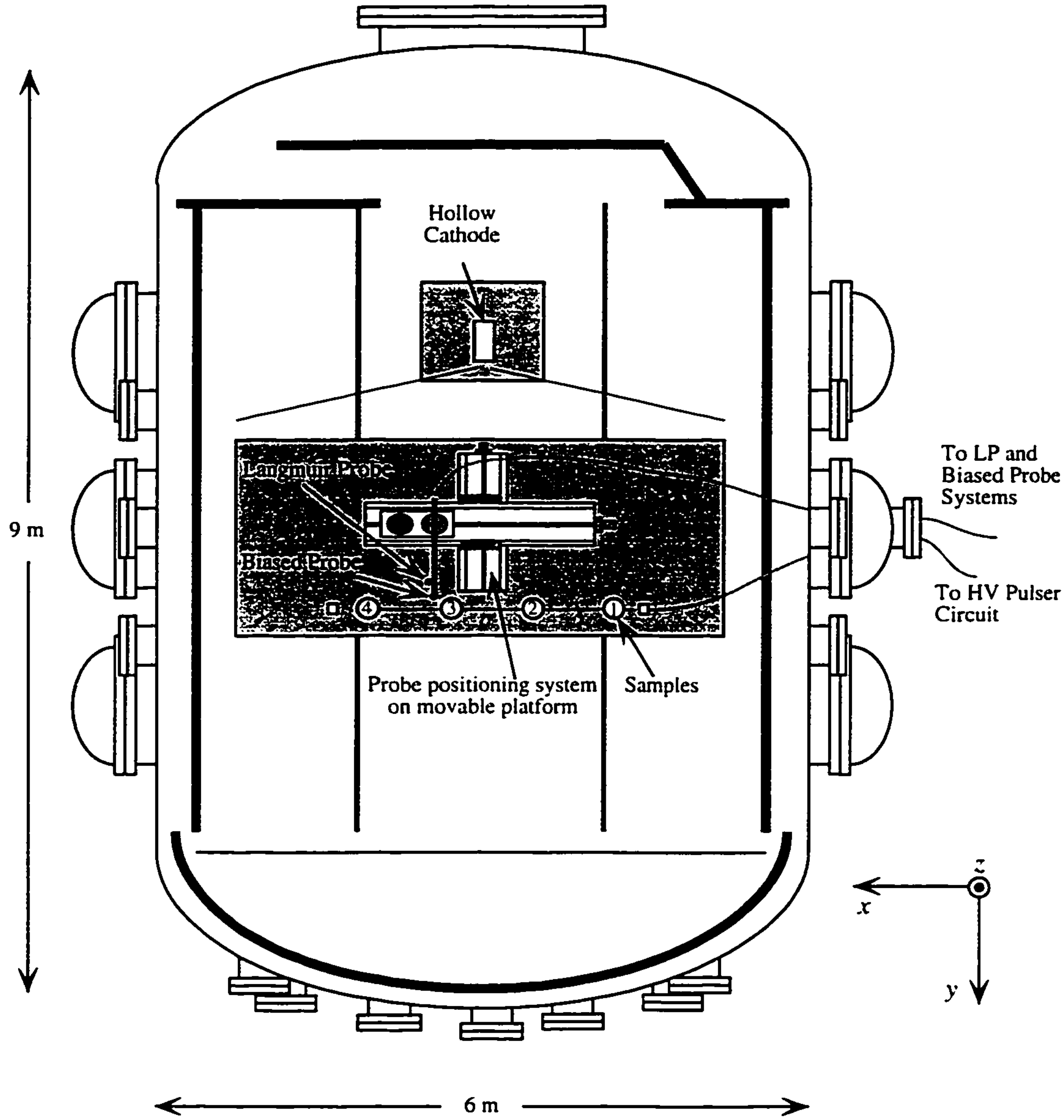

Figure 3.5: Setup of the plasma chamber for the transient–HV–sheath experiments showing the location of the samples, hollow cathode assembly, and the biased and Langmuir probes.

Table 3.1: Plasma densities nearest the sample locations for each of the nine HCA operating conditions.

Oper. Cond.	Gas	n_e at sample, $\times 10^{12}$ m^{-3}			
		Sample 1	Sample 2	Sample 3	Sample 4
1	krypton	2.8	3.3	3.3	3.0
2	krypton	9.0	9.7	9.4	7.5
3	krypton	0.87	1.1	1.1	1.1
4	argon	0.95	1.1	1.1	1.1
5	argon	1.2	1.4	1.4	1.4
6	argon	0.82	0.98	0.99	0.97
7	xenon	1.2	1.4	1.4	1.3
8	xenon	5.8	6.5	6.3	5.4
9	xenon	2.4	2.7	2.6	2.3

5.1.1). Both planar and cylindrical geometries were chosen such that differences in the sheath evolution around these two could be compared. Table 3.2 lists the physical characteristics of each of the four samples.[6]

Table 3.2: Table listing sample geometries and materials used during transient-HV-sheath experiments.

Sample Number	Sample Type	Material	Dimensions
1	bare plate	stainless steel	15.2 (w) × 22.9 (h) × 0.013 (thick) cm
2	insulated plate	Teflon®-covered stainless steel	15.2 (w) × 22.9 (h) × 0.121 (thick) cm [plate: 0.013 cm (thick), Teflon: 0.059 cm (thick)]
3	insulated cylinder	ceramic-covered copper wire	0.318 (dia.) × 61.6 (len.) cm [wire: 16 AWG (0.130 cm dia.), ceramic: 0.094 cm (thick)]
4	bare cylinder	tinned copper wire	16 AWG (0.130 cm dia.) × 59.1 (len.) cm

[6] It was originally intended to cover the wires with Teflon as well. In preliminary tests, however, the connection with the SHV connector arced when the HV was applied, thus necessitating the use of a ceramic coating instead.

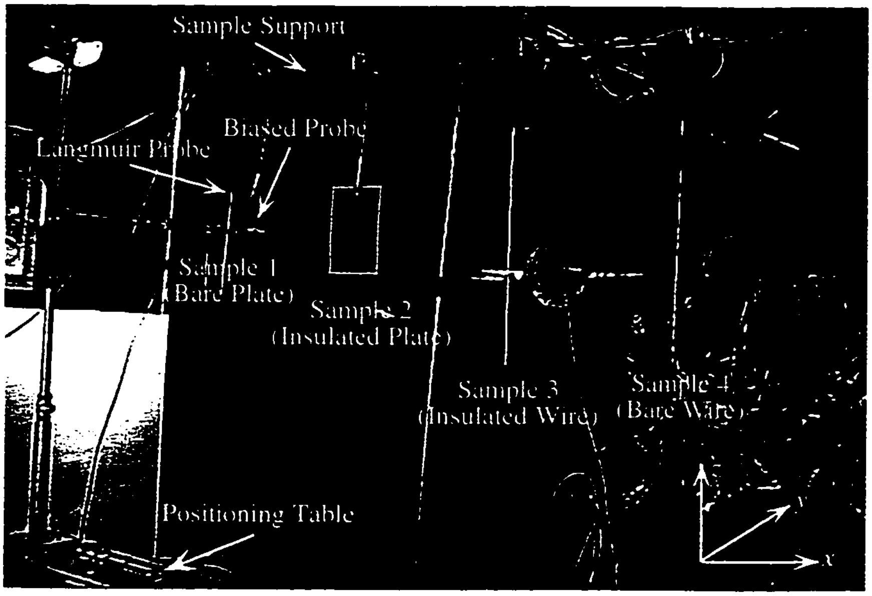

Figure 3.6: Picture of the chamber and samples as set up for the transient–HV–sheath experiments.

The pulsed negative HV was delivered to each of the samples via separate HV coaxial cables. The metallic portion of each sample was connected to the center pin of an SHV connector, whereas the cable shields were connected to a metallic support structure that was grounded to the chamber and supported the samples (Figure 3.6).

3.3.3 Test Equipment

The test equipment used during the transient–HV–sheath experiments included a high–voltage power supply and switch, TTL pulse generator, oscilloscope, electrometer, high–voltage probe, current probe, and computer controller (Figure 3.7). The oscilloscope and electrometer were connected via an IEEE–488 bus to a computer controller which set equipment parameters and stored data. Detailed descriptions of the equipment used and their function is listed below.

High–Voltage Power Supply An ORAM DSRR 5–1A power supply capable of delivering 1 A at 5 kV provided the negative HV to the HV switch. A capacitor–and–resistor network ($C_1 = 200$ nF, $R_1 = 2180\ \Omega$, and $R_2 = 100$ kΩ) was used to stabilize the HV supply because it does not regulate well under small nor transient loads.

High–Voltage Switch A Directed Energy, Inc. GRX-3.0K-H solid–state HV pulser was used to switch on and off the HV to the sample. The supply is designed to drive capacitive loads and will generate an output voltage swing of up to 3 kV with a peak output current of 30 A (0.1 A continuous). This provides very flat voltage pulses into capacitive loads such as transmission lines. The switch is controlled by an input TTL–level signal. The GRX-3.0K-H is capable of producing pulses with risetimes $\lesssim 45$ ns into a 150–pF load at ± 3000 V.

TTL Pulse Generator A BK Precision 3300 pulse generator provided the TTL–level pulse signals to the HV switch.

Oscilloscope A Tektronix TDS540 oscilloscope captured all signal waveforms. This 4–channel oscilloscope has a bandwidth of 500 MHz and has the capability of sampling up to 1 Gsample/s on a single channel (or 500 Msample/s on two channels and 250 Msample/s on four channels) through successive sampling techniques.

Electrometer A Keithley 2410 source electrometer was used to drive the Langmuir probe (LP) system. The electrometer measured the current collected by the LP as it was swept from -20 to 20 V. The LP was moved via the positioning table. LP measurements were used to measure electron temperatures and number densities of the HCA plasma plume near each of the samples.

High–Voltage Probe A Tektronix P6015 1000:1 HV probe was used to measure the HV output of the HV switch. The probe risetime is $\leq$ 4.5 ns.

Current Probe A Tektronix AM 503 current–probe amplifier and Tektronix A6302 current probe were used to measure current delivered to the samples. The full bandwidth of the probe is DC to 50 MHz with a risetime of $\leq$ 7 ns.

Computer Controller An Apple Macintosh Quadra running LabVIEW™ software from National Instruments was used to set equipment parameters and to store data via an IEEE–488 bus.

In addition to the equipment shown in Figure 3.7, a positioning table was used to move the LP and BP at each sample. The 4 samples and the probe positioning system were located in the plasma chamber as shown in Figure 3.5.

3.3.4 Comments on the Experimental Setup and Apparatus

3.3.4.1 Biased Probe

The BP was fashioned from a 6.0–in. (15.2–cm) section of semi–rigid cable which had 1.0 in. (2.5 cm) of the outer copper shielding removed and an additional 1.48 cm of the Teflon®insulation removed to expose the center conductor (0.94–mm diameter). This conductor was bent at a right angle with respect to the cable axis and sealed into position with ceramic epoxy (see Figure 3.8). The right–angle construction allowed the BP to move in close to the samples under test and ensured that there would be no distributed–sheath effect along the length of the BP which could affect the current collected by it.

With reference to Figure 3.4, the operation of the BP was as follows. The BP was biased to a positive voltage ($\sim$ +6 V) to ensure that it was collecting primarily electrons from the plasma. Storage batteries were used for biasing to eliminate the

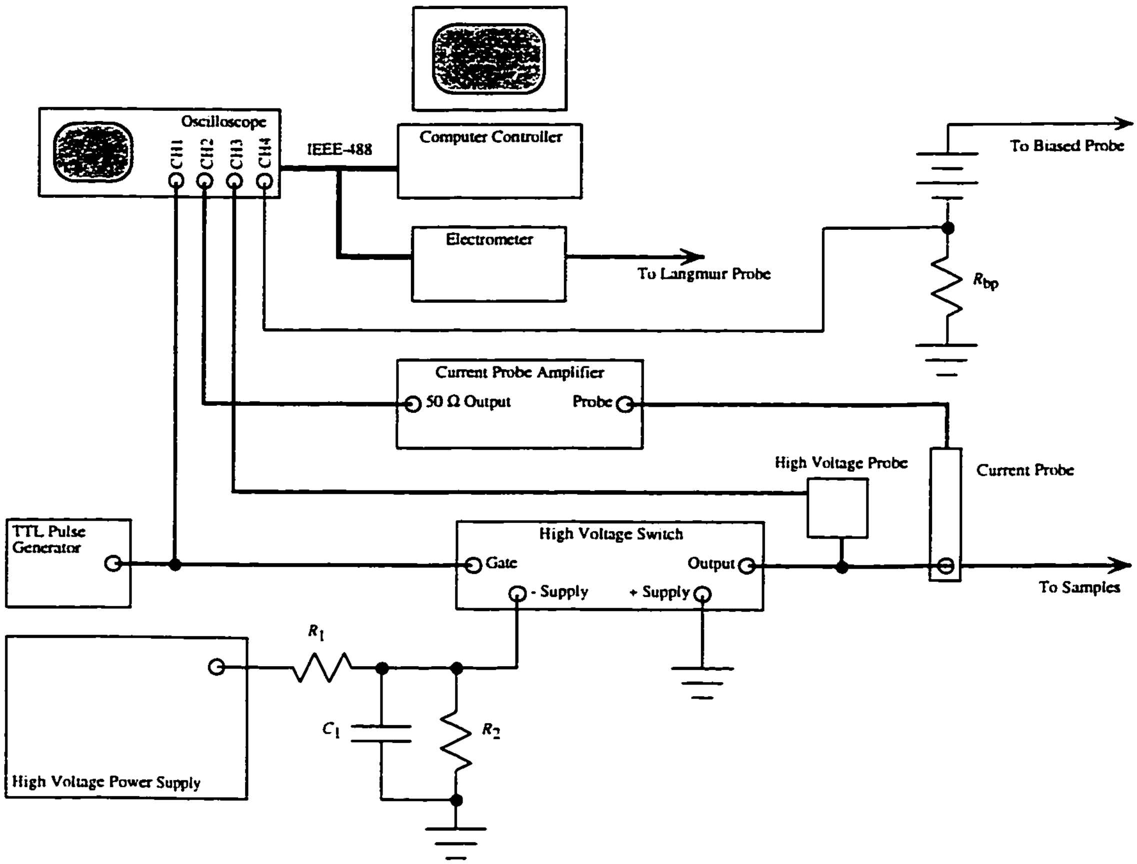

Figure 3.7: Diagram of the test–equipment setup used during the transient–HV–sheath experiments showing the high–voltage pulsing system, current probe, electrometer, computer controller, and biased–probe setup.

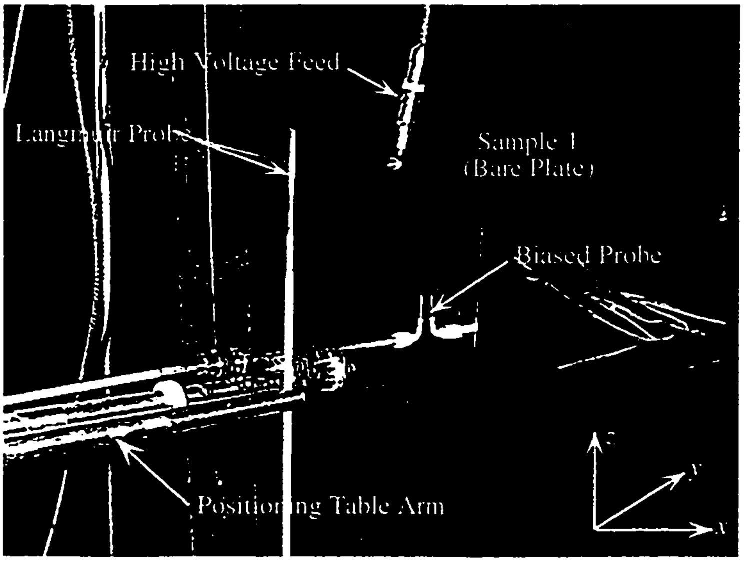

Figure 3.8: Picture of the biased probe at sample 1 (bare plate).

effect of any power–supply capacitance on the BP current response.[7] The presence of such a capacitance would have lead to an undesirable additional RC time constant in the voltage response measured across the resistor $R_{\mathrm{bp}} = 9.97$ kΩ. The current to the probe was calculated from the voltage, V_{bp}, measured across the resistor. To avoid using a differential probe for the V_{bp} measurement, the resistor R_{bp} was placed between ground and the battery. Hence, the true voltage seen by the electrons at the BP tip included the voltage drop across this resistor in addition to the biasing (battery) voltage. Even at the highest densities, however, $|V_{\mathrm{bp}}| < 0.5$ V, and so this effect was neglected.

When negative HV pulses were applied to the samples under test, ion–matrix sheaths, which were almost completely devoid of electrons, formed around the samples. As the sheath edge traveled past the BP position, the current collected by it

[7]The importance of using storage batteries was advised by *Okuda* [1963a].

fell essentially to zero. In the case of the insulated samples, as the dielectric charged up, the voltage seen by the plasma fell and hence the sheath eventually collapsed. By analyzing the time histories of the BP responses, we can determine sheath size and propagation and collapse velocities [*Okuda*, 1963a,b,c; *Shamim et al.*, 1991].

3.3.4.2 Adverse Effects of Long Line Lengths

There were many benefits to performing these experiments in the large PEPL vacuum chamber as outlined in Appendix B. However, one disadvantage of the large chamber was the long lengths of coaxial cable required to reach the samples and the BP. These cables added large parasitic capacitances to the overall circuit which increased the minimum measurable risetimes. Table 3.3 lists the properties of the HV and BP signal cables, and Table 3.4 gives the lengths and total capacitances added to the circuits by each cable.

Table 3.3: Properties of the HV and signal cables used in the plasma chamber experiments [*Cooper Industries*, 1989, p. 139].

Cable	Use	Impedance, Ω	Capacitance, pF/ft (pF/m)	Propagation Velocity, % c
Belden 89259	HV	75	17.8 (58.4)	78
Belden 89907	BP signal	50	25.4 (83.3)	80

The HV switch is capable of producing risetimes $\lesssim 45$ ns into a 150–pF load at 3000 V; however, the capacitances of the HV cables were $\sim$ 3 to 6 times this. Hence, the HV risetimes provided to the samples were longer than 45 ns. Figure 3.9 shows a typical HV–pulse waveform for sample 1. The −500–V excitation along the sample–1 cable has a risetime of $\sim$ 75 ns. It is also interesting to note that the propagation time along this cable can be easily determined using the time–domain–reflectometry (TDR) technique. The TDR response begins with a half step (since

Table 3.4: Lengths and total capacitances of the HV and signal cables used in the plasma chamber experiments.

Cable	Length, in. (m)	Total Capacitance, pF
HV sample 1	305 (7.75)	452
HV sample 2	546 (13.87)	810
HV sample 3	546 (13.87)	810
HV sample 4	682 (17.32)	1012
BP signal	410 (10.41)	868

the cable initially looks like a 75–Ω load to the matched driving impedance). Upon arrival at the open–circuited end, the signal is reflected and the full applied voltage is seen at the source. The measured two–way propagation time of $\sim$ 60 ns corresponds well with the calculated value of $\sim$ 66 ns.

The parasitic capacitance of the BP cable limits the highest frequency component of the signal which can be resolved. The RC time constant for the BP cable capacitance and R_{bp} is $\tau_{\mathrm{bp}} = 8.7$ μs, which means the highest resolvable frequency is on the order of 100 kHz. This means that the electron response cannot be resolved since $\tau_{pe} \sim 100$ ns. However, the ion response can be resolved since $\tau_{pi} \sim 50$ μs.

When the large PEPL chamber is used for these experiments, the BP cable length cannot be reduced. However, there is one possible method of reducing the frequency limitation mentioned above, although it was not used in these experiments. This method involves buffering the signal inside the chamber at the BP with a current–mode amplifier such as a video driver. These video drivers are designed to drive coaxial–cable capacitances at high frequencies and may increase the measurable frequency range.

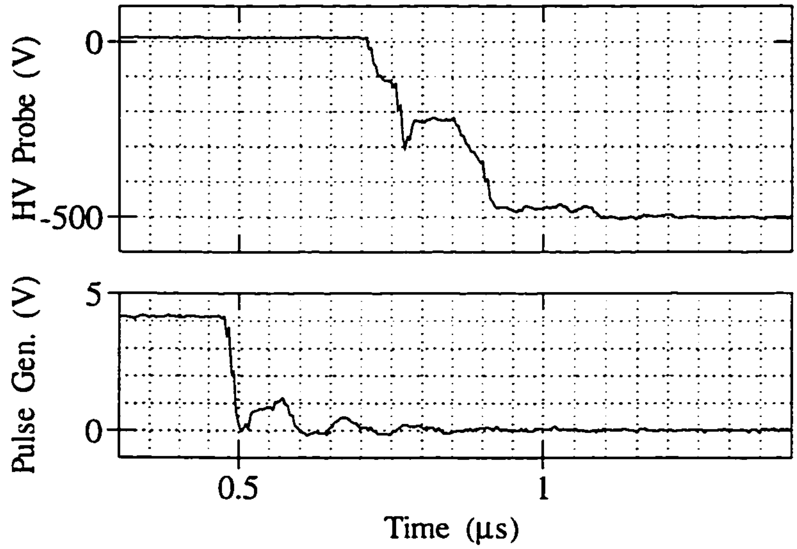

Figure 3.9: Typical HV–pulse waveform as measured by the 1000:1 HV probe for sample 1. Clearly visible in the waveform is a risetime of $\sim$ 75 ns and the propagation time along the open–circuited cable. The HV pulse was triggered by the TTL signal from the pulse generator.

3.3.4.3 Current Probe

Although collected, the current–probe (see Figure 3.7) data proved unusable because the positioning–table servo–motor amplifiers produced excessive ground–loop noise, which adversely affected the signal and was unable to be removed from the data.

3.3.5 Test Description

For each test, a pulse–train of 1.8-ms–duration, negative HV pulses was applied to each sample. These applied voltages are listed in Table 3.5.[8] The BP was then positioned near each sample under test, downstream from the HCA but upstream

[8] Voltages larger than -900 V applied to sample 3 caused an undetermined arcing problem in the experimental system. The arcing may have been caused by the impedance presented to the HV pulser by the insulated cylinder.

from each sample. For all 4 samples there were similar arrays of predetermined BP locations—roughly corresponding to 1.3, 2.5, 5.1, 17.8, 25.4, 38.1, 50.8, and 76.2 cm from the sample (see Figure 3.10)—in addition to finer steps selected during each experiment for the transition region at the sheath edge (*e.g.*, see the region between 5.1 and 10.2 cm in Figure 3.11). The BP signal was then collected by the oscilloscope which was triggered from the TTL pulse generator (see Figure 3.7) and continuously averaged 16 waveforms.

Table 3.5: Magnitude of the negative HV pulses applied to each of the samples for each HCA operating condition.

Oper.	Applied–Voltage Magnitudes, $\lvert V_a \rvert$			
Cond.	Sample 1	Sample 2	Sample 3	Sample 4
1	[500, 1000]	[500, 1000]	[500, 900]	[500, 1000, 2000]
2	[500, 1000]	[500, 1000]	[500, 900]	[500, 1000, 2000]
3	[500, 1000]	[500, 1000]	[500, 900]	[500, 1000, 2000]
4	—	—	[500, 900]	[500, 1000, 2000]
5	—	—	[500, 900]	[500, 1000, 2000]
6	—	—	[50, 100, 200, 350, 500, 900]	[50, 100, 200, 350, 500, 1000, 2000]
7	—	—	[500, 900]	[500, 1000, 2000]
8	—	—	[500, 900]	[500, 1000, 2000]
9	—	—	[500, 900]	[500, 1000, 2000]

3.3.6 Experimental Results

These experiments were designed to characterize the temporal and voltage–dependent response of the plasma sheaths surrounding bare and insulated conductors as pulsed, negative high–voltages were applied. Due to the long cable lengths required for both applying the HV and measuring the plasma's response via the BP, the initial electron response could not be examined. In addition, these long line lengths caused the frequency response of the BP signal to be on the order of the ion plasma

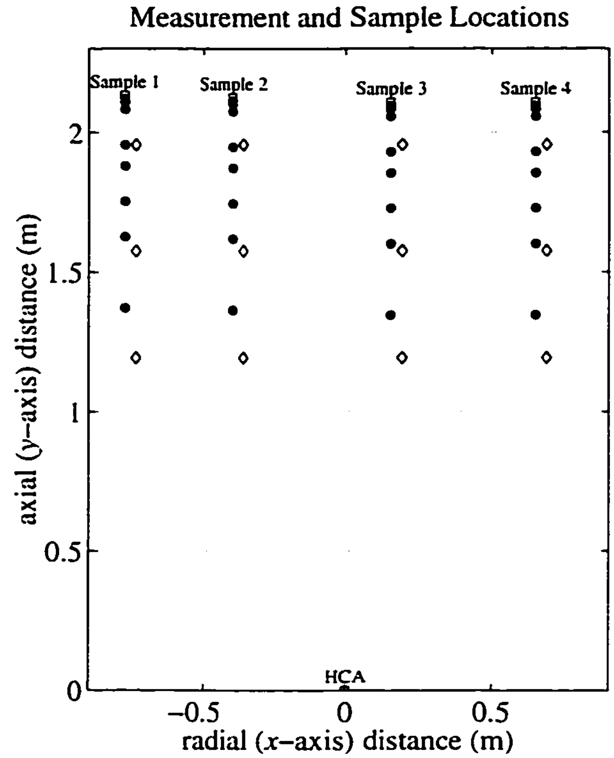

Figure 3.10: Locations of the biased- and Langmuir-probe measurements—marked with filled circles and open diamonds, respectively—with respect to the hollow cathode assembly (HCA) and the samples, which are marked with squares.

frequency. Hence, the ions were not "motionless" in a strict sense, even during the earliest portion of the BP signal. Given these limitations, however, useful data could be obtained on approximate ion-matrix-sheath size and the nature of the sheath collapse for the insulated samples.

Figures 3.11 and 3.12 provide plots of typical BP data for an insulated and a bare sample: samples 3 and 4, respectively. A brief description of these figures will aid in their interpretation. These two figures are basically "waterfall" plots with the additional characteristic that each BP trace is tied to a point on the distance axis. Each BP trace is marked with a symbol that is the same as that marking the line representing the zero–current reference point for the BP trace. This line also represents the BP location where the trace was collected. The distance from the zero line to the BP trace is the collected BP current at any given time; the BP–current scale is given at the top trace and is used for all traces. The BP current is related to the local electron density as discussed in the opening paragraphs of Section 3.3.4.1 and in Section 3.3: when $I_{\text{bp}} \to 0$, then $n_e \to 0$; the converse is also true.

3.3.6.1 Pseudo–Static Sheath Distances

As was mentioned, one of the goals of these experiments was to determine the ion–matrix–sheath distances around the samples. Due to the frequency–response limitation of the BP data, however, the data provide instead the location of what we term the "pseudo–static" sheath edge. (We use the term pseudo–static to describe the time–period after the electrons were expelled but before a large number of ions were collected and the steady–state sheath profile was established.) The BP data was reduced in the following manner to accomplish this task. The point at which the BP did not remain at zero current following the drop in the current signal marked the location of this distance. For example, in Figure 3.11 the pseudo–static sheath–edge distance was achieved at $9.7\,^{+1.5}_{-0.5}$ cm, because at this distance the BP collects a finite electron current after electron expulsion; hence, the BP must be outside of the region containing only ions, *i.e.*, the ion–matrix sheath. We performed this analysis for all BP traces and plotted these distances versus normalized units ($|V_a|/n_{e0}$, where n_{e0} is in units of 10^{12} m^{-3}) in Figure 3.13.

Figure 3.13 provides some interesting results which require an explanation. First, it is clearly seen that the data points follow the functional forms of the calculated values for both the plates [Equation (3.14)] and the cylinders [Equation (3.15)].

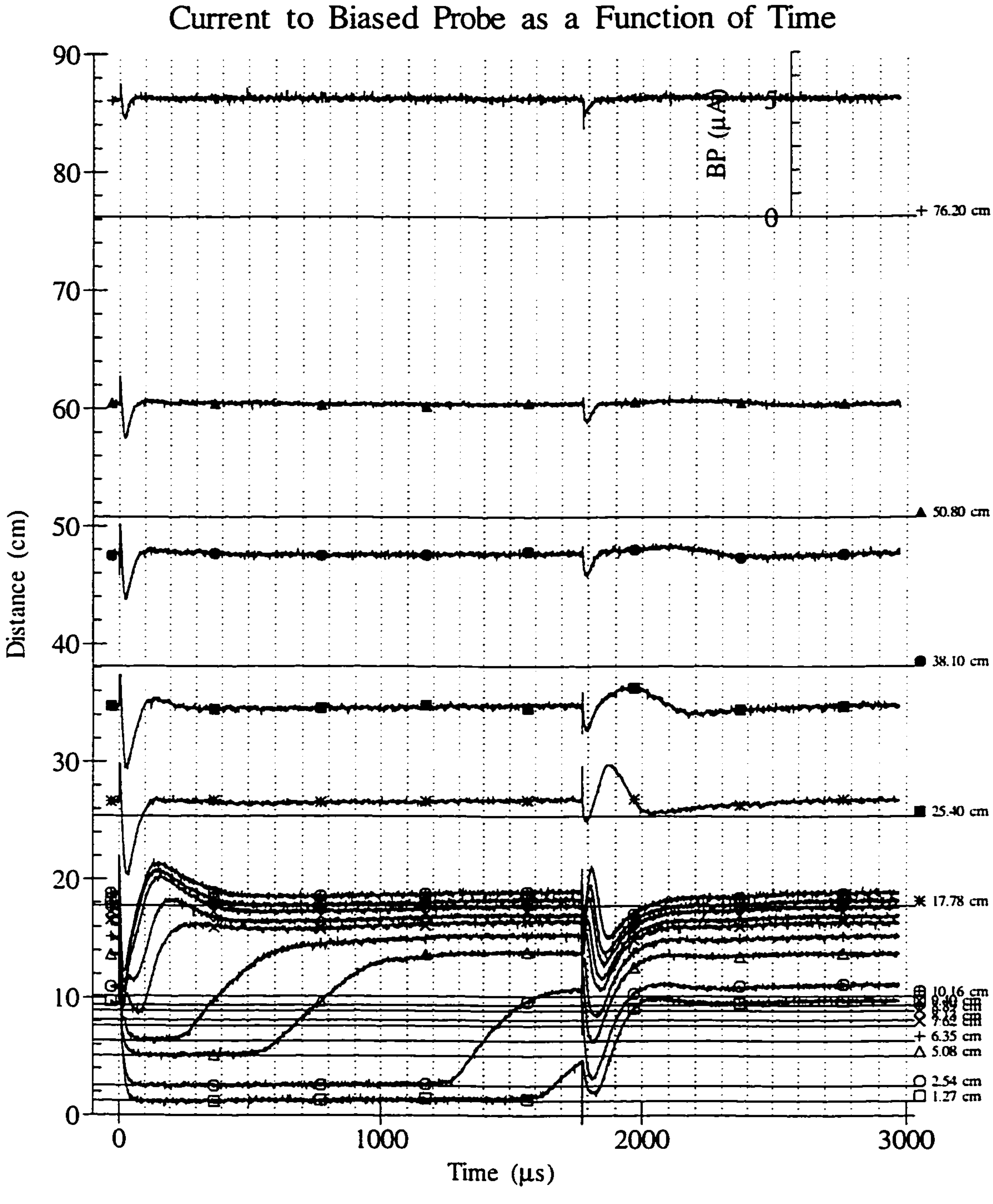

Figure 3.11: Current collected by the biased probe as a function of time and distance from the insulated cylinder (condition 4, sample 3). At time $t = 0$, a -500–V, 1.8–ms pulse was applied to the sample.

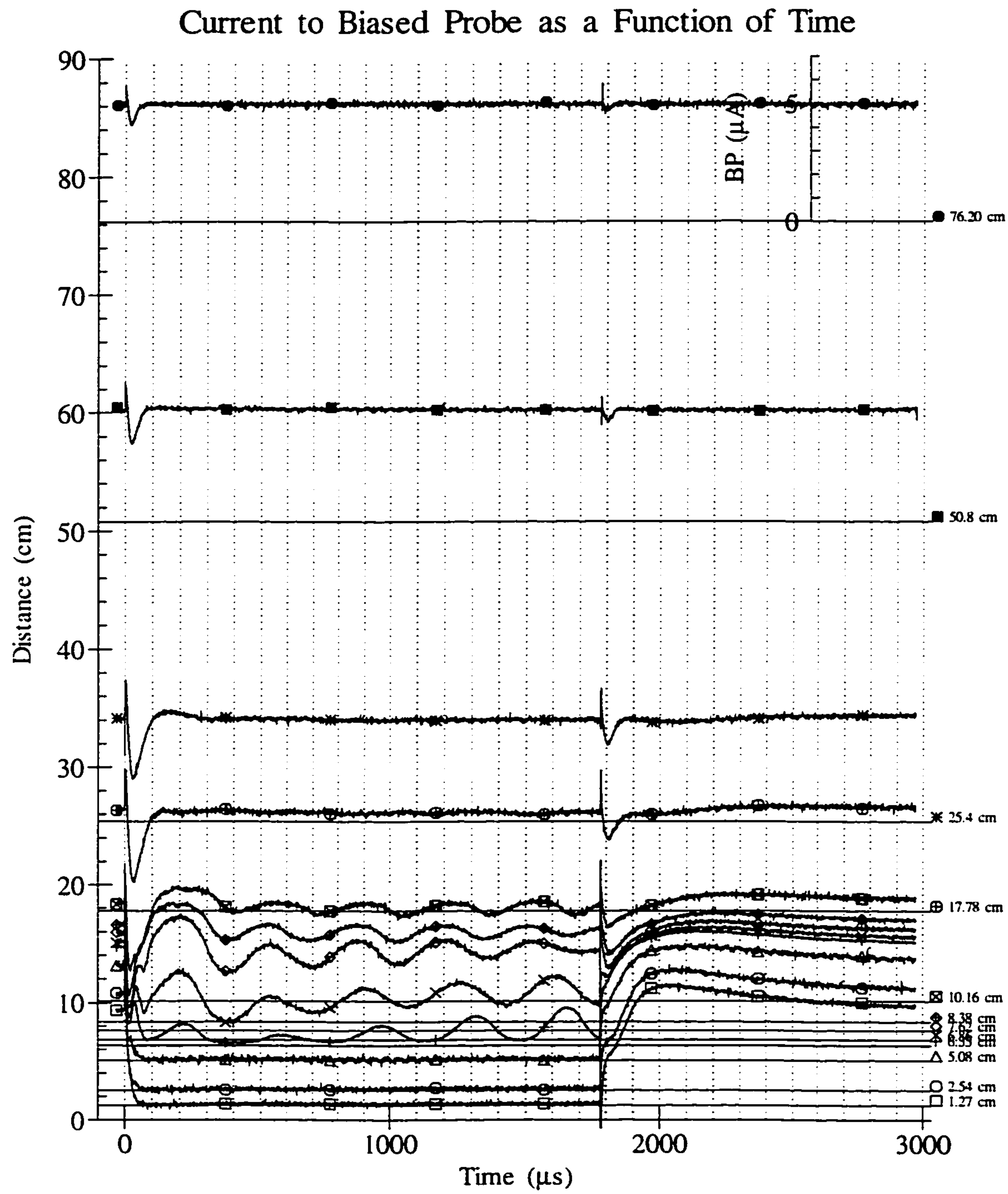

Figure 3.12: Current collected by the biased probe as a function of time and distance from the bare cylinder (condition 4, sample 4). At time $t = 0$, a −500–V, 1.8–ms pulse was applied to the sample.

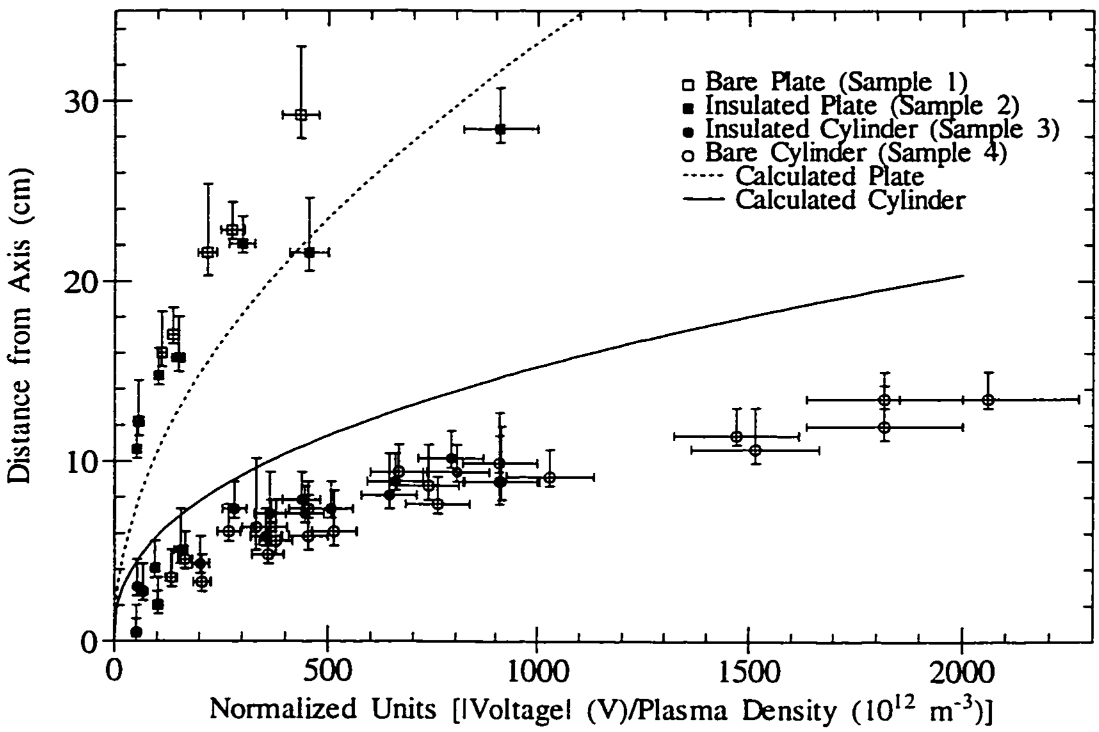

Figure 3.13: Experimentally determined pseudo–static sheath–expansion distances for each of the four samples as a function of normalized–voltage units. Calculated values are from Equation (3.14) for the plate and Equation (3.15) for the cylinder.

However, for the cylinders the calculated curve overpredicts the data points, whereas for the plates the calculated curve tends to underpredict the data points. The reasons for these discrepancies may be due to the following mechanisms. In the case of the plates, the discrepancy is possibly due to the sheath having begun to evolve into its Child–Langmuir size (since, as was stated, the ions have begun to move), and the measurements reflecting this. In the case of the cylinders, the discrepancy may be due to the sheath edge, which was initially sharp, having begun to broaden, *i.e.*, evolve from a step into a gradual slope. This would cause the BP to register a current before the true sheath edge, which would tend to underpredict the location of the sheath edge. Both of these mechanisms are related to the frequency–response limitation of the BP data.

The second interesting result, although not entirely unexpected, is that the plasma's initial response does not depend on whether or not the sample was insulated. That is, for the formation of the ion–matrix sheath, only the applied voltage (or alternately, the applied charge) on the conductor determines this distance.

3.3.6.2 Sheath Collapse

Figure 3.11 very clearly shows that the established sheath around the insulated samples eventually collapsed, a process which started some amount of time after the HV pulse was applied. In addition, the BP data at distances farther from the sample show this response earlier, indicating that the sheath collapse has some velocity, as expected. This velocity is dictated by the insulating material and its thickness, the local plasma density, and the voltage seen across the sheath. The sheath collapse is caused by the applied potential (applied charge) becoming shielded as the ions are collected to the surface of the insulator. Hence, the voltage seen across the sheath decreases, which causes the sheath distance to decrease.

The properties of the insulating material affect the collapse velocity and time required for complete collapse. These properties include the thickness and the relative permittivity[9] of the material. In effect, the insulated conductor acts like a capacitor which charges due to the collection of ions to its surface. The sheath collapse was not systematically examined and is left as future work. We do note, however, that sheath–collapse times are on the order of several milliseconds for the insulated cylinder and 10's of milliseconds for the insulated plate. Full characterization of the sheath

[9]The relative permittivity, ε_r, of the ceramic (alumina) coating of the wire is 9.0–9.4 [*Vesuvius McDanel*, 1993, p. 17] and that of Teflon®which coated the plates is 2.1 (see Table 5.2).

collapse would allow the sheath model to be extended from the ion–plasma–period timescale to DC steady–state.

3.3.6.3 Additional Test for Sheath Collapse

We performed an additional simple test to verify the collapse of the sheath around the insulated conductor. For this test, we used the current–source mode of the Keithley 2410 source electrometer. This mode sources a specified current and changes the sourced voltage to keep the output current constant. In this mode, the electrometer can be used for floating–probe measurements by specifying zero current output and measuring the resulting voltage necessary to hold the current at zero.[10] The electrometer was placed in this mode and its output was attached to the BP which was subsequently scanned in towards both the insulated and the bare cylinders which were held at -500 V. For the case of the insulated cylinder, the floating probe was moved to within 0.50 cm (on the order of λ_D) from the sample without any change in source voltage. This observation indicates that the sheath had collapsed around the insulated cylinder and that the ions collected to the insulator's surface were shielding the applied–voltage perturbation from the bulk of the plasma. For the case of the bare cylinder, however, at ~ 4 cm from the sample, the required source–voltage quickly climbed above 20 V, which was the electrometer's limit. This observation indicates that the sheath had not collapsed, but rather that the sheath edge was far from the sample since the perturbing field protruded a large distance from the sample.

---

[10] Appendix C describes the plasma floating potential in more detail.

3.3.6.4 Sheath–Edge Oscillation Around Bare Cylinder

An interesting oscillation was noted in the BP signal after HV application to sample 4 (bare cylinder) under several plasma conditions. This oscillation can be clearly seen in Figure 3.12 between the 6.35–cm and 10.16–cm distances. To determine the oscillation frequency, the spectral content of a subset (consisting of $2^{13} = 8192$ points) of each dataset was analyzed via the Fast Fourier Transform (FFT) technique. Each subset was first detrended by subtracting the mean and then a Hanning window with overlap was used during the FFT analysis. Due to the relatively small number of points and the 5–MHz sampling frequency, the resulting FFT had a resolution of approximately 600 Hz. The mean frequency for all BP traces which exhibited this oscillation was $\sim$ 3100 Hz with a standard deviation of 800 Hz. No trend with respect to plasma density or ion mass was able to be discerned. There are several interesting items to note about the oscillations:

- A decaying of the signal magnitude was observed in some of the datasets; however, for most of the signals no noted decay occurred in the 1.8 ms that the pulse was applied. Indeed, to examine this observation, several datasets were captured with much longer HV pulses applied.

- For many of the cases, there appears to be some amount of time necessary after the beginning of the HV pulse to establish the oscillations.

- The oscillations are not noticed under similar conditions at the insulated cylinder, nor are they noticed at the plates.

- The oscillatory response was not always uniform in frequency.

- Voltage pulses larger than ~ -300 V were required to excite the oscillations.

It is proposed that this oscillation may be the result of a forced lower–hybrid response being established in the plasma since the frequency is on the order of the lower hybrid frequency, although a bit higher. Also, the orientation of the local magnetic field in the chamber (discussed in Section B.2.4 of Appendix B) is such that the motion of the ions at the sheath edge has a component that is approximately perpendicular to the B–field, which is a mechanism for generating lower–hybrid waves as discussed in Section 2.1.3.

3.3.6.5 Additional Observations and Future Work

The presentation and discussion of the experimental results in the sections above show that the captured dataset contains many useful results and some intriguing observations. Unfortunately, some of these intriguing observations have yet to be fully examined since they were beyond the scope of this work. Full analysis of the results is left as future work.

The additional features of the dataset deserve more detailed analyses, which should include:

- Examination of the sheath collapse velocities due to dielectric charging, which was discussed briefly in Section 3.3.6.2.
- Determination of the mechanism causing the oscillation noted in the BP signal after HV application to the bare cylinder, which was discussed briefly in 3.3.6.4.
- Examination of the motion of the density depression caused be removal of the insulated conductor's applied voltage and the implication of this motion. This pronounced response can be seen clearly in Figure 3.11 after time $t = 1.8$ ms. This response should be contrasted with that of the bare cylinder (Figure 3.11) which does not exhibit the same response.

3.4 Particle–in–Cell Simulations

The purpose of the particle–in–cell (PIC) simulations was to quantitatively and qualitatively examine the temporal and spatial sheath surrounding a plasma–immersed cylinder under several different excitations. The PIC method provides a convenient way to examine the sheath response due to different excitations and plasma parameters (*e.g.*, plasma density, electron temperature). In effect, the method provides a "computer laboratory", in which stimuli, plasma densities and temperatures, and constituent masses can be quickly modified and the effects of the modifications examined.

3.4.1 PIC Background

The PIC plasma–simulation method uses computers to simulate the motion of charged particles in a plasma [*Dawson*, 1983; *Birdsall and Langdon*, 1985]. Even a low–density plasma can have millions of particles per cubic centimeter, so PIC simulations do not attempt to solve for the motion of all the particles in given plasma problem, but rather only a subset of so–called "super–particles". The PIC modeler must be resourceful in choosing simulation parameters that model the statistics of a physical system within the limitations imposed by the computer system.

PIC simulation codes generally start with the Lorentz force equation on a particle,

$$\frac{d\mathbf{p}_k}{dt} = \frac{q_k}{m_k}(\mathbf{E} + \mathbf{v}_k \times \mathbf{B}), \tag{3.27}$$

where $\mathbf{p}_k$ is the particle momentum, q_k/m_k is the charge–to–mass ratio, $\mathbf{E}$ is the electric field, $\mathbf{v}_k$ is the velocity, $\mathbf{B}$ is the magnetic field, and $k = e, i$ depending on particle species. The momentum is then related to the velocity by

$$\mathbf{p}_k = \frac{m_k \mathbf{v}_k}{\sqrt{1 - \mathbf{v}_k \cdot \mathbf{v}_k / c^2}}. \tag{3.28}$$

For non–relativistic particles, $\mathbf{p}_k \simeq m_k \mathbf{v}_k$. After finding $\mathbf{p}_k$, the particle is moved by solving

$$\frac{d\mathbf{r}_k}{dt} = \mathbf{v}_k, \tag{3.29}$$

where $\mathbf{r}_k$ is the particle position. Each particle has a charge Q_k associated with it chosen such that the initial density distribution will be properly computed when the charge from each particle is interpreted onto the mesh [*Faehl et al.*, 1994]. Similarly, by weighting the quantities $Q_k \mathbf{v}_k$ onto the mesh, the current densities are constructed.

In order to solve (3.27), the E– and B–fields are needed and are obtained by solving Maxwell's equations. In a linear, isotropic medium Maxwell's equations are

$$\nabla \times \mathbf{E} = -\frac{\partial \mathbf{B}}{\partial t}, \tag{3.30a}$$

$$\nabla \times \mathbf{H} = \frac{\partial \mathbf{D}}{\partial t} + \mathbf{J}, \tag{3.30b}$$

$$\nabla \cdot \mathbf{J} = -\frac{\partial \rho}{\partial t}, \tag{3.30c}$$

and the derived equations

$$\nabla \cdot \mathbf{D} = \rho, \tag{3.31a}$$

$$\nabla \cdot \mathbf{B} = 0, \tag{3.31b}$$

where

$$\mathbf{D} = \varepsilon \mathbf{E}, \tag{3.32a}$$

$$\mathbf{B} = \mu \mathbf{H}, \tag{3.32b}$$

and $\mathbf{J}$, ε, μ, and ρ are known functions of space and time. In (3.30b), $\mathbf{J}$ is the sum of particle currents and conduction currents $\mathbf{J}_c = \sigma \mathbf{E}$. Thus, this set of equations comprises a self–consistent model for the temporal and spatial evolution of both the fields and particles.

In the simulation domain, conductors, insulators, and semiconductors are defined on a mesh by defining appropriate values of σ and ε at each point. Generally, $\mu = \mu_0$ everywhere and both vacuum and plasma–filled regions are assigned values of $\varepsilon = \varepsilon_0$. The Courant condition, discussed in Section 3.4.2, must be satisfied in order to ensure stability of the field–solving algorithm.

3.4.2 Simulation Parameter Selection

In order to avoid numerical instability due to the finite–differencing algorithm used in PIC codes, the choice of simulation parameters must adhere to the following inequality known as the *Courant-Friedrichs–Lewy condition*, or simply as the *Courant condition* [*Courant et al.*, 1928; *Dawson*, 1983; *Kunz and Luebbers*, 1993], given here for Cartesian coordinates,

$$v_{\text{max}}\Delta t \leq \frac{1}{\sqrt{\frac{1}{(\Delta x)^2} + \frac{1}{(\Delta y)^2} + \frac{1}{(\Delta z)^2}}}, \tag{3.33}$$

where v_{max} is the maximum wave phase velocity expected (usually the speed of light, c); Δx, Δy, and Δz are the grid–spacing components; and Δt is the simulation timestep.

There are several other conditions which also must be satisfied in order to ensure numerical stability in full electromagnetic codes:

- The timestep, Δt, must be chosen to satisfy the leapfrog stability requirement of $\omega\Delta t < 2$ [*Hockney and Eastwood*, 1988]. The term ω represents the highest frequency of interest, *e.g.*, the electron plasma and cyclotron frequencies. However, for reasonably accurate integrations of the electron orbits, timesteps much smaller than this must be chosen. This requirement is similar to the Nyquist sampling criterion.

- The grid spacing components (*e.g.*, Δx) should be not much larger than the Debye length in order to avoid a nonphysical instability caused by the grids. A good rule–of–thumb is to choose $\Delta x \leq 3\lambda_D$ [*Matsumoto and Omura*, 1993]. The grid spacing must also be chosen smaller than any physical distances that the simulation is required to resolve. Examples of distances of interest include wavelengths, Debye lengths, and sheath thicknesses.

- To ensure the accuracy of the computed results, Δx, Δy, and Δz must be made a small fraction of the minimum wavelength for which accurate results are desired. A general rule–of–thumb is to set these length to $\sim 0.1\lambda$, where λ is the wavelength in the medium [*Kunz and Luebbers*, 1993].

For electrostatic simulations, the criterion for stability is similar but different: instead of a condition on wave propagation, a condition exists for particle motion. Specifically, the spatial and temporal steps (Δx and Δt, respectively) must satisfy the constraint [*Humphries*, 1990, p. 561]

$$\Delta t < \frac{\Delta x}{v_{\text{part}}}, \tag{3.34}$$

where v_{part} is the particle velocity, typically the electron velocity. This condition simply states that electrons must not travel more than one spatial mesh location in a timestep. If Δt is too long such that the electron location on the mesh is not unambiguously fixed at each timestep, then nonphysical transport mechanisms can occur numerically which have no physical basis.

3.4.3 Scaling Simulation Parameters

In any PIC simulation, the choice of timestep and grid size must be related to the physical frequencies and distances of the problem. In PIC simulations, the frequencies of interest are the electron plasma, electron cyclotron, ion plasma, and ion cyclotron frequencies and the distances (scale–lengths) of interest are the Debye length, and if a static magnetic field exists, the electron and ion gyroradii. In most cases, it is the relationship of the various frequencies which is most important. Examining the equations for electron plasma and ion plasma frequencies, we note that the ratio of the two is simply the square root of the ratio of the ion to electron mass, *i.e.*,

$$\frac{\omega_{pe}}{\omega_{pi}} = \sqrt{\frac{m_i}{m_e}}. \tag{3.35}$$

In addition, the ratio of the electron to ion cyclotron radii is equal to the ratio of the ion to electron mass, *i.e.*,

$$\frac{r_{ce}}{r_{ci}} = \frac{m_i}{m_e}. \tag{3.36}$$

As mentioned in Section 3.4.2, the simulation requires that the timestep be chosen such that $\omega \Delta t < 2$ for the highest frequency in the problem, usually the electron plasma frequency. If the physical mass ratio were used, then the simulation would require several thousand timesteps in order to describe just one oscillation of the lowest frequency. Therefore, in practical simulations, a different mass ratio is normally used: *i.e*, one that is sufficiently large to separate the frequencies, but sufficiently small to allow the simulation to complete in a reasonable amount of time. When this technique is used, the results are interpreted as dimensionless ratios which can be interpreted in terms of the physical mass ratio [*Hockney and Eastwood*, 1988].

3.4.4 The Object–Oriented Particle–in–Cell (OOPIC) Code

The Object-Oriented Particle–in–Cell (OOPIC) code was chosen for this work. OOPIC is a 2–1/2 dimensional (also called "2D–3V") simulation code written in C++ which makes importing new physics modules possible, *e.g.*, boundary conditions and sources. The code was chosen because it is publicly available, has an excellent graphical user interface (GUI), and is relatively easy to learn. OOPIC was developed by the Plasma Theory and Simulation Group at the University of California at Berkeley. The specific implementation of OOPIC used in these simulations is the X–Windows version known as XOOPIC (modified Version 2.0). For a more complete description of the OOPIC code, please see *Verboncoeur et al.* [1995].

The OOPIC code allows the user to choose from several solution–algorithm options for electrostatic simulations. One such option is a multigrid solver. The multigrid iteration technique has the characteristic of fast convergence which makes it useful for solving the large number of equations in PIC codes. The convergence speed does not deteriorate when the discretization is refined, whereas classical methods slow down when grid size is decreased [*Hackbusch*, 1985].

3.4.5 Boundary Conditions

When defining a PIC simulation region, there are two groups of boundary conditions (BC's) to consider: field BC's and particle BC's. These two groups can be diverse and complex and depend on the simulation and the desired results. The BC's used in the present simulations are described below.

Periodic Boundaries Specification of periodic boundaries may be made in OOPIC, which allows particles to flow out one boundary and into the opposite boundary. Thus, the effective length of the simulation region can be made infinite in the periodic direction.

Conductors OOPIC includes boundary conditions for the electric fields at the surface of ideal conductors and allows potentials (of various static and functional forms) to be applied to them. In addition, particles may be absorbed at the conductor surface. This means that conductors may collect current, float, and/or be driven by sources.

Dielectrics/Insulators OOPIC also allows dielectric surfaces and regions to be defined. The ε_r for the material is specified, as well as whether charges are to be collected, absorbed, or reflected.

3.4.6 Simulation Setup

OOPIC allows the user to choose either a rectangular or cylindrical coordinate system. For simulating a cylinder immersed in an unmagnetized plasma, we have utilized cylindrical geometry since the problem lends itself to a cylindrical coordinate system in which the cylinder is oriented along the z–axis.[11] The as–implemented simulation region employing cylindrical geometry is shown in Figure 3.14. The radius of the simulation region covers the distance from the conductor radius ($r_a = 0.065$ cm, same as experimental sample–4 wire) out to 1 m. The width of the simulation region is 2 cm and the boundary at $z = 0$ cm is periodic with that at $z = 2$ cm, which means the simulation is essentially 1–dimensional (only r–dependent).

Two non–physical constructs were used in the simulation domain in order to facilitate the simulations. The first was a conducting wall placed at the $r = 1$ m point to clamp the potential at large distances to 0 V. The second was a dielectric wall placed one grid point in front of this outer conducting cylinder. This dielectric ($\varepsilon_r = 1$ with particle reflection specified) was used to complete the containment of the particles within the simulation region. Thus, particles could only be lost due to collection at the central–conductor surface; all other particles were either passed between the boundaries at $z = 0$ cm and $z = 2$ cm or reflected at $r \approx 1$ m. Because of this second non–physical construct, some particle bunching occurred near $r \approx 1$,

[11] Inclusion of an external static magnetic field in cylindrical geometry can only be implemented if the field is z– or φ–directed.

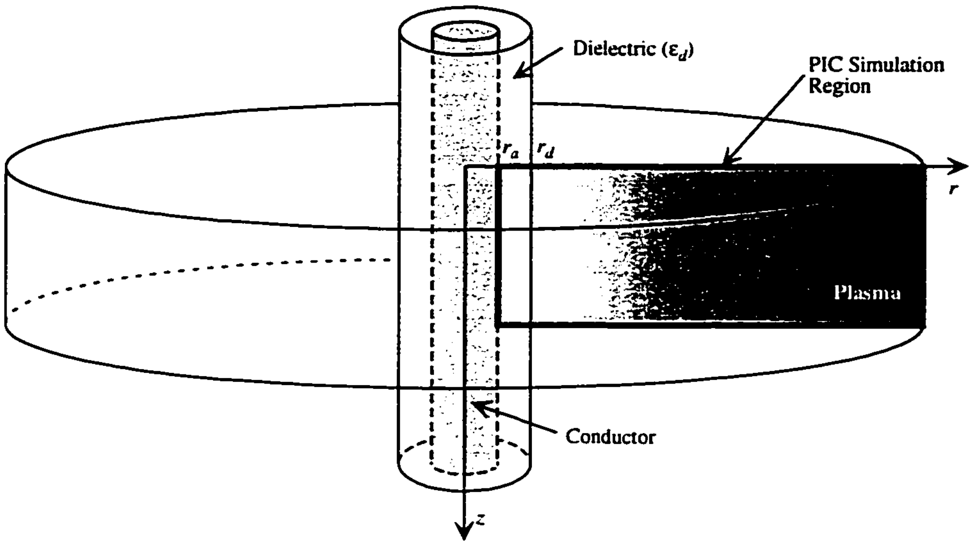

Figure 3.14: Interpretation of cylindrical geometry in PIC simulations: the simulation region is symmetric in the φ–direction; hence, the number of simulation particles increases in the r–direction since more particles exist in the integrated cylindrical shell at that point. Note: PIC–region aspect ratio is not drawn to scale.

especially at the higher conductor potentials. However, since this bunching region was far enough removed from the center conductor and sheath regions, it did not adversely affect the simulations.

The temporal evolution of the number of electron and ion computer particles is shown in Figure 3.15. Due to the 1–grid–point space between the conductor and reflecting dielectric at $r \approx 1$ m, the particles in that region were eventually permanently lost to the simulation region. This loss is seen in the sharp initial drop in electron particle number, and the drops during the application of voltage after $t = 500$ ns. The ions are lost as well in the 1–grid–point space and also continually lost due to collection at the center conductor since they are the attracted species.

Figure 3.16 shows a sample plot of the "electron phase space" data output pro-

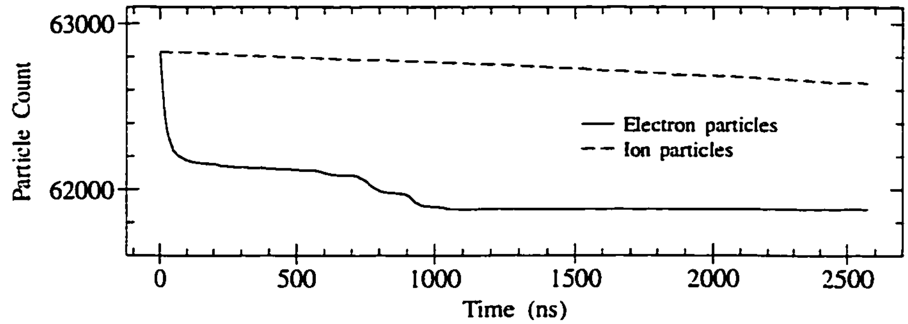

Figure 3.15: Plot showing the temporal evolution of the number of electron and ion computer particles in a typical OOPIC simulation.

vided by OOPIC after simulation initialization. The location of each electron super–particle is shown as a point in that plot. The apparent increase in particle density as a function of radial distance in Figure 3.16 is due to the choice of cylindrical geometry. Since more particles exist in the integrated cylindrical shells further from the axis, the number of simulation particles increases in the r–direction. The density, though, is uniform throughout the simulation region.

Although the PIC results were two–dimensional (*i.e.*, r and z), only the r–direction provided any meaningful variation in data. As was mentioned above, the simulations are really only 1–d in nature; that is, there was little z–direction variation. Hence, in processing the PIC output, we employed an averaging scheme at each r–value (*e.g.*, electron density, ion density, potential, electric field) whereby all z–values were averaged together to provide a single set of r–values. Effectively, this is as if several 1–d simulations were run simultaneously and, as such, the averaging was a useful method for smoothing out the simulation results.

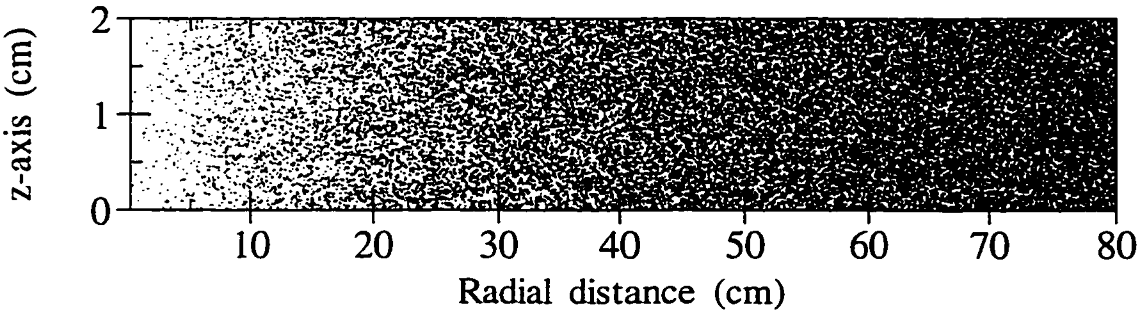

Figure 3.16: Sample plot of the "electron phase space" data output provided by OOPIC after the initialization of the simulation. The location of each electron super–particle is shown as a point in this plot. The density is indeed uniform; however, the increase in point density along the r–axis (radial) is caused by the larger total particle numbers in the cylindrical shells further from the axis. The "ion phase space" output looks similar. Note: the z–axis has been expanded.

3.4.7 PIC Simulation Results

This section presents the results of several PIC simulations: voltage step, voltage drop, sinusoidal (RF) input, and fast voltage step. These simulations allow us to verify the sheath model as developed via analysis and experiments earlier in this chapter. For each simulation, the specifics of its implementation are listed and then results are presented. It should be noted that for all simulations there was a 0.5 μs wait ($\sim 5\tau_{pe}$) before application of the perturbing signal.

3.4.7.1 Voltage Step ($\tau_{pe} \ll \tau_{ar} \ll \tau_{pi}$)

The purpose of this set of PIC simulations was to examine the plasma's response to a negative high–voltage step applied to an uninsulated cylinder. More specifically, we examined the temporal and spatial evolution of the sheath and the electric and potential distributions. The parameters used in the simulations are listed in Table 3.6. The plasma was established with an $n_e = n_i = 10^{12}$ m^{-3}, $\theta_e = \theta_i = 1.0$ eV, and $m_i = 10^5 m_e$ (on the order of actual physical mass ratio; causes the ions to be approximately immobile). The risetime of the pulse, τ_{ar}, was chosen to fall in the range between the electron and ion plasma periods, *i.e.*, $\tau_{pe} \ll \tau_{ar} \ll \tau_{pi}$. Each computer particle represented 10^6 physical particles, the ion motion was subsampled every 10 timesteps, an electrostatic multigrid solver was used, and the timestep was 500 ps. Other information pertaining to the simulation setup is provided in Section 3.4.6.

Table 3.6: Summary of PIC simulation parameters for voltage step excitation ($\tau_{pe} \ll \tau_{ar} \ll \tau_{pi}$). (XOOPIC input file listing may be found in Appendix E, Section E.2.1.)

Parameter	Nomenclature	Value(s)
Physical parameters		
initial electron density	n_e	10^{12} m^{-3}
initial ion density	n_i	10^{12} m^{-3}
initial electron temperature	θ_e	1.0 eV
initial ion temperature	θ_i	1.0 eV
electron charge	q_e	-1.602×10^{-19} C
ion charge	q_i	$+1.602 \times 10^{-19}$ C
input excitation	—	step
signal delay	τ_{delay}	0.5 μs
conductor voltage rise–time	τ_{ar}	1 μs
conductor peak voltage	V_a	$\in [-500, -1000, -1500, -2000]$ V
r-axis range	l_r	0.065–100 cm
z-axis range	l_z	0–2 cm
Simulation parameters		
timestep	Δt	5.0×10^{-10} s
ion to electron mass ratio	m_i/m_e	100,000
physical to computer particle ratio	n_{pc}	10^6
geometry	—	cylindrical, periodic in z
r-axis grid points	n_r	128, uniform spacing
z-axis grid points	n_z	8, uniform spacing
solver	—	electrostatic: multigrid
ion subcycling	—	10

We begin by presenting the results of the spatial and temporal evolution of the electron density surrounding the conducting cylinder. Figure 3.17 shows both the electron and ion densities for several times before, during, and after application of a −500–V step to the cylindrical conductor. There are several interesting items about the plasma sheath which can be noted in these plots. First, because the voltage risetime is longer than the electron plasma period ($\tau_{ar} \gg \tau_{pe}$), the position of the electron sheath edge increases along with the rising voltage. Second, the sheath is very nearly a hard edge, that is, n_e goes from zero within the sheath to the ambient plasma density in a distance on the order of 1–2 cm ($\sim$ 1–3λ_D). Third, the sheath is truly an "ion–matrix" sheath since it is devoid of electrons and the ions remain almost motionless.

It should be mentioned that the density values are numerically noisier close to $r = 0$ in these plots because there are fewer super–particles as $r \rightarrow 0$. This means that these super–particles have a heavier weighting with respect to density than farther ones do, which reduces the effect of the averaging and the results appear noisier. (see Figure 3.16).

The next series of plots shows the spatial and temporal evolution of the potential distribution and electric field surrounding the conducting cylinder. Figure 3.18 shows these quantities for several times before, during, and after application of a −500–V step to the cylindrical conductor (the times correspond to those of Figure 3.17). Again, there are several interesting items to note in these plots. First, the E–field is contained within the sheath region for all timesteps, where containment is evidenced by the E–field falling to $\sim$ 0 V/cm at the sheath edge. In addition, for all timesteps the potential beyond the sheath edge is $\sim$ 0 V. Small disturbances are noticed in the region beyond the sheath edge, but the magnitudes of these are only a very small fraction of the excitation voltage. Second, as will be shown, the field distributions functionally agree with those that are derived analytically in Section 4.2.1 and shown

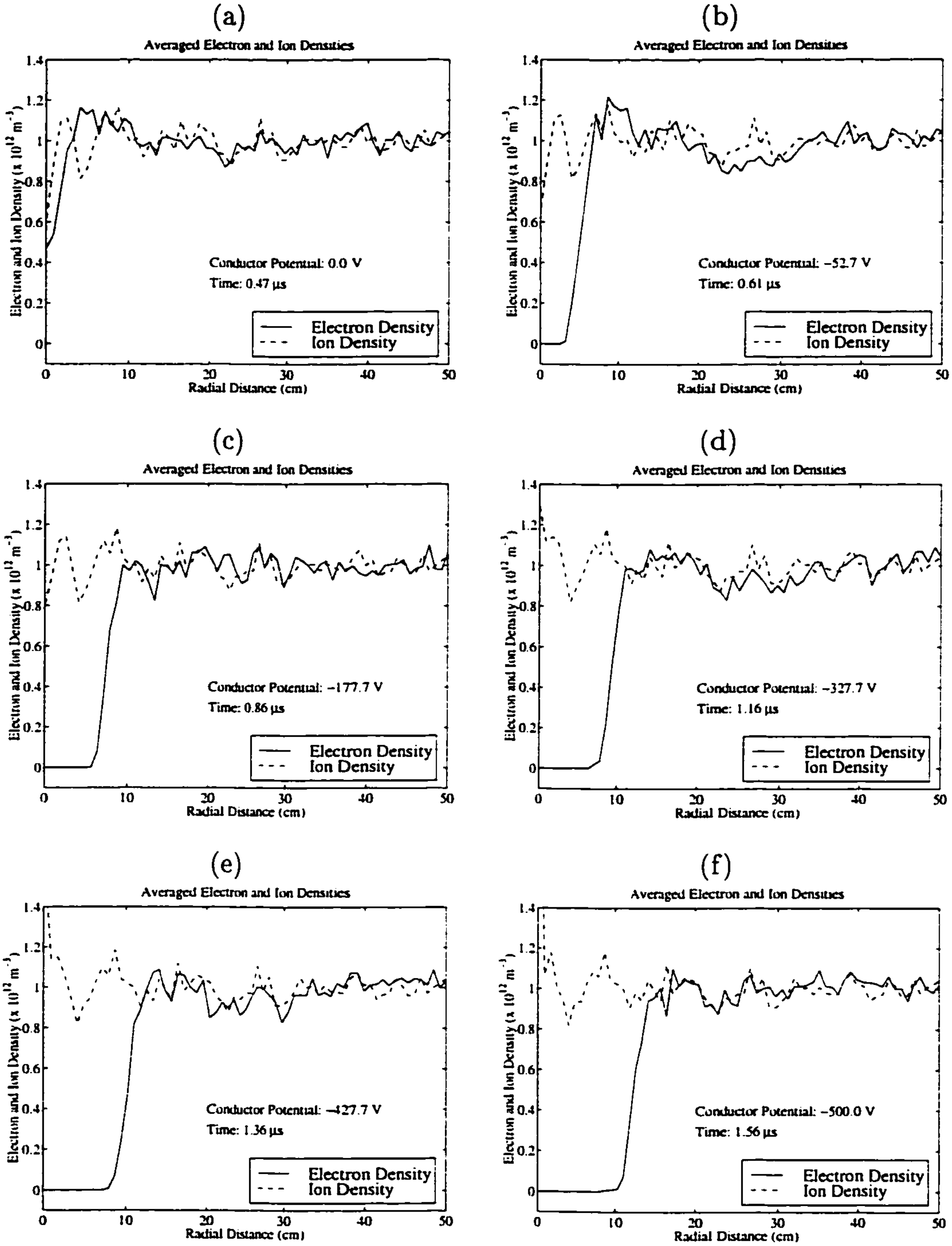

Figure 3.17: PIC simulation of electron and ion density vs. radial distance from the conductor (r_a = 0.65 mm) during application of a −500–V, 1–μs–risetime voltage step at t = 0.5 μs for $n_0 = 1 \times 10^{12}$ m^{-3}: (a) t = 0.47 μs, V_a = 0 V; (b) t = 0.61 μs, V_a = −52.7 V; (c) t = 0.86 μs, V_a = −177.7 V; (d) t = 1.16 μs, V_a = −327.7 V; (e) t = 1.36 μs, V_a = −427.7 V; (f) t = 1.56 μs, V_a = −500.0 V.

in Figure 4.4. This agreement is important since field containment is a necessary condition for the sheath–capacitance model developed in Chapter IV.

Figure 3.19 shows the PIC–derived ion–matrix–sheath expansion distances for a cylindrical geometry corresponding to that of sample 4 used in the plasma–chamber experiments. The plot was produced by determining the position of the sheath edge as a function of the excitation voltage throughout the duration of the voltage rise for $V_a \in [-500, -1000, -1500, -2000]$ V. This is justified for $\tau_{ar} \gg \tau_{pe}$ because the sheath–edge distance is a function of the current applied voltage, *i.e.*, the sheath edge is driven by the applied voltage. For the simulation results, the sheath edge was defined as the point where $n_e = 0.3n_{e0} \approx e^{-1}n_{e0}$. In addition to the PIC results, the analytical value calculated from Equation (3.15) is plotted. The agreement between the PIC results and the analytical values is very good over the entire voltage range.

3.4.7.2 Voltage Drop ($\tau_{pe} \ll \tau_{af} \ll \tau_{pi}$) With an Established Ion–Matrix Sheath

This PIC simulation examined the plasma's response to the removal of an applied voltage on an uninsulated cylinder, *i.e.*, a voltage drop from V_a to 0 V. The plasma was established as in the simulations of Section 3.4.7.1 ($n_e = n_i = 10^{12}$ m^{-3}, $\theta_e = \theta_i = 1.0$ eV, and $m_i = 10^5 m_e$). The falltime of the pulse, τ_{af}, was again chosen to lie in the range between the electron and ion plasma periods, *i.e.*, $\tau_{pe} \ll \tau_{af} \ll \tau_{pi}$. The bias voltage was established by providing a pulse input to the simulation with the parameters listed in Table 3.7. The method of applying a pulse ensured that the sheath grew to and was at the ion–matrix distance before the applied voltage dropped back to 0 V.

We begin by presenting the results of the spatial and temporal evolution of the electron density surrounding the conducting cylinder. Figure 3.20 shows both the

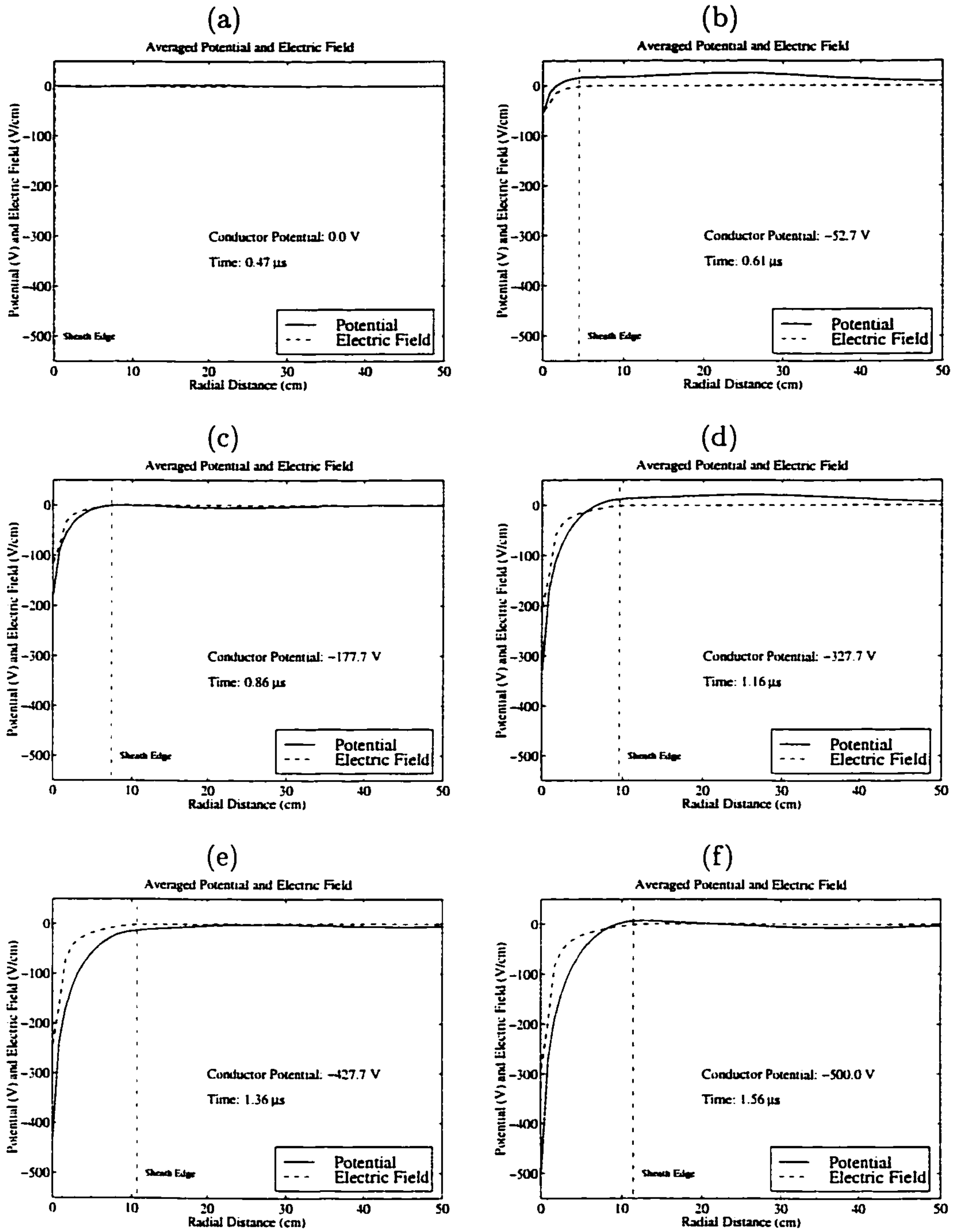

Figure 3.18: PIC simulation of potential and electric field vs. radial distance from the conductor (r_a = 0.65 mm) during application of a −500–V, 1–μs–risetime voltage step at t = 0.5 μs for $n_0 = 1 \times 10^{12}$ m^{-3}: (a) t = 0.47 μs, V_a = 0 V; (b) t = 0.61 μs, V_a = −52.7 V; (c) t = 0.86 μs, V_a = −177.7 V; (d) t = 1.16 μs, V_a = −327.7 V; (e) t = 1.36 μs, V_a = −427.7 V; (f) t = 1.56 μs, V_a = −500.0 V.

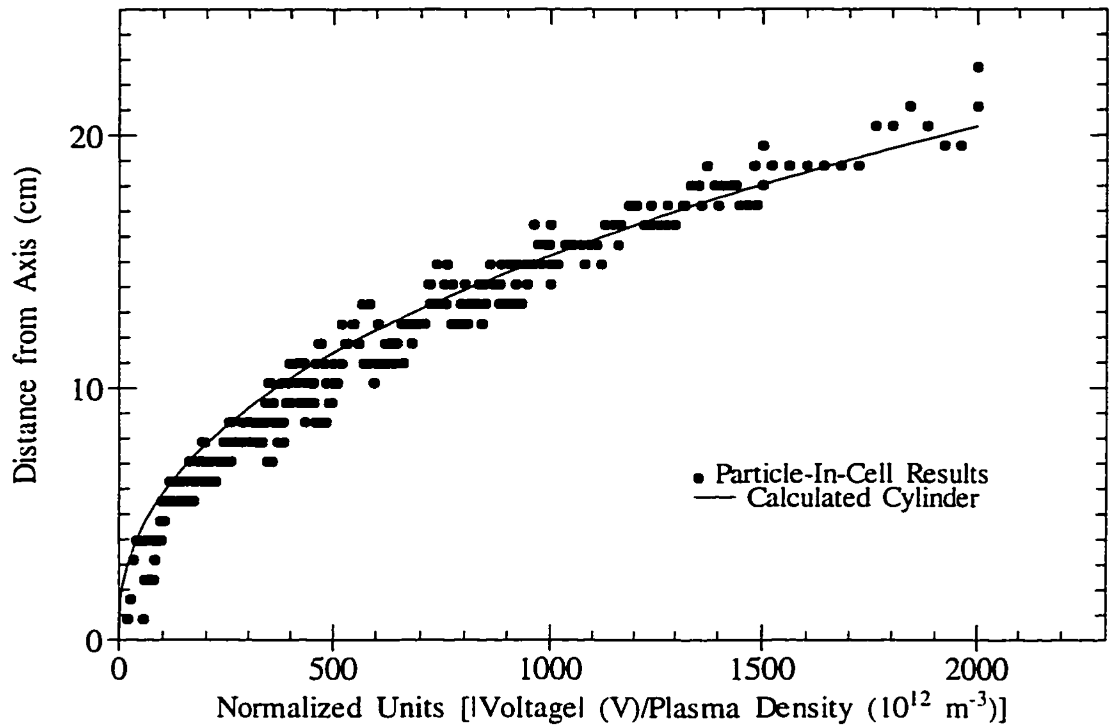

Figure 3.19: PIC simulation of ion–matrix–sheath expansion distances for cylindrical geometry corresponding to that of sample 4. Solid line is calculated from Equation (3.15).

electron and ion densities for several times before, during, and after removal of the −500–V bias on the cylindrical conductor. Items to note in these plots regarding the plasma sheath include: 1) the voltage–drop case is approximately the inverse of the voltage–rise case with respect to sheath location at a given bias voltage; 2) the sheath is still very nearly a hard edge and remains so as the voltage drops; 3) the sheath remains ion–matrix–like in nature since no electrons exist in the sheath region; 4) the ion density near the conductor has increased, indicating the ion density is becoming enhanced to due ion collection at the cylinder (note that Figure 3.17f also begins to show evidence of this).

The next series of plots given in Figure 3.21 shows the spatial and temporal

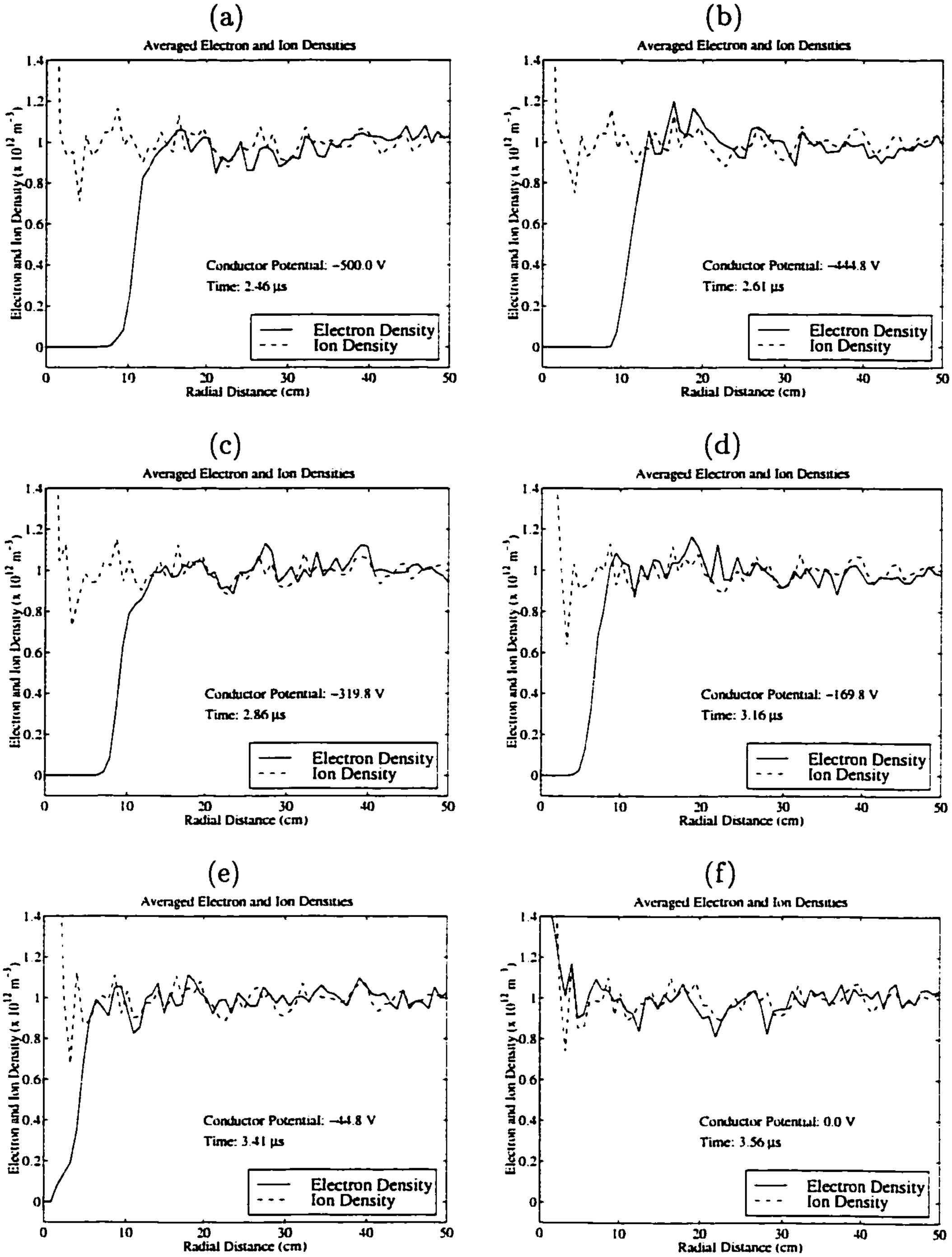

Figure 3.20: PIC simulation of electron and ion density vs. radial distance from the conductor ($r_a = 0.65$ mm) during removal of a -500–V bias via a 1-μs–falltime voltage drop at $t = 2.5$ μs for $n_0 = 1 \times 10^{12}$ m^{-3}: (a) $t = 2.46$ μs, $V_a = -500$ V; (b) $t = 2.61$ μs, $V_a = -444.8$ V; (c) $t = 2.86$ μs, $V_a = -319.8$ V; (d) $t = 3.16$ μs, $V_a = -169.8$ V; (e) $t = 3.41$ μs, $V_a = -44.8$ V; (f) $t = 3.56$ μs, $V_a = 0$ V.

Table 3.7: Summary of PIC simulation parameters for voltage–drop excitation ($\tau_{pe} \ll \tau_{af} \ll \tau_{pi}$). (XOOPIC input file listing may be found in Appendix E, Section E.2.2.) Note: only parameters which are different from those in Table 3.6 are listed.

Parameter	Nomenclature	Value(s)
Physical parameters		
input excitation	—	pulse
conductor voltage risetime	τ_{ar}	1 μs
conductor voltage plateau time	τ_{ap}	1 μs
conductor voltage falltime	τ_{af}	1 μs
conductor peak voltage	V_a	−500 V

evolution of the potential distribution and electric field surrounding the conducting cylinder. It should be noted that, as in the case of the voltage rise, the E–field is contained within the sheath region and the potential beyond the sheath edge is ~ 0 V for all timesteps.

3.4.7.3 Sinusoidal (RF) Input ($\omega_{pe} \gg \omega \gg \omega_{pi}$)

The voltage–drop simulation of Section 3.4.7.2 used as its input a pulse with parameters given in Table 3.7. The use of a sinusoidal input in this simulation is similar in that we wish to examine the ability of the sheath to "track" changes in V_a, provided that the spectral content of those changes falls in the range $\omega_{pe} \gg \omega \gg \omega_{pi}$. The input sinusoid had an excitation frequency of $f = 1$ MHz (see Table 3.8) and an offset bias such that V_a was always negative (see top panel of Figure 3.22).

Figure 3.22 plots the simulated and calculated sheath distances as a function of time with the sinusoidal input voltage provided for reference. There are several items to note in this figure. First, the simulated and calculated sheath distances agree very well. Second, there is no phase lag between the simulated and calculated sheath distances indicating that the sheath distance tracks the input waveform. Third, after

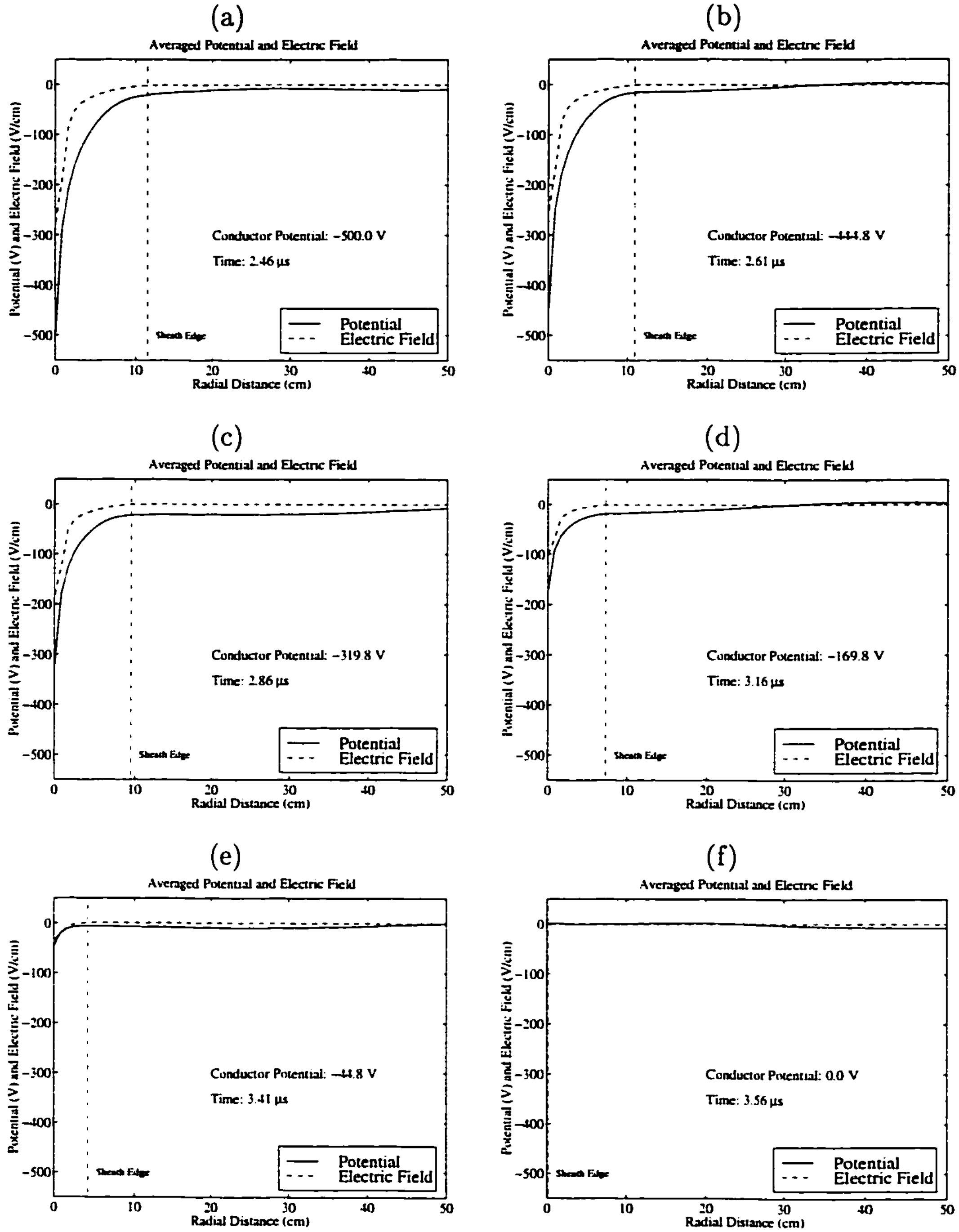

Figure 3.21: PIC simulation of potential and electric field vs. radial distance from the conductor ($r_a = 0.65$ mm) during removal of a -500–V bias via a 1-μs–falltime voltage drop at $t = 2.5$ μs for $n_0 = 1 \times 10^{12}$ m^{-3}: (a) $t = 2.46$ μs, $V_a = -500$ V; (b) $t = 2.61$ μs, $V_a = -444.8$ V; (c) $t = 2.86$ μs, $V_a = -319.8$ V; (d) $t = 3.16$ μs, $V_a = -169.8$ V; (e) $t = 3.41$ μs, $V_a = -44.8$ V; (f) $t = 3.56$ μs, $V_a = 0$ V.

Table 3.8: Summary of PIC simulation parameters for sinusoidal excitation ($\omega_{pe} \gg \omega \gg \omega_{pi}$). (XOOPIC input file listing may be found in Appendix E, Section E.2.3.) Note: only parameters which are different from those in Table 3.6 are listed.

Parameter	Nomenclature	Value(s)
Physical parameters		
input excitation	—	sinusoidal (RF)
excitation frequency	f	1 MHz
conductor peak voltage	V_a	−500 V

many sinusoidal oscillations (around $t = 8\ \mu$s in Figure 3.22), the sheath edge begins to evidence secondary perturbations, which may indicate a heating of the electrons at the sheath edge.

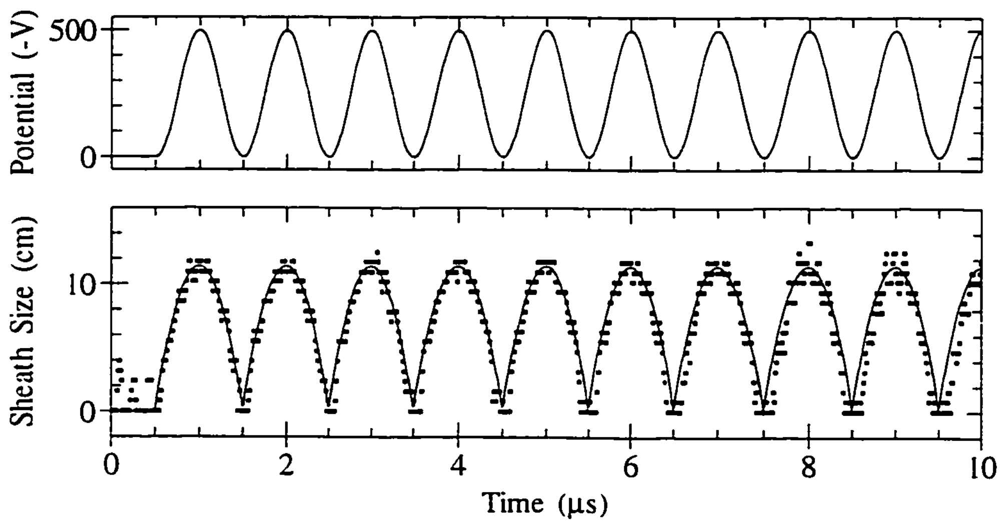

Figure 3.22: PIC simulation of a 1–MHz, offset RF sinusoid applied to the conducting cylinder showing applied voltage, simulated sheath distance (points), and calculated sheath distance (solid line) as a function of time.

The mechanism which causes stochastic heating of electrons at the sheath edge has been examined by many researchers, and in particular those in the field of capacitive RF–plasma generation [*e.g.*, *Lieberman*, 1988; *Raizer et al.*, 1995]. The mechanism has also been called "Fermi acceleration" [*Godyak et al.*, 1972] or "wave riding" [*Kushner*, 1986]. In brief, the mechanism works as follows. At the sheath edge, an electron that is reflected by the sheath experiences a change in energy: if the sheath moves away from the electron, then its energy decreases; conversely, if the sheath moves towards the electron, then its energy increases. Hence, at the oscillating sheath edge some electrons gain energy and others lose energy. But, when averaged over an oscillation period, the electrons experience a net energy gain and become heated.

Lieberman [1988] makes an interesting observation which agrees with the PIC results. He states that an essential feature of the stochastic–heating mechanism is the presence of an unhomogeneous sheath, *i.e.*, nonuniform ion density in the RF sheath. In this PIC simulation, we note that the heating begins only after the simulation time has passed a significant fraction of the ion plasma period (τ_{pi} = 28 μs for this simulation). In this amount of time the ions have begun to move and the ion density has begun to deviate from its previously uniform value, hence the sheath is no longer homogeneous and stochastic heating can begin.

This electron heating under continuous RF excitation results in dissipation in the plasma sheath. The heating causes the sheath to have a conductance [*Lieberman*, 1988], and as such represents a loss term. Hence, for a stationary system, this mechanism would have to be accounted for when dealing with losses, perhaps by adding the appropriate sheath–conductance term. However, for the cylinder in a flowing plasma—such as an electrodynamic–tether system at orbital velocities—new, unheated plasma is constantly being introduced. Hence, this kind of electron heating is expected to be less pronounced.

3.4.7.4 Fast Voltage Step ($\tau_{ar} < \tau_{pe}$)

In Section 3.2.4 we discussed how the electrons respond to fast changes in conductor potential, where by fast we mean $\tau_{ar} < \tau_{pe}$. In the PIC simulation described in this section, we used a step excitation with a risetime much faster than the electron plasma period (see Table 3.9), as opposed to that of Section 3.4.7.1, which had a step excitation with $\tau_{ar} > \tau_{pe}$. The results of this simulation were quite different from those of the "slow"-step simulation of Section 3.4.7.1

Table 3.9: Summary of PIC simulation parameters for fast voltage step excitation ($\tau_{ar} < \tau_{pe}$). (XOOPIC input file listing may be found in Appendix E, Section E.2.4.) Note: only parameters which are different from those in Table 3.6 are listed.

Parameter	Nomenclature	Value(s)
Physical parameters		
input excitation	—	step
conductor voltage risetime	τ_{ar}	10 ns
conductor peak voltage	V_a	−500 V

We begin by examining the E–field and potential–distribution results of this PIC simulation, which are shown in Figure 3.23. The plots of this figure are very different from those of Figures 3.18 and 3.21 in that the E–field is *not* contained within the sheath region during application of V_a and the potential is not ~ 0 V at the sheath edge. Instead, both penetrate deeply into the plasma region which indicates that the plasma was unable to respond in time to shield the disturbance [*Calder et al.*, 1993]. For example, in Figure 3.23c the applied voltage $V_a = -500$ V has already been established but the potential distribution indicates that this disturbance can be seen far from the conductor. This is unlike the case of Figure 3.18f in which the potential is ~ 0 V at $r_{\rm sh}$.

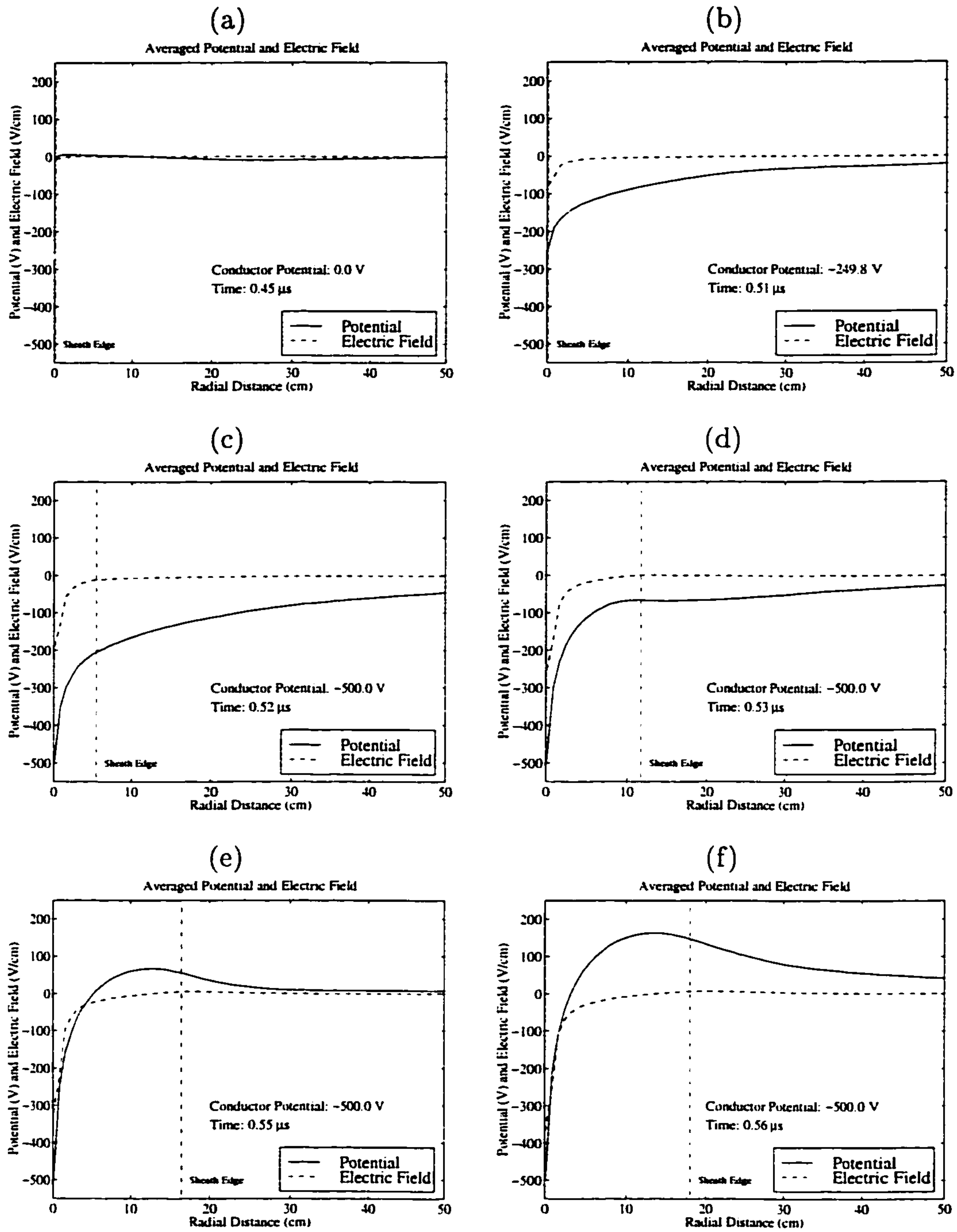

Figure 3.23: PIC simulation of potential and electric field vs. radial distance from the conductor ($r_a = 0.65$ mm) during application of a -500–V, 10–ns–risetime voltage step at $t = 0.5$ μs for $n_0 = 1 \times 10^{12}$ m^{-3}: (a) $t = 0.46$ μs, $V_a = 0$ V; (b) $t = 0.51$ μs, $V_a = -249.8$ V; (c) $t = 0.52$ μs, $V_a = -500.0$ V; (d) $t = 0.53$ μs, $V_a = -500.0$ V; (e) $t = 0.55$ μs, $V_a = -500.0$ V; (f) $t = 0.56$ μs, $V_a = -500.0$ V.

In addition to the lack of E–field and potential containment, the potential plots also show the beginning of the oscillating–field region caused by the motion of the electrons about their equilibrium position, which is the ion–matrix–sheath distance. This oscillation characteristic was described analytically in Section 3.2.4. Figure 3.24 plots the location of the sheath edge as a function of time and the oscillating sheath edge is clearly in evidence. An FFT of the temporal response of the sheath–edge position (also shown in Figure 3.24) yields a frequency of $f_{\rm ring} \sim 7.5$ MHz, which is on the order of the value of 6.3 MHz given by Equation (3.26). Clearly, however, more work is needed to predict more exactly this ringing frequency. If the simulation were to run for many ion plasma periods, it is expected that the amplitude of ringing would decrease due to loss mechanisms. The simulations performed by *Borovsky* [1988] and *Calder et al.* [1993], do indeed show that the ringing amplitude decreases at timescales on the order of the ion plasma period.

3.4.8 Comments on PIC Results

To finish this section on the PIC simulations, we make a few final comments about the simulations themselves and the validity of the results. The first comment relates to the choice of cylindrical geometry for the simulation domain. Choosing cylindrical geometry greatly simplified the simulation setup and allowed the sheath distances to be determined accurately. One might inquire, then, as to whether or not the cylindrical–geometry simulation domain could also be used to examine the evolution of the OML sheath. This knowledge would be required in order to extend the frequency response of this sheath model to $\omega \gtrsim \omega_{pi}$. Unfortunately, this is *not* possible using cylindrical geometry since its use causes non–physical results with respect to current collection. In this geometry, all particles within the sheath that

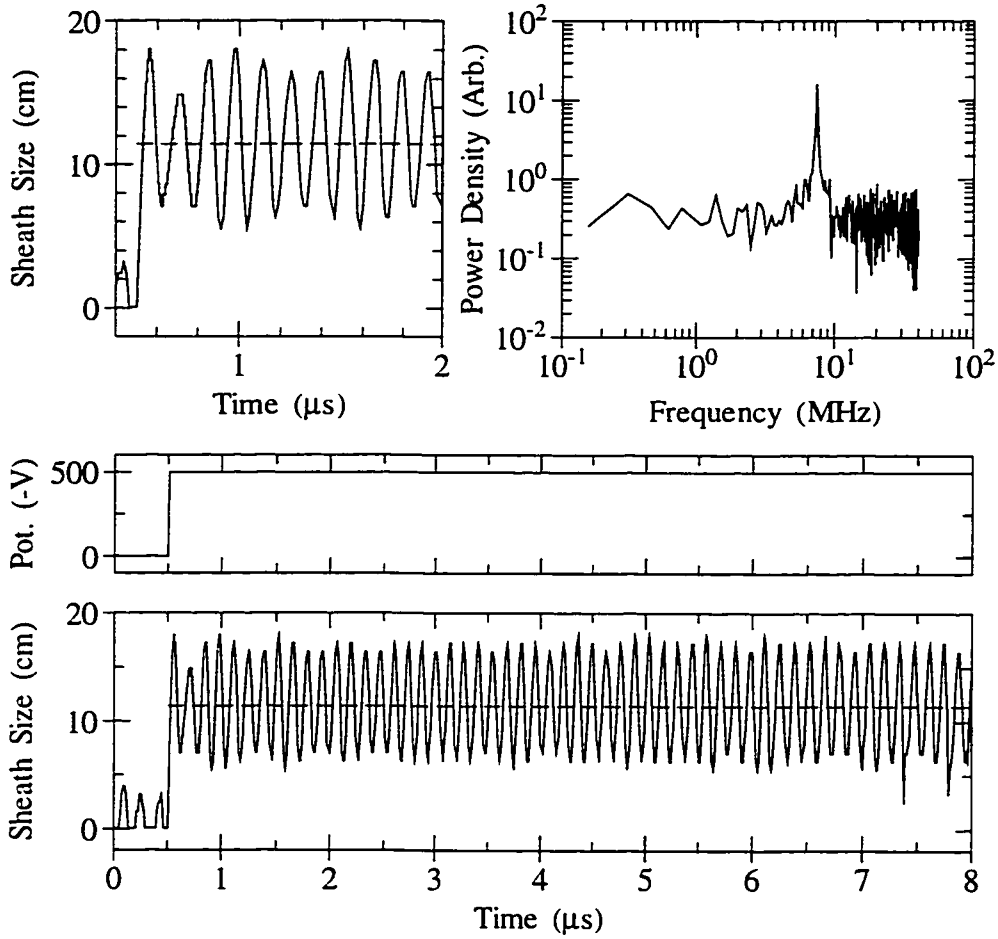

Figure 3.24: PIC simulation of oscillating sheath due to the rapid (τ_{ar} = 10 ns $\ll 2\pi/\omega_{pe}$) application of a −500–V step at t = 0.5 μs for n_0 = 1×10^{12} m^{-3}. Shown in the figure are the sheath distance as function of time and equilibrium ion-matrix distance (dashed line), the conductor potential, expanded plot of sheath distance near voltage transition to V_a, and an FFT of the oscillating sheath showing $f_{\rm ring} \sim 7.5$ MHz.

are accelerated to the central cylinder are collected as current, which is not the case in OML current–collection physics. In order to accurately model the OML physics, a rectangular–geometry grid should be used with an infinite cylinder placed in the middle of the simulation domain. However, a simulation of this type presents several difficulties, including a large number of grid points and plasma–containment issues. Using rectangular geometry, however, would allow specification of a flowing plasma in order to examine the sheath physics at orbital velocities. These simulations are left as future work.

The second comment relates to PIC simulations of the plasma response around insulated cylindrical conductors, a geometry which resembles that of the TSS–tether. In order to specify a thin insulation thicknesses (on the order of a few millimeters or less), a nonuniform gridding scheme had to be employed which increased the grid spacing from very fine near the conductor to large near the 1–m edge. Unfortunately, this gridding scheme introduced an excessive amount of numerical noise in the simulations caused by particles not satisfying the Courant condition for particle motion as discussed in Section 3.4.2. Simulations performed using a uniform grid with specifications similar to those of the bare–conductor simulations meant that the minimum–specifiable insulator thickness was $\sim$ 1 cm, clearly much larger than that of the TSS geometry (see Figure 5.1a in Chapter V). The few simulations which were run with insulated conductors, however, corroborated the experimental observation (Section 3.3.6.1) of insulator irrelevance to the formation of the ion–matrix sheath.

3.5 Description of Transient Plasma–Sheath Model

At this point, we recap the temporal and voltage–dependent sheath model as developed in this chapter. In the following chapters this model is used as the basis for the distributed–circuit transmission–line model. The sheath model is valid in the frequency regime between the electron and ion plasma frequencies, and for large negative applied voltages, $|V_a| \gg kT_e/q$. In this frequency regime, the E–field from the conductor is contained within the sheath region, which is an important result allowing us to develop a sheath–capacitance model in the next chapter. The model describes the ion–matrix–sheath radius as a function of applied voltage, $r_{\mathsf{sh}}(V_a)$, and, in the specified frequency regime, does not depend on whether or not the conductor is insulated. The equation for $r_{\mathsf{sh}}(V_a)$ is

$$r_{\mathsf{sh}}(V_a) \simeq \sqrt{3}\left(\frac{V_a\varepsilon_0}{q_e n_0}\right)^{5/12} r_a^{1/6} \text{ for } r_{\mathsf{sh}} \gg r_a. \tag{3.37}$$

Although this equation may appear relatively simple, it is an important result in that it is non–transcendental, unlike the exact expression. This allows it to be used easily as the basis of the circuit model we develop for use in the SPICE circuit–simulation code.

CHAPTER IV

Electrodynamic–Tether Circuit Model

Having developed a model of the voltage–dependent sheath in Chapter III, we now employ that model as the basis of a nonlinear transmission–line model of the electrodynamic tether. Although we focus here on the electrodynamic tether (and, in particular, the TSS tether), the model can also be applied to general negative–HV pulse propagation along bare and insulated cylinders in cold, low–density plasmas.

This chapter begins with a qualitative description of negative–HV pulse propagation along electrodynamic tethers. We then develop a circuit model of the tether transmission line with parameters based on the voltage–dependent sheath. The final section of this chapter discusses qualitatively the nonidealities of the model and presents possible refinements and extensions as future work.

4.1 Description of Negative–High–Voltage Pulse Propagation

At the most fundamental level, the conducting cylinder of our tether transmission line forms a channel along which charge can flow from a source at one end to a (possible) sink at the other. The flowing charge, in turn, comprises the current flowing along the cylinder; hence, we have signal propagation along the tether. As in the previous chapter (*cf.* Section 3.2), we can also consider this situation as the propagation along the tether of a voltage disturbance caused by flowing applied charge. Hence, we are able to talk about high-*voltage* pulse propagation along the tether.[1]

As described in Section 2.3.2 and shown in Figures 2.6 and 2.7, the tether has two potential structures representing the non-current-flowing (open-circuited) and current-flowing (closed-circuited) states. These states are the initial and final conditions of the transient case which occurs when a load impedance is connected or disconnected from the system. The switch closure takes a finite amount of time to propagate along the tether because of the physical separation of the system's two ends. The pulse front which propagates is actually the initial portion of a step function in tether voltage. That is, before the appearance of the pulse, a given section of tether is at some voltage with respect to the surrounding plasma as defined by the mode's potential structure. After the pulse front passes this section of tether, a new voltage is established for this tether portion based on the new potential structure.

There are four timescales to consider when examining the propagation of the pulse along the tether. These timescales are shown in the schematic of Figure 4.1. Each of these four timescales is the linked to the timescale of the interaction of the surrounding plasma with the tether section during the voltage change as described in Chapter III. The first timescale is linked to the initial electrical disturbance as the pulse front moves along the tether. Since this timescale is on the order of a fraction of the speed of light, the plasma is not able to respond on this timescale and the sheath remains fairly static. The second is linked to the electron–response timescale, which is on the order of the electron plasma period, τ_{pe}. Because of their low mass, the electrons are quickly repelled away from the tether surface as the negative voltage is

[1]This is an important explanation because it allows voltage pulses to be specified as inputs to the circuit model we develop, which is simpler than specifying charge (current) pulses.

established along the tether, and the tether section becomes biased negatively due to the pulse front having moved past the section of tether. The third timescale is linked to the ion response time and is on the order of the ion plasma period, τ_{pi}. After the electrons have been blown out of the region surrounding the tether, an ion–matrix sheath forms and the ions begin to respond to the voltage disturbance. The fourth timescale is the time it takes to re–establish a steady–state–sheath structure around the tether. For the bare tether, this steady–state sheath is generally an OML sheath. For the insulated tether, the sheath structure is similar to what existed before the mode change, *i.e.*, the sheath has collapsed.

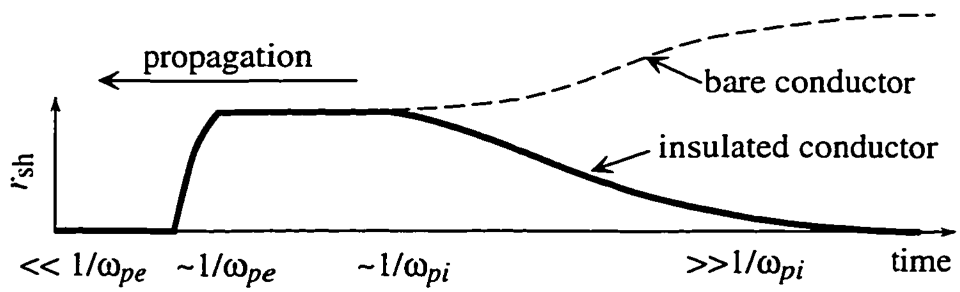

Figure 4.1: Schematic of negative–HV pulse propagation along electrodynamic tethers.

For the model we develop here, we restrict ourselves to the frequency range $\omega_{pe} \gg \omega \gg \omega_{pi}$. Alternatively, we can state that we restrict ourselves to pulses which have risetimes, plateaus, and falltimes that fall in the range $\tau_{pe} \ll \tau \ll \tau_{pi}$, since a Fourier decomposition of these pulses gives frequency components in the allowable frequency range. Restricting ourselves to these pulses and excitation frequencies means that we are really only concerned with the second timescale for pulse propagation discussed above. On this timescale, r_{sh} is a function of V_a only, and not also a function of time.

Although we have restricted ourselves to $\omega_{pe} \gg \omega \gg \omega_{pi}$, a few comments about extremely high excitation frequencies (*i.e.*, $\omega \gg \omega_{pe}$), are in order. At these excitation frequencies, the tether–plasma system appears as a simple, single conducting wire in vacuum. The reason for this is that, at these frequencies, the plasma is unable to significantly respond to the perturbations caused by the voltage on the wire. In 1899, *Sommerfeld* theoretically demonstrated the possibility of a propagating surface–wave mode along a round conductor.[2] The mode is a TM wave with components H_φ, E_r, E_z, and is azimuthally symmetric. The mode exists only for finite conductivity and is loosely bound to the conductor's surface. *Goubau* [1950, 1951] studied the suitability of this surface–wave mode for practical transmission–line systems and found that a single small–diameter conducting wire will propagate an axially symmetric surface–wave mode with low attenuation, but that the fields extend a considerable distance from the conductor. In addition, he found that a thin dielectric coating and/or otherwise–modified surface (*e.g.*, small ridges[3]) allows the wave mode to propagate even with perfect conductivity and helps to restrict the extent of the field.

The above discussion tells us that, on the smallest timescales (the leading edge of the pulse), there does exist an E_z component that drives charge down the wire. Hence, charge that is pushed onto the conductor at one end is moved along the wire to the other end in an attempt to make the charge distribution along the wire uniform. At longer timescales, the primary field components are a radially directed electric field, E_r, and an axially symmetric magnetic field, H_φ. Since these two are the primary field components, the tether transmission line is approximately TEM for the longer timescales. As a TEM transmission line, we can define circuit parameters

[2]Sommerfeld's solution can be found in *Stratton* [1941, chap. 9].

[3]It is interesting to note that the description *Goubau* [1950] gives for such a wire is very much like the TSS tether, in which case the tether's insulation represents the thin dielectric coating and the ridges represent the spiral windings of the fine strands of copper wire (see Figure 5.1).

to describe the tether transmission line.[4] These circuit parameters can then form the basis of a distributed lumped–element model of the tether transmission line. Such a model allows for simulation of pulse propagation via readily available circuit–simulation programs such as SPICE.

4.2 Circuit–Model Approximation

Under the assumption of excitation frequencies in the range between the ion and electron plasma frequencies (*i.e.*, $\omega_{pi} \ll \omega \ll \omega_{pe}$), we can employ the voltage–dependent–sheath model developed in Chapter III in the development of a circuit–model approximation of the electrodynamic–tether transmission line valid for HV pulse propagation. The model of the tether/plasma system that we develop is, in effect, of a "non–static" coaxial transmission line, *i.e.*, a transmission line with voltage–dependent ("dynamic") parameters. In the frequency range $\omega_{pi} \ll \omega \ll \omega_{pe}$, the tether's E– and B–fields are contained locally allowing us to define an effective capacitance and inductance per unit length for the tether. In developing this model, we use the knowledge that the E–field is contained within the sheath region (as shown in Section 3.4.7.1 via PIC simulations) to develop the effective capacitance. We then find the effective inductance by showing that the B–field is also locally contained, but in a larger region that takes into account the location of the plasma return currents.

As mentioned, the capacitance and inductance per unit length derived in this section are based on the sheath distance, $r_{\rm sh}$, which is a function of the voltage applied across the sheath. Hence, the capacitance and inductance per unit length ultimately depend on applied voltage. For the tether geometry, Figure 4.2 shows

[4]See §3.2 of *Pozar* [1990] for a derivation of the Telegrapher's Equations—which use circuit parameters—from a field analysis of a coaxial transmission line.

r_{sh} as a function of applied voltage with $r_a = 0.43$ mm (TSS–tether geometry) and $n_e = 10^{12}$ m^{-3}.

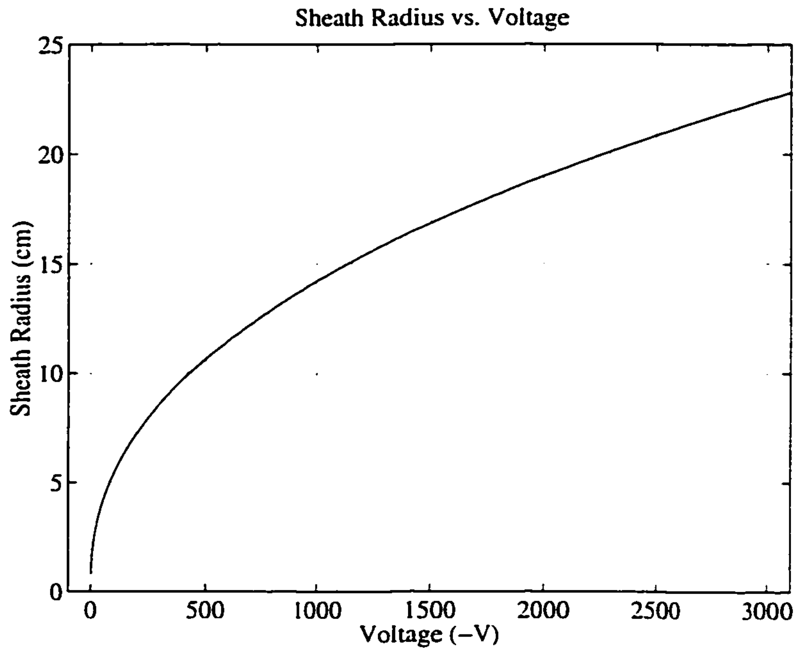

Figure 4.2: Plot of ion–matrix–sheath radius, r_{sh}, vs. applied voltage for a cylindrical tether geometry in an $n_e = 10^{12}$ m^{-3} plasma.

4.2.1 Coaxial Capacitor Approximation

In this section we examine the assumption that the cylinder–sheath–plasma system approximates a coaxial capacitor. Although we do assume a certain particle density distribution for the sheath and plasma, we make no *a priori* assumption of sheath distance, cylinder bias voltage, or surface charge density as we did in Sections 3.2.1 and 3.2.2.

We begin our investigation by specifying a simplistic sheath model in which the ions are motionless and the electrons move collectively [*e.g.*, *Perkins*, 1989; *Raizer et al.*, 1995, and others]. This assumption implies that the excitation frequency lies between the ion and electron plasma frequencies (*i.e.*, $\omega_{pi} \ll \omega \ll \omega_{pe}$). In addition, the following simple density distribution is assumed in the region surrounding the cylinder since the cylinder potential is negative:

$$n_e = \begin{cases} 0, & r_a < r < r_{\text{sh}} \\ n_0, & r > r_{\text{sh}}, \end{cases} \tag{4.1a}$$

$$n_i = n_0,\ r > r_a. \tag{4.1b}$$

This distribution is shown graphically in Figure 4.3. It should be noted that other distributions for the ion density yield similar results [for example *Hilbish*, 1967], as it is the step rise in electron density which is a requirement of this approximation. The assumption of a step rise in electron density is valid under large applied potentials where the electron content of the sheath is small with respect to the ion content. The PIC simulations of Sections 3.4.7.1 and 3.4.7.2 showed that for large V_a the electron density does indeed experience a nearly step–like rise at the sheath edge.

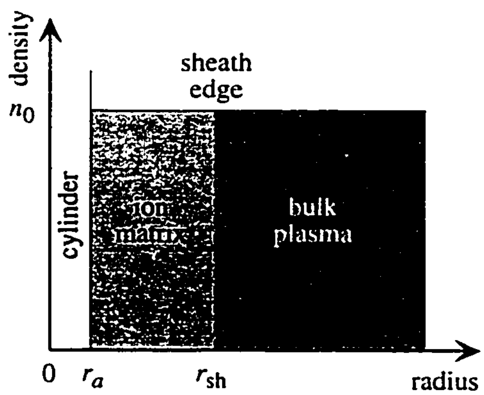

Figure 4.3: Simplistic model of an RF sheath surrounding a negatively biased cylinder immersed in a plasma.

We wish to solve for the electric field and potential distribution in the sheath region. We begin by writing Poisson's equation in cylindrical geometry[5] assuming that the fields vary only in the radial direction (*i.e.*, radial symmetry):

$$\frac{1}{r}\frac{d}{dr}\left(r\frac{dV}{dr}\right) = -\frac{q}{\varepsilon_0}\left(n_i - n_e\right). \tag{4.2}$$

Substituting the values of n_e and n_i from Equations (4.1a) and (4.1b) into Equation (4.2) and multiplying both sides by r,

$$\frac{d}{dr}\left(r\frac{dV}{dr}\right) = -\frac{qn_0}{\varepsilon_0} \times \begin{cases} r, & r_a < r \leq r_{\text{sh}} \\ 0, & r > r_{\text{sh}}. \end{cases} \tag{4.3}$$

We can now integrate Equation (4.3) once, and divide both sides by r to obtain the gradient of the potential which we recognize as simply the negative of the electric field (*i.e.*, $E = -\frac{dV}{dr}$), hence

$$E(r) = \frac{qn_0}{\varepsilon_0} \times \begin{cases} \frac{r}{2} + \frac{C_1}{r}, & r_a < r \leq r_{\text{sh}} \\ \frac{C_2}{r}, & r > r_{\text{sh}}, \end{cases} \tag{4.4}$$

where C_1 and C_2 are constants of integration which must now be found. In the plasma, the E–field must vanish, hence

$$C_2 = 0 \text{ for } r > r_{\text{sh}}.$$

C_1 is evaluated by requiring E to be continuous at $r = r_{\text{sh}}$, which means that

$$C_1 = -\frac{r_{\text{sh}}^2}{2} \text{ for } r_a < r \leq r_{\text{sh}}.$$

So, the E–field is found to be

$$E(r) = \frac{qn_0}{\varepsilon_0} \times \begin{cases} \frac{r}{2} - \frac{r_{\text{sh}}^2}{2r}, & r_a < r \leq r_{\text{sh}} \\ 0, & r > r_{\text{sh}}. \end{cases} \tag{4.5}$$

[5]A more general form of Poisson's equation is given by Equation (3.1).

To determine the potential distribution, we begin by radially integrating the E–field, yielding

$$V(r) = -\frac{qn_0}{\varepsilon_0} \times \begin{cases} \frac{r^2}{4} - \frac{r_{\text{sh}}^2}{2}\ln r + C_3, & r_a < r \leq r_{\text{sh}} \\ C_4, & r > r_{\text{sh}}, \end{cases} \tag{4.6}$$

where C_3 and C_4 are again constants of integration. If we reference the potential of the cylinder with respect to the plasma region and set[6] $V = V_p = 0$ for $r > r_{\text{sh}}$, then

$$C_4 = 0 \text{ for } r > r_{\text{sh}}.$$

Again, requiring continuity of V at $r = r_{\text{sh}}$ we can solve for C_3 yielding

$$C_3 = \frac{r_{\text{sh}}^2}{2}\left(\ln r_{\text{sh}} - \frac{1}{2}\right) \text{ for } r_a < r \leq r_{\text{sh}}.$$

Thus,

$$V(r) = -\frac{qn_0}{\varepsilon_0} \times \begin{cases} \frac{r^2}{4} - \frac{r_{\text{sh}}^2}{2}\ln r + \frac{r_{\text{sh}}^2}{2}\left(\ln r_{\text{sh}} - \frac{1}{2}\right), & r_a < r \leq r_{\text{sh}} \\ 0, & r > r_{\text{sh}}. \end{cases} \tag{4.7}$$

Before continuing with the derivation of the sheath capacitance, it is instructive to show how the pseudo–static sheath potential (Equation 4.7) and electric field (Equation 4.5) vary versus radial distance for the cylindrical–conductor case. These quantities were examined numerically via PIC simulations in Sections 3.4.7.1 and 3.4.7.2, and it is an important to show that the analytical equations and PIC simulations agree. Figure 4.4 plots the potential and electric field for $r_a = 0.65$ mm, $V_a = -500$ V, and $n_e = 10^{12}$ m^{-3} plasma, which are the same conditions used in the PIC simulations. The plot clearly shows that the potential drops from V_a at the conductor to 0 V at the sheath edge, r_{sh}. The electric field also falls to 0 V/cm

[6] Here we arbitrarily set V_p to 0 V primarily for the sake of simplicity. Since $V_a \gg V_p \sim 0$, this is justified.

at the sheath edge. Hence, the electric field is contained within the sheath region. Included in the plot are the PIC results that were plotted in Figure 3.18f showing excellent agreement, except for the PIC-derived E-field near the conductor that is probably due to the enhanced ion density close to the conductor (*cf.* Figure 3.17f and the discussion in Section 3.4.7.2). *Savas and Donohoe* [1989a] measured the potential distribution of the sheath above an RF-processing-plasma electrode[7]: their measurements show E-field containment in the sheath and potential-distribution drop-off very similar to that in Figure 4.4.

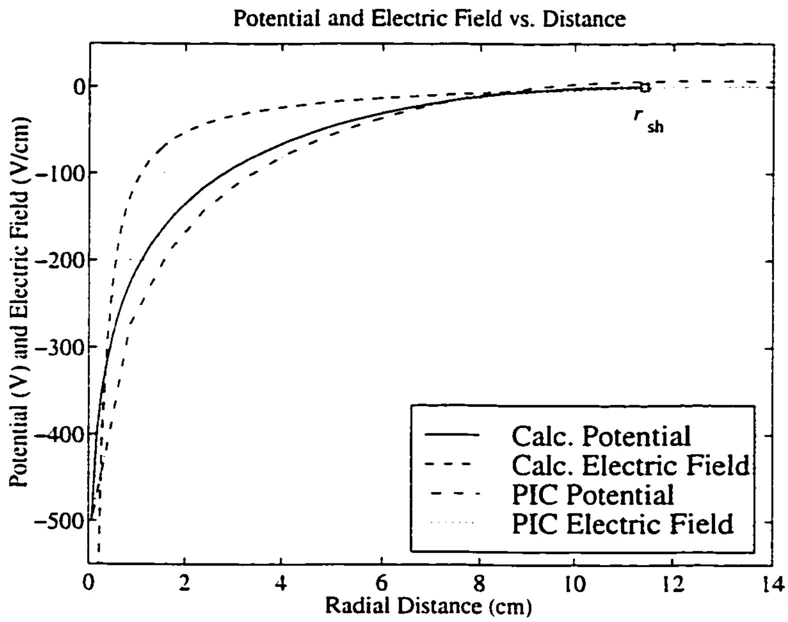

Figure 4.4: Plot of calculated and PIC-simulation-derived (Figure 3.18f) ion-matrix-sheath potential and electric field vs. radial distance for a cylindrical conductor with $r_a = 0.65$ mm, $V_a = -500$ V, and $n_e = 10^{12}$ m^{-3} plasma.

Returning to our derivation, now that we know the E-field and potential distribu-

[7]Their electrode was approximately planar surrounded by a Child-Langmuir sheath. See Figure 1.1a for a picture of the electrode.

tions of the sheath, we can search for the capacitance of the cylinder–sheath–plasma system. The surface charge density, ρ_{sa}, on the cylinder can be calculated using the standard conductor–dielectric condition (Gauss' Law) for an infinite cylinder

$$\rho_{sa} = \varepsilon_0 E_a, \tag{4.8}$$

where E_a is the E–field at the wall ($r = r_a$). Defining an incremental, or dynamic, capacitance per unit area as the derivative of the surface charge on the probe with respect to its potential[8] [*e.g.*, *Grard*, 1966; *Shkarofsky*, 1972],

$$\frac{C'_{\mathrm{sh}}}{A} = \frac{d\rho_{sa}}{dV_a}, \tag{4.9}$$

allows us to solve for C'_{sh} (the total capacitance) using our knowledge of E and V. From Equation (4.7) the potential at the wall is[9]

$$V_a = V(r_a) = -\frac{qn_0}{\varepsilon_0}\left[\frac{r_a^2}{4} - \frac{r_{\mathrm{sh}}^2}{2}\ln r_a + \frac{r_{\mathrm{sh}}^2}{2}\left(\ln r_{\mathrm{sh}} - \frac{1}{2}\right)\right]. \tag{4.10}$$

The surface charge density, ρ_{sa}, can be found by first determining E_a from Equation (4.5), and then substituting that into Equation (4.8), yielding

$$\rho_{sa} = qn_0\left(\frac{r_a}{2} - \frac{r_{\mathrm{sh}}^2}{2r_a}\right). \tag{4.11}$$

It is interesting to note that Equation (4.11) is equivalent to Equation (3.18) solved for ρ_{sa} with $r_{\mathrm{sh}} = r_{\mathrm{ch}}$. Using the chain rule, we can rewrite Equation (4.9) as

$$\frac{C'_{\mathrm{sh}}}{A} = \frac{d\rho_{sa}/dr_{\mathrm{sh}}}{dV_a/dr_{\mathrm{sh}}}, \tag{4.12}$$

and by finding the derivatives

$$\frac{d\rho_{sa}}{dr_{\mathrm{sh}}} = -\frac{qn_0 r_{\mathrm{sh}}}{r_a}, \tag{4.13a}$$

$$\frac{dV_a}{dr_{\mathrm{sh}}} = -\frac{qn_0 r_{\mathrm{sh}}}{\varepsilon_0}\ln\left(\frac{r_{\mathrm{sh}}}{r_a}\right), \tag{4.13b}$$

[8] Equation (4.9) is an alternate form of the equation $C = Q/V$.
[9] Note the similarity of this equation with Equation (3.9).

and substituting Equations (4.13a) and (4.13b) into Equation (4.12) we find

$$\frac{C'_{\mathrm{sh}}}{A} = \frac{\varepsilon_0}{r_a \ln\left(\frac{r_{\mathrm{sh}}}{r_a}\right)}. \tag{4.14}$$

Knowing that the area of the "wall" is $A = 2\pi r_a l$ for a cylinder allows us to rewrite (4.14) as

$$C'_{\mathrm{sh}} = \frac{2\pi\varepsilon_0 l}{\ln\left(\frac{r_{\mathrm{sh}}}{r_a}\right)}, \tag{4.15}$$

which we recognize as the equation for a coaxial capacitor with an inner radius r_a and outer radius r_{sh}. Since we desire a capacitance per unit length, $C_{\mathrm{sh}} = \frac{C'_{\mathrm{sh}}}{l}$, we can rewrite Equation (4.15) as

$$C_{\mathrm{sh}} = \frac{2\pi\varepsilon_0}{\ln\left(\frac{r_{\mathrm{sh}}}{r_a}\right)}. \tag{4.16}$$

Thus, we have shown that using a simple model for the plasma sheath, the cylinder–sheath–plasma system approximates a coaxial capacitor. This analysis also can be applied to planar and spherical geometries to show similar relationships. *Grard* [1966] performed such an analysis for the planar, cylindrical, and spherical geometries in a thin sheath (Child–Langmuir) limit for four different distribution models of electron and ion density surrounding a probe. Of the four distribution models, only three are relevant to this work because they assumed mobile electrons and stationary ions. Using these different distribution models he found that the derived capacitance values (for the planar case) are very similar notwithstanding the different initial distributions. It is also interesting to note that even though two of these three relevant models were developed with the abrupt–electron–sheath assumption—the same utilized here in deriving C_{sh}—one of the three models utilized a continuous change in electron density. *Grard* found that the differences in calculated sheath capacitances between the models decrease with larger and larger applied potentials.

4.2.1.1 Effective Capacitance for Insulated Tether

For the case of the insulated tether, two effective capacitances exist in series between the cylinder surface and the sheath edge (Figure 4.5). The first is denoted as C_d and is the capacitance between the cylinder (r_a) and the dielectric edge (r_d). The second is denoted as C_{sh} and is the "sheath capacitance" between r_d and the sheath edge (r_{sh}). C_d is a fixed capacitance which depends on the insulator thickness and dielectric constant, whereas C_{sh} varies as the sheath distance changes. The total capacitance, denoted C_{tot}, is found in the normal manner for series connected capacitors:

$$\frac{1}{C_{\text{tot}}} = \frac{1}{C_d} + \frac{1}{C_{\text{sh}}} \text{ or } C_{\text{tot}} = \frac{C_d C_{\text{sh}}}{C_d + C_{\text{sh}}}. \tag{4.17}$$

However, since $r_{\text{sh}} \gg r_d \gtrsim r_a$, then $C_d \gg C_{\text{sh}}$, which implies that $C_{\text{tot}} \approx C_{\text{sh}}$ for large applied voltages.

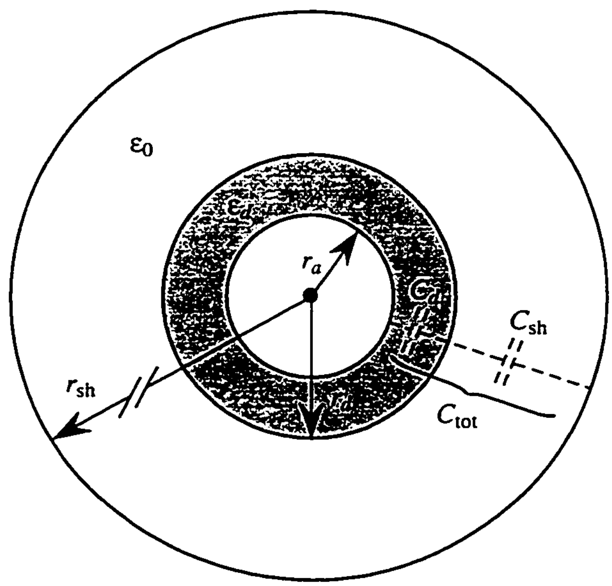

Figure 4.5: Geometry of dielectric–coated cylinder and plasma sheath showing effective capacitances.

For the geometry of Figure 4.5, Figure 4.6 plots the per-unit-length sheath capacitance, C_{sh}, and total capacitance, C_{tot}, against applied voltage. The value of C_d, which results from the static insulator-conductor geometry, is 128 pF/m (calculated from TSS values: $r_a = 0.43$ mm, $r_d = 1.27$ mm, $\varepsilon_d = 2.5$). The two values differ by approximately 1 pF/m ($\sim$ 10%) for large applied voltages, with this discrepancy increasing as voltage is decreased (or, equivalently, as r_{sh} decreases). For this reason, both capacitances C_d and C_{sh} are implemented in the circuit model to increase accuracy.

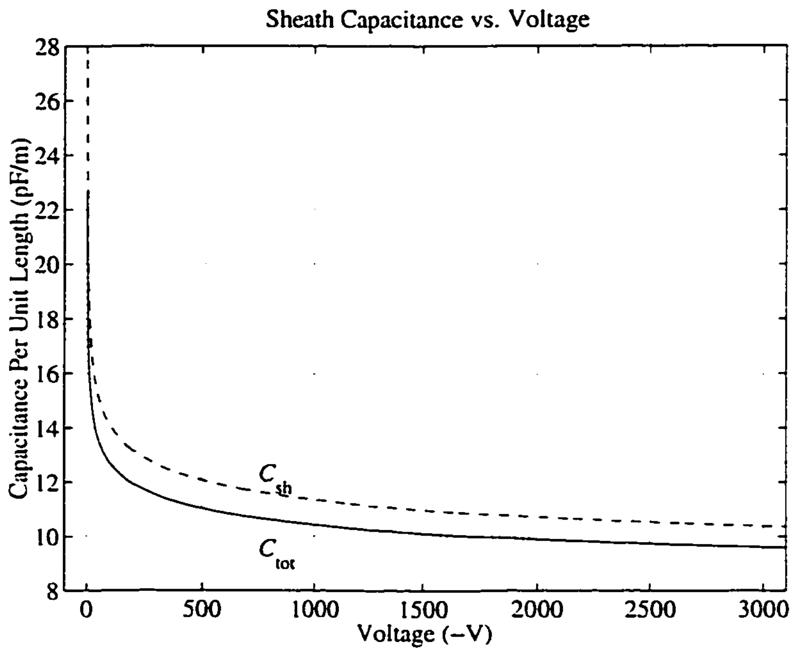

Figure 4.6: Plot of per-unit-length sheath capacitance, C_{sh}, and total capacitance, C_{tot}, vs. applied voltage for an insulated-cylinder geometry in an $n_e = 10^{12}$ m^{-3} plasma.

4.2.2 Coaxial Inductance Approximation

The inductance of a typical coaxial transmission line can be determined through a calculation of the stored magnetic energy of the system. In the typical coaxial line, the magnetic fields are confined to the region between the two conductors since a return current flows in the outer conductor that is equal and opposite to that of the center conductor; hence, the magnetic fields are confined. In the absence of a return conductor, as in the case of electrodynamic tethers, some other mechanism for confining the magnetic field is needed, otherwise calculated inductance would be (nearly) infinite.[10] To confine the magnetic fields, we make certain assumptions on the location of the return current based on a physical argument. This assumption places a lower limit on the excitation frequency based on the magnetic diffusion time and introduces a loss component.

4.2.2.1 Magnetic Skin Depth

At this point we need to examine the response of a plasma to a changing external magnetic field. We will do this by describing a concept called the *magnetic skin depth*, which is denoted δ_m.[11] Although a perfectly conducting plasma will exclude a changing magnetic field just as a perfect conductor does, magnetic fields can penetrate a distance δ_m into a plasma because of electron inertia. Equivalently, we can say that it is bulk plasma currents which flow to exclude the external field rather than surface currents at the sheath edge.

In this analysis the following assumptions are made: collisions are ignored, ions are motionless, the plasma has zero resistivity, and the magnetic field (caused by

[10] It would be exactly infinite if the tether were infinitely long and in a vacuum.

[11] This derivation is based on that found in §12.5 of *Humphries* [1990], which was developed for electron–beam propagation in a plasma.

the wire current) is monotonically increasing with time. For simplicity, we assume a planar geometry with sharp boundaries (Figure 4.7), *i.e.*, the wire–generated magnetic field occurs outside the sharp plasma boundary of uniform plasma density ($n_0 = n_e = n_i$).

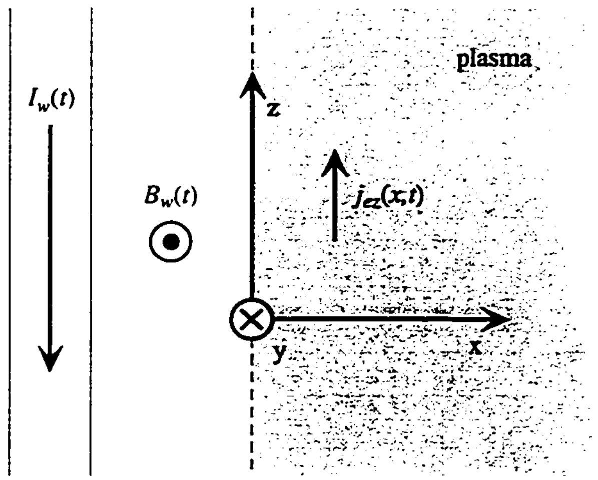

Figure 4.7: Simplified geometry for deriving the magnetic skin depth of a plasma.

The plasma responds as follows. The induced plasma electron current, j_{ez}, opposes the current in the wire, I_w, and hence tends to exclude the wire–generated magnetic field (denoted B_w) from the plasma. That is, the wire current moving in the $-z$ direction (*i.e.*, wire electrons are moving in the $+z$ direction) generates an applied B–field in the $-y$ direction. The induced E–field from the changing applied B–field—given by Faraday's Law—accelerates plasma electrons in the $-z$ direction (*i.e.*, plasma current flows in the $+z$ direction).[12] If we denote the plasma–electron current density as $j_{ez}(x,t)$, then from Ampère's Law the spatial variation of the

[12]This response is a manifestation of Lenz' Law.

magnetic field due to the plasma current is given by

$$\frac{\partial B_y(x,t)}{\partial x} = -\mu_0 j_{ez}(x,t). \tag{4.18}$$

The electric fields in the plasma induced by the changing magnetic flux are determined by Faraday's Law:

$$E_z(x,t) = -\int_x^\infty \frac{\partial B_y(x',t)}{\partial t} dx', \tag{4.19}$$

where we have extended the integral to $+\infty$, which is an approximation that is valid if strong–field exclusion holds deep into the plasma region. If we neglect the effect of the magnetic field on the electron orbits in order to simplify the derivation, then the electrons move only in the $-z$ direction and their acceleration is given by (remembering that $F = ma = qE$)

$$\frac{\partial v_{ez}(x,t)}{\partial t} = a_{ez}(x,t) = \frac{q_e E_z(x,t)}{m_e} = \frac{-q_e}{m_e}\int_x^\infty \frac{\partial B_y(x',t)}{\partial t} dx'. \tag{4.20}$$

Since $q = -q_e$, we see that electrons are indeed accelerated in the $-z$ direction.

We now wish to integrate Equation (4.20) over time from $t' = 0$ to the time of interest, $t' = t$. We assume $B_w(0) = 0$ so that $v_{ez}(x,0) = 0$ and $B_y(x,0) = 0$. Recalling that $j_{ez} = q_e n_e v_{ez}$, then the integration yields

$$v_{ez}(x,t) = \frac{j_{ez}(x,t)}{q_e n_0} = \frac{-q_e}{m_e}\int_x^\infty B_y(x',t)dx'. \tag{4.21}$$

Taking the partial derivative of Equation (4.21) with respect to x yields

$$\frac{\partial j_{ez}(x,t)}{\partial x} = \frac{-q_e^2 n_0 B_y(x,t)}{m_e}. \tag{4.22}$$

Now, if we take the partial derivative of Equation (4.18) with respect to x and substitute Equation (4.22) for $\partial j_{ez}(x,t)/\partial x$, we find an equation for the spatial variation of B_y at time t, *i.e.*,

$$\frac{\partial^2 B_y(x,t)}{\partial x^2} = \frac{\mu_0 q_e^2 n_0}{m_e} B_y(x,t) = \frac{q_e^2 n_0}{c^2 \varepsilon_0 m_e} B_y(x,t) = \frac{\omega_{pe}^2}{c^2} B_y(x,t). \tag{4.23}$$

The solution of Equation(4.23) subject to the boundary condition $B_y(0,t) = B_w(t)$ is

$$B_y(x) = B_w \exp\left(\frac{-x}{\delta_m}\right), \tag{4.24}$$

where δ_m is the magnetic skin depth defined as

$$\delta_m = c/\omega_{pe}. \tag{4.25}$$

A typical value of δ_m for an $n_e = 10^{12}$ m^{-3} ionospheric plasma is 5.3 m. From Table A.1 found in Appendix A, we see that $\delta_m \gg r_{ce}$ and $\delta_m \sim r_{ci}$. The electrons within the skin-depth region are hence magnetized, but the ions are not. In any case, due to the frequency requirement that $\omega \gg \omega_{pi}$, the ions are motionless. One other point we need to make before continuing is that the above derivation was performed for planar geometry; however, the same of magnetic skin depth [Equation(4.25)] is typically also applied to cylindrical geometry by many researchers [*e.g.*, *Humphries*, 1990].

The effect of the plasma skin depth is to cause the RF B–field generated by the current-carrying wire to diminish more quickly than it would in a vacuum. In Figure 4.8 we plot the B–field from a current-carrying wire in vacuum ($B \propto 1/r$) and in plasma. The field is plotted external to the sheath ($r_{\mathrm{sh}} = 10$ cm in this plot), since the sheath's motionless ions do not affect the B–field. Clearly seen is the reduction of the field due to the skin-depth effect. In addition, as the plasma density increases and, hence, the skin depth decreases, the RF B–field diminishes even more quickly. Several researchers have made measurements of this effect and have found that the measurements agree well with theory [*Denisov et al.*, 1984; *Sugai et al.*, 1994].

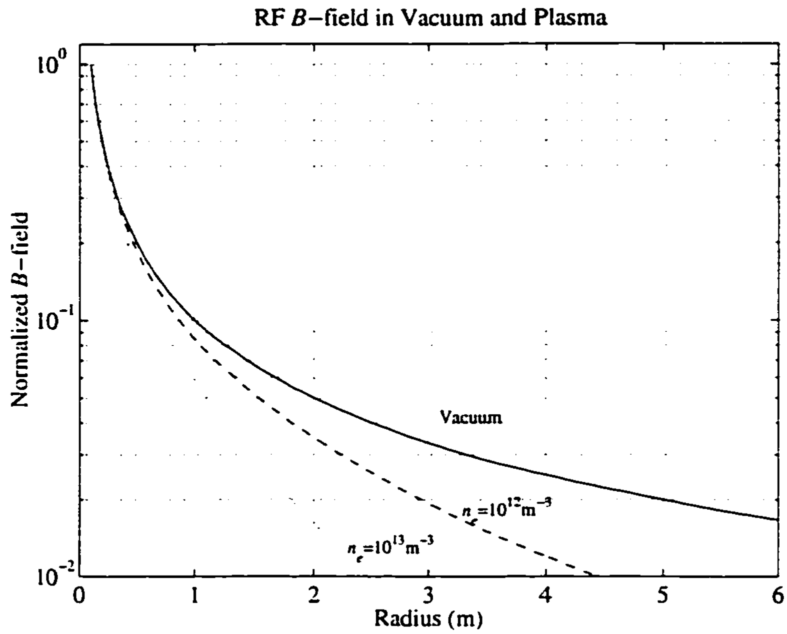

Figure 4.8: Comparison between the RF B–field around a current–carrying wire in vacuum and in plasma. The skin–depth effect of the plasma causes the RF B–field in a plasma to diminish more quickly than in the vacuum case. In addition, as the plasma density increases (and, hence, the skin depth decreases), the RF B–field diminishes even more quickly.

4.2.2.2 Return–Current Spatial and Temporal Variation

As developed in Section 4.2.2.1 above, the concept of the magnetic skin depth shows that 1) due to the penetration of the magnetic field into a collisionless (zero resistivity) plasma, inductive axial electric fields drive a plasma return current and, 2) the magnetic–field distribution is approximately contained within the skin–depth region. For a plasma with nonzero resistivity, however, the spatial distribution of the return current will change as a function of time. This change has two immediate consequences: 1) a lower limit is placed on the excitation frequency for magnetic–field confinement (a requirement for a transmission–line mode), and 2) dissipative losses are introduced due to B–field and plasma–current diffusion. We will examine these consequences in the discussion below.

Plasma resistance results from collisions which interrupt the directed flow of the particle motion. In a weakly ionized plasma, ionized particles collide and exchange momentum with charged and neutral particles in addition to undergoing Coulomb collisions, which are electric–field deflections that occur when particles pass close to each other. In a fully ionized plasma most collisions are Coulomb collisions. When the electron drift velocity, v_d, that causes the plasma current is much less than the electron thermal velocity, v_{te}, then the current density is proportional to the applied electric field as specified by Ohm's Law,

$$\mathbf{E} = \eta_p \mathbf{j}_e. \tag{4.26}$$

The volume resistivity, η_p, of the plasma is defined as

$$\eta_p = \frac{m_e \nu_{ei}}{q^2 n_e}, \tag{4.27}$$

where ν_{ei} is the average electron–ion collision frequency. In Equation (4.26), the effects of the magnetic field are ignored.[13]

The electron–ion collision frequency can be estimated for the case of electrons with Maxwellian distribution and singly charged ions via the following equation [*Chen*, 1984][14]

$$\nu_{ei} \simeq \frac{q^4 n_e \ln(\Lambda)}{16\pi\varepsilon_0^2 \sqrt{m_e}(kT_e)^{3/2}}, \tag{4.28}$$

where the quantity Λ is the *plasma parameter* defined by

$$\Lambda = 12\pi n_e \lambda_D^3 = 9\left[\frac{4\pi}{3} n_e \lambda_D^3\right] = 9N_D. \tag{4.29}$$

[13]See §5.7 in *Chen* [1984] for a discussion of these effects, which when included transform Equation (4.26) into the *generalized Ohm's law*.

[14]*Humphries* [1990] provides a similar expression with slightly different coefficient in the denominator. Since ν_{ei} is derived via consideration of collision probability, slightly different results will be obtained depending on assumptions. Only an order–of–magnitude estimate is needed here.

Equation (4.29) shows that the plasma parameter is proportional to the number of particles in a Debye sphere, N_D (see Section 2.1.1).

The timescale for the diffusion of the magnetic field into the plasma is given by[15]

$$\tau_d \simeq \frac{\mu_0 L_B^2}{\eta_p}, \tag{4.30}$$

where L_B is the scale length of the spatial variation of $\mathbf{B}$, which we will specify as the region in which the wire's RF B-field is contained. This distance is on the order of the magnetic skin depth, δ_m. Thus, Equation (4.30) can be rewritten in our case as

$$\tau_d \simeq \frac{\mu_0 \delta_m^2}{\eta_p}. \tag{4.31}$$

For a typical ionosphere with $n_e = 10^{12}$ m^{-3} and $\theta_e = 0.1$ eV, $\nu_{ei} \simeq 1130$ Hz which means $\eta_p \simeq 40$ mΩ·m and, hence, $\tau_d \simeq 880$ μs.

As Equation (4.31) indicates, the interaction between inductive and resistive effects determines the diffusion of the plasma return current. *Chen* [1984] states that τ_d can also be considered as essentially the time it takes for the magnetic–field energy to be dissipated in the plasma by Joule heating. Initially, the plasma return current is distributed such that the inductance is minimized, *i.e.*, it is localized to the region nearest to the wire. At later times, the plasma current spreads itself to minimize the resistance. At all times, however, the net plasma return current must equal the wire current, only the spatial distribution of this return current changes with time. When the wire current is modulated at a frequency $\omega \gg 2\pi/\tau_d$, the return current will remain localized; however, some of the current will be dissipated.

[15] Another way of considering the diffusion is as the spreading of the plasma return current; this is discussed in more detail in Section 4.4.1. See §6.4 in *Chen* [1984] for a derivation of the magnetic diffusion time and §12.6 in *Humphries* [1990] for a derivation of the current decay time, similar concepts developed via different methods.

Another proposed loss mechanism from current–carrying wires in magnetoplasmas is electron–whistler–wave radiation [*Stenzel and Urrutia*, 1990; *Stenzel et al.*, 1993; *Urrutia et al.*, 1994]. Over the years, Stenzel and Urrutia have performed many experimental investigations regarding current closure in plasmas in what has been termed the electron magnetohydrodynamic (EMHD) regime [*Kingsep et al.*, 1990]. EMHD is the limiting case of multicomponent MHD in which ion motion can be neglected and electron motion maintains quasineutrality. In addition, in this regime the electrons are fully magnetized while the ion–cyclotron effects are negligible due to the short time scales ($1/\omega_{ce} \ll t \ll 1/\omega_{ci}$) and/or small spatial scales ($r_{ce} \ll L_s \ll r_{ci}$) involved [*Stenzel et al.*, 1993]. One of the characteristic properties of EMHD is the transport of magnetic fields by currents which may strongly supplement diffusion when considering penetration of an external magnetic field into a plasma [*Kingsep et al.*, 1990].

Both of these loss mechanisms and their impact on the model developed here are discussed more in Section 4.4.1.

4.2.2.3 Magnetic Field Surrounding Current–Carrying Wire

The magnetic field in the region surrounding the tether can be found via application of Ampère's Law in integral form, which is written

$$\oint_C \mathbf{H} \cdot d\mathbf{l} = \int_S \mathbf{j} \cdot d\mathbf{S} = I. \tag{4.32}$$

For a long cylindrical wire (ideally infinite) carrying a current I_w, the H–field is symmetric and φ–directed,

$$\mathbf{H} = \frac{I_w}{2\pi r}\hat{\varphi}. \tag{4.33}$$

Thus, for the geometry shown in Figure 4.9, the H–field is[16]

$$H_\varphi \simeq 0 \text{ for } 0 < r < r_a \tag{4.34}$$

and

$$H_\varphi = \frac{I_w}{2\pi r} \text{ for } r_a < r < r_{\text{sh}}. \tag{4.35}$$

The electron return current is carried in the region $r_{\text{sh}} < r < r_c$, where $r_c = r_{\text{sh}} + \delta_m$ and we assume that the current density is constant throughout this shell.[17] That is, we assume a *volume* return current and not simply a *surface* return current as is typically assumed for coaxial transmission lines. The total return current through the radius r is then simply the product of the return current density j_e described in Section 4.2.2.2 above and the area $\pi(r^2 - r_{\text{sh}}^2)$. Since the total electron return current must equal I_w, then $j_e\pi(r_c^2 - r_{\text{sh}}^2) = I_w$. The H–field in this region can then also be determined via Equation (4.32), yielding

$$2\pi r H_\varphi = I_w - I_w \left(\frac{\pi r^2 - \pi r_{\text{sh}}^2}{\pi r_c^2 - \pi r_{\text{sh}}^2} \right),$$

which can be rewritten as

$$H_\varphi = \frac{I_w}{2\pi r} \left(\frac{r_c^2 - r^2}{r_c^2 - r_{\text{sh}}^2} \right) \text{ for } r_{\text{sh}} < r < r_c. \tag{4.36}$$

Finally,

$$H_\varphi \simeq 0 \text{ for } r > r_c \tag{4.37}$$

---

[16]We make the approximation $H_\varphi \simeq 0$ for $0 < r < r_a$ since we are dealing with RF, not DC, currents. At RF, the currents are confined to the skin depth of the wire. Another way of looking at this is that the external inductance we derive here is much larger than the internal inductance of the wire. Hence, we can ignore this component.

[17]For planar geometry, the area under the current–density curve (the total current density) with a skin depth of δ_m is found to be equal to

$$\int_0^\infty |j_{ez}|dx = \int_0^\infty j_{ez0} \exp(-x/\delta_m)dx = -\delta_m j_{ez0} \exp(-x/\delta_m)\Big|_0^\infty = \delta_m j_{ez0}.$$

That is, one can assume that the current density maintains a constant j_{ez0} to a depth equal to a skin depth and zero thereafter [*Balanis*, 1989, pp. 209–210].

since all wire current is canceled by electron return current flowing in the return–current shell. Thus, the complete equation for H_φ valid for $r = 0 \to \infty$ is

$$H_\varphi = \frac{I_w}{2\pi r} \times \begin{cases} 0, & 0 < r < r_a \\ 1, & r_a < r < r_{\text{sh}} \\ \left(\dfrac{r_c^2 - r^2}{r_c^2 - r_{\text{sh}}^2}\right), & r_{\text{sh}} < r < r_c \\ 0, & r > r_c. \end{cases} \tag{4.38}$$

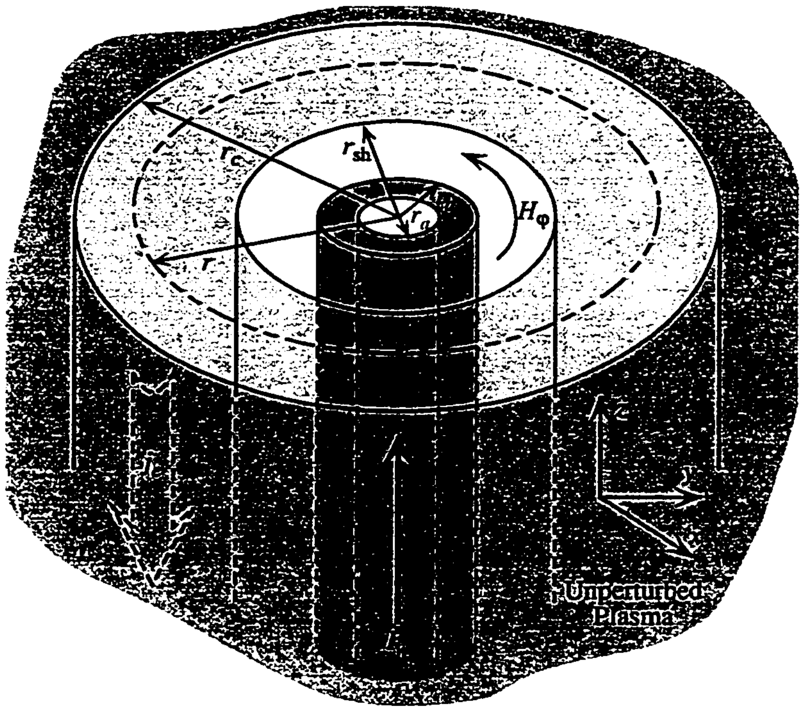

Figure 4.9: Simplified geometry for deriving the inductance of the tether in the plasma.

4.2.2.4 Inductance Solution via Stored–Magnetic–Energy Approach

To find the inductance of the system, we begin by finding the magnetic energy, U_H, stored by the system which is given by

$$U_H = \frac{1}{2}\iiint_V \mathbf{B}\cdot\mathbf{H}dV = \frac{1}{2}\iiint_V \mu\mathbf{H}\cdot\mathbf{H}dV. \tag{4.39}$$

Since $U_H = \frac{1}{2}LI^2$, we can determine the inductance per unit length, L, with knowledge of U_H determined from Equation (4.39) above. From the values for H_φ given in Equations (4.38), we see that that magnetic energy stored per unit length is

$$U_H = \underbrace{\frac{1}{2}\mu_0\int_0^{2\pi} d\varphi\int_{r_a}^{r_{\text{sh}}}\frac{I_w^2}{4\pi^2 r}dr}_{U_{\text{sh}}} + \underbrace{\frac{1}{2}\mu_0\int_0^{2\pi} d\varphi\int_{r_{\text{sh}}}^{r_c}\frac{I_w^2}{4\pi^2 r}\left(\frac{r_c^2 - r^2}{r_c^2 - r_{\text{sh}}^2}\right)^2 dr}_{U_c}. \tag{4.40}$$

The first term on the right–hand side of Equation (4.40)—which we labeled U_{sh}—represents the magnetic energy stored in the sheath region. This term evaluates to the usual expression of the magnetic energy stored in a coaxial line with inner radius r_a and outer radius r_{sh}, *i.e.*,

$$U_{\text{sh}} = \frac{\mu_0 I_w^2}{4\pi}\ln\left(\frac{r_{\text{sh}}}{r_a}\right), \tag{4.41}$$

which means that

$$L_{\text{sh}} = \frac{\mu_0}{2\pi}\ln\left(\frac{r_{\text{sh}}}{r_a}\right). \tag{4.42}$$

The second term on the right–hand side of Equation (4.40)—which we labeled U_c—is the portion of the magnetic energy stored in the magnetic skin–depth region, that is, the region from r_{sh} to r_c. The electron return current attenuates the H–field from the wire and limits the extent of the field as was shown in Section 4.2.2.1. This second term evaluates to

$$U_c = \frac{\mu_0 I_w^2}{16\pi}\left[\frac{4r_c^4\ln\left(\frac{r_c}{r_{\text{sh}}}\right) - 3r_c^4 - r_{\text{sh}}^4 + 4r_c^2 r_{\text{sh}}^2}{(r_c^2 + r_{\text{sh}}^2)^2}\right], \tag{4.43}$$

which means that

$$L_c = \frac{\mu_0}{8\pi}\left[\frac{4r_c^4\ln\left(\frac{r_c}{r_{\text{sh}}}\right) - 3r_c^4 - r_{\text{sh}}^4 + 4r_c^2 r_{\text{sh}}^2}{(r_c^2 + r_{\text{sh}}^2)^2}\right]. \tag{4.44}$$

The total inductance is then

$$L = L_{\text{tot}} = \frac{\mu_0}{2\pi}\ln\left(\frac{r_{\text{sh}}}{r_a}\right) + \frac{\mu_0}{8\pi}\left[\frac{4r_c^4\ln\left(\frac{r_c}{r_{\text{sh}}}\right) - 3r_c^4 - r_{\text{sh}}^4 + 4r_c^2 r_{\text{sh}}^2}{(r_c^2 + r_{\text{sh}}^2)^2}\right]. \tag{4.45}$$

For the cylindrical tether geometry, Figure 4.10 plots the per-unit-length sheath inductance, L_{sh}, the return-current inductance contribution, L_c, and the total inductance, L_{tot}, against applied voltage. It is interesting to note that the contributions to L_{tot} from L_{sh} and L_c are approximately complimentary: as L_{sh} increases due to increasing applied voltage (indicating that more of the total stored magnetic energy is contained within the sheath radius), the magnetic energy in the return-current shell decreases. This effect is due to the coaxial system's logarithmic dependence on geometry and the fact that $r_c = \delta_m + r_{\text{sh}} \simeq \delta_m \gg r_a$. This effect lets us write the inductance as approximately

$$L \approx L_{\text{approx}} = \frac{\mu_0}{2\pi}\ln\left(\frac{\delta_m}{2r_a}\right), \tag{4.46}$$

which indicates that the inductance is approximately what would be derived if all return current flowed as a surface current at a radius of $\delta_m/2$. L_{approx} is plotted in Figure 4.10 as well where it is seen that it closely approximates the L_{tot} value.

Finally, Figure 4.10 reveals a very interesting result. That is, the total inductance of the tether system is approximately constant over the entire range of applied voltage. This means is that our circuit model will not require specification of a voltage-dependent inductance, thus greatly simplifying the circuit model. It is expected, however, that dissipative losses will be higher at lower voltages since more magnetic energy is stored in the return current shell and hence subject to the dissipative losses that are described in Section 4.4.1.

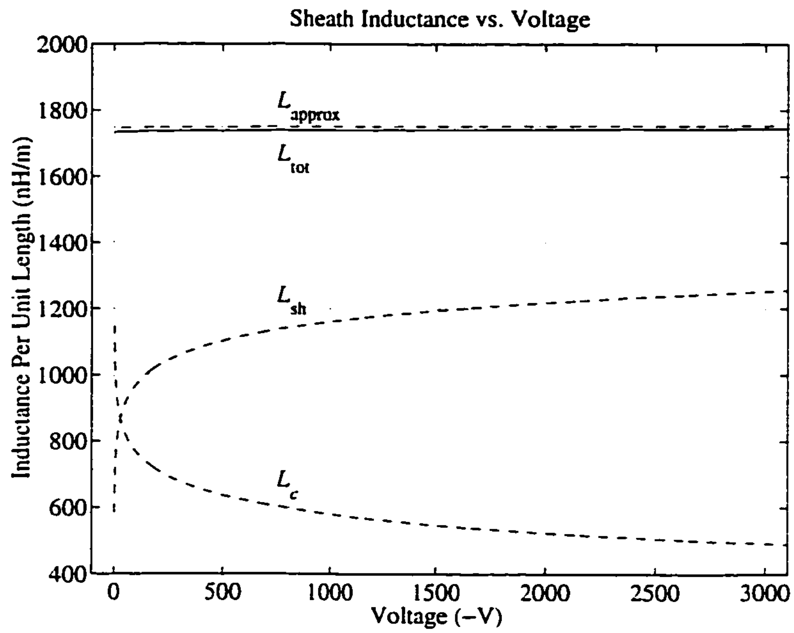

Figure 4.10: Plot of per-unit-length sheath inductance, L_{sh}, return-current contribution, L_c, total inductance, L_{tot}, and inductance approximation, L_{approx}, vs. applied voltage for the cylindrical geometry in an $n_e = 10^{12}$ m^{-3} plasma.

4.2.2.5 Comments on Importance of Inductance Inclusion

The inductance–per–unit–length parameter generally has been neglected in previous transmission–line models of electrodynamic tethers and other plasma–immersed conductors. For example, *Arnold and Dobrowolny* [1980] exclude inductance and so avoid integrating the rate of change of current in their computer model. Although their approach was dynamic, enabling both the transient behavior of the wire and its final equilibrium state to be determined, the model was limited to charging timescales $t \gtrsim 0.1$ ms. *Osmolovsky et al.* [1992] include the inductance term in a generalized description of their model, but then set the inductance parameter to zero before performing calculations. In their case, this was warranted because they were only interested in excitation frequencies $\sim$ 100–1000 Hz.

In general, the absence of an inductance term in these previous models is justified because those models are not concerned with examining electromagnetic–signal propagation effects. In addition, the excitation frequencies employed were low enough (or timescales of interest long enough) such that $R \gg \omega L$. In the model developed here, we must include the inductance term because we wish to examine propagation effects. Also, in our case $R \ll \omega L$ since excitation frequencies fall in the range $\omega_{pe} \gg \omega \gg \omega_{pi}$. Hence, the inductance term is important to the impedance of the line.[18]

4.2.3 Tether Characteristic Impedance and Propagation Velocity

Having developed parameters for capacitance and inductance per unit length, we can calculate the characteristic impedance of and propagation velocity along the tether transmission line. Since the capacitance is a function of voltage, then both impedance and propagation velocity are functions of voltage. The characteristic impedance of a general transmission line is given by the equation

$$Z_0 = \sqrt{\frac{R + j\omega L}{G + j\omega C}}. \tag{4.47}$$

In our case, we assume $G = 0$ (insulated tether), $R \ll \omega L$, and $L =$ constant, in which case Equation (4.47) becomes

$$Z_0(V_a) \simeq \sqrt{\frac{L}{C(V_a)}}. \tag{4.48}$$

Equation (4.48) is plotted in Figure 4.11 for several values of plasma density; the figure clearly shows that as n_e decreases, Z_0 increases. The propagation (phase)

[18]It should be noted that in our model, we assume a constant $R = R_{dc}$, although to be completely correct $R \propto \sqrt{\omega}$ due to the skin depth. However, L will always dominate R in the frequency range $\omega_{pe} \gg \omega \gg \omega_{pi}$.

velocity for a general transmission line is given by

$$v_{\text{prop}} = v_p = \frac{1}{\sqrt{LC}}, \tag{4.49}$$

which, for our transmission line becomes

$$v_{\text{prop}}(V_a) = v_p(V_a) = \frac{1}{\sqrt{LC(V_a)}}. \tag{4.50}$$

Equation (4.50) is plotted in Figure 4.12 for several values of plasma density; the figure clearly shows that as n_e decreases, v_p increases.

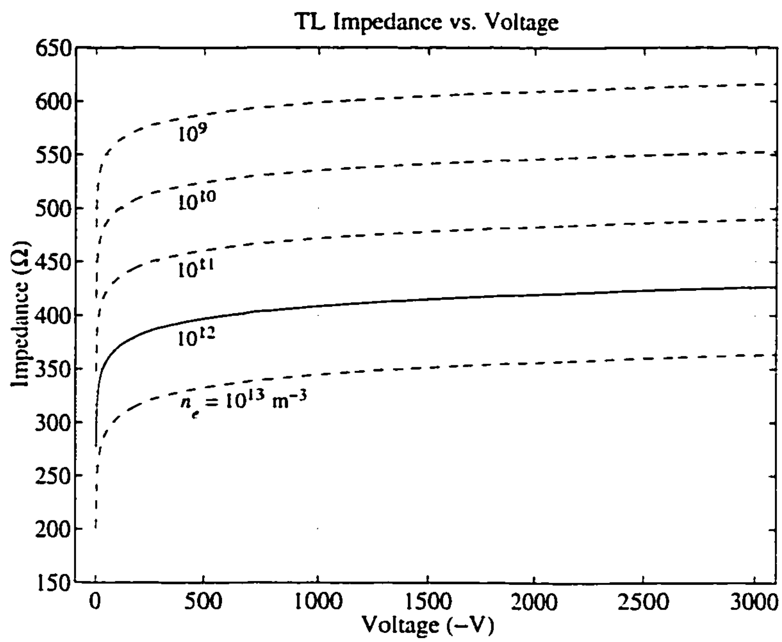

Figure 4.11: Plot of tether transmission–line impedance vs. applied voltage for the cylindrical tether geometry for various plasma densities. Solid line represents an $n_e = 10^{12}$ m^{-3} plasma.

Several other researchers have reported on propagation velocities along plasma–immersed conductors. *James* [1993] experimentally determined a small–signal group speed $v_g = 0.6c \simeq 1.8 \times 10^8$ m/s for sheath waves along the OEDIPUS–A 958–m

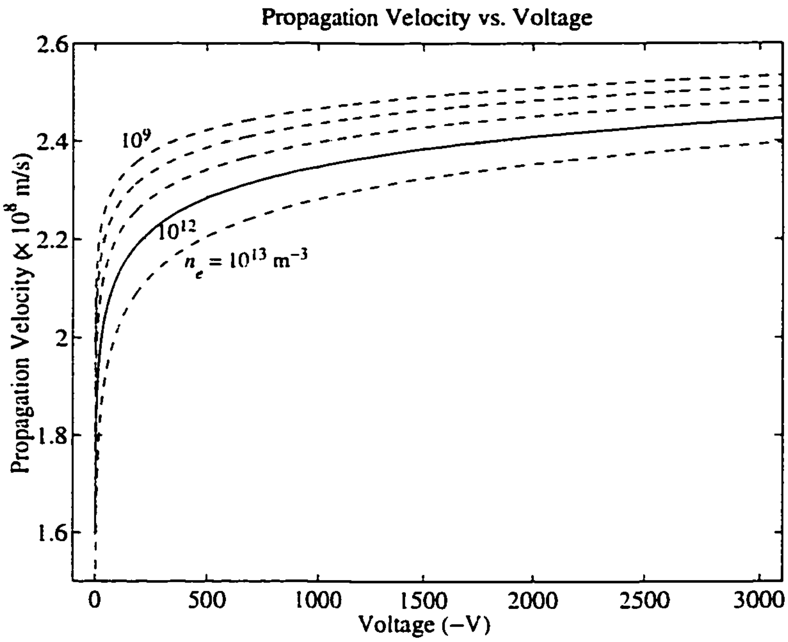

Figure 4.12: Plot of tether transmission–line propagation velocity vs. applied voltage for the cylindrical tether geometry for various plasma densities. Solid line represents an $n_e = 10^{12}$ m^{-3} plasma.

tether (see Section 2.5). This measurement agrees well with the model presented here, given the appropriate parameters for their system: $r_a = 0.26$ mm, $r_d = 0.66$ mm, $r_{\rm sh} = r_a + \lambda_D \sim 1.25$ cm, and $n_e \sim 10^{11}$ m^{-3}. However, unlike the model presented here, their model was based on a voltage–independent (*i.e.*, fixed) sheath distance. They also found the coupling of sheath waves to the tether to be extremely efficient and that, once coupled, the sheath waves propagated with little loss. Sheath waves were observed to reflect several times from either end before damping out.

Stenzel and Urrutia [1990], while not presenting any specific measurements, make the following observations about the propagation speed of switched currents along a magnetic–field–aligned wire in plasma[19]:

[19]Section 4.4.1 discusses in more depth their experiments and results as well as how those results relate to this work. For reference when reading this quote: $n_e \sim 10^{18}$ m^{-3}, $\theta_e \approx 10\theta_i \sim 2$ eV,

"[The propagation speed] is observed to be essentially the same as that in vacuum, $v \leq c$. Conventional transmission line theory predicts that the propagation speed ($v \propto 1/\sqrt{LC}$) [Note: the formula given in their paper contains an error but is given here correctly] is greatly reduced by the high plasma dielectric constant, $\varepsilon_\perp = 1 - \omega_{pe}^2/(\omega^2 - \omega_{ce}^2) \approx \omega_{pe}^2/\omega_{ce}^2$, to $v \approx c/100$. However, the shielding effect prevents the magnetic field B_φ from penetrating rapidly for the short duration of axial current propagation ($\Delta r = \sqrt{t/\mu_0\sigma_\parallel} \approx 5$ mm for $t = (2.5 \text{ m})/c \approx 8$ ns). Thus, the energy flow $\mathbf{E} \times \mathbf{H}$ occurs along the wire surface rather than through the bulk of the plasma, which would have slowed down the propagation speed to that of whistlers. . . ."

It is interesting to note that, while *Stenzel and Urrutia* do not indicate observing a sheath–wave response, they do observe local containment of the magnetic field. This observation suggests that they, too, observed a transmission–line mode localized to the wire.

4.2.4 Comments on Circuit–Model Approximations

One of the more interesting features of the circuit model as developed here is its employment of highly nonlinear, dynamic transmission–line parameters. These parameters resulted from the nonlinear, dynamic nature of the sheath distance which was a function of voltage, $r_{\text{sh}}(V_a)$. For example, in the voltage range $V_a \sim 0$ to -500 V, the total capacitance per unit length for the TSS–tether geometry varies from ~ 23 pF/m to ~ 11 pF/m, and does so in a highly nonlinear manner (see Figure 4.6). In contrast, from -500 to -3000 V, the capacitance decreases only 2 pF/m

$B_0 \sim 10$ G, $l_{\text{wire}} = 2.5$ m.

in an approximately linear manner. This nonlinear capacitance, in turn, causes the transmission-line characteristic impedance also to be nonlinear.

In addition to tether transmission lines, one of the potential applications of this type of circuit-model (as mentioned in Section 1.1.1) is in the analysis of the spatial variation of potential along electrically long plasma-processing electrodes. For most RF-plasma-processing facilities, it is generally assumed that the instantaneous electrical potential is constant across the electrode surface [*e.g.*, *Raizer et al.*, 1995, chap. 1]. This assumption breaks down as electrode length is increased and higher powers are used since large-amplitude, higher-order harmonics develop along the electrode surface. *Savas and Plavidal* [1988] state that the electrode-plasma system in this case can be treated as a lossy transmission line. Using this approximation, they develop a set of simple approximate formulas for inductance and capacitance per unit length, and hence for wave velocity. Without providing any justification for their derivations, they base their capacitance formula on the sheath thickness and inductance formula on the magnetic skin depth as we have done here. This model allows them to predict potential variations on the electrode surface layer that are larger than have been assumed previously. In addition, their preliminary measurements showed potential variations along the electrode's length for all frequency components, which is in agreement with their predictive model. *Stevens et al.* [1996] performed experiments to examine the RF skin-depth effect in ICRF plasmas. Specifically, they addressed the question of how RF fields propagate along the plasma-electrode surface and whether that propagation affects the bias uniformity. They found the RF wavelength and phase velocity along the electrode surface to be reduced by a factor of ~ 5 compared to free space; thus, in certain situations the bias uniformity could be affected. Their formulation, however, was based on Trivelpiece-Gould modes

[*Trivelpiece and Gould*, 1959] which are space–charge waves.

4.3 Tether Incremental Circuit Model

Having demonstrated that we can define both a capacitance and an inductance per unit length for the plasma–immersed conductor, we now set about developing an incremental circuit model of the electrodynamic tether. This model is shown in Figure 4.13 and consists of the elements R, L, E, C_d, R_p, $C_{\text{sh}}(V_{\text{sh}})$, and $j_{\text{sh}}(V_{\text{sh}})$ per unit length, Δz. The values for R, L, E, C_d, and R_p are fixed values which are either measured or calculated. The remaining two, $C_{\text{sh}}(V_{\text{sh}})$, and $j_{\text{sh}}(V_{\text{sh}})$, are varying parameters which we describe in more detail below. We also describe R_p, a heretofore unmentioned fixed parameter.

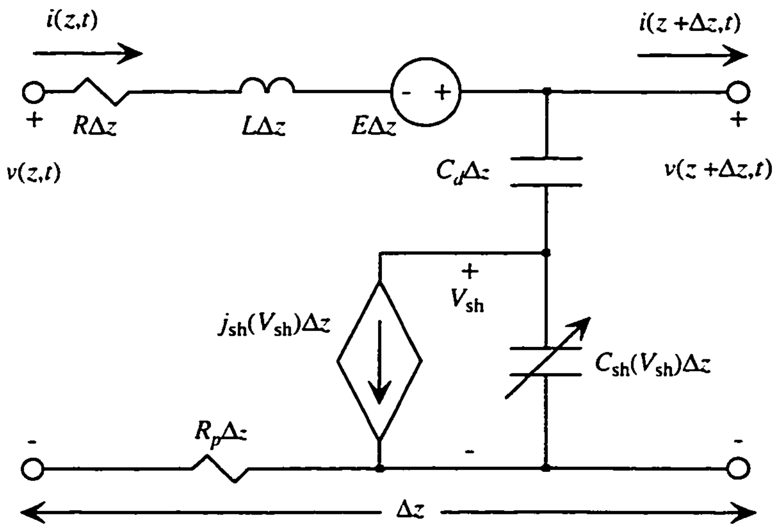

Figure 4.13: Tether incremental circuit model which shows R, L, E, C_d, R_p, $C_{\text{sh}}(V_{\text{sh}})$, and $j_{\text{sh}}(V_{\text{sh}})$ per unit length, Δz.

Up until this point, we have been concerned with the nonlinear sheath capacitance as a function of the applied potential, V_a, and not the sheath potential, V_{sh}, as shown in the figure. For an insulated tether, such as the TSS tether, the sheath capacitance is a function of the V_{sh} because a "charged–up" dielectric will shield the conductor voltage. That is, in the steady state, the sheath is collapsed since there is no voltage across it; all voltage appears across the dielectric (*cf.* Sections 2.2.4 and 3.3.6.2 on sheath collapse). When the sheath has collapsed, it is generally at a distance on the order of 1–3 Debye lengths away from the conductor. As mentioned in Section 2.4, different researchers give different values depending on the ratio r_a/λ_D and other factors. In this model, we assume a minimum sheath distance, $r_{sh,min} \simeq 2\lambda_D$.

The other varying parameter we have included in the circuit model is a current–per–unit–length term that also depends on sheath voltage. The functional form of this term is determined by the timescale of interest. Since we have confined ourselves to $\tau_{pe} \ll \tau \ll \tau_{pi}$, we are only interested in electron current because on this timescale, electrons can redistribute themselves but ions are motionless. Hence, electron current can be collected but not ion current.[20] The functional form for this term is that of Equation (2.18), *i.e.*, OML current collection. Technically, OML collection is valid only when $|V_a| \gg kq/T_e$ and electron collection has a different functional form for smaller values of V_a.[21] This effect only occurs over a very small region and, as such, is ignored—an approximation made by others [*e.g.*, *Morrison et al.*, 1978; *Arnold and Dobrowolny*, 1980]. Since there is no ion current collection, then for $V_{sh} < 0$, $j_{sh} = 0$. As one final point, if we are interested in timescales $\tau \gg \tau_{pi}$ and ignore dynamic–sheath effects, then we should include an OML–collection term for ions. With this inclusion and ignoring inductive effects, the incremental circuit model becomes very similar to that of *Arnold and Dobrowolny* [1980].

[20]There is also a small ion ram current which is not included in the model. See Section 4.4.2 for a discussion of this approximation.

[21]See the description of Langmuir probes in Appendix C which discusses this transition region known as the "electron retardation region."

In Figure 4.13, the resistance per unit length, R_p, resulting from the plasma's specific resistivity is included in the return (bottom) leg of the incremental circuit. The plasma resistance, however, is much less than the wire's per-unit-length ohmic resistance, R. To show this, we estimate R_p's value via the usual manner of determining resistance from a specific resistance, in which we use the electron return-current area for cross-sectional area, *i.e.*, $A \sim \pi\delta_m$ for $\delta_m^2 \gg r_{\rm sh}$, which yields

$$R_p \sim \frac{\eta_p}{\pi\delta_m^2}. \tag{4.51}$$

For the parameters given in Sections 4.2.2.2 and 4.2.2.4, $R_p \sim 0.5$ mΩ/m $\ll R \sim 0.1$ Ω/m. Hence, the resistive losses due to R will dominate those due to R_p.

4.4 Circuit–Model Nonidealities

The circuit–model approximation we have developed here has several nonidealities due to assumptions or approximations made. In this section we cover these nonidealities and state qualitatively what their effect is on the model as developed. The assumptions and/or simplifications leading to nonidealities include 1) no radiation losses, 2) stationary ions, and 3) no ponderomotive effects. Left as future work is a determination of the exact effect that these assumptions have on the model as well as possible enhancements to minimize or remove these nonidealities.

4.4.1 Magnetic–Field Dissipation and Radiation Effects

Although we have assumed an unmagnetized plasma to this point, it is important to address the issues present with external magnetic fields since the ionosphere is actually a magnetoplasma due to the presence of the geomagnetic field, $\mathbf{B}_E$ (Section 2.1.4). In addition, electrodynamic tethers generally utilize the geomagnetic field to generate motional $\mathbf{v}_s \times \mathbf{B}_E$ *emf* along the tether, and thus desire as an optimal configuration that motion is across field lines, although some tether systems prefer field–aligned configurations.

4.4.1.1 Experimental Work on Pulsed Currents in Magnetoplasmas

In a series of laboratory experiments, *Stenzel and Urrutia* examined the temporal and spatial response of the plasma and EM–fields due to pulsed currents along wires immersed in magnetoplasmas [*Stenzel and Urrutia*, 1990; *Stenzel et al.*, 1992, 1993; *Urrutia et al.*, 1994]. Their work was directed toward understanding the concept of magnetoplasma current closure in the EMHD regime. Their experiments were inherently AC due to the pulsed nature of the current, but they applied their results to DC–current–carrying tethers via the method of linear superposition, which they claim is valid when plasma parameters are not significantly perturbed by the injection and collection of current. Some researchers, however, have questioned the pulsed–electrode approach as not fully simulating the steady motion of a DC current system [*e.g.*, *Donohue*, 1991].

Stenzel and Urrutia [1990] make some very interesting claims about time–varying currents to conductors in plasmas. They claim that pulsed currents, either to an electrode or to an insulated wire, penetrate into the plasma at the characteristic group velocity of a whistler wave packet, $v_g = 2c\sqrt{\omega\omega_{ce}/\omega_{pe}^2}$ for $\omega \ll \omega_{ce}$. The implication of this is that time–varying currents are carried by *waves* and not by *particles* as would be inferred from probe theory. The current front propagates at the speed of electron whistlers even when slower ions are collected to negatively biased electrodes.

When applied to insulated wires (*i.e.*, tethers), their results show fundamental differences in plasma response depending on the wire's orientation with respect to the magnetic field. When the wire is oriented parallel to the external magnetic field (Figure 4.14a), diffusion effects dominate the plasma response, whereas when the wire is oriented perpendicular to the field (Figure 4.14b), wave propagation dominates [*Stenzel and Urrutia*, 1990]. Hence, for an arbitrary orientation with respect to the magnetic field, both radiative and dissipative losses can occur.

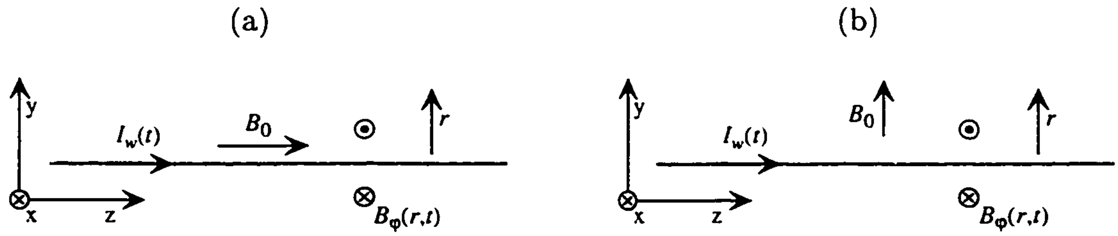

Figure 4.14: Geometry of an insulated wire carrying a pulsed current $I_w(t)$ with wire (a) oriented parallel to the magnetic field and (b) perpendicular to the magnetic field. In both cases, motion of wire is in the $+x$–direction.

We begin by examining the configuration of a wire oriented parallel to the external magnetic field as is shown in Figure 4.14a. In this orientation, magnetic–diffusion effects dominate. When a pulsed current is applied to the wire, a φ–directed (azimuthal) magnetic field develops around the wire. However, the time variation of the field slows down at increasing radial distances from the wire as determined by the diffusion equation, the solution of which was used to define the magnetic–diffusion time, τ_d, in Section 4.2.2.2. The diffusion effect is shown graphically in Figure 4.15, in which it can be seen that the risetimes of the wire's B–field increase at larger distances from the wire indicating that the B–field is diffusing into the plasma.

The penetration of the B–field into the plasma is impeded by induced shielding currents, which are shown in Figure 4.16. These currents can be found by the

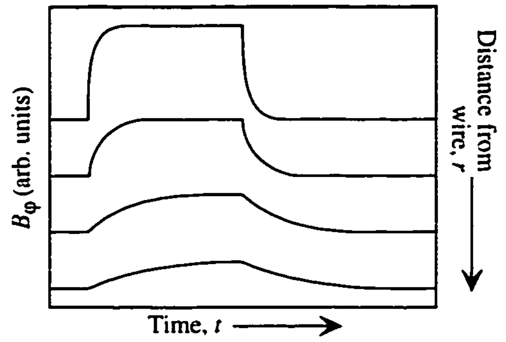

Figure 4.15: Time variation of the azimuthal magnetic field $B_\varphi(t)$ from a current-carrying wire in a plasma at increasing distances from the wire. The magnetic field diffuses radially into the plasma as seen by the increasing risetimes at increasing distances. Adapted from *Stenzel et al.* [1993].

following equation,

$$\mathbf{j}(r,t) = \frac{1}{\mu_0}\nabla\mathbf{B} = \frac{1}{\mu_0 r}\frac{\partial r B_\varphi}{r}. \tag{4.52}$$

As implied in Figure 4.16, the current density is distributed in a shell around the wire (this shell–like behavior was utilized in the inductance derivation of Section 4.2.2.3 and is shown graphically in Figure 4.9). Although initially localized close to the wire, the current spreads radially and decays in magnitude as time increases. The shielding current is of the same magnitude but oppositely directed during switch–on and switch–off of the wire current. During switch–on, the shielding current impedes the field penetration and during switch–off it slows down the rapid decay of the field (Lenz' Law).

Figure 4.17 shows the magnetic field $B_\varphi(r)$ produced by the plasma currents at different times after the wire current has been switched off. This field, which represents stored magnetic energy, is dissipated by ohmic losses $\mathbf{j}\cdot\mathbf{E} = \sigma_\parallel j_{ez}^2$, where $\sigma_\parallel = 1/\eta_\parallel$ is the Spitzer conductivity. This energy is lost and as such does not couple

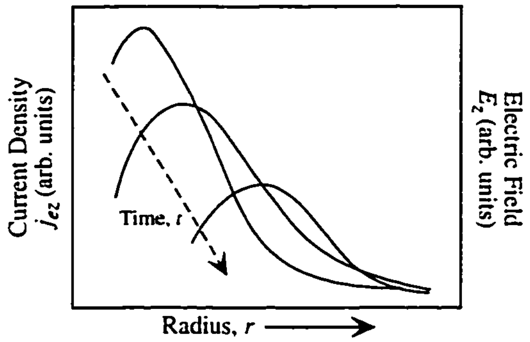

Figure 4.16: Induced axial plasma current $j_{ez}(r)$ flowing in a shell parallel to the wire plotted at different times after wire current is switched on or off (current direction will be in opposite directions). The current diffuses radially outward in time. The induced electric field $E_z(r, t)$ can be calculated via Ohm's Law $j_{ez} = \sigma_{\parallel} E_z$. Adapted from *Stenzel et al.* [1993].

back into the wire.

The second configuration we examine is that of the wire oriented perpendicular to the external magnetic field (Figure 4.14b). In this orientation, whistler–wave–radiation effects are claimed to dominate over resistive losses. When a pulsed current is applied to the wire, a φ–directed (azimuthal) magnetic field develops around the wire as in the parallel case. In this configuration, however, the shielding currents do not diffuse resistively as with the parallel case; rather, they couple to a propagating wave. This wave was identified by *Stenzel and Urrutia* [1990] as a whistler wave. Figure 4.18a shows the B_x field components[22] at a fixed distance from the wire. The plasma (B_{plas}), vacuum (B_{vac}), and difference terms ($\Delta B = B_{\text{plas}} - B_{\text{vac}}$) are plotted as a function of time. Figure 4.18b plots an expanded–time view of the ΔB_x–term at increasing distances from the wire, clearly showing a wave–like disturbance

[22] B_x represents the x–directed component of B_φ if one is moving along the y–axis (see Figure 4.14b).

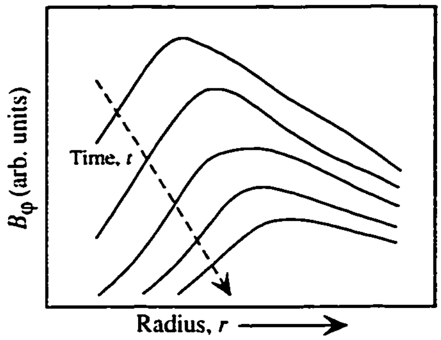

Figure 4.17: Radial profile of the azimuthal magnetic field $B_\varphi(r)$ at different times after wire current is switched off. The stored magnetic energy is dissipated in the plasma as Joule heating. Adapted from *Stenzel et al.* [1993].

propagating from the wire, which is claimed to be at whistler–wave group velocities. The wave was seen to have a nearly constant group velocity and weak amplitude decay.

4.4.1.2 Implications for the Circuit Model

The experimental work of *Stenzel and Urrutia* overviewed in the above section has several implications for the circuit model as developed. For a tether arbitrarily oriented with respect to the magnetic field, both dissipative and radiative losses can occur. The dissipative losses result from the conversion of the wire's magnetic field into Joule heat and occur when the tether is oriented parallel to $\mathbf{B}_E$. When oriented perpendicular to $\mathbf{B}_E$, then radiative losses can occur as magnetic–field energy propagates away from the tether.

In our circuit model, we have accounted for ohmic losses due to the plasma's resistivity via the R_p parameter but have not included a parameter to account for radiative losses. Although we excluded external–magnetic–field effects for the general

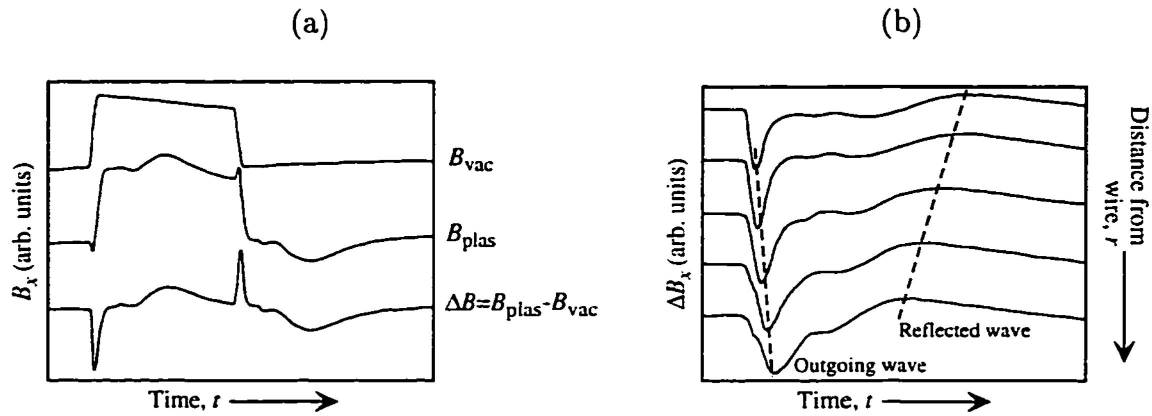

Figure 4.18: Time–varying magnetic field from current pulse along a wire oriented perpendicular to $\mathbf{B}_0$ of a magnetoplasma: (a) transient field $\Delta B = B_{\text{plas}} - B_{\text{vac}}$ caused by induced plasma currents, (b) transient field ΔB_x at increasing distances from the wire showing wave–like propagation characteristics. Also seen is the dispersed reflected wave. [*Note*: time axis has been expanded from that of (a)]. Adapted from *Stenzel et al.* [1993].

$\mathbf{B}_E$ orientation, the inclusion of ohmic losses in our model has actually anticipated the case of parallel orientation with $\sigma_{\|} \to \sigma_p = 1/\eta_p$. The radiative losses, on the other hand, have not been included since the radiation resistance is not known.[23] The total loss would include the effects of both dissipative and radiative losses.

[23]It may be possible to determine an upper bound for radiation resistance by considering the tether as a traveling-wave antenna in the limiting case, *i.e.*, when the transmission-line mode breaks down. In this case the radiation resistance can be calculated from equations given by *Walter* [1965] for traveling-wave antennas. There are two basic types of traveling-wave antennas, an unterminated line (standing-wave distribution) and the terminated line (wave antenna). The unterminated line more closely approximates our case, for which the total radiation resistance, R_r, of a low-loss line is given by the following equation

$$R_r = 72.45 + 30\ln(2L_a/\lambda) - 30\mathrm{Ci}(4\pi L_a/\lambda)\ \Omega \simeq 72.45 + 30\ln(2L_a/\lambda)\ \Omega \text{ for } L_a \gg \lambda,$$

where Ci is the cosine integral. This equation applies only at frequencies for which the antenna is an integral number of half wavelengths. At intermediate frequencies, R_r follows a curve which oscillates above and below the resonant values [*Stratton*, 1941, p. 444]. In any case, the value of R_r due to whistler-wave radiation is likely to be different.

4.4.2 Flowing– vs. Stationary–Ion Assumption

The stationary–ion assumption implies that no ions are collected to the tether. In reality, there is at times an ion ram current that is collected by the tether due to the mesothermal ions flowing past the tether and impinging on the tether surface. However, the term is very small since there is (relatively) no sheath–enhancement factor to increase their effective collection area; only the surface area of the tether facing the ram direction will collect current. The level of this ion ram current is $j_{ir} \simeq 2q_i r_d n_i v_s \approx 3.0\ \mu\mathrm{A/m}$ for an $n_e = 10^{12}\ \mathrm{m}^{-3}$ plasma, but it is only present when the ion–matrix sheath is formed by electrons moving away from the conductor due to applied voltage. This is so because, without the applied voltage, electrons are readily collected to neutralize these collected ions in order that the dielectric does not charge up.

4.4.3 Ponderomotive Effects

The electrostatic force due to the voltage applied to the conductor is not the only force experienced by the electrons. In an oscillating nonuniform field, electrons also experience what is called the "ponderomotive force", denoted $\mathbf{F}_P$, which for a single electron is given by the following equation [*Chen*, 1984]

$$\mathbf{F}_P = -\frac{1}{4}\frac{q^2}{m_e\omega^2}\nabla(E^2), \tag{4.53}$$

where E is the amplitude of the sinusoidal field oscillation. This force is nonlinear and tends to push electrons outward in an oscillating E–field. This outward force results from the following mechanism. As they oscillate, the electrons move farther in the half cycle when they are moving from a strong–field region to a weak–field region than vice versa; hence, there is a net drift.

For pulse excitation with pulse length $\tau_a \gg \tau_{pe}$, this force does not exist since there is no continuous sinusoidal oscillations excited at the sheath edge. For the rapidly applied pulse, *i.e.*, pulse risetime $\tau_{ar} \ll \tau_{pe}$, the sheath edge will oscillate as shown in Section 3.2.4. Hence, this force can provide a significant contribution to the total force felt by the electron and, in particular, when it is near the electrode [*Calder et al.*, 1993]. For RF excitation, the sheath edge oscillates as well and so the ponderomotive force is expected to aid in pushing the electrons further out. For the RF case, *Laframboise et al.* [1975] state that since this force is expressed as a gradient of the E-field, its presence is equivalent to adding a term $V_a = (q/4m_e\omega^2)E^2$ to the static potential seen by the electrons. However, their results were based on the assumption that $\omega \gg \omega_{pe}$, so it is unclear exactly how the force affects electrons in the range $\omega \ll \omega_{pe}$. Examination of the effect of the ponderomotive force is left as future work.

4.4.4 Other Effects

There are several other simplifying assumptions used in the derivation of the circuit model which should be examined as future research. For example, the electrons in the return current shell are not unmagnetized as assumed in Section 4.2.2.1, but magnetized primarily by $\mathbf{B}_E$.[24] This effect was ignored—and, hence, the generalized Ohm's Law [*Chen*, 1984] not used—in the derivation of the return current's spatial and temporal variation (Section 4.2.2.2). In addition, the effect of the geomagnetic field and any $\mathbf{E} \times \mathbf{B}_E$ drifts of the electrons was ignored. As another example, the assumption of constant current in the return-current shell could be made more realistic by specifying a nonuniform distribution. Such a modification would change the

[24]The magnetic field from the wire's current for most realizable currents is generally below the geomagnetic-field level in the return current shell.

inductance value slightly, but the approximation of constant inductance will most likely hold reasonably well.

CHAPTER V

Circuit–Model Simulations and Applications

In this chapter we discuss the SPICE implementation of the incremental circuit model as developed in the previous chapter and the results of the SPICE simulations. We use the example of the TSS tether for our model implementation; however, the model can be readily applied to other conductor and tether geometries through the proper determination of equivalent parameters. We begin with a material description of the TSS tether, which we use to derive the per–unit–length circuit parameters needed. We then discuss in detail the model's implementation in SPICE and the results of the simulations for various excitations. We finish with some of the potential applications of the circuit model.

5.1 Circuit Model for TSS Tether

In this section, we describe in detail the electrical properties of the TSS tether. Since these circuit-model parameters depend on the material properties and the geometry of the TSS tether, we present a description of the tether first and then a description of each of the per–unit–length parameters for this incremental model.

5.1.1 TSS Tether Description

The TSS tether was manufactured for Lockheed–Martin Corporation[1] by the Cortland Cable Company of New York and consists of a Nomex®core that is wrapped with 10 strands of 34–AWG (0.16–mm) copper wire.[2] The copper wires are covered with a layer of clear Teflon®FEP (0.305–mm thick), a layer of Kevlar®29 which acts as a strength member, and finally an outer layer of Nomex braid[3] (Figure 5.1a and b). The outer radius of the tether, r_d, is 1.27 mm and the radius of an equivalent center conductor, r_a, is 0.43 mm [*Martin Marietta*, 1992; *Bonifazi et al.*, 1994].

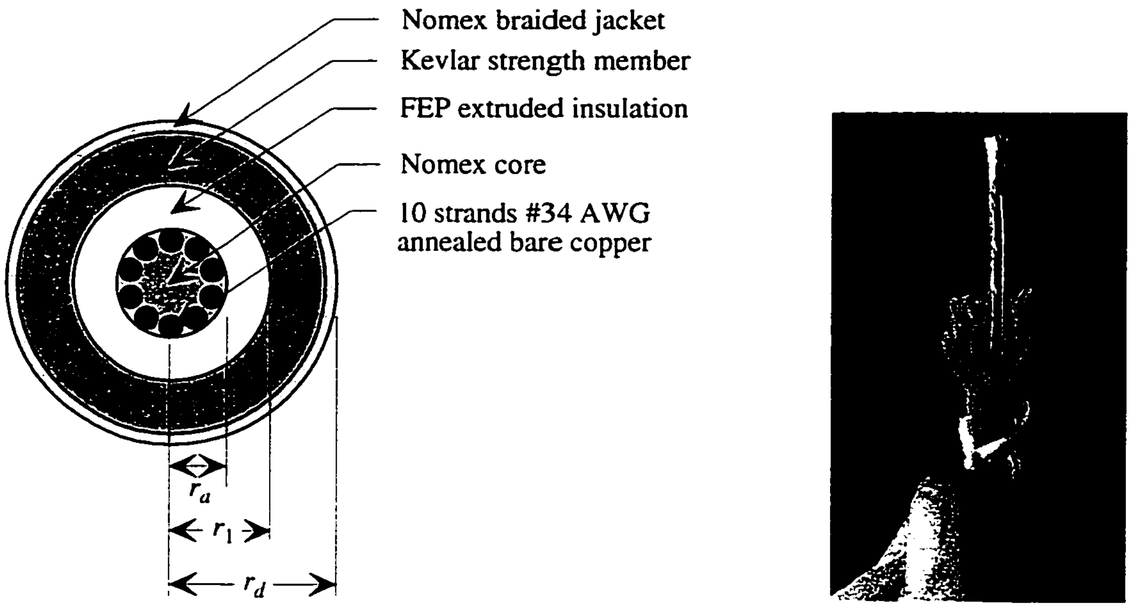

(a) (b)

Figure 5.1: The Tethered Satellite System (TSS) insulated, conducting tether: (a) cross–sectional view showing material makeup, (b) photograph showing construction (NASA photograph).

[1] At the time the tether was delivered they were called the Martin–Marietta Corporation.
[2] For our model, we approximate the twisted conductors as a solid conductor shell.
[3] Nomex®, Teflon®, and Kevlar®are DuPont registered trademarks.

5.1.2 Per–Unit–Length Circuit Parameters

For the insulated–tether geometry, the incremental circuit model presented in Section 4.3 and shown in Figure 4.13 consists of the elements R, L, E, C_d, R_p, $C_{\text{sh}}(V_{\text{sh}})$, and $j_{\text{sh}}(V_{\text{sh}})$ per unit length, Δz. As mentioned previously, the values for R, L, E, C_d, and R_p are fixed values that are either measured or calculated and $C_{\text{sh}}(V_{\text{sh}})$ and $j_{\text{sh}}(V_{\text{sh}})$ are parameters that vary with sheath voltage. In this section we give values for these parameters with the assumption, when required, of an $n_e = 10^{12}$ m^{-3}, $T_e = 1160$ K ionospheric plasma. The values for the parameters are summarized in Table 5.1 at the end of the section.

The resistance–per–unit–length parameter is a measured quantity. The DC resistance of the tether was measured as $R = 0.103$ Ω/m at 20 °C [*Bilén et al.*, 1994].

The value for the inductance–per–unit–length parameter is given by Equation (4.46). For the tether in the ionosphere, $L \simeq 1750$ nH/m.

The parameter for the *emf* generated per unit length is $E = -|\mathbf{v}_s \times \mathbf{B}_E|$. As described in Section 2.3.1, the TSS system experienced the following conditions: $v_s \simeq 7.3$ km/s in the reference frame of the Earth's rotation and $B_E \sim 35000$ nT (from Table A.1 in Appendix A) while the included angle between the velocity and magnetic vectors varied in a roughly sinusoidal fashion due to the 28.5° orbital inclination. TSS–1 achieved a peak potential just under −60 V at the 267–m tether length (−0.22 V/m). At the longer 19.7–km deployment of TSS–1R, this potential was close to −3500 V (−0.18 V/m). We have chosen a value of −0.2 V/m as being representative of the *emf* levels achieved.

The parameter for dielectric capacitance per unit length is calculated from the tether's geometry and an assumption about the dielectric constant of the materials of which it is fabricated. Due to the composite structure of the tether, ε_r is not uniform throughout the dielectric coating. However, we can define an effective permittivity, ε_{eff}, by considering the insulated cylinder system as two capacitors in series, yielding

$$\varepsilon_{\text{eff}} = \frac{\varepsilon_1 \varepsilon_2 \ln\left(\frac{r_d}{r_a}\right)}{\varepsilon_1 \ln\left(\frac{r_d}{r_1}\right) + \varepsilon_2 \ln\left(\frac{r_1}{r_a}\right)},$$

where ε_1 is the relative permittivity in the region $r_a < r < r_1$, r_1 is the distance to the boundary between ε_1 and ε_2, and ε_2 is the relative permittivity in the region $r_1 < r < r_d$. Applying this analysis to the TSS tether with $r_1 \simeq (r_a + r_d)/2$ and the permittivities listed in Table 5.2 we find $\varepsilon_d = \varepsilon_{\text{eff}} \approx 2.5$. Hence, using the standard equation for coaxial capacitance we find $C_d = 128$ pF/m.

The per-unit-length plasma-resistivity parameter is a value calculated from Equation (4.51) given in Section 4.3 and is $R_p \sim \frac{\eta_p}{\pi \delta_m^2} \approx 0.5$ mΩ/m.

The per-unit-length sheath-capacitance parameter is calculated as a coaxial capacitor with an inner radius at r_d and outer radius at r_{sh}. The outer radius, however, is a function of sheath voltage, V_{sh}, with the functional form given in Equation (3.37). Hence, the sheath capacitance can be written as a function of sheath voltage, *i.e.*,

$$C_{\text{sh}}(r_{\text{sh}}) = \frac{2\pi\varepsilon_0}{\ln\left(\frac{r_{\text{sh}}}{r_d}\right)} \qquad \Longrightarrow \qquad C_{\text{sh}}(V_{\text{sh}}) = \frac{2\pi\varepsilon_0}{\ln\left[\frac{\sqrt{3}}{r_d}\left(\frac{V_{\text{sh}}\varepsilon_0}{q_e n_0}\right)^{5/12} r_a^{1/6}\right]}. \tag{5.1}$$

This equation is valid only when $V_{\text{sh}} < 0$, so the question arises of what to do for values of $V_{\text{sh}} \geq 0$. Also, as stated in Section 3.5, Equation (5.1) is only truly valid for $|V_{\text{sh}}| \gg kT_e/q$, *i.e.*, large sheath voltages. We alleviate both of these issues, however, with the assumption of a minimum sheath distance, $r_{\text{sh,min}} \simeq 2\lambda_D$ (see Section 4.3). Hence, C_{sh} has a maximum value for low voltages by choosing for $r_{\text{sh}} = \max[r_{\text{sh}}(V_{\text{sh}}), r_{\text{sh,min}}]$ and using this value in Equation (5.1). The typical value for sheath capacitance is $C_{\text{sh}}(V_{\text{sh}}) \simeq 134/\ln(6.3|V_{\text{sh}}|)$ pF/m.

The final parameter is the per-unit-length collected electron current, which is also a function of the sheath voltage. This parameter was discussed in Section 4.3 and is calculated from Equation (2.18): $j_{\text{sh}}(V_{\text{sh}}) = -240\sqrt{V_{\text{sh}}}\ \mu\text{A/m}$.

Table 5.1: Tether–transmission–line circuit parameters per unit length. Typical values are given for an $n_e = 10^{12}\ \text{m}^{-3}$, $T_e = 1160$ K ($\theta_e = 0.1$ eV) ionospheric plasma.

Param.	How Determined	Equation	Typical Value
R	measured	—	0.103 Ω/m
L	calculated	$\simeq \frac{\mu_0}{2\pi} \ln\left(\frac{\delta_m}{2r_a}\right)$	1750 nH/m
E	chosen	$= -\lvert \mathbf{v}_s \times \mathbf{B}_E \rvert$	−0.2 V/m
C_d	calculated	$= \frac{2\pi\varepsilon_d}{\ln\left(\frac{r_d}{r_a}\right)}$	128 pF/m
R_p	calculated	$\sim \frac{\eta_p}{\pi\delta_m^2}$	0.5 mΩ/m
$C_{\text{sh}}(V_{\text{sh}})$	calculated	$\simeq \frac{2\pi\varepsilon_0}{\ln\left[\frac{\sqrt{3}}{r_d}\left(\frac{V_{\text{sh}}\varepsilon_0}{q_e n_0}\right)^{5/12} r_a^{1/6}\right]}$, $V_{\text{sh}} < 0$	$134/\ln(6.3\lvert V_{\text{sh}}\rvert)$ pF/m
$j_{\text{sh}}(V_{\text{sh}})$	calculated	$= 2\sqrt{2} r_d n_{e0} q_e v_{te} \sqrt{\frac{qV_{\text{sh}}}{kT_e}}$, $V_{\text{sh}} > 0$	$-240\sqrt{V_{\text{sh}}}\ \mu$A/m

Table 5.2: Relative permittivities of the materials that make up the Tethered Satellite System tether.

Material	Relative Permittivity	References
Nomex®	2.1–2.5	*DuPont* [1992], p. 3; *Shugg* [1995], p. 328
Teflon®	2.1	*DuPont* [1996], p. 11; *Shugg* [1995], p. 142
Kevlar®29	3.3–3.8	*DuPont* [1986], p. 47

5.2 SPICE Implementation of Circuit Model

This section presents the implementation of the circuit model in SPICE, transient simulations run with model, and analysis of the simulation results.

5.2.1 Simulation Setup

Transient simulations of the circuit model were performed using HSPICE (version H96) optimizing analog–circuit–simulation software developed by Meta–Software, Inc., which is similar to the standard Berkeley Simulation Program with Integrated Circuit Emphasis (SPICE).[4] The electrodynamic–tether circuit model was implemented as an HSPICE deck with which transient analyses could be performed. Inputs to the deck included only the following parameters: tether voltage or *emf*, number of tether increments, increment length, plasma density, and initial tether current (used to set source bias voltage). From these few input parameters, all necessary component values were calculated. The HSPICE input deck for these simulations may be found in Section E.1 of Appendix E. Also given in that section is a brief description of the HSPICE version of SPICE.

5.2.1.1 Implementation of Incremental Circuit Model

The incremental length was chosen such that $\Delta z \ll \lambda$ along the tether transmission line. From Figure 4.12 in Section 4.2.3, we see that the slowest expected velocity to be $\sim 1.6 \times 10^8$ m/s, and the highest frequency or frequency component of interest is required to be $f \ll f_{pe}$, which we select as $f \sim 1$ MHz. Hence, $\lambda_{\text{min}} \sim (1.6 \times 10^8$ m/s$)/(10^6$ Hz$) = 160$ m. A choice of 4–m increments for Δz yields a minimum of 40 increments per wavelength. Each section of the transmission line then has its parameter values multiplied by this Δz value.

In Section 5.1.2 above, Table 5.1 lists the per–unit–length circuit parameters

[4] In this section's discussion, we differentiate between functions available in the standard Berkeley SPICE and those that are particular to HSPICE. We do this by using the term "HSPICE" only when the particular feature or function is specific to it, otherwise the term "SPICE" is used. HSPICE can be run in Berkeley SPICE compatibility mode, which allows it to handle standard SPICE decks, but the reverse is not necessarily true.

that make up each of the N incremental lengths. Most of these parameters have a straight-forward implementation in SPICE, but the parameters for $C_{sh}(V_{sh})$ and $j_{sh}(V_{sh})$ utilized HSPICE's `max()` function to ensure that they are realizable over the entire voltage range. This requirement is also explained in Section 5.1.2.

The entire tether circuit is then assembled as a ladder network of N incremental sections as shown in Figure 5.2. This requires assembling sections together in expanding subcircuits (`.subckt`), *i.e.*, the $1000\Delta z$–increment subcircuit is made from ten $100\Delta z$–increment subcircuits, and so on. When started, SPICE expands subcircuits and provides each node with an internal number; the entire circuit is then as if N sections had been laboriously assembled. Because SPICE expands the subcircuits in this manner, the simulations avoid any potential artifacts that a grid–within–grid scheme might cause, such as resonances at each grid level. A transmission–line circuit consisting of $N = 5000$ increments were used, which equates to an 20–km–long tether. This length was chosen for two reasons: 1) 20–km is the length of practical tether systems such as TSS and 2) this length allows the applied pulses and sinusoidal waveforms to be adequately resolved at different sections along the transmission line.

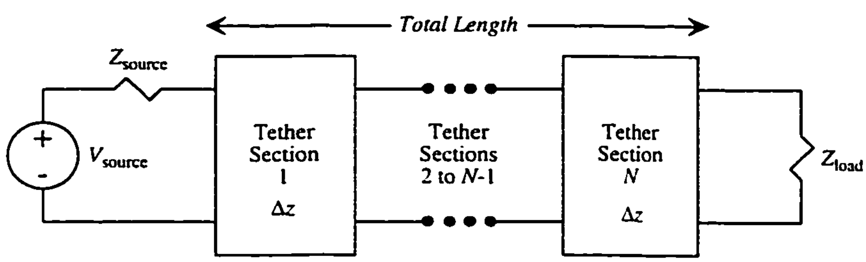

Figure 5.2: Tether circuit model as implemented in SPICE showing ladder network of N Δz increments, source and load impedances, and source voltage.

5.2.1.2 Source and Load Models

For a general tether system, there are several methods for producing tether–voltage modulations, *i.e.*, forced oscillations, which include 1) periodically producing current increases, decreases, or breaks[5]; 2) varying the source and/or load impedances; and 3) changing parameters and control voltages of the contactors and emitters.[6] In addition to the sourcing method employed, the transfer function of the system must also be considered as explained in Appendix D. For a physical system, which would include some type of deployer mechanism, any undeployed insulated tether will provide additional inductance, capacitance, and resistance to the source impedance. Hence, for a system like TSS, which had its sourcing function (in this case a switched load) on the opposite side of a large tether reel from the tether, any pulses launched onto the line were modified due to their travel through the undeployed tether wound on the tether reel. These effects may be minimized in future systems by such methods as placing the switch at the satellite and/or ensuring that the tether is fully deployed with (almost) none remaining on the deployer reel.

For these circuit simulations, we utilize a voltage source controlled by pulse and sinusoidal functions. In addition, we set the bias voltage of the source such that during the entire forcing function, $V_{\mathrm{sh}} < 0$ along the length of the tether. This requires establishing a negligible current ($\sim 1\ \mu$A) in the tether. For our SPICE

[5]The current–breaking method was employed on TSS–1 and the effect of these transients was examined by *Bilén et al.* [1995] (see also Appendix D, Section D.1).

[6]This pulsed–electron method was also employed on TSS–1 and the effect of these transients was examined by *Bilén et al.* [1997] (see also Appendix D, Section D.2). The electron pulses caused the Orbiter's potential to be quickly modified and this technique was the basis of a new Functional Objective (FO13B) implemented for use on TSS–1R. The hope was that by quickly changing the potential of the Orbiter via FPEG emissions, a voltage pulse could be launched along the tether which upon return could be measured by the fast data–collection system on SETS: the current mode monitor (see Section D.1.2 and *Agüero et al.* [1994] for a description of the CMM). Unfortunately, the 3 FO13B's in the timeline were scheduled to run after reaching full deployment. Due to the unfortunate tether break, these experiments were never performed.

model we tie the negative terminal of V_{source} to the ground node. The source and load impedances are set equal to the transmission line's characteristic impedance for zero volts across the sheath, *i.e.*, $Z_{\text{source}} = Z_{\text{load}} = Z_0(0)$. Using this value, of course, means that Z_{source} and Z_{load} are only matched to Z_0 with no voltage across the sheath. When the pulse is launched or when it reaches the other end, reflections will necessarily occur at these terminations, which is a well-known problem for nonlinear-transmission-line simulations [*Carter et al.*, 1995].

5.2.1.3 Numerical-Integration Method

When performing transient simulations with HSPICE (or any SPICE), several choices of integration method are available to the modeler. The choice of which method to use depends on the circuit being simulated, with each method providing slightly different results. The accuracy and stability of the method employed are important factors for how well the result predicts the "correct" solution. In general, at each timestep some finite amount of error is introduced because the numerical-integration algorithm can only approximate the correct solution. The introduced error is a measure of the accuracy of the integration method and is known as the *local truncation error.* The way in which the local truncation error accumulates over time is a measure of the stability of the integration method. For a method to be stable, it must produce a result which closely approximates the actual solution over a large number of timesteps. That is, the method may overestimate the solution at some timesteps and at others underestimate it, but over a large number of timesteps, the integration should closely approximate the solution.

In HSPICE, there are two choices of integration method available: the TRAP (trapezoidal) and the GEAR methods.[7] In general, the TRAP method is more

[7]The Backward-Euler method, which can be considered as a third choice, is available as a subset

accurate and the GEAR method is more stable. The TRAP method tends to be best for simulating most types of electronic circuits (*e.g.*, low–voltage) and is faster than the GEAR method. It would appear, then, that the TRAP method would be the correct one to use. There are, however, two failure mechanisms of the TRAP method which should be mentioned. These are *trapezoidal oscillation*, which occurs when the integration step size is too large to follow the curvature of the given function, and *accumulated error*, which usually occurs in periodic circuits and long transient simulations. The GEAR method, on the other hand, does not suffer from trapezoidal oscillation or accumulated error, but may suffer from local truncation error, especially on circuits with highly nonlinear or switching waveforms. An excellent discussion of the trade–offs and failure mechanisms of the various SPICE integration schemes can be found in Chapter 4 of *Kielkowski* [1994].

We determined that it was necessary to use the GEAR integration method for these transmission–line simulations. This was mainly due to the fact that the TRAP method introduced a nonphysical oscillation in the results. Fortunately, however, in HSPICE the GEAR method uses a local truncation algorithm which provides a higher degree of accuracy and prevents errors from propagating. In addition, timestep reversal is utilized for better accuracy [*Meta–Software*, 1996a]. A description of the GEAR integration scheme may be found in *Gear* [1971a, chap. 11] and its application to network analysis is described in *Gear* [1971b].

5.2.2 SPICE Simulation Results

Similar to the PIC simulations in Section 3.4, for the SPICE simulations we excited the transmission line with pulsed and RF–sinusoidal voltages. The results of these simulations are presented in this section.

---

of the TRAP method since the two formulations are similar.

5.2.2.1 Pulse Excitation

The first set of simulations employed pulse excitation of the transmission line. The applied pulse had the following properties: voltage magnitude across sheath,[8] $V_{sh} \sim -570$ V; $\tau_{ar} = \tau_{ap} = \tau_{af} = 1$ μs. The results of these pulse–excitation simulations are shown in Figures 5.3 and 5.4. The figures plot the sheath voltage, V_{sh}, on linear and log scales and sheath capacitance, C_{sh}, as a function of time for five positions along the transmission line: section $N = 1$ (initial), $N = 1000$, $N = 2000$, $N = 3000$, and $N = 4000$.[9] Every 1000 sections represents 4 km. Note that the time axis increases to the right, which means that signals located more to the right occur *later* in time. Figure 5.3 shows the simulation results for a lossy line which includes R and R_p, whereas Figure 5.4 shows the simulation results for a lossless line where R and $R_p \simeq 0$.

The pulse–excitation simulations show some very interesting results. First, for the lossy case only, the resistance of the conductor adds an RC time constant to the applied pulse. Upon removal of the applied voltage, a residual voltage is still seen across the dielectric and sheath capacitances which takes some time to dissipate through the RC system. This means that even after the applied voltage has been removed, a small voltage appears across the sheath, forcing it to be a larger distance away than if that residual voltage did not exist. This effect is not noticed in the lossless case since there is no resistive losses (*i.e.*, no RC–time–constant effect). Because this voltage can exist for some time, it will have a physical effect on the ions that is not modeled by this implementation since ions are assumed motionless.

[8]Note: the source voltage was approximately twice this, but due to the $Z_0/(Z_0 + Z_{\text{source}})$ voltage divider, the voltage actually placed onto the line was approximately halved.

[9]Section $N = 5000$ is not plotted since that is the section immediately preceding the load. Due to the inevitable impedance mismatch at the load, there will be some non–negligible effect on the waveform at the final section.

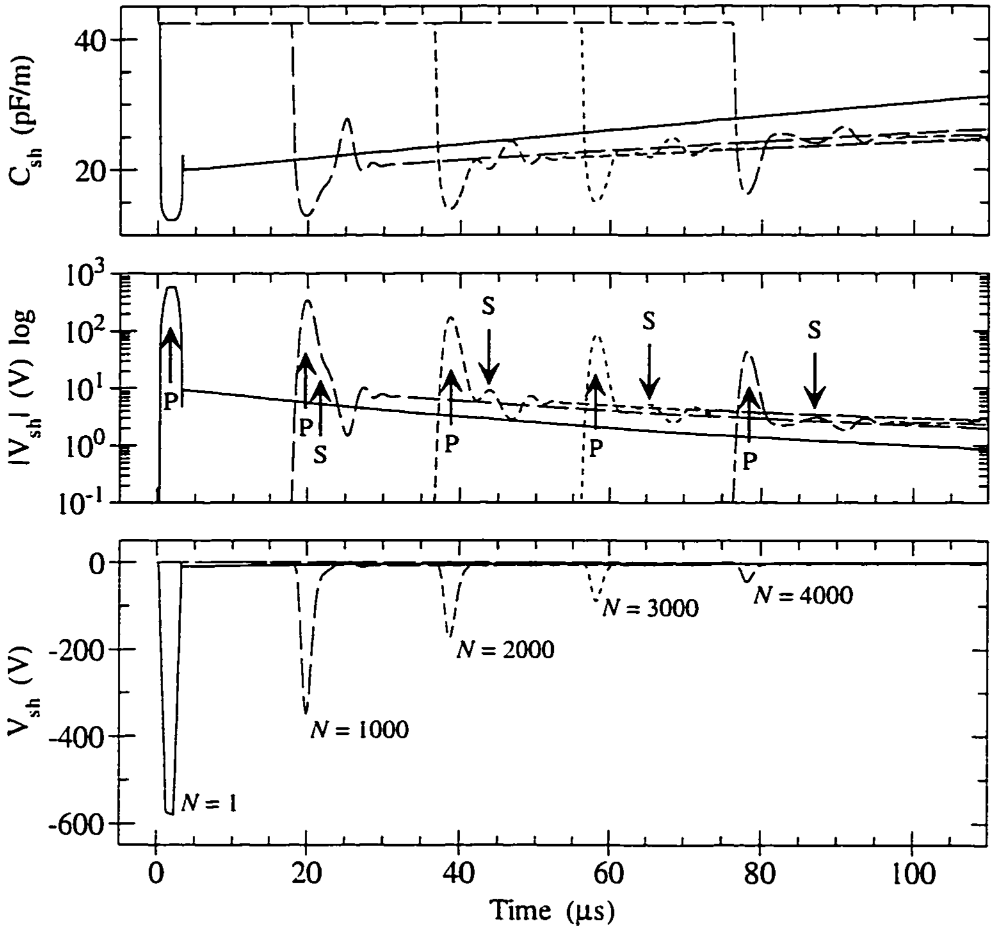

Figure 5.3: Transient SPICE simulation of an excited high–voltage pulse on the lossy tether transmission line. Plotted are the voltage across the sheath, V_{sh}, on linear and log scales and the sheath capacitance, C_{sh}, as a function of time. The five curves represent values at the indicated section number of a 5000–section (20–km) tether transmission line. The progress of the primary pulse is marked with "P", and the evolution and progress of a secondary pulse is marked with "S".

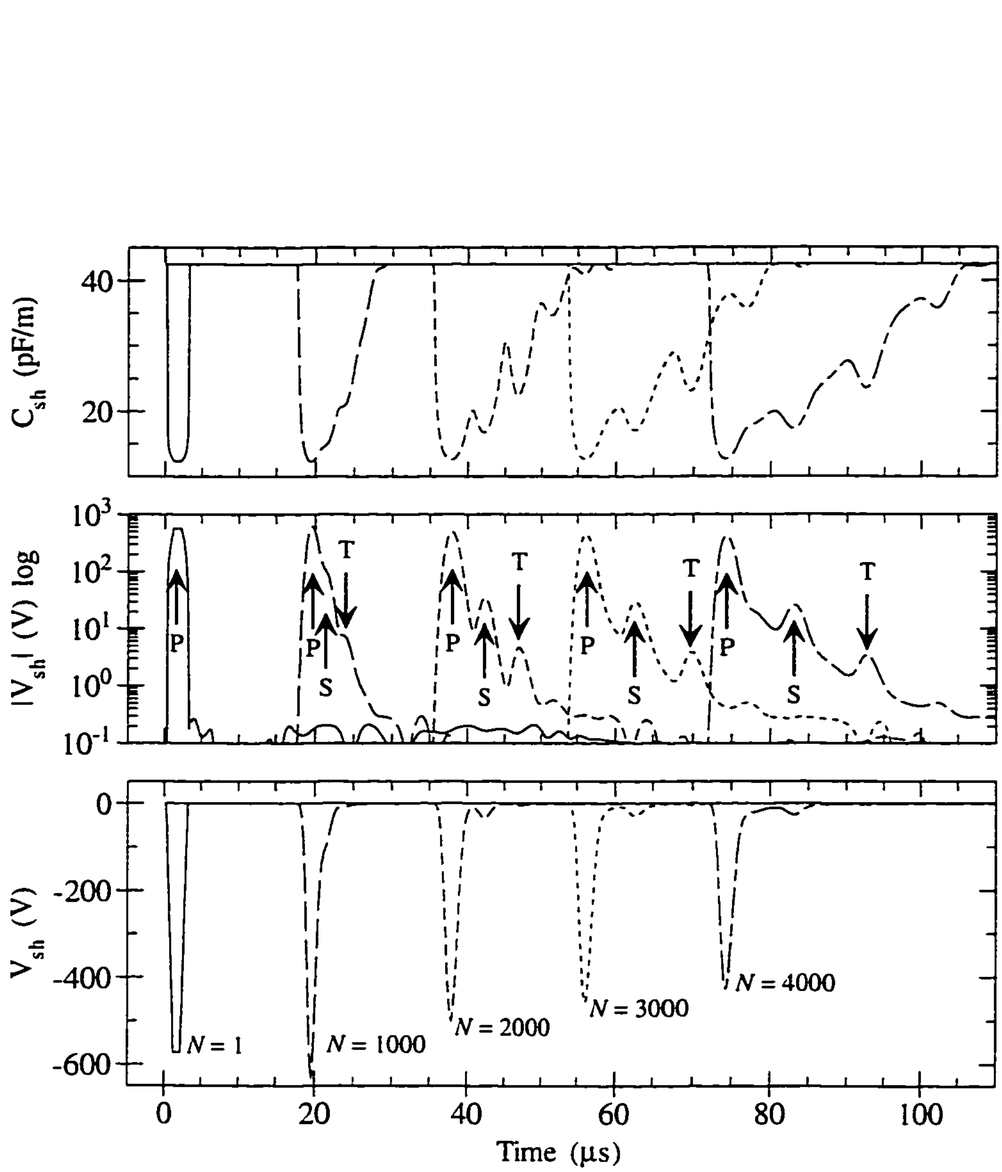

Figure 5.4: Transient SPICE simulation of an excited high–voltage pulse on the lossless tether transmission line. Plotted are the voltage across the sheath, V_{sh}, on linear and log scales and the sheath capacitance, C_{sh}, as a function of time. The five curves represent values at the indicated section number of a 5000–section (20–km) tether transmission line. The progress of the primary pulse is marked with "P", and the evolution and progress of a secondary ("S") and tertiary ("T") pulse are also marked.

Second, for both lossy and lossless cases, the shapes of the curves for the logarithmically plotted $|V_{\mathrm{sh}}|$ and for C_{sh} are very similar. This is to be expected since the sheath capacitance is logarithmically dependent on sheath voltage [*cf.* Equation (5.1)]. The third observation, which is also related to sheath capacitance, is that the nonlinearity of the sheath capacitance is very pronounced; only a small voltage (~ -10 V) needs to be seen across the sheath before its capacitance changes significantly as was shown in Figure 4.6.

Fourth, the width of the primary disturbance (marked "P" for "primary" in the figures) remains approximately the same as it travels the length of the transmission line, although it becomes reduced in magnitude. The amplitude loss is much more pronounced for the lossy case. In addition to the primary pulse, a lower-voltage tail at the trailing edge of the pulse (marked "S" for "secondary" in the figures) begins to form. This secondary pulse can already be seen at section $N = 1000$, but becomes more pronounced at later sections. The secondary pulse is also more pronounced on the lossless line. In addition, on the lossless line we see the formation of a tertiary pulse (marked "T") which propagates at an even slower velocity since its voltage is lower still. The formation of additional pulses is not completely unexpected behavior, since we know that higher voltages travel faster along the line due to their increased propagation velocity as compared to lower voltages. The nonlinear propagation-velocity characteristic of this transmission line is shown in Figure 4.12.

If we determine the propagation velocities of the primary and secondary pulses, we find $v_{\mathrm{prop}} \sim 2.2 \times 10^8$ m/s for the primary and $v_{\mathrm{prop}} \sim 1.8 \times 10^8$ m/s for the secondary. Referring to the values plotted in Figure 4.12, we see that these simulated propagation velocities agree well with the calculated values given that larger voltages constitute the primary pulse and much lower voltages constitute the secondary pulse (and the tertiary, etc., pulses for the lossless case). There are two possible mechanisms for the formation of these additional pulses. The first explanation may simply be that the lower–voltage, lower–frequency components of the initial pulse (*i.e.*, the pulse's Fourier components) are propagating at a slower velocity due to their lower voltage. The second possible explanation is more intriguing. This type of response—that of a pulse breaking apart into two or more pulses—is also noticed on nonlinear transmission lines which admit solitons, as was overviewed in Section 2.6.2. Might the tether allow soliton propagation, at least if it has very low loss? This possibility is very intriguing because it would open up many potential applications because solitons can propagate over long distances with (almost) no distortion. The possibility of soliton propagation along tether transmission lines definitely should receive more attention and should be examined as future work

5.2.2.2 Sinusoidal Excitation

The second type of simulation excited the transmission line with an RF sinusoid that had the following properties: voltage magnitude across sheath, $V_{\rm sh} \sim -1200$ V; $f = 100$ kHz.[10] Figure 5.5 plots the results of this RF–sinusoid–excitation simulation at various points along the lossless line (R and $R_p \simeq 0$). The figure plots the sheath voltage, $V_{\rm sh}$, and sheath capacitance, $C_{\rm sh}$, as a function of time for three positions along the transmission line: sections $N = 1$ (initial), $N = 2000$, and $N = 4000$.

The RF–sinusoidal–excitation simulation shows the very important result that the sinusoidal waveform steepens as it propagates along the transmission line—an effect noticed on many other nonlinear transmission lines (see Figure 2.11). Because of this steepening effect, significant harmonic distortion will be added to any sig-

[10]Strictly speaking, this frequency does not satisfy the criterion $f \gg f_{pi}$. However, there was some attenuation which was much more pronounced at the higher frequencies, so a lower frequency was used here.

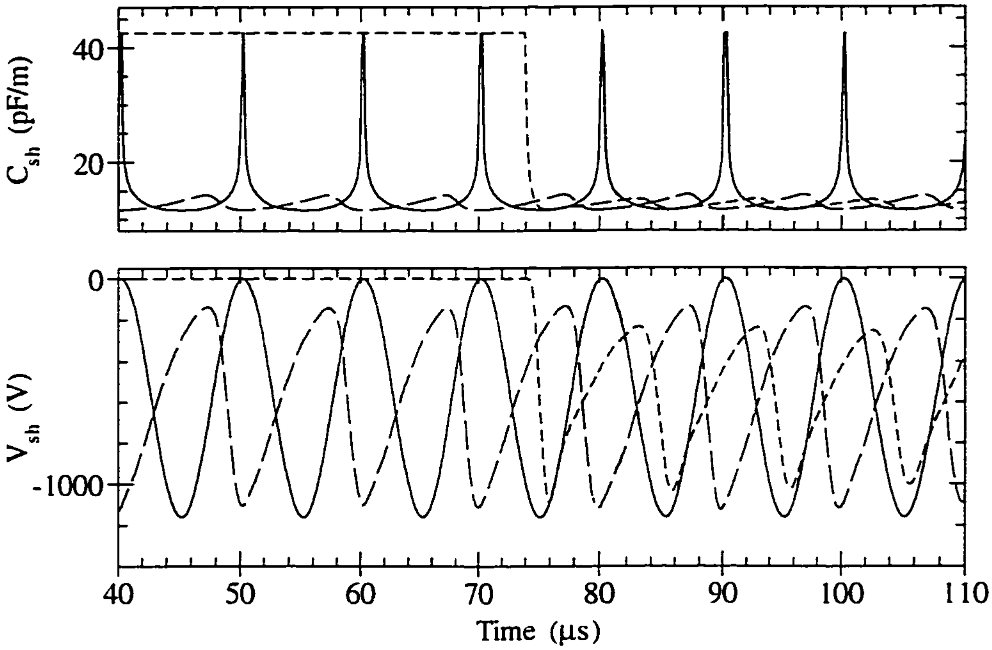

Figure 5.5: Transient SPICE simulation of a high–voltage 100–kHz sinusoid excited on the lossless tether transmission line. Plotted are the voltage across the sheath, V_{sh}, and the sheath capacitance, C_{sh}, as a function of time. The three curves represent values at sections $N = 1$ (initial, solid line), $N = 2000$ (long–dashed), and $N = 4000$ (short–dashed) sections of a 5000–section (20–km) tether transmission line.

nal propagating along the transmission line. An analysis of this added harmonic distortion was made by taking FFTs of the waveform at various points along the transmission line and plotting the energy in the fundamental and the first four harmonics. The results of this analysis are plotted in Figure 5.6. What is seen in Figure 5.6 is that the harmonic amplitudes quickly build up within the first 4 km and then much more slowly thereafter; the energy in the harmonics comes from the energy in the fundamental. This is important information for several reasons: 1) the quick buildup in the harmonics means that for all practical tether lengths, the propagated signal is likely to be distorted; 2) for long tether lengths the distortion builds up much more slowly after the initial buildup. Perhaps this second point suggests that the tether is closer to a soliton line than other nonlinear lines since the steepening to "shock wave" does not occur as quickly as would be expected.

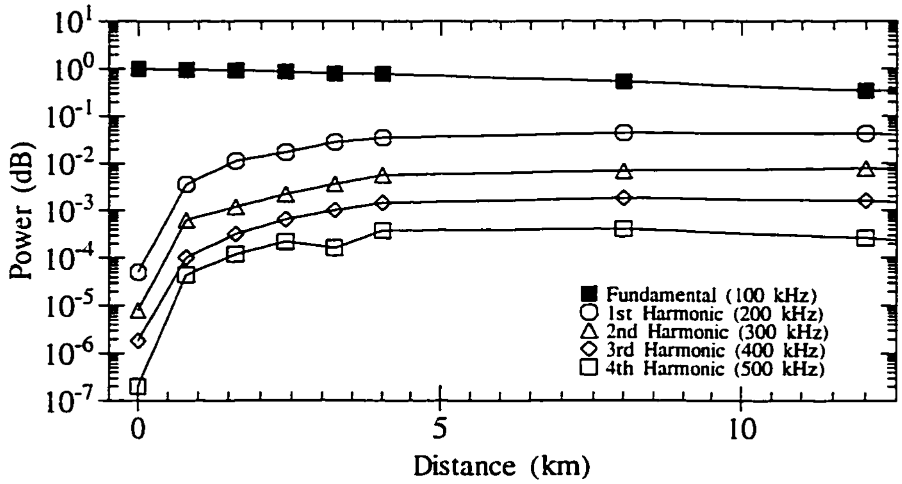

Figure 5.6: FFT–derived powers in the fundamental and first four harmonics of a propagating sinusoid as a function of distance along the tether transmission line.

5.2.3 Comments on Simulation Results

A few comments about the simulations are made here. First, it is not known what effect the sharp cutoff for sheath capacitance has on the overall model. This effect should be examined more closely and perhaps the cutoff smoothed out if justified. In the simulation it was observed that $V_{sh} < 0$ for almost all times, hence $j_{sh}(V_{sh})$ rarely contributed to the functioning of the model. Removing this term from the model reduced computational complexity and the simulation ran faster. Finally, the magnitude of the sheath capacitance's nonlinearity is much larger than that of a typical nonlinear or soliton transmission line.

5.3 Tether Circuit–Model Applications

In this section we briefly discuss some potential applications for and the utility of the circuit model developed. The model developed here can be used to 1) predict time–domain reflectometry responses along the tether transmission line from which it may be possible to reconstruct impedance profiles; 2) predict pulse and waveform propagation morphology; and 3) be implemented together with endpoint models to predict overall tether system responses to various stimuli.

5.3.1 Time–Domain Reflectometry

Time–domain reflectometry (TDR), also sometimes known as pulse reflectometry, is a technique which consists of sending an impulse down a transmission line and recording the reflected energy—the "echo"—as a function of time. The reflected TDR waveform measurement provides insight into the physical structure of the device under test (DUT), which may be the transmission line itself [*e.g.*, *Hsue and Pan*, 1997], devices and parasitics positioned along the length of the line [*e.g.*, *Dascher*, 1996], or devices at the end of the line [*e.g.*, *He et al.*, 1994]. The characteristics of the DUT(s) can be determined from knowledge of both the incident and reflected signals. The TDR technique has the advantage of being able to accurately model nonlinear devices.[11]

The shortest pulse length that can be launched onto this transmission–line model is on the order of τ_a = 1–3 μs for an $n_e = 10^{12}$ m^{-3} plasma. This pulse length, in turn, places a lower limit on the spatial resolution of any TDR measurements. To get a idea for what kind of resolution is possible with a TDR measurement, a 3–μs,

[11]Nowadays, the TDR technique is often accomplished by applying a Fourier transform to frequency–domain data. While the transform technique has found much utility, especially for microwave–circuit measurements, the "old" method of applying an actual pulse continues to find areas of use.

−500–V pulse traveling $\sim 2.3 \times 10^8$ m/s yields a minimum spatial resolution $\gtrsim 700$ m.

Several simulations were run to ascertain if TDR can be used as a novel application of electrodynamic tethers. Figure 5.7 shows one such simulation wherein a pulse was launched along a lossless tether transmission line that had a step discontinuity in plasma density (from $n_e = 10^{12} \rightarrow 10^{10}$ m^{-3}) at section $N = 3000$; the value of Z_{load} was left at the $Z_0(0)$ value of the first portion of the line. Although somewhat artificial, such a situation could occur if the upper half of the tethered system were to fly into a deep density depression with sharply defined features. The simulation results show very clearly two return pulses, the first is due to the change in plasma density at $N = 3000$ and the second is due to the mismatch at the load. Do these reflections make sense in the classic sense of TDR? To answer this, we remember that the reflection coefficient, Γ, at an impedance discontinuity on a transmission line is given by the equation

$$\Gamma = \frac{Z_{\text{load}} - Z_0}{Z_{\text{load}} + Z_0}, \tag{5.2}$$

where Z_{load} is either a load impedance or a new transmission line impedance. (Note: this equation does not take into account the voltage dependencies of the characteristic impedance.) As plasma density decreases, Figure 4.11 shows that Z_0 increases. Hence, at the step change in plasma density we would expect a positive Γ, and indeed the return pulse from this discontinuity is the same polarity. Conversely, at the load we would expect a negative Γ, and indeed the return pulse from the load is positive. This simple demonstration shows that TDR applications along tethers may hold promise for future systems.

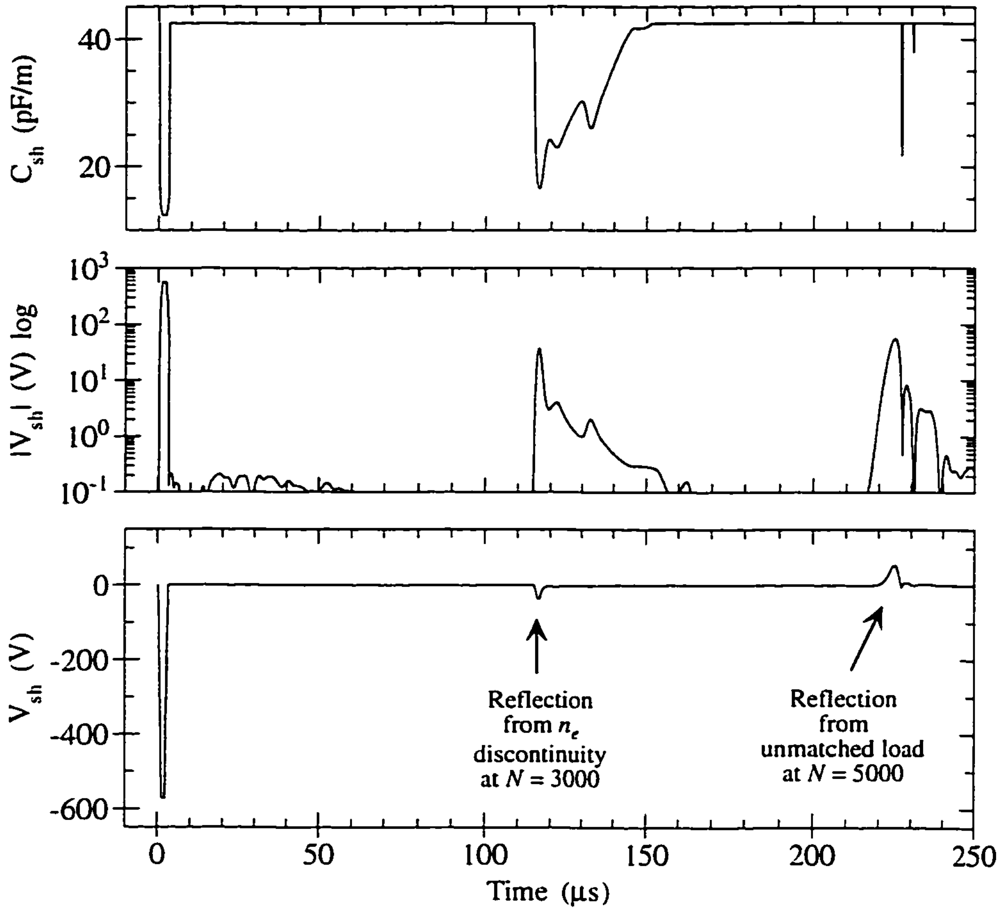

Figure 5.7: Time–domain–reflectometry simulation with a pulse along a lossless tether transmission line that had a step discontinuity in plasma density and a unmatched load impedance.

5.3.2 Predications of Pulse and Signal Morphology

This circuit model promises to have utility for examining the propagation of undesirable high–voltage signals along the lengths of structures in ionospheric plasma. In addition, with signals for which propagation is desired, this model can help to understand and predict the manner in which the signal will mutate from its original shape. Such predictive simulations should help to ascertain, for example, how much harmonic distortion is added to a high–voltage RF signal on the tether. The utility of this model for determination of harmonic–distortion estimation was shown in Section 5.2.2.2.

CHAPTER VI

Conclusions and Recommendations for Future Work

In recent years, long conductors—both bare and insulated—have been flown in the ionosphere as antennas and as integral parts of electrodynamic–tether systems. In the near future, construction of facilities such as the *International Space Station* will make large spacecraft support structures more commonplace. Because these long conductors and structures are surrounded by the ionospheric plasma medium, the plasma–conductor interaction must be taken into account to ensure that the spacecraft operate properly. Unfortunately, to date there has not been much investigation into the physical processes of electromagnetic propagation particular to increased conductor lengths, especially for high–voltage excitation.

6.1 Summary and Conclusions of Research

This research investigated and characterized the general propagation behavior of electromagnetic pulses along conductors in cold, low–density plasmas. As a specific *application*, electrodynamic tethers in the ionosphere were used. As a specific *example*, a TSS–geometry tether transmission line was used. The models developed, however, can be readily extended to other tether geometries, in addition to other plasma–(insulator)–conductor geometries for which the conductor diameter is on the order of or smaller than the Debye length or, alternately, much smaller than the sheath distance. A more involved, but still possible, extension of the model can be made to general conductor geometries including pseudo–planar, which has smaller sheath dimensions in relation to the object dimensions.

This investigation first developed a voltage–dependent sheath model valid in the frequency regime between the electron and ion plasma frequencies and for negative high voltages. The sheath model was developed analytically and verified via plasma–chamber experiments and particle–in–cell computer simulations.

Using this voltage–dependent sheath model, a circuit model was developed for electrodynamic–tether transmission lines that incorporates the high–voltage sheath dynamics. The transmission–line circuit model was implemented with the circuit–simulation program SPICE. Implementing the circuit model in SPICE allows complete tether systems to be modeled by including circuit models of the endpoints (which "launch", or produce, the perturbations on the tether) with the tether model itself. Several different excitation methods were employed and the simulation results analyzed.

6.1.1 Voltage–Dependent Sheath Model

The dynamic–sheath model that was developed is valid in the frequency regime between the electron and ion plasma frequencies, and for large negative applied voltages, $|V_a| \gg kT_e/q$. The sheath model is based on the ion–matrix–sheath radius as a function of applied voltage. In the specified frequency regime, the E–field from the conductor is contained within the sheath region and the sheath model was found to be independent of the presence of conductor insulation. Although an exact equation for ion–matrix–sheath distance is given, a relatively simple approximation to the sheath distance as a function of sheath voltage was derived. Because the approximation is non–transcendental—unlike the exact expression—it was able to be readily applied as the basis of the circuit model developed for use in the SPICE circuit–simulation code.

Qualitative discussions of the sheath's response for frequencies higher and lower than this assumed regime are given as well, although this information was not used in the development of the transmission–line circuit model. However, these discussions do suggest directions for future research.

6.1.2 Tether Transmission–Line Model

The voltage–dependent, dynamic–sheath model developed was used as the basis of a circuit–model approximation of the electrodynamic–tether transmission line valid for HV–pulse and RF–sinusoid excitation. The model assumes that the excitation frequency, or the highest frequency component of interest, falls in the range between the ion and electron plasma frequencies (*i.e.*, $\omega_{pi} \ll \omega \ll \omega_{pe}$). The model of the tether–plasma system that was developed is, in effect, of a "non–static" coaxial transmission line, *i.e.*, a transmission line with voltage dependent ("dynamic") parameters. In the frequency range $\omega_{pi} \ll \omega \ll \omega_{pe}$, the tether's E– and B–fields were shown to be contained locally, which allowed an effective capacitance and inductance per unit length to be defined. The verification of the E–field containment within the sheath region was used to develop the effective sheath capacitance. The effective inductance was developed by showing that the B–field is contained within a larger region that takes into account the location of the plasma return currents. It was found that the capacitance is a highly nonlinear function of sheath voltage but that the inductance remains approximately constant for the parameters of interest to electrodynamic tethers in the ionosphere. These capacitance and inductance parameters were included with per–unit–length resistance and induced–*emf* elements to form the complete lumped–parameter model. Using the TSS–tether geometry as an example, plots for all parameters as a function of sheath voltage are given as well as plots for characteristic impedance and propagation velocity.

The tether circuit model was implemented using the SPICE circuit–simulation program. This implementation was then used to examine the tether's transmission–line characteristics as well as pulse and RF–sinusoidal propagation and morphology. The pulse was seen to propagate at speeds in good agreement with calculated propagation velocities. The input RF–sinusoid waveform was observed to become more steep as it propagated past various section of the transmission line.

6.2 Recommendations for Future Work

Throughout this dissertation, suggestions for future research efforts are given. These suggestions, for the large part, may be categorized into future work related to 1) the voltage–dependent sheath model and 2) the tether transmission–line model.

6.2.1 Future Work Related to Sheath Model

Perhaps the most important limitation of the sheath model is the assumption of excitation frequencies in the range between the ion and electron plasma frequencies. This range allowed an ion–matrix–sheath assumption to be employed in the derivation of the voltage–dependent sheath radius. Extension of the sheath model to lower frequencies (*i.e.*, $\omega \lesssim \omega_{pi}$) would involve determining how the sheath evolves. For most tether geometries, the sheath that evolves is the orbital–motion–limited sheath, for which no currently known rigorous theory of sheath evolution exists.

Theories exist for Child–Langmuir sheath evolution (*cf.* Section 2.2.3). Extension of the model to $\omega \ll \omega_{pi}$ for the insulated conductor would require examining how the dielectric charges and how this shields the conductor's potential. Preliminary research presented herein shows that this could be on the order of several milliseconds. Extension to frequency regimes higher than ω_{pe} would involve inclusion of the ponderomotive force and radiation effects.

The captured dataset from the plasma–chamber experiments was shown to contain many useful and intriguing results. Some portions of the dataset have only been given a cursory analysis because they were beyond the scope of this work or not relevant to the sheath model that was developed. Additional analyses of interest include 1) examination of the sheath collapse times and velocities due to dielectric charging; 2) determination of the mechanism causing the oscillation noted in the biased–probe signal after HV application to the bare cylinder; and 3) examination of the motion of the density depression caused by removal of the insulated conductor's applied voltage and the implication of this motion.

Additional PIC simulations should be performed to examine 1) the temporal and spatial evolution of the OML sheath; 2) dielectric charging and sheath collapse for tether geometries; and 3) the sheath physics around the conductor at orbital velocities using flowing plasmas.

6.2.2 Future Work Related to Transmission–Line Model

With respect to the transmission–line model, the most important efforts remaining involve experimental verification of individual pieces of the model and its assumption of distributed effects. Certain assumptions were employed in this research to make the model distributed. Direct distributed results were not possible for the three reasons mentioned earlier (Section 1.3): 1) Earth–bound experimental chambers are large enough to contain only a few tens of meters of tether transmission line; 2) particle–in–cell simulations of such a system are not possible due to the computational costs of simulating even a few tens of meters; 3) the unfortunate break of the TSS–1R tether before achieving full deployment kept possible measurements of pulse propagation from being performed.

In terms of remaining theoretical analyses, there are several which should be pursued. First, more work should be done concerning the magnetic skin depth and its effect on inductance. The assumption of constant current in the return–current shell could be made more realistic by specifying a nonuniform distribution. Second, the implications for the inductance derivation of magnetized electrons in the return–current shell should be examined. Third, a better bound of the radiation losses present and how to account for them should be determined. This will require determining the nature of the excited waves (*e.g.*, whistlers) and how much of that energy is lost due to radiation.

As a final suggestion for future research, more detailed examinations should be made concerning optimal designs and configurations of electrodynamic–tether systems. These examinations can be quickly made using the SPICE model developed in this research. Many different system can be set up and simulated in a short amount of time. Previously developed models of satellite and Orbiter interactions with the plasma based on Tethered Satellite System mission data can be used with this circuit model as the endpoints of the complete electrodynamic–tether system.

APPENDICES

APPENDIX A

Summary of Ionospheric Parameters

Table A.1 of this appendix summarizes the ionospheric plasma parameters used in this work. These parameters are typical of the ionosphere at approximately 300–km altitude (low Earth orbit). The ionosphere is a good example of a cold, low–density plasma.

Table A.1: Table summarizing typical ionospheric parameters at a low–Earth–orbit altitude of 300–km.

Parameter	Nomenclature	Equation	Typical Value
neutral density	n_e	—	10^{15} m^{-3}
electron density	n_e	—	10^{12} m^{-3}
ion density	n_i	—	10^{12} m^{-3}
electron temperature	T_e	—	1160 K
	θ_e	—	0.1 eV
ion temperature	T_e	—	1160 K
	θ_i	—	0.1 eV
ion mass (O^+: $Z_i = +1$)	m_i	—	2.66×10^{-26} kg
geomagnetic field strength	$\lvert \mathbf{B}_E \rvert = B_E$	see §2.1.4	35000 nT (0.35 G)
electron thermal velocity	v_{te}	$\sqrt{\frac{kT_e}{m_e}}$	1.33×10^5 m/s
ion thermal velocity	v_{ti}	$\sqrt{\frac{kT_i}{m_i}}$	776 m/s
electron plasma freq.	$\omega_{pe} = \omega_p$	$\sqrt{\frac{n_e q^2}{\varepsilon_0 m_e}}$	56.4 Mrad/s
	f_{pe}	$\frac{\omega_{pe}}{2\pi}$	8.98 MHz
ion plasma freq.	ω_{pi}	$\sqrt{\frac{n_i Z_i^2 q^2}{\varepsilon_0 m_i}}$	329 krad/s
	f_{pi}	$\frac{\omega_{pi}}{2\pi}$	52.3 kHz
electron cyclotron freq.	ω_{ce}	$\frac{qB_0}{m_e}$	6.16 Mrad/s
	f_{ce}	$\frac{\omega_{ce}}{2\pi}$	908 kHz
ion cyclotron freq.	ω_{ci}	$\frac{Z_i q B_0}{m_i}$	209 rad/s
	f_{ci}	$\frac{\omega_{ci}}{2\pi}$	33.3 Hz
upper hybrid freq.	ω_{uh}	$\sqrt{\omega_{pe}^2 + \omega_{ce}^2}$	56.7 Mrad/s
	f_{uh}	$\frac{\omega_{uh}}{2\pi}$	9.03 MHz
lower hybrid freq.	ω_{lh}	$\approx \sqrt{\omega_{ce}\omega_{ci}}$	35.9 krad/s
	f_{lh}	$\frac{\omega_{lh}}{2\pi}$	5.71 kHz
Debye length	λ_D	$\sqrt{\frac{\varepsilon_0 k T_e}{q^2 n_e}}$	2.35 mm
electron cyclotron radius	r_{ce}	$\frac{m_e v_{e,\perp}}{qB} = \frac{v_{te}}{\omega_{ce}}$	2.15 cm
ion cyclotron radius	r_{ci}	$\frac{m_i v_{i,\perp}}{qB} = \frac{v_{ti}}{\omega_{ci}}$	3.71 m
plasma parameter	Λ	$12\pi n_e \lambda_D^3$	4.89×10^5
electron–ion collision freq.	ν_{ei}	$\frac{q^4 n_e \ln(\Lambda)}{16\pi\varepsilon_0^2 \sqrt{m_e}(kT_e)^{3/2}}$	1130 Hz

APPENDIX B

The Far–Field Plasma Environment of a Hollow Cathode Assembly

The capability of generating a plasma environment closely resembling that found in the ionosphere is highly desirable to researchers who wish to examine ionospheric–plasma phenomena in a controlled setting. The hollow cathode assembly (HCA) and Michigan Large Chamber Plasma Facility (MLCPF) provide just such a capability. The HCA provides a low–temperature, low–density, fairly uniform plasma in its far–field, and the MLCPF allows ample room such that the effects of plasma confinement—*i.e.*, interaction with the walls and support structures—can be reduced to a minimum.

This appendix shows that the HCA provides, in the far–field, a fairly uniform ionospheric–level plasma environment. The data presented and analyzed in this report were primarily collected over three days (23–25 June 1997) in support of work investigating the temporal evolution of high–voltage (HV) sheaths around insulated and uninsulated conductors in an "ionospheric" plasma (see Section 3.3). The HCA was operated at a total of nine different operating conditions. In this appendix, each of these nine operating conditions is summarized and their corresponding far–field plasma environments analyzed.

B.1 Experimental Apparatus

B.1.1 Plasma Chamber Description

The University of Michigan Plasmadynamics and Electric Propulsion Laboratory (PEPL) has as its centerpiece the Michigan Large Chamber Plasma Facility (MLCPF), a cylindrical, stainless–steel–clad tank which is 9 m long and 6 m in diameter. The MLCPF is the largest vacuum chamber of its kind at any university in the United States. The facility is supported by six 32,000 l/s diffusion pumps backed by two 2000 cfm (56,600 l/s) blowers and four 400 cfm (11,300 l/s) mechanical pumps. These pumps give the facility an overall pumping speed of over 100,000 l/s at 10^{-4} torr.[1] Figure 3.5 (Section 3.3) is a diagram of the MLCPF as it was set up for the HV testing and HCA far–field plasma–environment characterization.

The positioning table, also shown in Figure 3.5, contains two rotary platforms on two transverse linear stages. This setup provides two degrees of freedom as well as angular freedom in the horizontal plane, *i.e.*, radial (x–plane), axial (y–plane), and θ. Altitude (z–plane) is fixed. The entire system is mounted on a movable platform allowing measurements to be made throughout the chamber. The system can sweep two probes at a time at radial speeds in excess of 60 cm/s, with a positioning accuracy of 1 mm.

B.1.2 Hollow Cathode Assembly Description

A hollow cathode assembly (HCA) was used as the source for simulating ionospheric plasma. The HCA created a low temperature plasma ($\theta_e \lesssim 1.5$ eV) by establishing a discharge between a hollow cathode chamber and a positive keeper electrode.

[1] In Winter 1998, the MLCPF underwent a major facilities upgrade: the internal cladding was removed and four nude cryopumps were added. These cryopumps have a combined pumping speed of 300,000 l/s on air and 140,000 l/s on xenon and provide the ability to reach a high–vacuum of 10^{-6} to 10^{-7} torr.

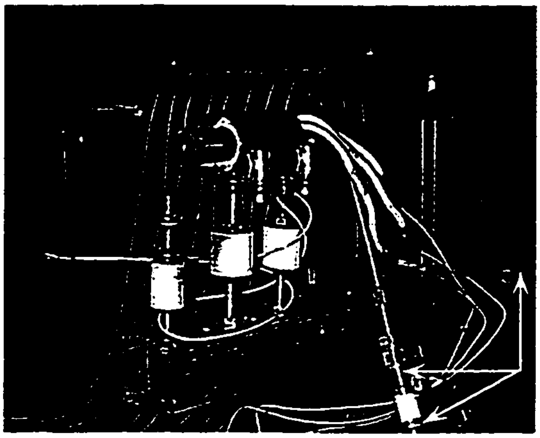

Figure B.1: Picture of the hollow cathode assembly as set up for these experiments.

Plasma density was varied by adjusting the flow rate. Figure B.1 shows a picture of the HCA as it looked during these tests. Table B.1 gives a summary of the nine different HCA operating conditions.

Table B.1: Summary of the operating conditions of the hollow cathode assembly.

Oper. Cond.	Gas	Flowrate, sccm	Discharge Voltage, V	Discharge Current, A	Tank Pressure, $\times 10^{-5}$ torr
1	krypton	10.2	14.8	3.97	4.9
2	krypton	19.2	14.8	3.97	4.9
3	krypton	4.3	19.3	3.97	4.9
4	argon	12.9	17.2	3.97	4.9
5	argon	18.3	15.8	3.97	5.2
6	argon	14.8	16.5	3.97	5.1
7	xenon	2.3	15.5	3.97	4.5
8	xenon	6.9	14.8	3.97	5.2
9	xenon	3.9	17.1	3.97	4.8

The general operation of HCA's has been studied extensively in the literature. An excellent bibliographic reference on hollow cathode discharge research up to 1984 is *Mavrodineanu* [1984]. Several recent works have examined the plasma environment generated by an HCA [*Parks et al.*, 1982; *Gerver et al.*, 1990; *Parks et al.*, 1993; *Conde et al.*, 1997]. Additionally, many works have also investigated interested in the interaction of the HCA plume with an ambient plasma [*Hastings*, 1987; *Parks and Katz*, 1987; *Iess and Dobrowolny*, 1989; *Vannaroni et al.*, 1992], although this is not our case.

B.1.3 Measurement Equipment

The measurement equipment used during the experiments included an electrometer, computer controller, magnetometer, and the aforementioned positioning table. The electrometer was connected via an IEEE–488 bus to a computer controller which set equipment parameters and stored data. A more detailed description of the equipment used and their function is listed below.

Electrometer A Keithley 2410 Source Electrometer was used to drive the Langmuir Probe (LP) system. The electrometer measured the current collected by the LP as it was swept from −20 to 20 V. The LP was positioned via the positioning table. LP measurements were used to determine electron temperatures and number densities of the HCA plasma plume.

Computer Controller An Apple Macintosh Quadra running LabVIEW software from National Instruments was used to set equipment parameters and to store data via an IEEE–488 bus.

Magnetometer The Shuttle Electrodynamic Tether System (SETS) aspect magnetometer (AMAG) was used to determine the orientation and strength of the geomagnetic field present in the plasma chamber. This instrument provides three–axes absolute–field measurements with 468–nT resolution.

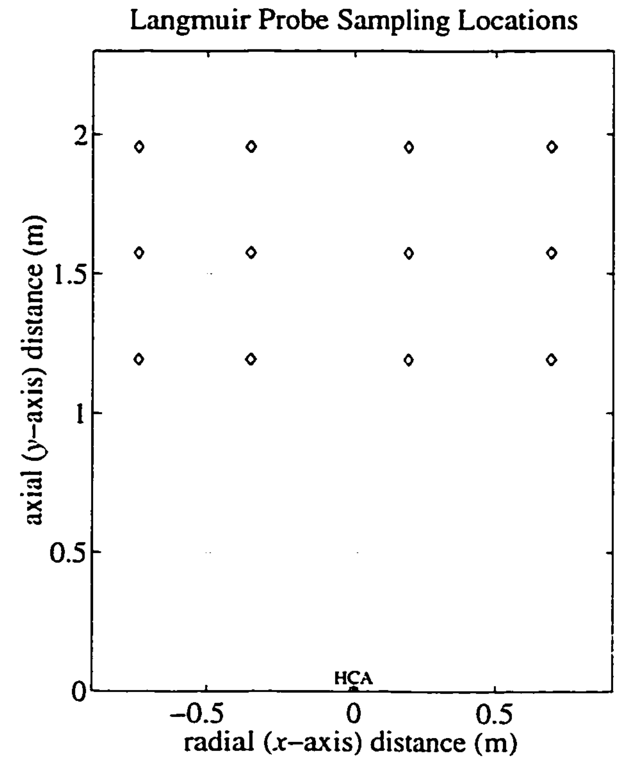

Figure B.2: Locations of the Langmuir probe measurements with respect to the hollow cathode assembly (locations are marked with diamonds).

Positioning Table The positioning table was used to position the LP throughout the far–field region of the HCA plume.

B.1.4 Langmuir Probe Measurement Positions

The Langmuir probe measurements were made at 12 locations throughout the chamber for each of the nine HCA operating conditions. The 12 locations are shown in Figure B.2 as diamonds. The measurement space covers an area of about 1.4 m × 0.7 m, with the closest measurement made about 1.2 m away from the HCA. The measurement space is oriented fairly symmetrically about the axis of the HCA plume. The location of the HCA is at the (0,0) point of Figure B.2.

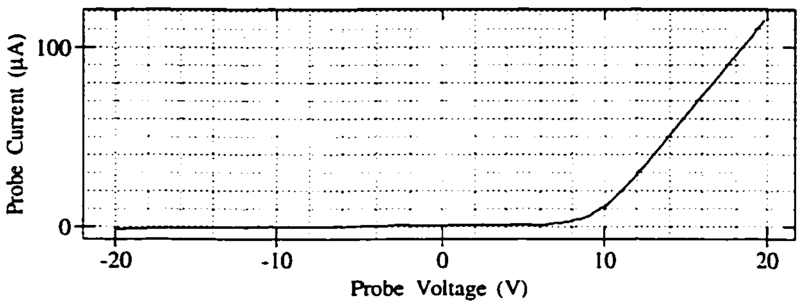

Figure B.3: A sample current–voltage characteristic for the cylindrical Langmuir probe used in this experiment (data is from Condition 7, sample 2, point closest to the HCA—see Figure B.10).

B.2 Experimental Results

B.2.1 Electron Densities

The electron density throughout the measurement region was determined via the Langmuir probe method as outlined in Appendix C. The LP bias voltage was swept from −20 to 20 V in 200 steps and the resulting current was measured via the electrometer. The LP tip was cylindrically–shaped, 48.9–mm long with 3.9–mm diameter, and was mounted on a triaxial boom. A typical I–V characteristic from this experiment is shown in Figure B.3.

Using the n_e values obtained through analysis of the LP data, contour plots of n_e throughout the measurement region were produced for each of the nine HCA operating conditions (see Table B.1). A cubic interpolation of the data collected at the 12 locations provides a smooth estimate of n_e throughout the measurement region. The plots in Figures B.4–B.12 show the electron density in the HCA plume for each of the nine operating conditions. Table B.2 gives a summary of the plasma environment as measured by the LP.

There are some items to note in the data presented in Figures B.4–B.12. First,

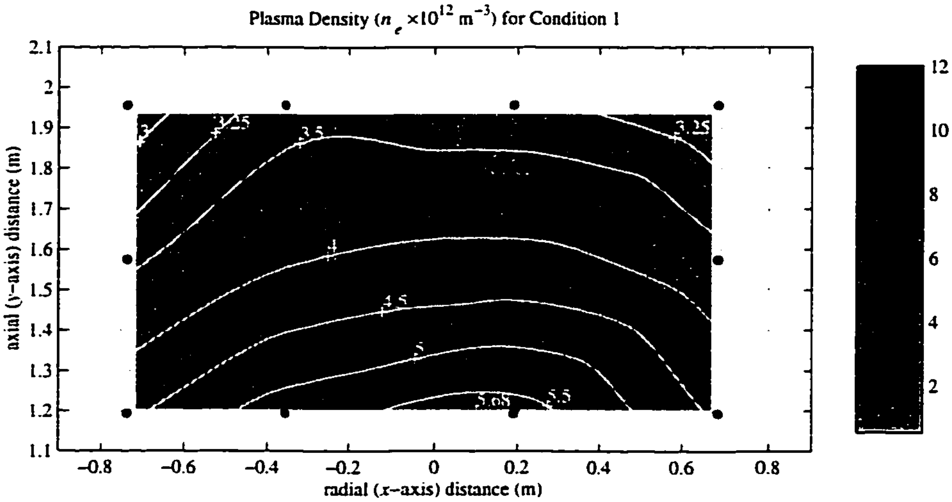

Figure B.4: Spatial distribution of electron density for condition 1.

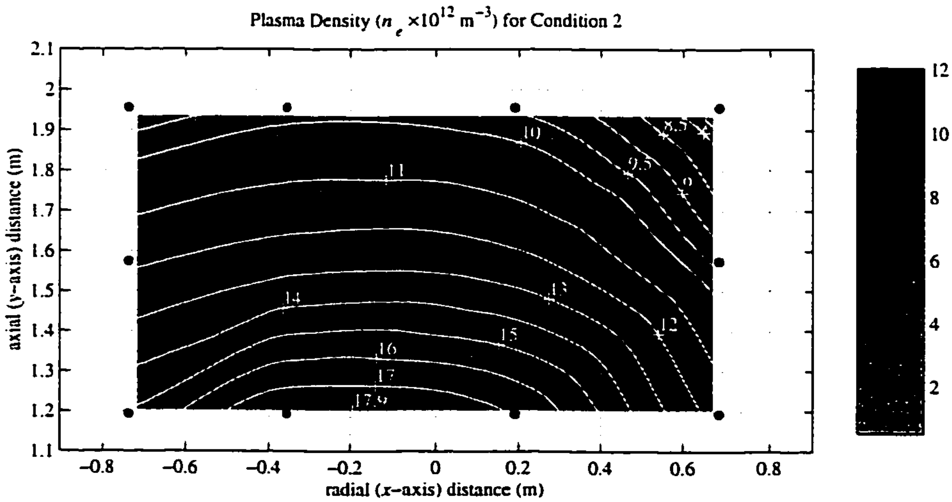

Figure B.5: Spatial distribution of electron density for condition 2.

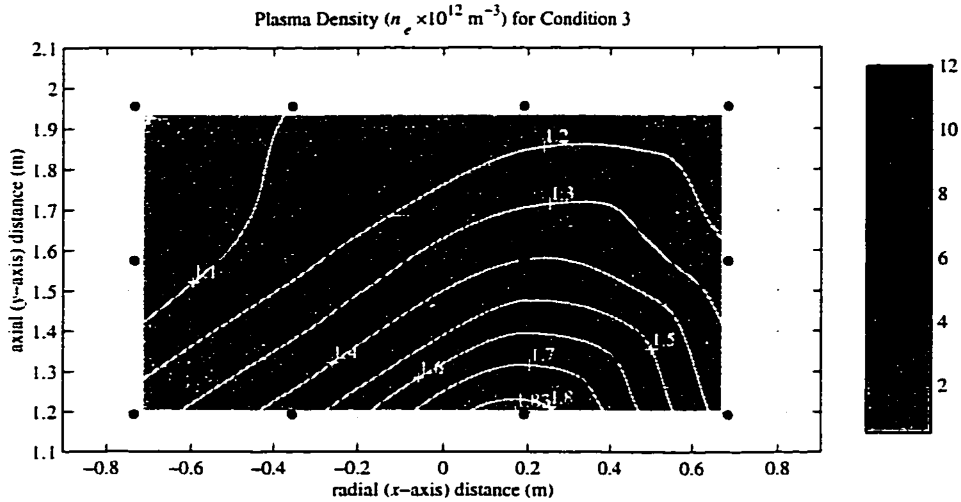

Figure B.6: Spatial distribution of electron density for condition 3.

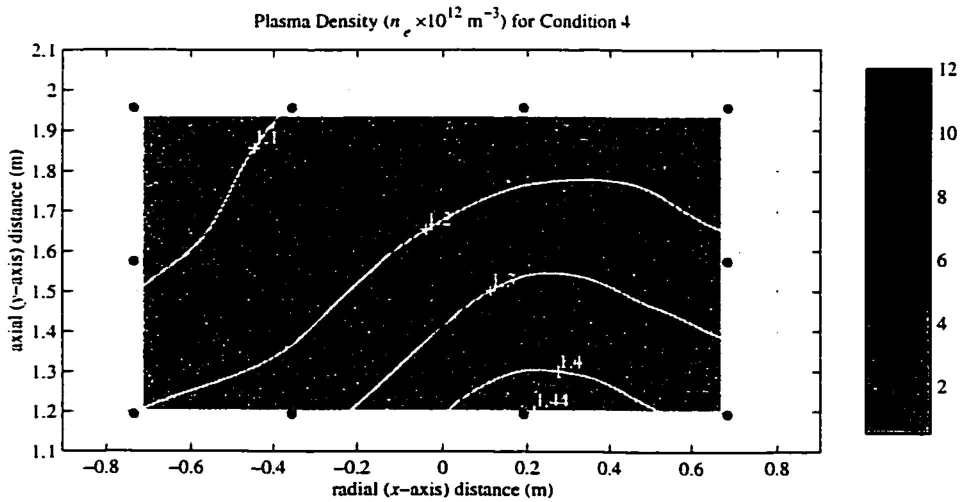

Figure B.7: Spatial distribution of electron density for condition 4.

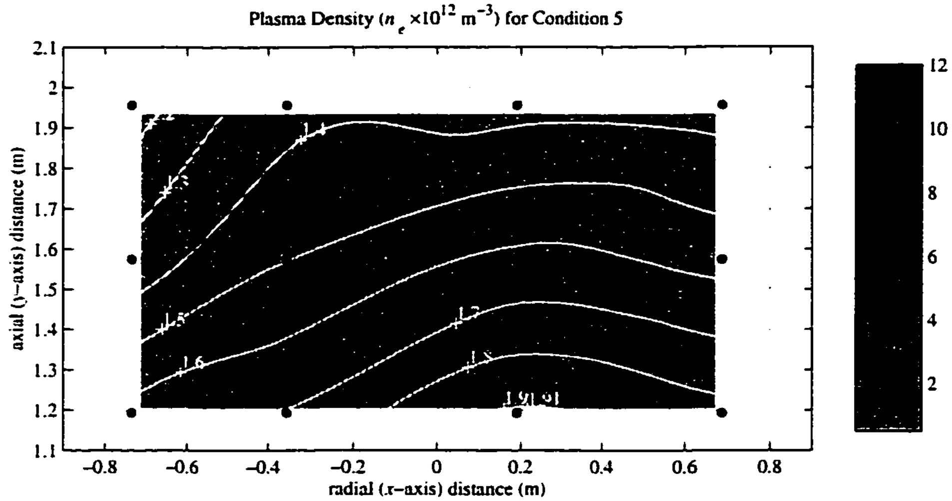

Figure B.8: Spatial distribution of electron density for condition 5.

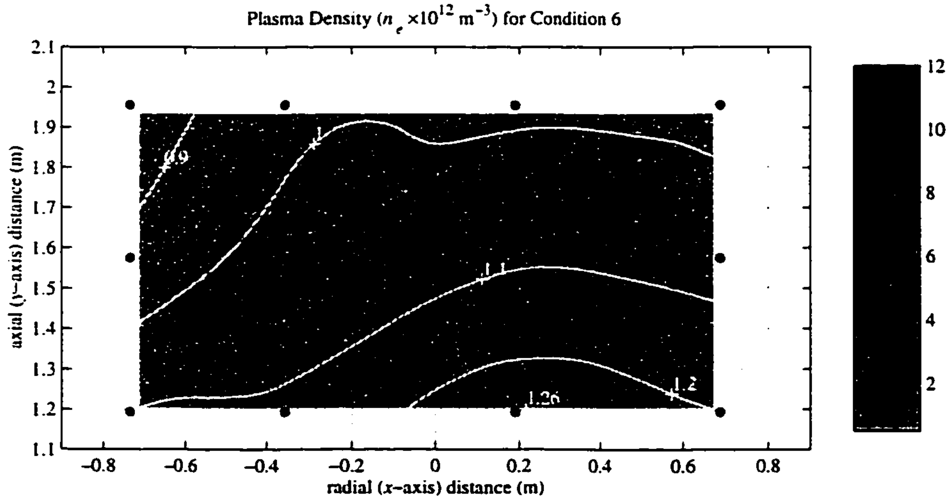

Figure B.9: Spatial distribution of electron density for condition 6.

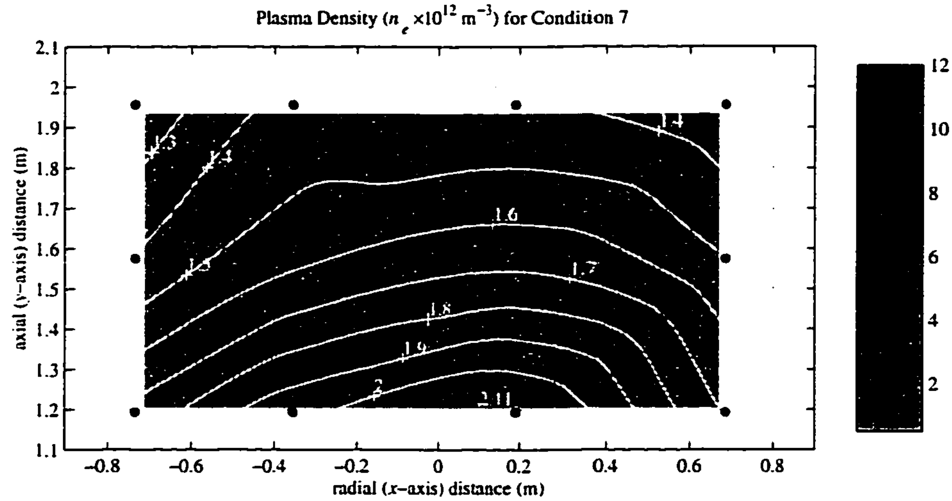

Figure B.10: Spatial distribution of electron density for condition 7.

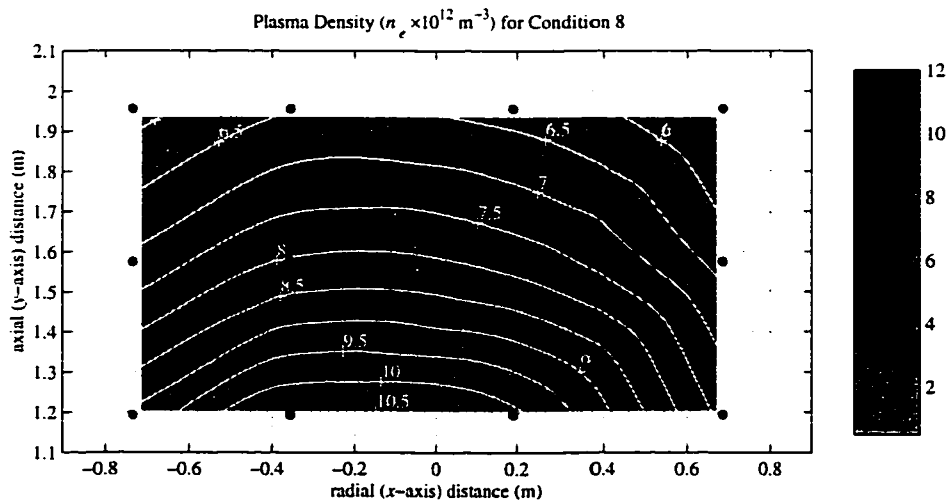

Figure B.11: Spatial distribution of electron density for condition 8.

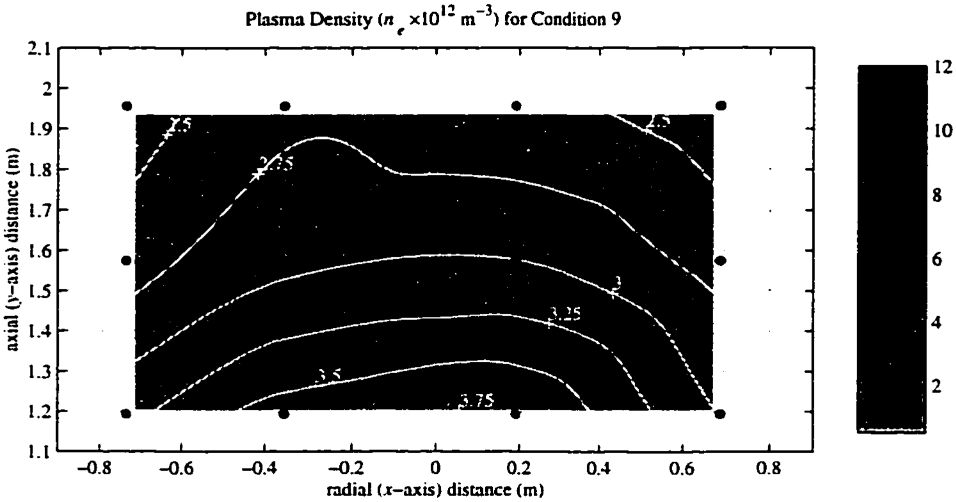

Figure B.12: Spatial distribution of electron density for condition 9.

most of the plots appear to have slighter higher densities to the right of the HCA. It is believed that this was due to the HCA pointing slightly to the right of the center line. Second, although the region is undersampled, fairly good density profiles can be interpolated due to the uniform nature of the plasma plume.

B.2.2 Ion Densities

The ion density throughout the measurement region was determined via the Langmuir probe method. These values were all within a factor of 2 of the electron densities providing important corroboration of the results.

B.2.3 Electron Temperatures

The electron temperature throughout the measurement region was determined via the Langmuir probe method. These values fell within the range 0.9 to 1.5 eV.

Table B.2: Summary of the HCA plasma environment for each of the nine operating conditions.

Oper. Cond.	Gas	Ion Mass, $\times 10^{-26}$ kg	Mean n_e (std. dev.), $\times 10^{12}$ m^{-3}	Mean θ_e (std. dev.), eV	Fig. Num.
1	krypton	13.92	3.9 (0.9)	0.9 (0.1)	B.4
2	krypton	13.92	11.9 (3.3)	1.1 (0.3)	B.5
3	krypton	13.92	1.2 (0.3)	1.0 (0.2)	B.6
4	argon	6.63	1.2 (0.1)	1.0 (0.2)	B.7
5	argon	6.63	1.5 (0.2)	1.1 (0.3)	B.8
6	argon	6.63	1.0 (0.1)	1.8 (0.2)	B.9
7	xenon	21.80	1.6 (0.3)	1.5 (0.1)	B.10
8	xenon	21.80	7.5 (1.7)	1.4 (0.1)	B.11
9	xenon	21.80	2.9 (0.4)	1.5 (0.1)	B.12

B.2.4 Chamber Ambient Magnetic Field

The ambient magnetic field in the chamber was measured with the SETS AMAG. In terms of AMAG coordinates, the following field components were measured on 2 February 1995 during thermal-vacuum testing of the SETS payload, $\mathbf{B}_{\text{AMAG}} = -4.26\hat{x} + 0.97\hat{y} - 8.01\hat{z} \times 10^3$ nT, or $|\mathbf{B}_{\text{AMAG}}| = 9.12 \times 10^3$ nT. Performing a coordinate system rotation such that the coordinates are those shown in Figure 3.5, the magnetic field in the chamber is $\mathbf{B}_{\text{chamber}} = -1.83\hat{x} + 7.86\hat{y} - 4.26\hat{z} \times 10^3$ nT.

Such a low value for the ambient magnetic field in the chamber may at first seem incorrect. The location of the chamber is 42°17.98′41″ N lat., 83°41.61′98″ E long., where the IGRF–90 geomagnetic field model indicates the ambient geomagnetic field should be $\mathbf{B}_{\text{IGRF}} = 1.83\hat{x} - 0.19\hat{y} + 5.32\hat{z} \times 10^4$ nT and $|\mathbf{B}_{\text{IGRF}}| = 5.63 \times 10^4$ nT, where $\hat{x}$ is directed North, $\hat{y}$ is directed East, and $\hat{z}$ is directed into the Earth. The chamber is made of stainless steel which is ordinarily non–magnetic [*Bozorth*, 1951, p. 147], and as such should not greatly affect the field. However, the chamber is housed in a building where the local field is greatly reduced. Even before the SETS instrument was moved into the chamber itself, the field inside the PEPL building but outside the chamber was measured at $|\mathbf{B}_{PEPL}| = 1.39 \times 10^4$ nT. In addition, the correct functioning of the AMAG was verified both before and after thermal–vacuum testing. Thus, the reduction in field strength seen inside the chamber can be explained.

B.3 Summary

The data collected and analyzed here show that the far–field plasma environment of the HCA simulates well ionospheric plasmas. The obtainable density range is between $\sim 10^{12}$ to 10^{13} m^{-3} and higher. This does not quite cover the range of nighttime/daytime and solar minimum/maximum plasma densities, but if tests are performed farther back in the chamber, lower densities ($\sim 10^{11}$) can be found. In addition, the obtainable electron temperatures are in the range of $\simeq 0.9$ to 1.5 eV. These values are slightly higher than those found in the ionosphere ($\theta_e \simeq 0.1$ eV), but not appreciably so. Electron temperature could possibly be lowered in future experiments by injecting cold gas at the exit of the HCA keeper. The plasma is fairly uniform over a large region, varying by only a factor of 2 from side to side and front to back of the measurement space used in this study.

There are several aspects of the HCA plasma environment which do deviate from ionospheric plasmas. The first is the strength of the geomagnetic field. The field strength measured in the chamber is about an order of magnitude smaller than that in the ionosphere. This, however, is not necessarily disadvantageous since the addition of Helmholtz coils would allow for varying magnetic field orientations without much interference from the ambient geomagnetic field. The second deviation is the heavier gases needed for HCA operation. The three gases used here (argon, krypton, and xenon) are all heavier than the primary ionospheric constituent: oxygen. In our test we did attempt to use neon which is close in mass to oxygen, but the discharge voltage and mass flow rate required would produce a plasma much denser than ionospheric levels at 1–2 m from the HCA exit plane. The third deviation has to do with plasma flow. Most *in situ* investigations in the ionosphere are made on moving spacecraft with orbital velocities high enough that the ion flow is effectively a directed beam. The HCA does not provide such a directed flow, and hence motional effects cannot be readily studied in the current HCA configuration.

APPENDIX C

Langmuir Probe Measurement Theory

A Langmuir probe (LP) immersed in plasma is used to measure electron and ion densities; electron temperature; and plasma and floating potentials. An LP is a metal collector to which a swept voltage is applied and the resulting plasma current is measured. The resulting I–V curve is analyzed to extract the plasma parameters. The simplicity of LP construction and operation has ensured their wide use as a plasma diagnostic tool, despite the sometimes difficult task of accurately extracting plasma parameters from the LP trace.

To illustrate the LP method, Figure C.1 shows a theoretical I–V curve for a cylindrical LP immersed in a plasma. This I–V curve represents the sum of the electron and ion probe currents, i_{ep} and i_{ip}, collected from the plasma region surrounding the probe. Tracing the curve from left to right (or, alternatively, as the probe is biased less negatively and more positively), we first encounter the ion saturation region. In this region the probe is biased sufficiently negative to prohibit electrons from reaching it, and hence the probe current is due almost entirely to ions. As the probe is biased more positively, some of the plasma electrons are able to overcome the probe potential and produce an exponentially increasing current. As the probe is biased even more positively, we encounter the electron saturation region in which electrons

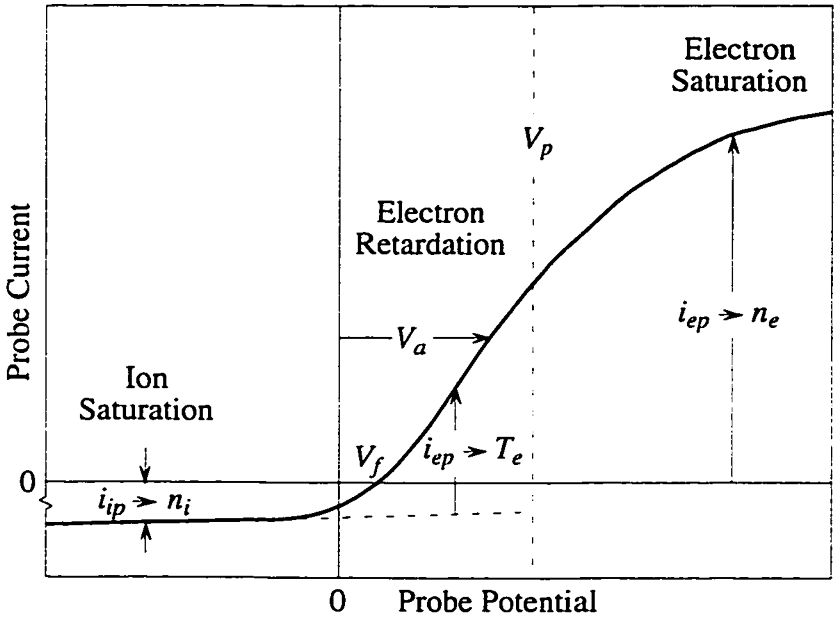

Figure C.1: A theoretical current–voltage characteristic for a cylindrical Langmuir probe immersed in a plasma. The figure shows the regions of the curve where n_e, n_i, and T_e can be calculated as well as the locations of V_f and V_p. Note that the current scale in the ion saturation region has been enlarged for clarity. After *Krehbiel et al.* [1981].

are primarily collected.

C.1 Extracting Plasma Parameters

As outlined above, the LP I–V curve has three distinct regions: ion saturation, electron retardation, and electron saturation. Proper analysis of the curve in these three regions respectively yields the ion density (n_i), electron temperature (T_e), and electron density (n_e). In addition, the plasma potential (V_p) and probe floating potential (V_f) can also be determined. Probe geometry is very important to the analysis. For all equations shown here we assume a cylindrical probe with radius $r_a \lesssim \lambda_D$, where λ_D is the Debye length defined in Section 2.2.1. This assumption is also known as the the orbital–motion–limited (OML) regime, which was described in Section 2.2.2.2. If the condition that $r_a \lesssim \lambda_D$ is not met, then Child–Langmuir (CL) probe theory must be used (Section 2.2.2.1).

The ion density is determined from the ion current, i_{ip}, measured in the ion saturation region of the LP I–V curve. In this region, the probe is biased negatively to collect primarily ions. Because of the heavier mass of the ions, they are not easily collected and hence the current measured is usually very small. The ion current to the probe in this region (assuming a non–flowing plasma[1]) is given by the following equation[2]:

$$i_{ip} = n_i A_p q_i \frac{2}{\sqrt{\pi}} \left(\frac{kT_i}{2\pi m_i}\right)^{0.5} \left(1 - \frac{qV_{ap}}{kT_i}\right)^{0.5} \quad \text{for } V_{ap} < 0, \tag{C.1}$$

where

n_i ion plasma density (per m^3);

A_p probe collection area (m^2);

T_i ion temperature (K);

m_i ion mass (kg);

q_i ion charge (1.602×10^{-19} C);

V_{ap} probe voltage with respect to plasma potential (V), *i.e.*, $V_{ap} = V_a - V_p$, where V_a is the applied potential and V_p is the plasma potential.

For large negative applied voltages ($\frac{qV_{ap}}{kT_e} \ll -1$), Equation (C.1) can be approximated as

$$i_{ip} \approx n_i A_p q_i \frac{2}{\sqrt{\pi}} \left(\frac{-qV_{ap}}{2\pi m_i}\right)^{0.5} \quad \text{for } V_{ap} < 0. \tag{C.2}$$

Additionally, Equation (C.2) can be rearranged to find n_i for a given probe current

[1] For a flowing plasma, such as would be encountered on a spacecraft, the equation would have to take into account the velocity vector of the probe with respect to the plasma. For inclusion of the velocity term see *Krehbiel et al.* [1981].

[2] Note the similarity of this equation with Equation 2.18

i_{ip} as

$$n_i = \frac{i_{ip}}{A_p}\frac{\pi}{q_i}\left(\frac{-m_i}{2qV_{ap}}\right)^{0.5} \quad \text{for } V_{ap} < 0. \tag{C.3}$$

The electron temperature is determined from the probe response in the electron retardation region by the following equation:

$$T_e = \frac{v_1 - v_2}{\ln(i_1 - i_2)}, \tag{C.4}$$

where the pairs v_1–i_1 and v_2–i_2 are two points on the I–V curve in the electron retardation region. Equation (C.4) derives from the equation for i_{ep} from the retarded electrons

$$i_{ep} = n_e A_p q_e \left(\frac{kT_e}{2\pi m_e}\right)^{0.5} \exp\left(\frac{qV_{ap}}{kT_e}\right) \quad \text{for } V_{ap} > 0, \tag{C.5}$$

where

n_e electron plasma density (per m^3);

q_e electron charge (-1.602×10^{-19} C);

T_e electron temperature (K);

m_e electron mass (9.109×10^{-31} kg).

Note that knowledge of n_e is not required to obtain T_e. When the LP I–V curve is plotted logarithmically, the curve in this region will approximate a straight line for a Maxwellian plasma, and hence T_e is simply the slope of the logarithmic line. In addition, the point where the I–V curve begins to break from the exponential response (or the point where the logarithmically straight line begins to curve) is known as the plasma potential, V_p. The point where the probe current is zero is known as the floating potential, V_f, since this is the voltage required to maintain zero net current to the probe. Another way of looking at V_f is that it is the potential an isolated body immersed in a plasma would maintain so that the condition of zero net current would be satisfied.

The electron density can be determined from the electron current, i_{ep}, measured in the ion saturation region of the LP I–V curve. In this region, the probe is biased positively to collect primarily electrons. Because the electrons are lighter than the ions, they are easily collected and hence the current measured is much larger than the ion current. The electron current is given by

$$i_{ep} = n_e A_p q_e \frac{2}{\sqrt{\pi}} \left(\frac{kT_e}{2\pi m_e}\right)^{0.5} \left(1 + \frac{qV_{ap}}{kT_e}\right)^{0.5} \text{ for } V_{ap} > 0. \tag{C.6}$$

For large positive applied voltages ($\frac{qV_{ap}}{kT_e} \gg 1$), Equation (C.6) can be approximated as

$$i_{ep} \approx n_e A_p q_e \frac{2}{\sqrt{\pi}} \left(\frac{qV_{ap}}{2\pi m_e}\right)^{0.5} \text{ for } V_{ap} > 0. \tag{C.7}$$

Additionally, Equation (C.7) can be rearranged to find n_e for a given probe current i_{ep} as

$$n_e = \frac{i_{ep}}{A_p} \frac{\pi}{q_e} \left(\frac{m_e}{2qV_{ap}}\right)^{0.5} \text{ for } V_{ap} > 0. \tag{C.8}$$

C.2 Langmuir Probe Measurement Errors

There are several sources of error inherent in the LP method. For stationary probes, the two largest errors include surface contamination effects and probe–end effects. Contaminants on the surface of the LP can act as an insulating layer causing voltage drops across the layer. These insulating contaminants can cause a capacitive charging effect which can distort the I–V curves and yield falsely high T_e values. Providing a method to clean the probe periodically can help to alleviate the contamination effects. One such method is to briefly apply high potentials (> 100 V) to the probe such that the collector will draw large fluxes of high–energy electrons which bombard and clean the surface.

Probe–end effects is another source of error in LP measurements. To reduce these effects a triaxial boom is often used. By biasing the middle shield to the probe voltage, fringing fields near the boom can be reduced to a minimum. The probe tip also has fringing fields which would not occur if the probe were infinite in length. The equations for electron and ion current given here assume an infinite cylindrical collector. For practical (*i.e.*, shorter) collectors, however, the equations deviate from the theoretical values. At extremely high potentials where the LP sheath is large, the LP will begin to look like a spherical source and the I–V characteristic will look like that of a sphere.

APPENDIX D

Transient Response of the Tethered Satellite System

This appendix includes the slightly modified versions of two papers [*Bilén et al.*, 1995, 1997] in which a transient circuit model of the Tethered Satellite System was developed and TSS–1 mission data analyzed. Both of these papers used a rigid coaxial model of the TSS tether which is valid under the low–voltage conditions of the TSS–1 mission.

D.1 Transient Response of TSS–1 in the Ionosphere

[This section is adapted from Bilén, S. G., B. E. Gilchrist, C. Bonifazi, and E. Melchioni, "Transient response of an electrodynamic tether system in the ionosphere: TSS–1 first results," *Radio Science*, **30**(5), 1519–1535, 1995.]

D.1.1 Introduction

In recent years, orbiting space tethered satellites have seen their first flight demonstrations as dedicated flight systems. It is now possible to deploy and retrieve tethered satellites from NASA's space shuttle using the Tethered Satellite System (TSS), which was first flown in 1992 [*Dobrowolny and Melchioni*, 1993; *Dobrowolny et al.*, 1994a]. In addition, a second, simpler tether system called the Small Expendable

Deployer System (SEDS) [*Carroll*, 1993; *Lorenzini and Carroll*, 1991] has had three successful flights as a secondary payload on board Delta–II rockets in 1993 and 1994. SEDS is capable of deploying, but not retrieving, both small and large satellites from expendable launch vehicles and free flyers, as well as from the space shuttle.

While a variety of novel concepts are now being studied which utilize one or several spacecraft attached to a tether up to 100 km long [*Penzo and Ammann*, 1989], early flights have principally emphasized electrodynamic applications using tethers with conducting wires [*Godard et al.*, 1991; *James and Whalen*, 1991; *Dobrowolny and Melchioni*, 1993; *Dobrowolny et al.*, 1994a; *Kawashima et al.*, 1988; *McCoy et al.*, 1993; *Sasaki*, 1988]. Motion of the conducting tether relative to the ambient magnetized plasma of the near Earth environment generates substantial $(\mathbf{v}_s \times \mathbf{B}_E) \cdot \mathbf{l}$ potentials, where $\mathbf{v}_s$ is the tether motion through the local plasma, $\mathbf{B}_E$ is the Earth's magnetic field, and $\mathbf{l}$ is the vector end–to–end length of the tether [*Banks et al.*, 1981; *Dobrowolny*, 1987; *Banks*, 1989]. This electromotive force can be made to drive current through the tether if adequate electrical contact is made with the surrounding plasma [*Arnold and Dobrowolny*, 1980; *Banks et al.*, 1981; *Martínez–Sanchez and Hastings*, 1987; *Banks*, 1989; *Agüero et al.*, 1994].

Adequate understanding of the current–voltage (I–V) characteristics of electrodynamic tether systems will be fundamental to their effective scientific and technological utilization. Suborbital rocket experiments have previously shown that collecting double probes' capability of drawing current from the ionosphere through a conducting tether is due to either low–level potentials or higher potentials using on–board power supplies [*Godard et al.*, 1991; *Katz et al.*, 1989; *Kawashima et al.*, 1988; *Neubert et al.*, 1990; *Sasaki*, 1988]. Initial assessment of I–V characteristics for an orbiting electrodynamic tether system has begun with the first Tethered Satellite System

(TSS–1) mission, which flew in 1992 [*Agüero et al.*, 1994; *Thompson et al.*, 1993]. Recently, the Plasma Motor Generator (PMG) orbital tether experiment studied the use of plasma emissions at each tether end to enhance current collection from the ionosphere [*McCoy et al.*, 1993].

A complete understanding of an electrodynamic tether system requires description of both steady state and transient electrical response. Here, we provide first reports of its transient electrical response which showed strong dependency on ionospheric conditions. To understand the observations, it was necessary to apply circuit models of the TSS–1 electrical system [*Bilén et al.*, 1994; *Martin Marietta*, 1990] and extend earlier models of electrodynamic tether systems in the ionosphere [*Arnold and Dobrowolny*, 1980; *Banks et al.*, 1981; *Banks*, 1989; *Dobrowolny*, 1987; *Greene at al.*, 1989] to properly interpret the TSS–1 results. Understanding the transient behavior of an electrodynamic tether system is of particular importance to applications utilizing tether current pulses or modulation such as for low–frequency wave generation and detection of natural electric field transient signatures.

In Section D.1.2 the TSS–1 mission and SETS experiment system will be introduced and their operation described. Section D.1.3 provides observations of the transient tether voltage response as collected during ground tests and the TSS–1 mission. Section D.1.4 describes the electrodynamic tether system transient model. A comparison between experiment and model prediction is presented in Section D.1.5. Finally, Section D.1.6 presents concluding remarks as well as directions for future research.

D.1.2 TSS Missions

TSS–1 was a joint mission between NASA and ASI (Italian Space Agency). TSS–1 deployed an electrically conductive, 1.6–m–diameter Italian-built satellite to a distance of 267 m above the payload bay of the Space Shuttle *Atlantis*, which was at an approximate ionospheric altitude of 296 km. The satellite was connected to the shuttle via an electrodynamic tether—an electrically conducting, insulated wire—and the interaction of this wire with the Earth's magnetic field induced a potential across the tether reaching values near 60 V which allowed tether currents approaching 30 mA.

Figure D.1a gives a functional diagram of the TSS–1 electrical configuration appropriate for steady state, or slowly varying, conditions discussed in this Appendix. Figure D.1a also indicates the method used to control the tether current and the location of the voltage and current sensors. Central to the results reported here was the Shuttle Electrodynamic Tether System (SETS), a TSS–1 instrument which made high-resolution measurements of the induced potential using its high-impedance voltage monitor. SETS also controlled current flow through the tether using switched loads and active electron beam emissions. A full description of SETS is given by [*Agüero et al.*, 1994], whereas the TSS–1 mission is overviewed separately [*Dobrowolny and Melchioni*, 1993; *Dobrowolny et al.*, 1994a]. To measure I–V tether characteristics, the SETS experiment could selectively place resistive loads between the tether end and the shuttle's electrical ground, allowing current to flow through the tether from the ionospheric plasma. The load connections were made with and without electron beam emissions from the SETS fast–pulse electron generator (FPEG) which was connected to the orbiter electrical ground. Because of the orbitally induced potential polarity, the TSS–1 satellite was typically biased to attract electrons to its conducting surfaces while the orbiter either attracted ions to its main engine bells, its primary conducting surfaces, or emitted electrons from the FPEG. (See Figure D.1b for current and voltage conventions.) The Core Equipment's (CORE) electron gun (not shown in Figure D.1a) was also capable of emitting electrons directly from the tether connection [*Bonifazi et al.*, 1993]. For steady state conditions, the system I–V response was primarily determined by available *emf*, ionospheric density, and circuit resistance [*Agüero et al.*, 1994; *Gilchrist et al.*, 1992; *Thompson et al.*, 1992, 1993].

Prior to the mission, the electrical properties of the TSS tether and tether deployment system were characterized [*Bilén et al.*, 1994]. From this premission characterization, an equivalent electrical circuit, suitable for transient analysis, was developed for the tether deployment reel. The reel system contains 22 km of insulated tether wrapped on an aluminum spindle and can be considered as an inductor of approximately 12 H before deployment. An important difference between ground and space flight transient measurements is that Earth ground connections are replaced with contact to the ionospheric plasma at both the satellite and orbiter as shown in Figure D.2. While an Earth ground can be thought of as representing a large (ideally infinite) supply of charge carriers at low impedance, the ionospheric plasma contains only a limited quantity of charge carriers which varies in magnitude primarily according to solar and other geophysical parameters.

In our analysis, data from two SETS instruments was used (Figure D.1a): the DC tether voltage monitor (TVMDC) and the current mode monitor (CMM). The TVMDC was the primary measurement of steady state tether potential. The voltage transients were measured with the CMM, which is a DC coupled burst measurement of the tether potential applied to the load resistor bank and has three gain states: $\times 1$,

(a)

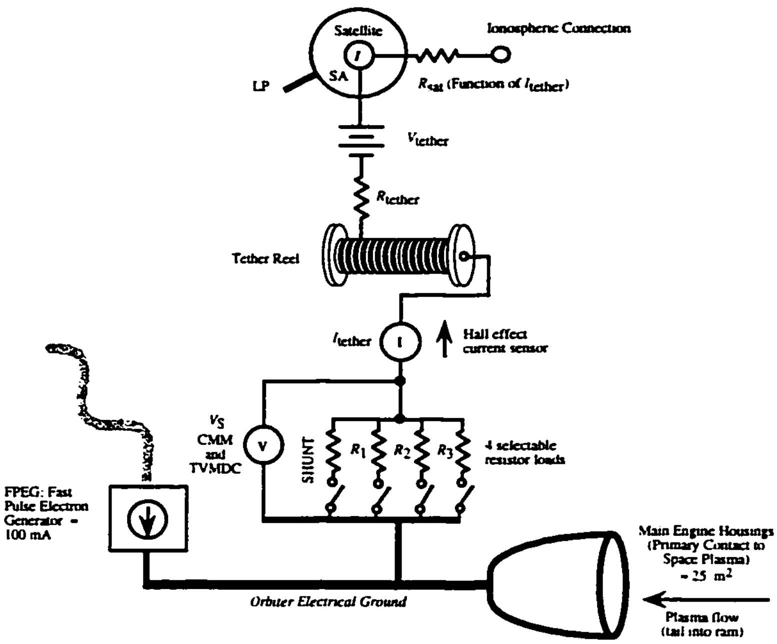

(b)

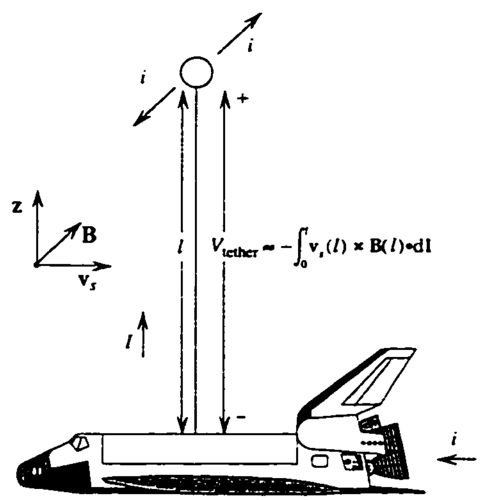

Figure D.1: The TSS–1 system. (a) System level diagram of TSS–1 showing the placement of the SETS FPEG, TCVM, CMM, and load resistors; the SCORE ammeter (SA); and the RETE Langmuir Probe (LP). (b) Electrical conventions.

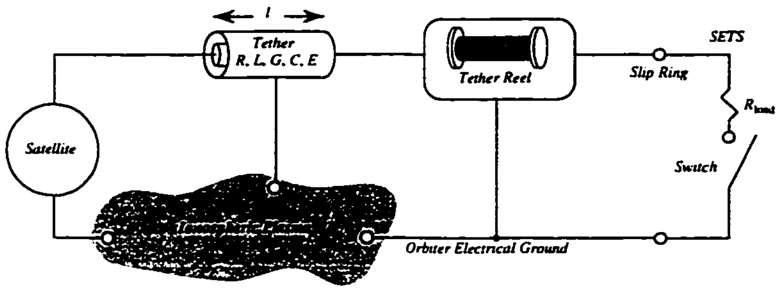

Figure D.2: Simplified TSS–1 circuit schematic showing satellite, tether, tether reel, and SETS.

×10, and ×100. The CMM is an 8–bit digitizer (resolution: ×1, 39.4 V; ×10, 3.96 V; and ×100, 0.397 V) with a programmable sample rate of up to 10 Msample/s. During TSS–1, the CMM was filtered with a 12–kHz double–pole low–pass filter. The CMM signal is available only through a burst mode (BM) channel which can handle up to 4 captures with a total of 32 ksamples each before downloading them in the telemetry stream. For the experiments discussed in the present analysis, the CMM measurements were made at ×10 and ×100 gains at a rate of 32 kHz. More information on these instruments is given by [*Agüero et al.*, 1994].

For the results reported here, we have utilized current measurements made at the satellite end of the tether by the Satellite Core Equipment (SCORE) [*Bonifazi et al.*, 1994]. The SCORE satellite ammeter (SA) is a low pass filtered (1 Hz) resistor type current meter with 8–bit resolution and four current measurement scales (±10 mA, ±100 mA, ±500 mA, and ±5 A). Gain scales are automatically changed by gain control logic which detects overflow/underflow conditions. The SA measurement accuracy is ±1% full scale over all scales.

An estimation of the ionospheric plasma density was obtained from Langmuir probe (LP) measurements made by the Research on Electrodynamic Tether Effects

(RETE) experiment [*Dobrowolny et al.*, 1994a]. This probe was located on the tip of one of the two satellite deployable booms. Every 3.2 s, a 60–ms probe voltage sweep was executed and the current recorded in the telemetry. After the mission, the probe's I–V characteristics were analyzed to obtain the plasma density and temperature. Due to several systematic effects caused by the probe hardware, the total error of the plasma density determination has been estimated to be on the order of 10–15% [*Butler et al.*, 1994]. Because the separation between the orbiter and the satellite was a maximum of 267 m during TSS–1, it was assumed that the plasma density measured at the satellite was the same as that around the shuttle in the absence of thruster firings or other localized effects.

D.1.3 Observations

The timeline of the TSS–1 mission consisted of several different functional objectives (FOs), or experiments, performed sequentially. The transient events investigated here occurred during SETS functional objective number 14 (SETS14 or FO14), of which there were a total of nine performed during the TSS–1 mission. Table D.1 summarizes the Greenwich Mean Time (GMT) start, tether length, ionospheric plasma density, and tether current for each of these nine FOs. Although the primary purpose of this FO was to examine vehicle charging, it provided useful switching transient data as well.

During each SETS14 FO, the TSS–1 circuit (Figure D.1a) was closed briefly via the SHUNT load resistor ($R_{\mathrm{SHUNT}} \approx 15\,\Omega$) a total of nine times. The SHUNT was switched in for 2 s, allowing the tether current to be measured, and then out again for at least 15 s. Immediately before the SHUNT was switched out, CMM data collection was started in order to capture the resulting tether voltage transient as

Table D.1: Summary of TSS–1 Shuttle Electrodynamic Tether System Functional Objective 14.

SETS14 Event	GMT, ddd/hhmm:ss	Tether Length, m	Ionospheric Density, $\times 10^{11}$ m^{-3}	Tether Current Range, mA
1	218/1837:46	224.2	1.85–3.54	7.1–9.1
2	218/1859:50	224.2	3.08–6.71	16.4–22.0
3	218/1924:47	224.2	2.16–2.81	12.1–13.2
4	218/1952:13	224.2	5.70–6.84	17.5–19.4
5	218/2031:06	224.2	3.84–6.43	20.5–22.0
6	218/2117:42	223.6	5.41–6.58	10.2–19.7
7	218/2155:27	222.9–204.4	1.37–4.79	4.9–10.2
8	218/2233:09	69.6–52.8	N/A[a]	3.9–5.5
9	218/2310:52	11.3	N/A[a]	0.0[b]

[a]No RETE LP data was collected after 218/2200:00.
[b]Below satellite ammeter (SA) resolution.

seen at the SETS instrument.

A switching transient test performed before the mission provided a baseline of the expected peak transient voltage levels for a given tether current and tether length. From these premission tests the normalized peak tether voltage transient, V_{peak}, was expected to be between -30.0 and -29.6 V/mA of initial current for the mission deployed length of 0 to 267 m. The peak transient levels experienced during the mission under all ionospheric conditions and all tether deployed lengths can be seen in Figure D.3. The least squares fit to this data yields $V_{\text{peak}} = -29.3$ V/mA, which agrees very well with the expected value. Thus the peak transient voltage is predictable and based on two parameters: tether length and initial tether current.

Figure D.4 shows three different switching transients captured during the TSS–1 mission (Figures D.4b, D.4c, D.4d) and one from premission testing (Figure D.4a) for comparison. The peak values of these transients have been normalized to 1.0 to allow for easier comparison of the oscillations. These transients can be described as having the general shape of an underdamped, second order response. Two additional

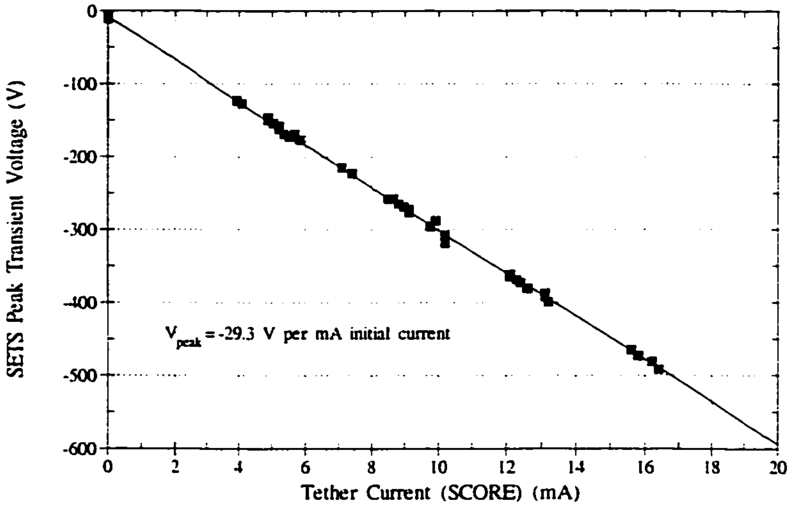

Figure D.3: Peak transient voltage versus tether current taken during SETS14s.

characteristics of the tether voltage transient are how fast the oscillations decay from peak value and how symmetrical those oscillations are about the quiescent tether voltage. Figure D.4 indicates that both the transient decay and its symmetry were affected by the ionospheric density. When the density was relatively high (*e.g.*, Figure D.4b), the mission transients approached premission transient characteristics, whereas when the density was lower (*e.g.*, Figure D.4d), the transients were highly asymmetrical and the magnitude of their oscillations diminished faster.

To show the relationship between plasma density and asymmetry in the tether voltage transients, a time sequence where the plasma density changed significantly in a short period of time was chosen. This time sequence was part of SETS14 number 2 (see Table D.1), and comprises the first six switching transients of that FO. Figure D.5 shows the tether potential, tether current, SHUNT closure times, plasma density, and observed transient for each event in this sequence. Also included are simulated voltage transients which are discussed in Section D.1.5. Over the course of these six

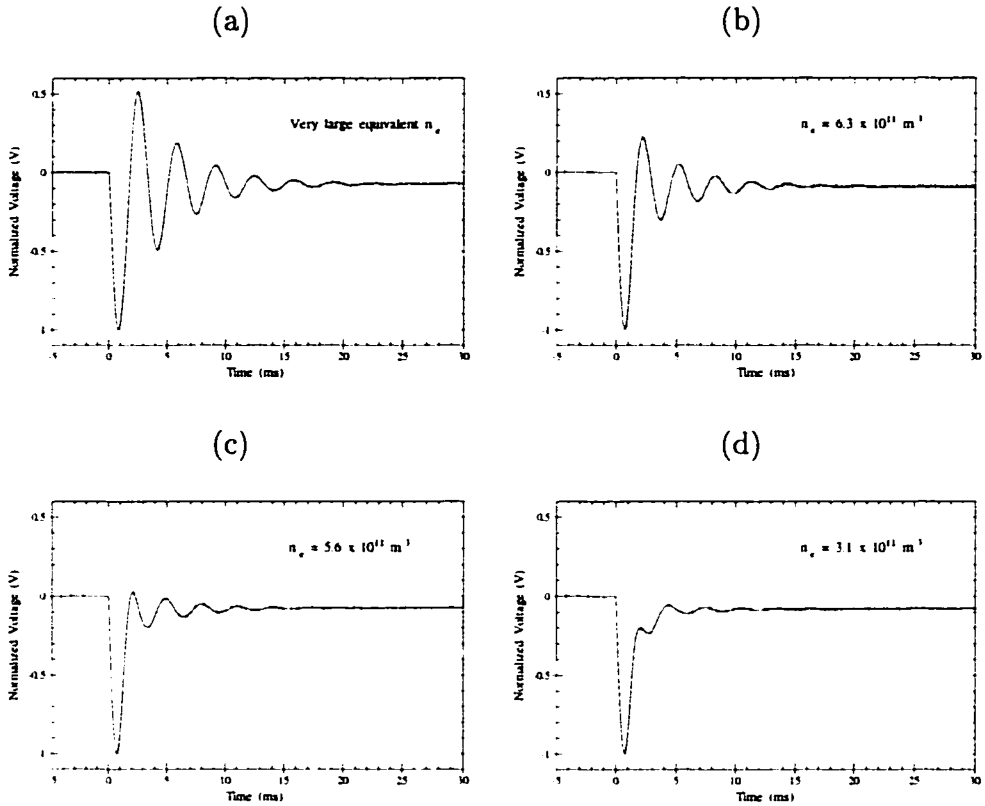

Figure D.4: Normalized switching transients taken under the following conditions: (a) premission calibration, 0–m deployed tether (fully–wound reel), 13.29–mA initial current, −402.0–V peak transient, very large equivalent n_e; (b) collected at Greenwich Mean Time (GMT) 218/2118:45, −4.9° latitude, 226.7° longitude, 223.63–m deployed tether, 10.24–mA initial current, −319.2–V peak transient, dayside ionosphere, $n_e = 6.3 \times 10^{11}$ m^{-3}; (c) collected at GMT 218/2122:34, −11.8° latitude, 239.4° longitude, 223.63–m deployed tether, 15.75–mA initial current, −473.1–V peak transient, dayside ionosphere, $n_e = 5.6 \times 10^{11}$ m^{-3}; (d) collected at GMT 218/1859:56, −1.6° latitude, 70.3° longitude, 224.15–m deployed tether, 16.38–mA initial current, −492.3–V peak transient, nightside ionosphere, $n_e = 3.1 \times 10^{11}$ m^{-3}.

switch closures, the plasma density increases fairly steadily by about a factor of 2. The increase in plasma density results in more current flowing through the tether during switch closure, which in turn increases the peak transient level as explained above. (Transient responses 2 through 6 of Figure D.5 have initial peaks that are clipped at -500 V, which is the limit of the CMM's $\times 10$ range). The plasma density increase also affects the symmetry of the transient responses, with each successive transient becoming more and more symmetric and decaying less rapidly.

However, the magnitude of the initial current also determined the system transient response. That is, when the tether current was low enough, then the oscillations of the transients approached symmetry even in lower plasma densities. To show this, a time sequence was chosen where the plasma density remained relatively constant but the tether current was reduced due to an Orbiter thruster firing which reduced the ability to collect current in the near vicinity of the orbiter [*Gilchrist et al.*, 1993]. This time sequence was part of SETS14 number 6 (see Table D.1), and comprises three switching events of that FO. Figure D.6 shows the tether potential, tether current, SHUNT closure times, plasma density, and transient responses for this triplet. It can be seen that the middle event experiences a factor–of–2 reduction in tether current before the switch opening. The resulting transient is noticeably different from those surrounding it in that its oscillations are symmetrical.

Another characteristic to note in the transient voltage data is that the temporal spacing between local voltage maxima and minima is nonuniform at lower plasma densities (compare Figures D.4b and D.4d). In other words, at low plasma densities, the apparent resonant frequency of the circuit changes as the voltage oscillates.

D.1.4 Transient Model of an Electrodynamic Tether System

A model of TSS–1 and its interaction with the ionosphere has been developed to account for the variability and asymmetry seen in the mission transients. The observations which are explained by our model include 1) greater transient oscillation damping and asymmetry at lower ionospheric plasma densities; 2) peak transient voltage dependency on only two parameters, tether length and initial tether current (not on local ionospheric density); and 3) nonuniform temporal spacing between local transient voltage maxima and minima at low plasma densities.

The first observation, asymmetry of the transient oscillations, was qualitatively interpreted as the inability of the ionosphere to provide enough reverse current when required to do so by the TSS circuit. This fact can be understood by the following qualitative description. Immediately after switch opening, the current in the tether and reel continued to flow in the same direction though decreasing in magnitude. At the same time, the voltage across the system peaked due to the large inductance presented by the tether reel. When the voltage reached and went past its peak value, current in the system went to zero and reversed direction. (Current through any inductance, such as the TSS tether reel, is 90° out of phase with the voltage across the inductance.) This reverse current requires ions to be collected at the satellite, which has a much smaller ion collection area than the orbiter. When the plasma density was higher, the ionosphere was capable of supplying a large ion current (in the low–current regime experienced during TSS–1), but when the density was lower, it was unable to provide the required current. Hence the transient voltage response became asymmetric, as if a lossy diode had been placed in the circuit, as shown in Figure D.5. However, even at lower plasma densities, if the required current was low enough, the transient response was symmetrical, as seen in Figure D.6.

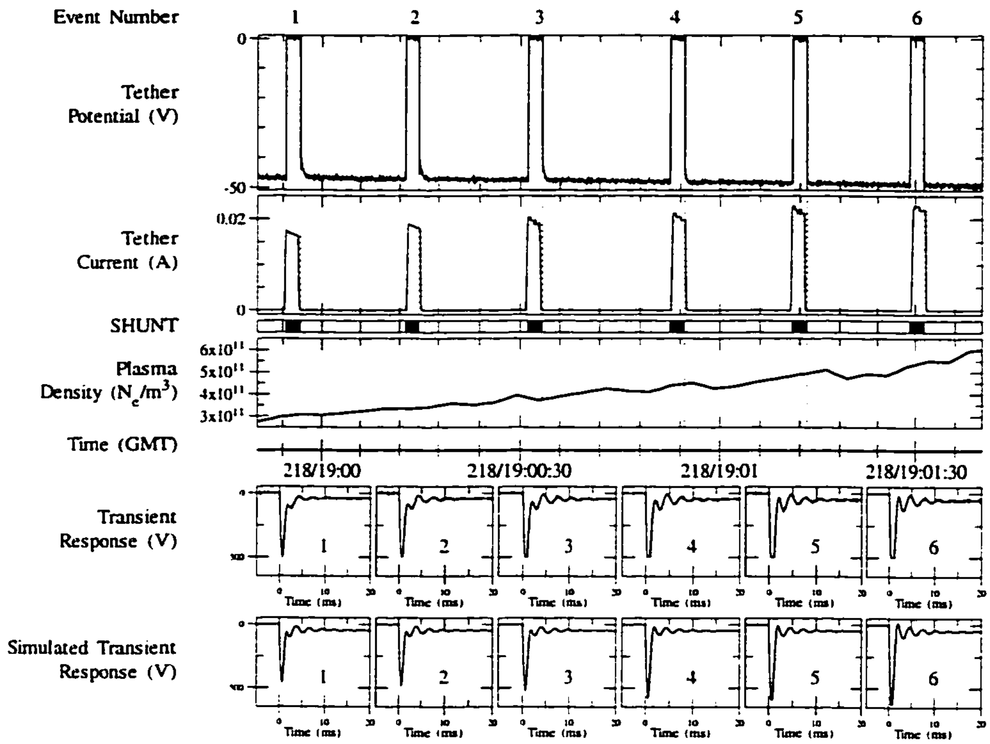

Figure D.5: Plot of the first six switch closings during SETS14 number 2 showing tether potential, tether current, plasma density, SHUNT closures, transient response, and simulated transient responses for each event. Although the tether potential remains relatively constant during all six events, the plasma density increases by a factor of 2, and its effect on the transient responses is very noticeable.

The second observation deals with the independence of peak transient voltage on ionospheric density. During steady state current flow prior to switch opening, ions are collected at the orbiter and electrons are collected at the satellite; the current level established in the tether is only as large as the ionospheric plasma can provide or is limited by the tether resistance [*Thompson et al.*, 1993]. This established current flows through the tether reel and causes the initial transient voltage peak when interrupted as the load resistor is disconnected. Other than setting the initial current, the ionospheric plasma does not affect the transient response until ions must

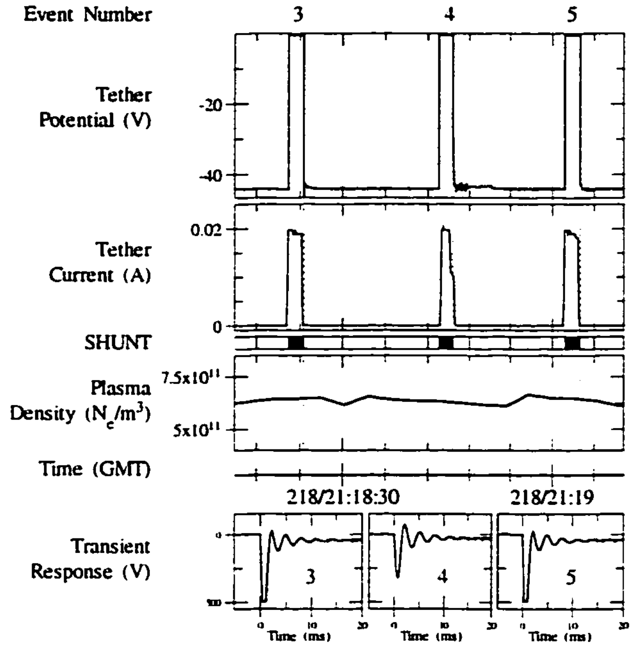

Figure D.6: Plot of three switch closings during SETS14 number 6 showing tether potential, tether current, plasma density, SHUNT closures, and transient response. Although the tether potential and plasma density remain relatively constant during these three events, the middle event experiences a factor–of–2 reduction in tether current before opening. The resulting transient is noticeably different from those surrounding it in that its oscillations are symmetric.

be attracted to the satellite which occurs only after achieving the peak voltage.

The third observation, nonuniform spacing of voltage maxima and minima at lower plasma densities, would tend to indicate nonlinearities in the components of the equivalent circuit model. It will be shown later that this is indeed the case for the tether end connectors, especially the TSS–1 satellite.

For the purpose of our discussion, the equivalent circuit model of TSS–1 with respect to transients has been divided into five sections: satellite, electrodynamic tether, tether reel, SETS, and orbiter, as shown in Figure D.7. An in–depth description of each is given below.

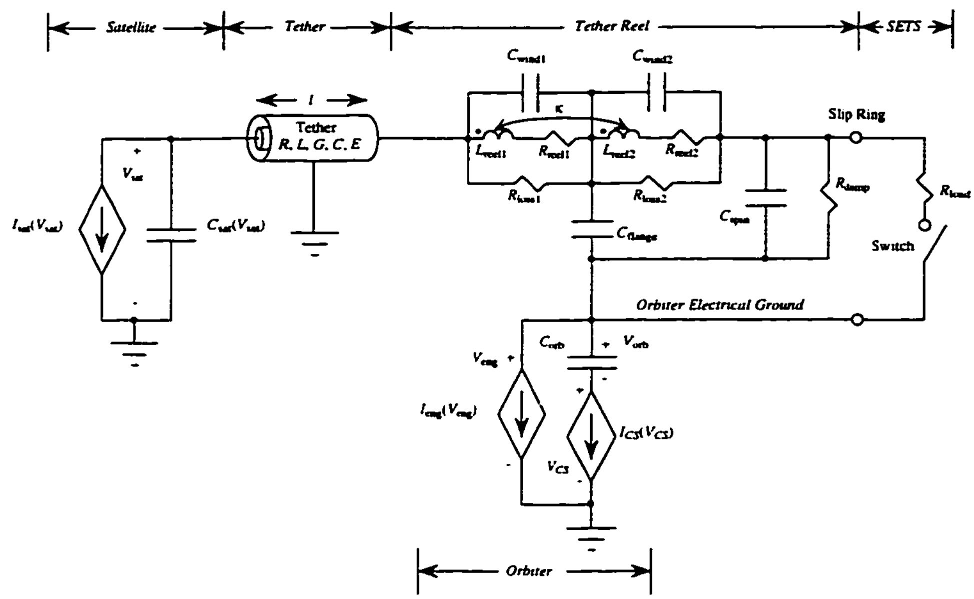

Figure D.7: Equivalent TSS–1 circuit model showing satellite, tether, tether reel, SETS, and Orbiter sections.

D.1.4.1 Satellite Model

For the low tether currents achieved during TSS–1, the satellite can be considered as a spherical Langmuir probe with 0.8–m radius. It has a conducting surface of aluminum skins painted with a highly conductive white thermal control coating [*Dobrowolny et al.*, 1994a] and is assumed to be a good conductor (estimates of paint resistance are less than 1 Ω). As a Langmuir probe, it has a characteristic I–V response or nonlinear conductance. A physical current source model, appropriate for the TSS–1 mission SETS14 FOs, was chosen in order to simulate this nonlinear conductance [*Brundin*, 1963; *Garrett*, 1981]. The model assumes a low potential linear ion ram flux and electron current collection levels which remained close to or less than thermal current capabilities of the satellite. The current to the satellite, I_{sat}, as a function of voltage, V_{sat}, neglecting magnetic, photoelectric, and secondary effects, is given by

$$I_{\mathrm{sat}}(V_{\mathrm{sat}}) = I_i(V_{\mathrm{sat}}) - I_e(V_{\mathrm{sat}}), \tag{D.1}$$

where $I_i(V_{\mathrm{sat}})$ is the incident ion current and $I_e(V_{\mathrm{sat}})$ is the incident electron current on the satellite surface. Equation (D.1), for $V_{\mathrm{sat}} \leq 0$, can also be written as

$$I_{\mathrm{sat}}(V_{\mathrm{sat}}) = A_i j_{ir}\left(1 - \alpha_i \frac{V_{\mathrm{sat}}}{\theta_{ir}}\right) + A_e j_{e0} \exp\left(\frac{V_{\mathrm{sat}}}{\theta_e}\right), \tag{D.2}$$

where

A_i ion collection area (m^2);

j_{ir} ion ram current density ($\mathrm{A/m}^2$)

$= qn_i v_s$, where ion thermal velocity is ignored;

q elementary charge magnitude (1.602×10^{-19} C);

n_i plasma density (per m^3)

$= n_e$;

v_s TSS velocity with respect to flowing plasma (m/s);

α_i ion sheath factor (0 for thin sheath, 1 for thick sheath);

A_e electron collection area (m^2);

j_{e0} electron current density ($\mathrm{A/m}^2$)

$= qn_e\sqrt{\frac{k\theta_e(11600\mathrm{K/eV})}{2\pi m_e}}$;

k Boltzmann's constant (1.38×10^{-23} J/K);

θ_e electron temperature (eV);

m_e electron mass (9.109×10^{-31} kg);

θ_{ir} ion ram energy (eV).

For the TSS–1 satellite, $A_i = \pi r_{\mathrm{sat}}^2$, where r_{sat} is the satellite radius, and represents the cross–sectional surface area of the satellite presented to the flowing mesosonic ion flux; $v_s = 7.5$ km/s; $A_e = 2\pi r_{\text{sat}}^2$ represents twice the satellite cross section to approximately account for field–aligned electron thermal current flow, the small electron gyroradius with respect to satellite radius, and ion wake effects; $\theta_e \approx 0.1$ eV; and $\theta_i \approx 5$ eV. The factor $(1 - \alpha V_{\text{sat}}/\theta_i)$ in Equation (D.2) represents a modification to the satellite ram cross–sectional area, A_i, to account for an increase in the effective impact radius for ions due to an expanded satellite sheath. If variation of satellite potential has little or no effect on ion collection, then α_i will be very small and the ion current is exclusively due to ram ion flux. On the other hand, if satellite potential variation strongly influences ion current collection, then α_i will be close to one and the total ion collection area is strongly influenced by the expanded sheath. This is analogous to the "thin" and "thick" sheath descriptions found in *Garrett* [1981]. If the sheath is "thin" with respect to satellite dimensions, then potential variations will have little effect on current collection, while if the sheath is "thick" then the potential variation has a large effect on current collection. The ion sheath factor, α_i, was determined qualitatively from the computer simulations to be 0.1, approximating a thin sheath. This implies that the expanded sheath over the ranges of plasma density experienced during TSS–1 contributed only little to the ion current collecting area of the satellite. A plot of the satellite I–V response for several different plasma densities can be seen in Figure D.8. Although important in a nominal mission, the electron saturation region is not important to this analysis because of the low positive satellite potentials generally experienced during TSS–1. Exploration of the system I–V response in the electron saturation region is a primary mission objective of TSS–1R [*Dobrowolny et al.*, 1994a], and it has been the subject of much theoretical study [*Banks et al.*, 1981; *Katz et al.*, 1989, 1993; *Laframboise and Sonmor*, 1993].

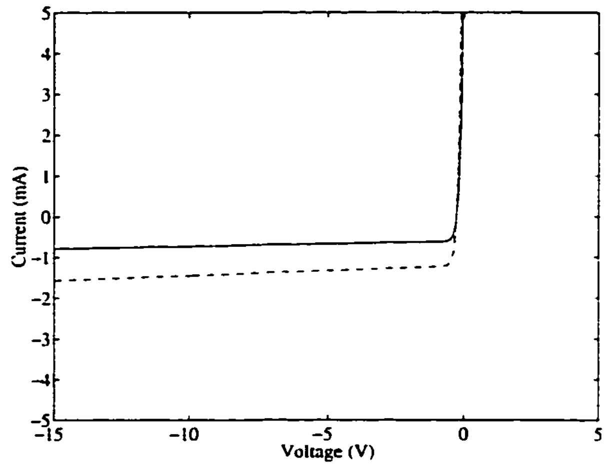

Figure D.8: Plot of current versus voltage for the satellite physical current source for plasma densities: 2.5×10^{11} m^{-3} (solid line), 5.0×10^{11} m^{-3} (dashed line), 7.5×10^{11} m^{-3} (dotted line).

In addition to the physical current source at the satellite describing ion ram and thermal electron currents, there exists an effective nonlinear satellite–to–plasma capacitance, designated C_{sat}, which is caused by sheath effects (Figure D.7). This capacitance can be modeled as a concentric spherical capacitor, with the satellite as the inner conductor and the plasma as the outer conductor separated by the plasma sheath thickness. One of the most recent works to study probe sheath capacitance is that of *Godard and Laframboise* [1986]; however, their analysis assumes a nonflowing plasma and does not provide the analytical expressions required in this analysis. *Crawford and Mlodmosky* [1964] develop an expression for C_{sat}, assuming that the sheath has planar symmetry ($\lambda_D \ll r_{\text{sat}}$), the sheath edge potential is zero, the vehicle velocity greatly exceeds the ion thermal velocity but is much lower than that of the electrons, and the repelled–species density is given by a Boltzmann factor. They also assume that the ion ram current is unchanging with potential, and thus changes in sheath and total surface charge with potential can result only from electron displacements. With these assumptions, they derive the following function for probe/plasma capacitance for $V_{\text{sat}} \leq 0$:

$$C_{\text{sat}}(V_{\text{sat}}) = \left(\frac{A_{\text{sat}}\varepsilon_0}{\lambda_D}\right) \frac{1 - \exp\left(\frac{V_{\text{sat}}}{\theta_e}\right)}{\sqrt{2\left[\exp\left(\frac{V_{\text{sat}}}{\theta_e}\right) - \frac{V_{\text{sat}}}{\theta_e} - 1\right]}}, \tag{D.3}$$

where

A_{sat} satellite area (m^2);

λ_D Debye length (m)

$= \sqrt{\frac{\varepsilon_0 \theta_e}{q n_e}}$;

ε_0 free space permittivity (8.85 x 10^{-12} F/m).

For the TSS–1 mission, the Debye length was in the range of approximately 2 to 6 mm. Therefore C_{sat} had a maximum value of approximately 20 nF at $V_{\text{sat}} \simeq 0$ V, and its effect on the circuit was small but still noticeable.

D.1.4.2 Electrodynamic Tether Model

The insulated, conducting tether was modeled as a coaxial transmission line using distributed lumped elements in a manner similar to *Arnold and Dobrowolny* [1980], *Greene at al.* [1989], and *Savich* [1989]. With this type of model, the outer conductor is formed by the ionospheric plasma which is concentric with an inner conductor on the order of a Debye length away from the center conductor. *James et al.* [1995] state that the tether, sheath, and surrounding plasma form an approximation to a coaxial RF transmission line to the degree that the surrounding plasma can be regarded as the outer conductor. The inner conductor of the TSS tether consists of 10 strands of annealed bare copper [*Bonifazi et al.*, 1994], which together approximate the solid center conductor of the coaxial model. This model consists of the standard resistance, inductance, capacitance, and conductance per unit length for coaxial lines (R, L, C, and G parameters) plus an additional E parameter, which represents the potential generated across each incremental length.

In our analysis, R was the measured series ohmic loss of the tether conductor, and the inductance per unit length, L, was included, whereas this parameter is often ignored [*Arnold and Dobrowolny*, 1980; *Greene at al.*, 1989]. The capacitance per unit length, C, was dependent on the location of the equivalent concentric outer shell formed by the plasma. For the static case, the plasma will be on the order of λ_D away from the conductor, which is greater than the thickness of the tether's dielectric coating. In this case, C can be readily calculated from the cylindrical geometry [*Arnold and Dobrowolny*, 1980]. With a decrease in plasma density, λ_D increases, and hence C will decrease; the converse is also true. Typical values used in this analysis were $R \approx 0.1$ Ω/m, $L \approx 350$ nH/m, and $C \approx 25$ pF/m. The conductance per unit length, G, was ignored since the tether is insulated and not bare. Finally, E varied depending on the orientation of the tether to the geomagnetic field.

D.1.4.3 Tether Reel Model

A simplified electrical model for the wound tether reel, adequate for the analysis of electrical transients presented here, has been developed based on preflight tests [*Bilén et al.*, 1994] and is shown in Figure D.7. The tether reel itself is a 48–inch–long (121.92 cm), fiberglass coated, hollow aluminum spindle which is 4.44 inches (11.28 cm) in diameter and has 38–inch (96.52 cm) aluminum flanges on each end [*Martin Marietta*, 1992]. Both the spindle and its flanges are electrically grounded to the orbiter. A detailed model of the tether wound on the deployer reel would contain every turn of the tether winding and all of the turn to turn mutual inductances and capacitances [*McNutt et al.*, 1974]. However, such a model would be prohibitively large. Therefore, a simpler, two–section network based on the complex representation was used and is valid for our transient analysis here provided that we consider only the primary reel resonance.

In this simple model, each of the two network sections contains half of the primary tether inductance, L_{reel}, and the tether series resistance, R_{reel}, and is coupled by the coupling coefficient κ. Each section has in parallel with it a small interwinding capacitance, C_{wind}, as well as a loss resistance, R_{loss}. Two additional capacitances exist between the wound tether and the reel structure: C_{spin} is the spindle capacitance and essentially represents the capacitance between the first two layers of tether and the spindle, and C_{flange} is the capacitance between the tether at the edges of each tether layer and the reel flange. An additional damping resistance, R_{damp}, is added in parallel with C_{spin} to match the damping coefficient of the premission data.

The reel model was optimized to match responses seen with a fully loaded tether reel, including switching transient level and decay constant, capacitive discharge, and pulse response. Due to the limited deployment of TSS–1, model parameters do not vary appreciably. Typical values are as follows: $L_{\text{reel1}} + L_{\text{reel2}} \approx 12$ H, $R_{\text{reel1}} + R_{\text{reel2}} \approx 2050\ \Omega$, $\kappa \approx 0.35$, $C_{\text{wind1}} = C_{\text{wind2}} \approx 2$ nF, $R_{\text{loss1}} = R_{\text{loss2}} \approx 0.8$ MΩ, $C_{\text{spin}} \approx 8$ nF, $C_{\text{flange}} \approx 5$ nF, and $R_{\text{damp}} \approx 300$ kΩ.

D.1.4.4 SETS Model

The SETS experiment for the SETS14 FO is modeled via a switch and a load resistor. As mentioned in Section D.1.3, SETS14 used the SHUNT load, which means $R_{\text{load}} \approx 15\ \Omega$. Not shown in Figure D.7 is a 12–kHz double–pole RC low–pass filter, which is also modeled in our analysis to account for the small effect of the measurement electronics.

D.1.4.5 Orbiter Model

Similar to the satellite model, the orbiter model (Figure D.7) is also based on physical current sources to model its interaction with the ionosphere at the low tether currents achieved. However, in this case two sources are placed between the orbiter and the ionosphere. The first source, $I_{\text{eng}}(V_{\text{eng}})$ models the interaction of the engine bells with the ionosphere. For I_{eng}, $A_i = A_e \approx 25$ m^2 and represents the collection area of the Orbiter's main engine bells [*Thompson et al.*, 1993], although somewhat larger values have also been suggested [*Hawkins*, 1988]. This value is dependent on the attitude of the orbiter, that is, whether the engine bells are in the Orbiter's ram or wake. For almost all SETS14s, the engine bells were in the ram. All other parameters are the same as for the satellite.

The second source, $I_{CS}(V_{CS})$, discharges the orbiter capacitance, C_{orb}, which is a physical capacitance resulting primarily from the layered dielectric coating on the orbiter cargo bay doors [*Liemohn*, 1976]. The subject of orbiter charging characteristics based on TSS–1 results is currently being analyzed and will be reported separately. For our analysis, we have assumed $A_i = A_e \approx 100$ m^2 for the case of I_{CS}. The orbiter capacitance, C_{orb}, was chosen to be 30 μF, although estimates of C_{orb} vary [*cf.* *Hawkins*, 1988; *Liemohn*, 1976]. Nonetheless, the orbiter end of the system model did not influence the transient voltage response to the same degree as the satellite and tether end. This was due to the fact that during the voltage transient the orbiter potential with respect to the plasma remained fairly constant. That is, typical transient voltage events lasted about 25 ms from switch opening, whereas the time constants for orbiter voltage decay from a charged level could be on the order of seconds. Therefore, selection of an exact value for C_{orb} is not important to this analysis since the orbiter end had little effect on transient response. Also, adding an orbiter engine sheath capacitance similar to C_{sat} was deemed unnecessary since its presence did not influence the transient response and its magnitude was significantly smaller than C_{orb}.

D.1.5 Analysis

Computer simulations were performed using HSPICE (version H93A) optimizing analog circuit simulation software developed by Meta–Software, Inc., which is similar to the standard Berkeley Simulation Program with Integrated Circuit Emphasis (SPICE). This was done by implementing the electrodynamic tether system model, described above and shown in Figure D.7, as an HSPICE deck and performing transient analyses on the circuit (see Appendix E, Section E.1.2 for a listing of this HSPICE deck). Inputs to the deck included only the following parameters: tether voltage, initial tether current, tether length, and ionospheric plasma density. From these input parameters, all necessary component values were calculated. For example, orbiter charging level was determined from the tether voltage and initial tether current. Tether length allowed HSPICE to calculate circuit component values of the tether reel as well as of the tether. The ionospheric plasma current flux used in the satellite and orbiter model, specifically j_{ir} and j_{e0}, were calculated from the ionospheric plasma density.

Figure D.9 shows HSPICE results of the electrodynamic tether system model under the same conditions as Figure D.4. In addition, Figure D.5 gives a comparison between measured transients of SETS14 number 2 and the simulated transients. Good agreement between simulated and measured transients was found for all SETS14s, where by good agreement we mean that the simulated peak transient levels, asymmetries, and the ringing frequency matched measured data within 10–20%.

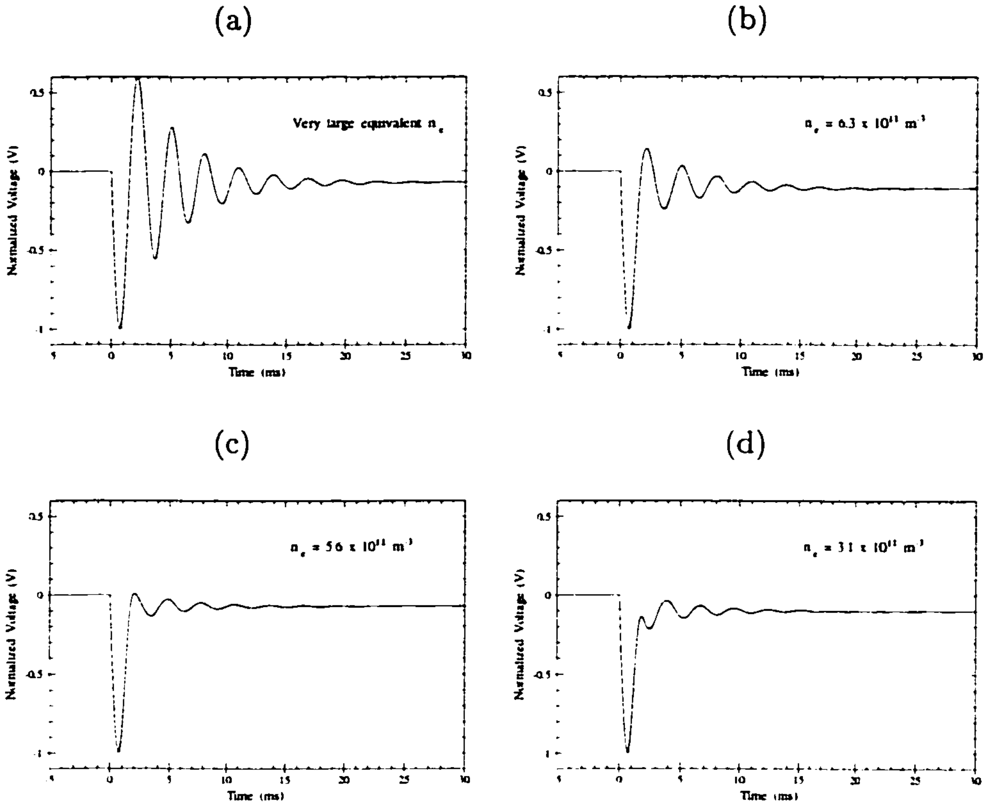

Figure D.9: Simulated switching transients showing characteristics similar to those in Figure 4. Plasma densities are the same as in Figure D.4: (a) very large equivalent n_e; (b) 6.3×10^{11} m^{-3}; (c) 5.6×10^{11} m^{-3}; (d) 3.1×10^{11} m^{-3}.

Although agreement between model and observations is quite good, there are several items which should be mentioned about the electrodynamic tether system model as developed here. First, the model is applicable only to short tether lengths (less than 1 km deployed) and low tether voltages ($|V_{\text{tether}}| \leq 200$ V). Although these two limitations are related (*i.e.*, short tether lengths correspond to low tether voltages), their explanations differ. The length limitation is due to the use of a simple coaxial model for the electrodynamic tether. The effect of the plasma anisotropy on the formation of return currents in the plasma near the tether dielectric coating for an equivalent TEM mode propagation was not modeled. Also, the equivalent tether deployer circuit was optimized for the short deployment length. The voltage limitation, on the other hand, is due to the limitation of the physical current source model which is applicable to low negative voltages.

Second, the model has been applied to nominal ionospheric plasma density levels encountered during TSS–1: from approximately 10^{11} m^{-3} to 10^{12} m^{-3}. This range could most likely be extended except that no TSS–1 data exists outside this range for verification.

Third, in our analysis we used a steady state model for current collection. We believe that this assumption is reasonable because ions have ample time to be accelerated to the satellite. The ion plasma frequency for O^+ ions of density 2×10^{11} m^{-3} is $f_{pi} = \frac{q}{2\pi}\sqrt{\frac{n_i}{\varepsilon_0 m_i}} \approx 23$ kHz, yielding an ion plasma period of $\tau_{pi} \approx 43\ \mu$s. Although moving, the satellite remains in contact with a given flux tube for approximately $\tau_{\text{contact}} = 2r_{\text{sat}}/v_s = 213\ \mu$s, a factor of 5 greater than τ_{pi}, indicating that ions have sufficient time to be accelerated to the satellite before it has moved away [*Ma and Shunk*, 1992]. An additional concern has to do with theoretical and experimental work on applying negative voltage steps to current probes [*Godard et al.*, 1991; *Ma and Shunk*, 1992; *Smy and Greig*, 1968]. These works indicate an initial ion current spike when a voltage step is applied, which then relaxes to a steady state value. Because of tether reel circuit, the TSS–1 satellite voltage had a finite rise time on the order of 0.5 ms, again, much larger than τ_{pi}. Thus no initial ion current spike should occur.

Fourth, the model indicates that large voltages (−200 to −400 V) can be developed across the satellite sheath during transients when the ionospheric plasma density is low. This occurs as the TSS–1 circuit attempts to reverse the tether current and collect ion current at the satellite end. Since Equation (D.2) was developed for low negative voltages, it is reasonable to question the indication of these high negative values. To address this question, we have examined the I–V response of another electrodynamic space tether experiment: the second Cooperative High-Altitude Rocket Gun Experiment (CHARGE–2) [*Kawashima et al.*, 1988; *Raitt et al.*, 1990]. The CHARGE–2 sounding rocket payload was divided into two sections which were electrically connected via an insulated, conducting tether, which was 426 m in length by the end of its flight. Using CHARGE–2 data, *Neubert et al.* [1990] indicate that ion current collected during voltage ramping of the CHARGE–2 mother payload from 0 to −450 V was roughly linear with respect to voltage as in Equation (D.2). Thus we believe that our model's indication of high negative voltage transients across the satellite sheath is realistic.

Fifth, the model is sensitive to the derived values for the satellite and tether capacitances. If the derived capacitances are too large, then the model no longer predicts asymmetric responses when it should, *i.e.*, at lower plasma densities. In addition, if they are too small, then too much asymmetry can occur at the lower densities. The sensitivity to these capacitances can be understood by realizing that since capacitors store charge, they can also source current. When the current reverses in the tether it has two sources: ion collection at the satellite, which is limited by ionospheric plasma density, and these capacitances. If these capacitances were too large, they would be able to provide the current necessary to make up the current deficit due to restricted ion collection at the satellite. Hence these capacitances would hide the ionospheric effects. Thus it is important that the values for these capacitances are properly determined.

Despite these concerns, the electrodynamic tether system model described here has proven successful at replicating the TSS–1 mission transient tether voltage response, showing good qualitative and quantitative agreement.

D.1.6 Summary and Future Work

The electrical transient response of the TSS–1 electrodynamic tether system in low Earth orbit has been investigated experimentally and by computer–based circuit simulations. The electrodynamic tether system model described in this work was implemented as an HSPICE deck, and transient analyses were performed on the implemented circuit. The model has proven successful at replicating the mission transient tether voltage response for the conditions experienced during TSS–1: short tether lengths, low tether voltages, and ionospheric plasma density levels from 10^{11} m^{-3} to 10^{12} m^{-3}.

At the heart of the analysis is an understanding of the physical interaction of the system with the surrounding ionospheric plasma. For the short deployment of TSS–1, the asymmetry of the transient response during low plasma densities was driven primarily by the I–V response of the satellite and to a lesser extent the tether/plasma interaction. The tether voltage transients were caused by the tether reel circuit, which provided a second–order underdamped response. However, if the tether reel were to be replaced with a different circuit, the ionospheric effects would still be present. The orbiter/plasma interaction, which in form is similar to that of the satellite, was not found to influence the TSS–1 transients; this is primarily due to the low tether current. It is anticipated that the interaction of both tether ends with the ionospheric plasma will influence the transient response when the tether is fully deployed during TSS–1R and the tether current reaches 200 mA. It is also anticipated that the 20–km length of the tether will play an important role in the system's transient response.

Future areas of research include improving the electrodynamic tether model to account for longer deployed tether lengths and for the anisotropic plasma of the ionosphere. With an improved tether model, it will be possible to determine how important the tether–plasma interaction will be to the overall transient response at the longer lengths. Adding FPEG and EGA models (see Section D.2 below) to the system model will allow examination of transients when either electron generator is firing or is fired, which did not occur during the SETS14 transients of this analysis.

D.2 Transient Potential Modification of TSS–1 Due to Pulsed Electron Emissions

[This section is adapted from Bilén, S. G., V. M. Agüero, B. E. Gilchrist, and W. J. Raitt, "Transient potential modification of large spacecraft due to electron emissions," *Journal of Spacecraft and Rockets*, **34**(5), 655–661, 1997.]

D.2.1 Introduction

Predicting steady–state and transient spacecraft potentials remains of fundamental importance for a variety of scientific and technological applications since the charging of spacecraft, either due to natural processes or active emission of charge, can alter the performance of sensitive instruments as well as induce possibly damaging charging levels [*Garrett and Whittlesey*, 1986]. The potential of large spacecraft, especially those operating with exposed high voltage systems such as the *International Space Station*, can be dramatically and rapidly modified due to a complex set of external and internal processes [*Hastings*, 1995]. These processes are also of importance to electrodynamic tether systems where active collection of current necessarily involves charging effects and transient switching responses [*Dobrowolny and Melchioni*, 1993; *Bilén et al.*, 1995].

To date, several experimental systems have flown to examine these processes. These systems include the Cooperative High Altitude Rocket Gun Experiments (CHARGE–2) suborbital rocket flown in December 1985 [*Kawashima et al.*, 1988], the Space Power Experiments Aboard Rockets (SPEAR–1) suborbital rocket flown in December 1987 [*Allred et al.*, 1988], and the first Tethered Satellite System (TSS–1) orbital mission flown in August 1992. In their experimental systems, CHARGE–2 and SPEAR–1 applied differential biasing between different parts of the rocket systems to alter their platform potential; CHARGE–2 and TSS–1 also used an electron generator [*Raitt et al.*, 1990].

With the exception of CHARGE–2, however, the spacecraft potential measurements made to date have been of relatively low temporal resolution. Although CHARGE–2 did make high–speed (10 MHz) spacecraft potential measurements, they were taken in short, 100–μs bursts spaced approximately 1 s apart. With the Shuttle Electrodynamic Tether System (SETS) on TSS–1, we were able to sample vehicle potential at fairly high rates (32 kHz) for longer periods of time (1–s bursts). These measurements allowed us to develop a detailed model of the Orbiter–tether–satellite (OTS) system and its interaction with the local plasma environment. This model allows us to predict the response of the TSS system to quickly changing potential modifications. It should be noted that the ability to make these Orbiter potential measurements was facilitated by using the tethered satellite as a remote plasma reference [*Agüero*, 1996].

During TSS–1, we had the unique opportunity to study the system's steady–state and high–speed transient response to spacecraft potential changes. Here we provide first reports of the TSS transient response to the firing of its electron generator into the local low–density ionosphere. In this work, we have expanded the tether system model developed by *Bilén et al.* [1995][1] to include a circuit model of the electron generator as well as a more accurate model of the plasma response at the Orbiter. The *Bilén et al.* model accounts for the variability and asymmetry seen in TSS–1 mission electrodynamic tether switching transients. These transients occurred when the TSS system switched from its current measuring mode to its voltage measuring mode. The observations used in the present analysis were made when TSS–1 was in its voltage measuring mode and the electron generator was actively and quickly modifying the Orbiter potential.

In this next section, the TSS–1 mission and SETS experiment system are introduced and their operation described. We then present the transient observations from the TSS–1 mission used in our analysis, describe the electrodynamic tether system transient model when flying through the ionosphere, and compare experiment with model predictions.

D.2.2 TSS/SETS Experiment System

TSS–1 was a joint mission between NASA and ASI (the Italian Space Agency) which flew onboard STS–46 in August 1992 [*Dobrowolny and Melchioni*, 1993; *Dobrowolny and Stone*, 1994b]. TSS–1 deployed an electrically conductive, 1.6–m–diameter Italian-built satellite to a distance of 267 m above the payload bay of the Space Shuttle *Atlantis*, which was at an altitude of approximately 296 km. The satellite was connected to the shuttle via an electrically conducting insulated wire, and the interaction of this wire with the Earth's magnetic field induced a potential across

[1]The model is also given earlier in this appendix in Section D.1.

the tether reaching values near 60 V which allowed tether currents approaching 30 mA.

Central to the results reported here is the SETS experiment which made high resolution measurements of the induced tether potential using a high impedance voltage monitor [*Agüero et al.*, 1994]. SETS also controlled current flow through the tether using switched loads and active electron beam emissions. To measure I–V tether characteristics, the SETS experiment could selectively place resistive loads between the tether end and the Shuttle's electrical ground, allowing current to flow through the tether from the ionospheric plasma. The load connections were made with and without 1–keV electron beam emissions from the SETS fast pulsed electron generator (FPEG) which was connected to the Orbiter electrical ground. Because of the orbitally induced potential polarity, the TSS–1 satellite was typically biased to attract electrons to its conducting surfaces while the Orbiter either attracted ions to its main engine bells—its primary conducting surfaces—or emitted electrons via the FPEG.

In the present analysis, data from three SETS instruments were used: the DC tether voltage monitor (TVMDC), tether current monitor (TCM), and current mode monitor (CMM). The TVMDC is the primary measurement of tether potential and features 16–bit resolution, 360 Hz sampling rate, and three gain states: $\times 1$, $\times 10$, and $\times 100$. The TCM is a Hall–effect probe which makes no direct contact with the tether circuit. It has a 16–bit resolution and a sample rate of 24 Hz. The CMM is a DC coupled burst measurement of the tether potential applied to the load resistor bank and also has three gain states: $\times 1$, $\times 10$, and $\times 100$. It is an 8–bit digitizer (1–bit resolution: $\times 1$—39.4 V, $\times 10$—3.96 V, and $\times 100$—0.397 V) with a programmable sample rate of up to 10^7 samples/s which can be used to capture transient events.

During TSS–1, the CMM was filtered with a 12–kHz double–pole low–pass filter. The CMM signal is available only through a burst mode (BM) channel which can handle up to 4 captures with a total of 32 ksamples each before downloading them in the telemetry stream. For the experiments discussed in the present analysis, the CMM measurements were made at $\times 10$ and $\times 100$ gains at a rate of 32 kHz. More information on these instruments can be found in *Agüero et al.* [1994].

The SETS fast–pulse electron generator (FPEG) was used to eject electrons from the orbiter to study the TSS current balance and Orbiter charging in different ionospheric conditions and under different TCVM resistive loads. The FPEG has two independent gun assemblies, each capable of emitting 1–keV electrons with a beam current of 100 mA per assembly. Each gun assembly has a separate filament power supply, high–voltage power supply, and solid-state high–voltage switch. Beam emission is controlled by the high–voltage switch which, when on, connects the filament directly to the high–voltage power supply. The FPEG electron beam can be pulsed at high rates due to the short, 100–ns rise– and fall–times of the high–voltage switch. The on– and off–times of the pulses can be programmed separately [*Agüero et al.*, 1994; *Banks et al.*, 1987]. For the data reported here, the FPEG was commanded to fire one filament (100 mA) with an on– and off–time of 13.1 ms, giving a pulse frequency of 38.2 Hz. The beam heads are aimed 23 degrees up from the Orbiter's $+y$–direction such that it fires over the starboard wing. Figure D.10 shows the location of the FPEG in the Orbiter's cargo bay.

The TSS tether deployer system consists of a large tether storage reel which is mechanically turned to wind tether on and off. This reel is a 121.9–cm–long, fiberglass coated, hollow aluminum spindle which is 11.3 cm in diameter and has 96.5–cm aluminum flanges on each end [*Martin Marietta*, 1992]. Both the spindle

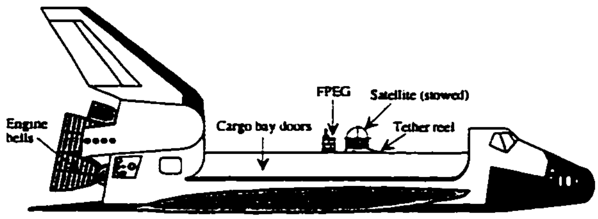

Figure D.10: Figure of TSS–1 showing the location of the satellite (stowed), tether reel, SETS FPEG, cargo bay doors, and engine bells.

and its flanges are electrically grounded to the Orbiter. Fully wound before satellite deployment, the system contains 22 km of insulated tether wrapped on the reel and can be considered electrically as an inductor of approximately 12 H with parasitic capacitances and resistances [*Bilén et al.*, 1995].

D.2.3 Observations

The observations used in this analysis were chosen because they met four criteria: 1) the FPEG was placed in a pulsing mode rather than a DC firing mode, 2) the TSS system was in a region of low local plasma density, 3) the CMM captured high speed voltage data, and 4) the CMM data were not limited by instrument resolution nor were saturated. Two such observations met these criteria and are listed in Table D.2. They occurred during one of the TSS–1 experiments called joint functional objective number 2 (JFO2, also called DEP1), of which there were a total of 98 performed. (A more detailed description and complete plots of JFO2 may be found in *Agüero et al.* [1994].) More specifically, the events occurred during JFO2 step 2 which characterizes the FPEG's ability to support current flow through the tether system. In this step, FPEG beam emissions occur as each TCVM load resistor is switched in and then out individually. In addition, a quick SHUNT closure ($\approx$ 40 ms in length) occurs at the beginning of the step and at this time the CMM captures data. For most of the JFO2 executions, the FPEG emitted a DC beam; however, there were a total of seven executions where the beam was instead pulsed at 38.2 Hz. Of these seven, five occurred in a region of low local plasma density such that the Orbiter potential could be quickly modified by the FPEG. Although the CMM captured high speed data during these five, in only two were the CMM data not limited by instrument resolution, allowing rigorous analysis.

Table D.2: Summary of TSS–1 Joint Functional Objective 2 used in analysis of transients due to FPEG firing.

DEP1 Event	GMT, ddd/hhmm:ss	Burst Mode Time, ddd/hhmm:ss	Estimated Density, $\times 10^{10}$ m^{-3}	Tether Length, m
30	217/2310:23	217/2312:05	3.2	25.9
31	217/2318:08	217/2319:50	5.2	44.7

These two observations are shown in Figure D.11a and D.11b which show the Orbiter potential modification via the FPEG pulsing. Shown in the figure is the tether potential, tether current, load resistor in use, Greenwich Mean Time (GMT), and the CMM captured transient response for the observations. The vertical dotted line in the figure is the time when the CMM burst data is collected. Also included in the figure is the simulated transient response which will be discussed later in this paper. Although the quick modification of the Orbiter potential can be seen in the tether potential measurement which was collected with the 360–Hz sampling rate TCVM, the data is aliased and is not easily resolved. The CMM measurement, which was collected at 32 kHz, shows that the Orbiter potential is easily modified by the FPEG and also that a second–order ringing response is excited by this firing. This second order–ringing has been shown to be the pulse response of the TSS tether deployer system [*Bilén et al.*, 1994], which is similar to the pulse response of a transformer [*Grossner*, 1983].

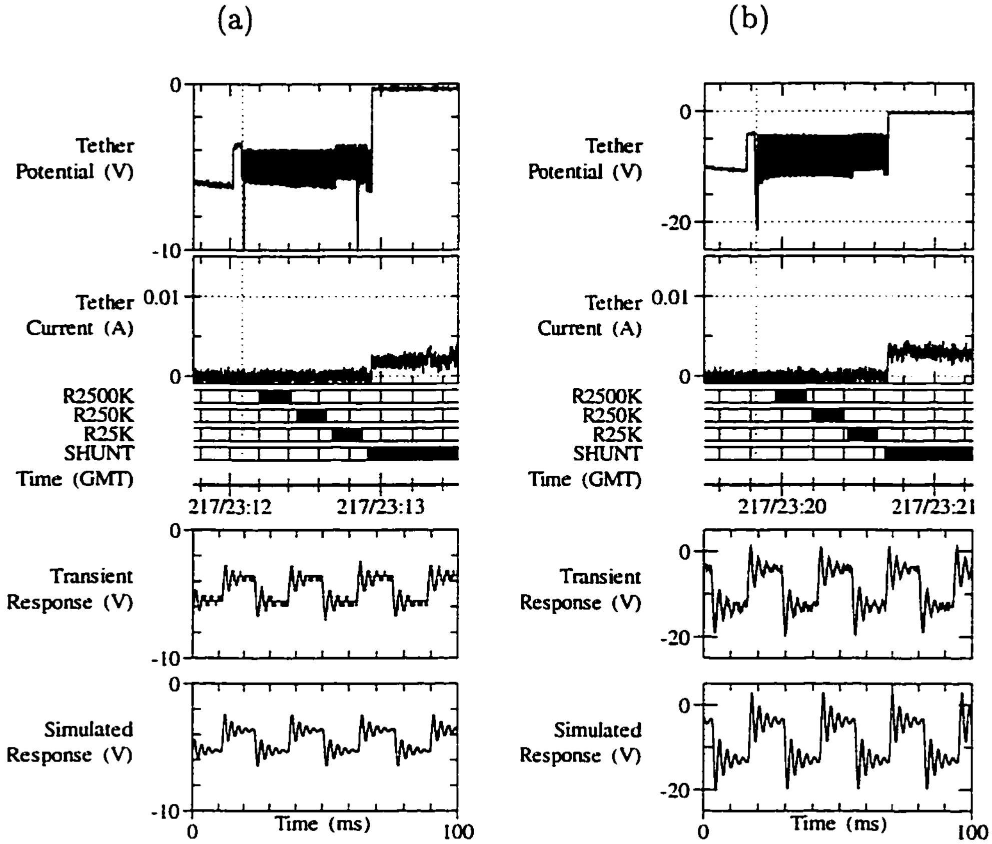

Figure D.11: Orbiter potential modification via electron generator pulsing for (a) JFO2 number 30 and (b) JFO2 number 31.

In order to analyze these observations, we must know the local ionospheric plasma density around the Orbiter. Normally, direct density measurements were made by the Research on Electrodynamic Tether Effect's (RETE) Langmuir probe. At the time of these observations, however, no direct density measurement was available. Thus, we estimate it using the technique of *Thompson et al.* [1993]. Their approach requires that the Orbiter be moving with a supersonic velocity, v_s, with respect to the ambient ions. They then assume an effective ion collection area, A_i, of the orbiter engine bells, and state that the ion ram current, I_{ram}, collected to the uncharged Orbiter is equal to the tether current, I_{tether}, such that

$$n_e = \frac{I_{\text{tether}}}{A_i q v_s}. \tag{D.4}$$

Since reasonable estimates of n_e from Equation (D.4) require $I_{\text{tether}} = I_{\text{ram}}$, two conditions affecting I_{tether} must be satisfied: the FPEG must not be firing and I_{tether} must not be limited by tether resistance. In order to satisfy the first condition, we cannot use I_{tether} from JFO2 step 2 since the FPEG is firing. Step 3 of JFO2, however, follows the same switching sequence as step 2 but without FPEG emissions and, although separated by 140 s, a reasonable value of I_{tether} and hence plasma density can be obtained during step 3. The second condition—that I_{tether} not be limited by tether resistance—was generally easily met when TSS–1 flew through regions of low plasma density. Because both conditions can be met, Equation (D.4) provides a reasonable estimate of plasma density for the observations reported in this Section (involving low Orbiter charging and available tether *emf* of less than 10 V). Estimates obtained are listed in Table D.2. The conclusion that the observations during this time period took place in low plasma density conditions is corroborated by observations discussed by *Oberhardt et al.* [1993] using the Shuttle Potential and Return Electron Experiment (SPREE) [*Oberhardt et al.*, 1994].

During the time of these observations, TSS was in its initial deployment phase and the orientation of the Shuttle was such that its engine bells were directed in the ram direction with its nose pitched down 37°, placing the payload bay into a deep wake. The satellite itself was in close proximity to the Shuttle and firing a neutral gas thruster to propel it away from the Orbiter. However, the neutral gas density in the payload bay was already sufficiently low to allow instruments with exposed high–

voltage systems to be turned on safely. Further, simultaneous FPEG operations with certain Orbiter thruster firings were separately shown to enhance plasma density in the payload bay using the SPREE instrument [*Oberhardt et al.*, 1993]. If significant density enhancement had occurred during the observational period discussed here, spacecraft positive charging would have been reduced.

D.2.4 Electrodynamic Tether System Model

We have expanded the model developed by *Bilén et al.* [1995] (given in Section D.1.4) to include a circuit model of the FPEG as well as a more complete electrical model of the Orbiter. Their model was used to successfully account for the ionosphere induced variability and asymmetry seen in TSS–1 mission electrical transients—the transient case which occurred when the TSS system switched between its current measuring mode and its voltage measuring mode. When TSS–1 was in the current measuring mode, a selectable load impedance (either 15 Ω, 25 kΩ, 250 kΩ, or 2.5 MΩ) was placed between the tether and the Orbiter which allowed a measurable current to flow. In the voltage–measuring mode, TSS–1 was in a configuration where only the high total impedance ($\simeq$ 35 MΩ) of the SETS and deployer core equipment (DCORE) voltage monitors was connected between the tether and the Orbiter end. In this case, negligible current flows along the tether and almost all of the voltage drop in the system occurs across this high impedance load allowing an accurate measurement of tether potential. The observations used in the present analysis were made when TSS–1 was in its voltage measuring mode.

For the purpose of our discussion, the expanded equivalent circuit model of TSS–1 has been divided into six sections: 1) satellite, 2) electrodynamic tether, 3) tether reel, 4) SETS, 5) Orbiter, and 6) FPEG as shown in Figure D.12. Since the first three have not been modified and are described in detail in *Bilén et al.* [1995] (and also in Sections D.1.4.1–D.1.4.3). The remaining three have been modified and more rigorous descriptions of these are given below. In our description, we will begin with the Orbiter section since it is most important and move in a counter–clockwise fashion through the remaining sections of Figure D.12. It should be noted that the model described here is applicable to transient analyses, *i.e.*, short timescales (10's of ms or less). For longer timescales (100's to 1000's of ms), the reader is referred to other models such as that developed by *Agüero* [1996].

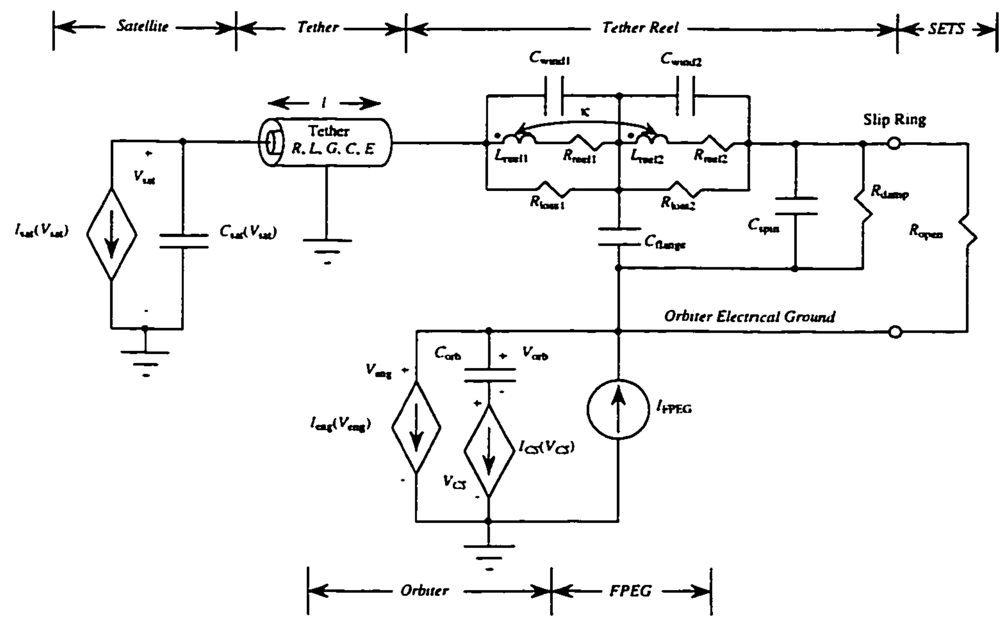

Figure D.12: Equivalent TSS–1 circuit model showing satellite, tether, tether reel, SETS, Orbiter, and FPEG sections.

D.2.4.1 Orbiter Model

The Orbiter surfaces (*i.e.*, its main engine bells and cargo–bay doors, see Figure D.10) can be considered as probes which are immersed in the surrounding ionospheric plasma and as such have characteristic I–V responses or nonlinear conductances. In order to simulate these nonlinear conductances, each conductance is based on a physical current source model as developed by *Brundin* [1963] and *Garrett* [1981]. This source model assumes a low potential linear ion ram flux and electron current collection levels which remain close to or less than the thermal current capabilities of the Orbiter, which is appropriate for the cases studied here.

In the Orbiter model, two physical current sources are placed between the Orbiter electrical ground and the ionosphere. The first current source represents the interaction of the Orbiter's engine bells with the ionosphere. (Although there are other conducting surfaces, the Orbiter's primary conducting surfaces are the engine bells.) The current to the engine bells, I_{eng}, as a function of voltage, V_{eng}, with respect to the local plasma and neglecting magnetic, photoelectric, and secondary effects, is given by

$$I_{\text{eng}}(V_{\text{eng}}) = I_I(V_{\text{eng}}) - I_E(V_{\text{eng}}). \tag{D.5}$$

Equation (D.5), for $V_{\text{eng}} \leq 0$, can be written as

$$I_{\text{eng}}(V_{\text{eng}}) = A_i j_{ir}\left(1 - \alpha_i \frac{V_{\text{eng}}}{\theta_{ir}}\right) + A_e j_{e0} \exp\left(\frac{V_{\text{eng}}}{\theta_e}\right), \tag{D.6}$$

where $j_{ir} = q n_i v_s$ when the ion thermal velocity is ignored and

$$j_{e0} = \left(q n_e \sqrt{\frac{k\theta_e(11600\text{K/eV})}{2\pi m_e}}\right).$$

For the first source, $A_i = A_e \approx 25\ \text{m}^2$ based on TSS–1 data and represents the approximate effective collection area of the Orbiter [*Thompson et al.*, 1993], although somewhat larger values for collection area have also been suggested [*Hawkins*, 1988; *Thompson et al.*, 1992]. The value A_i represents the approximate cross-sectional surface area presented to the flowing mesosonic ion flux and thus is dependent on the attitude of the Orbiter, that is, whether the engine bells are in the Orbiter's ram or wake. For the present observations, the engine bells were in the ram, therefore the full value of A_i is used. Other values for TSS–1 are $v_s = 7.5$ km/s, $\theta_e \approx 0.2$ eV, and $\theta_{ir} \approx 5$ eV.

The factor $(1 - \alpha_i V_{\text{eng}}/\theta_{ir})$ in Equation (D.6), where $V_{\text{eng}} < 0$, represents a modification to the effective engine–bell ram cross–sectional area, A_i, to account for an increase in the effective impact radius for ions due to an expanded plasma sheath. The ion sheath factor, α_i, is small if variation of engine bell potential has little or no effect on ion collection. In this case the ion current is exclusively due to ram ion flux. On the other hand, α_i is close to unity if engine bell potential variation strongly influences ion current collection. In this case, the total ion collection area includes the expanded plasma sheath. These two cases are analogous to the "thin" and "thick" sheaths described in *Garrett* [1981]. If the sheath is "thin" with respect to engine bell dimensions, then potential variations will have little effect on ion current collection, while if the sheath is "thick" then the potential variation has a large effect on ion current collection. The ion sheath factor, α_i, was determined qualitatively from the computer simulations to be 0.1, approximating a thin sheath. This choice of α_i implies that the expanded sheath contribution is only a fraction of the ion collection when the effective collecting area of the engine bells for these low charging magnitude events is taken as 25 m^2 (as assumed by *Thompson et al.* [1993]). Published work by *Agüero* [1996] provides an explanation for the reasonableness of this assumption by identifying in detail the current collection contributions to the charging balance for the range of negative charging events observed during TSS–1. The result being that the 25–m^2 area is a good average for the effective current collecting area of the Orbiter (including sheath contributions) when the Orbiter is charged to a magnitude in the range of the available *emf* for these events.

It should be noted that, as written, Equation (D.6) is strictly valid only for voltages $V_{\text{eng}} \leq 0$. To extend Equation (D.6) to $V_{\text{eng}} > 0$, which is necessary since FPEG emissions charge the Orbiter positively, we specify an electron saturation region such that the exponential term does not increase indefinitely. We specified this region in our current source model as $(I_{\text{eng}})_{V_{\text{eng}}>0} = A_e j_{e0}(1 + \alpha_e V_{\text{eng}}/\theta_e)$, where $A_e j_{e0}$ represents the thermal electron current collected by the Orbiter's engine bells which is allowed to grow as V_{eng} increases. The ion current term becomes insignificant in the positive regime since the electron current term dominates. With this addition, we obtain an I–V response similar to the classic cylindrical Langmuir probe I–V response.

The second current source, $I_{CS}(V_{CS})$, discharges the Orbiter capacitance, C_{orb}, which is a physical capacitance resulting primarily from the layered dielectric coating on the Orbiter cargo bay doors [*Liemohn*, 1976]. For our analysis, we have assumed $A_i = A_e \approx 100$ m^2 for the case of I_{CS}. The Orbiter capacitance, C_{orb}, was set at 30 μF, which is a reasonable value given the works of *Hawkins* [1988] and *Liemohn* [1976]. The initial voltage applied to C_{orb} was set at the value to which the Orbiter was charged. It should be noted that more recent work by *Agüero* [1996] indicates that C_{orb} may have different charging and discharging capacitances. These results, however, do not affect our circuit model since we are dealing with very short, transient events and not the longer time responses of that work.

D.2.4.2 FPEG Model

The FPEG is modeled as a 100–mA, pulsed, electron current source with a 38.2–Hz pulse frequency, a 50% duty cycle, and 100 ns rise and fall times. It connects the Orbiter electrical ground and the ambient plasma medium represented in our model by earth ground. In effect, when the FPEG current source is on, *i.e.*, the FPEG is firing, it is able to simply "dump" charge since the source is not voltage dependent.

D.2.4.3 SETS Model

The configuration of the SETS experiment can be modeled for the present observations by the 35–MΩ internal impedance of its and DCORE's voltage monitors, indicated in Figure D.12 as R_{open}. Also modeled, but not shown in Figure D.12, is a 12–kHz double–pole RC low–pass filter which is part of the SETS measurement electronics. This filter was found to have only a minimal effect on the observations reported here.

D.2.5 Analysis

Computer simulations were performed using an analog circuit simulation software package similar to the standard Simulation Program with Integrated Circuit Emphasis (SPICE). These simulations were done by implementing the electrodynamic tether system model, previously described and shown in Figure D.12, as a SPICE input deck and performing transient analyses on the circuit (see Appendix E, Section E.1.3 for a listing of this HSPICE deck). By modeling the response of the TSS–1 system via computer simulation, we were able to determine the relevant importance of each section of the TSS system during its transient response from FPEG emission. In the present analysis, we were able to determine that the Orbiter/ionosphere interaction was the primary effect on the overall circuit and that the satellite and tether interaction had very little effect when TSS–1 was in its voltage mode and the FPEG was quickly modifying Orbiter potential by firing into the local ionosphere. The importance of the Orbiter/ionosphere interaction is to be expected since only μA–level current flows through the tether in this mode, substantially reducing the effect of satellite/ionosphere interaction. This result is in contrast with what *Bilén et al.* [1995] (Section D.2.4) found when TSS–1 switched from its voltage to its current mode. In that case, the transient response was due primarily to the satellite/ionosphere interaction and the tether; the Orbiter effect was not significant.

Good qualitative agreement between the simulated and measured transients was found, in that the simulated transient voltage levels and ringing frequency matched the measured data within 10–20%. Figure D.11 shows the comparison between the measured transients of the two observations and the simulated transients. Finding agreement between simulation and measurement allowed us to verify the TSS circuit model which we developed and gave us confidence in the parametric studies (described below) which we performed using the model.

There are several limitations of the electrodynamic tether system model as developed here which may affect the agreement between the computer simulations and the observations as well as the results of the parametric studies. First, several of the parameter values used in the current source models are estimates rather than exact values since exact values are currently still the subject of active research. Specifically, the values for for Orbiter effective collection areas and Orbiter capacitance are estimates taken from the literature. Second, the derivation of plasma density has some amount of uncertainty due to the temporal displacement between the CMM measurement in JFO2 step 2 and the tether current measurement made in JFO2 step 3, from which plasma density is calculated. Fortunately, since $n_e \propto 1/A_i$, any error in plasma density based on the estimate of Orbiter engine bell collection area is not compounded in the engine bell current source model since $I_{\text{eng}} \propto n_e A_i$. Third, the FPEG model is idealized since the simplifying assumption was made that 100 mA of electron current is always ejected into the local ionosphere when the FPEG is firing. This simplifying assumption may not always be valid due to filament efficiency. Fourth, this model is limited to low Orbiter charging levels since the voltage dependent current source models used were developed for low charging levels. For conditions of higher positive and negative charging, the sources would need to be modified [*Agüero*, 1996].

Despite these limitations, our work shows that this simple circuit model can be used to accurately replicate, and hence also predict, transient spacecraft potential changes. We found that the Orbiter–ionosphere circuit, and specifically its current collection elements, was able to accurately model the magnitude of the transient spacecraft potential steps. Using our model, we performed parametric studies of the magnitude of spacecraft potential changes for varying plasma densities, FPEG currents, and electron collection areas. The results of these studies are shown in Figures D.13–D.15, respectively. In each of these studies only one parameter was varied while the others were the same as in event 31 and held constant. In each of these plots, model results are shown with the filled circles and the data point from event 31 is shown with the open square. It should be noted that these studies are included to show the capabilities of a relatively simple model and to examine trends. Indeed, these studies do indicate high levels of charging which exceed the limits of the low voltage Orbiter model.

In each of the parametric studies, the change in the spacecraft potential from floating potential as the FPEG is pulsed is measured. In Figure D.13, we see that

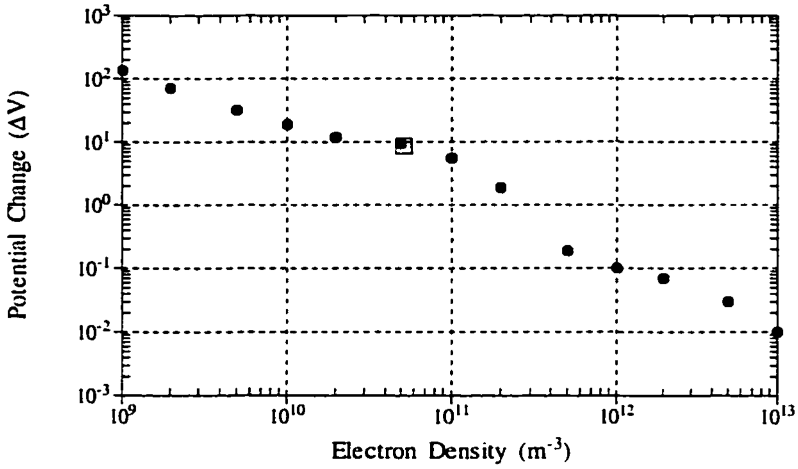

Figure D.13: Simulated spacecraft potential change due to FPEG pulsing as a function of plasma density (all other parameters are the same as Event 31).

as the plasma density (n_e) increases from a very low value ($\sim 10^9$ m^{-3}) to a high value ($\sim 10^{13}$ m^{-3}), the potential change drops from a very high value (> 100 V) to an almost negligible amount (< 0.01 V). This result indicates that in low densities the Orbiter could charge highly positive due to FPEG pulsing. In addition, the model predicts that the Orbiter transient charging due to FPEG pulsing would be greatly diminished if there is a locally enhanced electron flux. One other thing to note from this plot is expected transient charging levels for normal nighttime (low 10^{11} m^{-3}) and daytime (high 10^{11} m^{-3}) conditions. During nighttime, transient charging could be a few volts, whereas during daytime, only a few tenths of volts is expected. Figure D.14 shows that the magnitude of the FPEG discharge current (I_{FPEG}) also affects the magnitude of the potential change, increasing the magnitude as the current increases. Increasing the electron and ion collection area (A_e and A_i), as shown in Figure D.15, reduces the magnitude of the potential change. While these

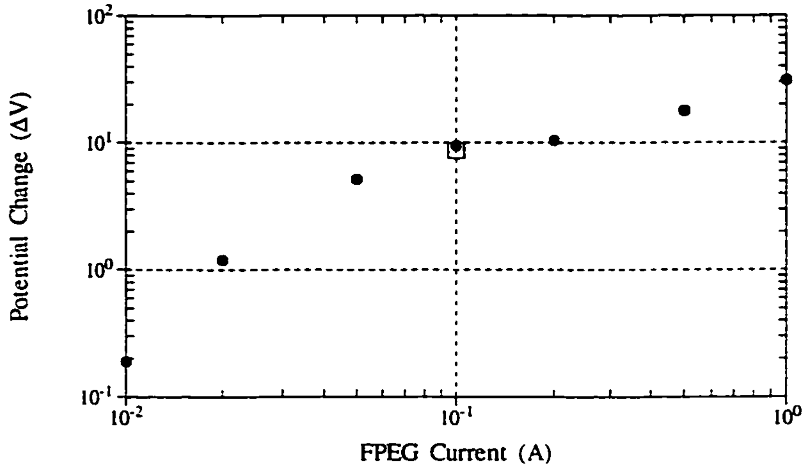

Figure D.14: Simulated spacecraft potential change due to FPEG pulsing as a function of FPEG current (all other parameters are the same as Event 31).

results are to be expected, they do show the importance of our model in predicting transient spacecraft potential changes.

In a manner similar to that presented here, circuit models can be developed of the interaction of other spacecraft, and in particular large spacecraft, with the ionosphere. In developing these models, it is extremely important to not only use proper current sources to model the spacecraft–plasma interaction, but also to identify any spacecraft subsystems which may be affected by potential changes and other spacecraft–plasma interactions. For example, the pulse response of the TSS tether reel subsystem elicited by the rapidly changing Orbiter potential provided up to a factor of 1.6 times the step voltage (*e.g.*, a 10–V change in Orbiter potential could result in 16–V peak voltage across the system).

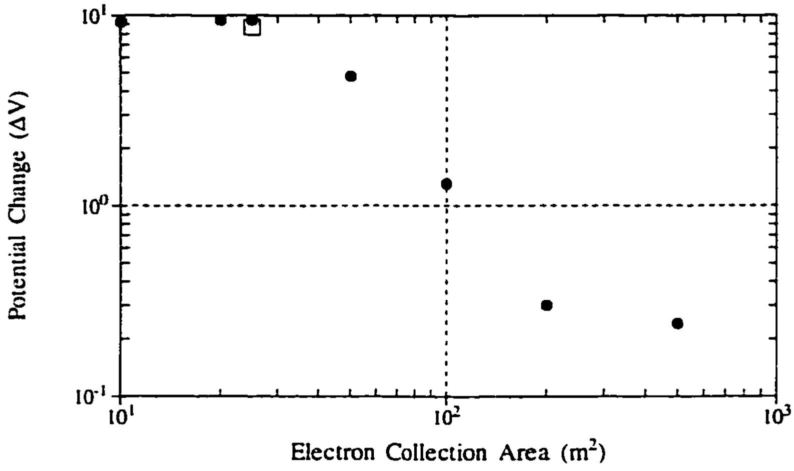

Figure D.15: Simulated spacecraft potential change due to FPEG pulsing as a function of electron collection area (all other parameters are the same as Event 31).

D.2.6 Summary

The electrical transient response of TSS due to the firing of an electron generator into the ionosphere has been investigated experimentally and by computer-based circuit simulations. Due to the low density of the surrounding ionospheric plasma, the FPEG was able to quickly modify the potential of the Shuttle orbiter. The resulting voltage transients were measured by the SETS experiment which could selectively sample the system voltage in high speed bursts. The computer simulation shows that the electrical transient response of the system is due to a combination of both the TSS electrical circuit and the modification of the Shuttle potential due to the FPEG firing into the surrounding ionospheric plasma. The computer model has proven successful at replicating the Orbiter transient voltage response for the conditions experienced during TSS-1. In addition, we were able to determine that when TSS-1 was in its voltage mode and the FPEG was quickly modifying Orbiter potential by firing into the local ionosphere 1) the Orbiter–ionosphere interaction was the primary effect on the overall circuit and 2) the satellite and tether interaction had very little effect. Using our model, we performed parametric studies of the magnitude of spacecraft potential changes for varying plasma densities, FPEG currents, and electron collection areas.

The results presented here have implications for the use of electron generators that actively modify the potential of its host spacecraft. These implications are based on an understanding of the physical interaction of TSS with the surrounding ionospheric plasma. For the TSS–1 case where the tether system was in its voltage mode and the FPEG was firing into a local ionosphere region of low plasma density, the voltage transient response was driven primarily by the I–V response of the Orbiter and the second-order underdamped response of the tether reel circuit. If the tether reel were to be replaced with a different circuit, however, the ionospheric effects described here would still be present, *i.e.*, the magnitude of the spacecraft potential changes. From our results, we have shown that transients can be caused not only by switching of currents in a tethered system, but also by electron emissions from one of the endpoints that quickly modify its potential.

APPENDIX E

Simulation Input Files

This appendix contains listings of the simulation input files for the two types of numerical simulations performed in support of this work: SPICE circuit simulation and XOOPIC particle–in-cell plasma simulation. Limited descriptions of the files are given; they are included here for documentation purposes.

E.1 SPICE Simulation Decks

This section documents the SPICE simulation input decks that were used for the simulations in this thesis. Because many variations of SPICE exist, each with its own capabilities and features, these decks are tailored to the circuit simulator used in this work: HSPICE. However, it may be possible to modify them to run under different SPICE simulators.[1] HSPICE was chosen because it is available on the Computer Aided Engineering Network (CAEN) in the College of Engineering at the University of Michigan. Because HSPICE is primarily used for simulating large integrated circuits, it is particularly suited for the large ladder networks of the tether transmission lines. In addition, the flexibility and ease of specifying elements with functional dependence made HSPICE particularly attractive in this research. When

[1] An excellent reference which details some of the differences between several major SPICE–based codes is *Kielkowski* [1994].

this work was begun, the software was owned and developed by Meta–Software, Inc. of Campbell, CA. In 1996, Meta–Software was purchased by Avant! Corporation of Sunnyvale, CA. Information specific to HSPICE may be found in the *HSPICE User's Manual* [*Meta–Software*, 1996a,b,c]. General information on SPICE codes may be found in the numerous books available on the code and its applications [*e.g.*, *Tuinenga*, 1988; *Kielkowski*, 1994].

It should be noted that the HSPICE input decks given in the following sections are often used to simulate a variety of aspects of the different circuits. This requires commenting out (adding a "*" in front of the line) certain portions of the code for the different simulation runs. The codes as presented here contain all the pieces necessary to perform the simulations, but in order to obtain the desired responses, will require some lines to be uncommented and others to be commented out. Some of the options affect convergence, some accuracy, and others speed. All must be used in a knowledgeable manner.[2] In addition, some of the commented lines were used during trouble–shooting sessions or when examining "what if?" scenarios.

One additional comment must be made concerning the formatting of these listings. All lines that begin with --> are a continuation of the previous line. Should the listing be used to generate an executable HSPICE input deck, these lines should be connected to the previous line by removing any spaces and line breaks. It is necessary to use this notation here because some of the line lengths are very long. Although HSPICE has a line–continuation character (a "+" in the first column), this apparently cannot be used within quoted strings.

[2]Again, see *Kielkowski* [1994] for methods of overcoming obstacles and interpreting outputs with SPICE.

E.1.1 Nonlinear Tether TL Model

This HSPICE input deck was utilized in the analyses of Chapter V and is based on the incremental model of Figure 4.13.

```
*  Modular circuit for examining conductor-insulator-plasma
*  transmission--line systems


**************************************************
*  status control options
*
.option post
*  if timestep problem, use one of these options
*.option lvltim=1
.option method=gear
*.option gshunt=1e-9
*.option dvdt=4
*  if convergence problem, use this option
*.option converge=2
*.option dcon=1
.option rmin=1.0e-15
*  since got numbers smaller than 1e-28
.option epsmin=1e-35
**************************************************


**************************************************
*  variable declarations
*  where:
*
*  itether      tether current (A)
*  vtether      tether voltage (V)
*  elecden      electron density (per m^3)
*  elecden2     2nd electron density (per m^3)
*  lentether    tether length (m)
*  incvolt      incremental tether emf (V/m)
*  electemp     electron temperature (eV)
*  electempk    electron temperature in Kelvin (K)
*  pi           pi value
*  epsilon0     permittivity of free space (F/m)
*  mu0          permeability of free space (H/m)
*  echrg        electronic charge (C)
*  k_boltz      Boltzmann's constant (J/K)
*  const_e      e value
*  elecmass     electron mass (kg)
*  clight       speed of light (m/s)
*
.param
+  itether=1u
*+  vtether=-4.0
+  elecden=1e12
+  elecden2=1e10
*+  lentether=44.7
*+  incvolt='vtether/lentether'
+  incvolt = -0.2
+  electemp=0.1
+  electempk='electemp*11600'
+  pi=3.14159265359
+  epsilon0=8.852e-12
```

```
+  mu0 = '4*pi*1.0e-7'
+  echrg=1.602e-19
+  k_boltz=1.38e-23
+  const_e=2.71828182846
+  elecmass=9.109e-31
+  clight=2.998e8
**************************************************


**************************************************
*  compute plasma parameters for given plasma density
*
*  lambdad       Debye length (m)
*  lambdad2      2nd Debye length (m)
*  wpe           electron plasma frequency (rad/s)
*  wpe2          2nd electron plasma frequency (rad/s)
*  dm            magnetic skin depth (m)
*  dm2           2nd magnetic skin depth (m)
*  vte           electron thermal velocity (m/s)
*
.param
+ lambdad='sqrt(epsilon0*electemp/(elecden*echrg))'
+ lambdad2='sqrt(epsilon0*electemp/(elecden2*echrg))'
*  note: equation for wpe calculated in this manner to avoid
*        the small number that echrg^2 would cause
+ wpe='sqrt((elecden*echrg)/(epsilon0)*(echrg/elecmass))'
+ wpe2='sqrt((elecden2*echrg)/(epsilon0)*(echrg/elecmass))'
+ dm='clight/wpe'
+ dm2='clight/wpe2'
+ vte='sqrt(k_boltz*electempk/elecmass)'
**************************************************


**************************************************
* transmission line impedance and parameters
* TSS tether values
*
*  r_a           radius of tether center conductor (m)
*  r_d           radius of tether dielectric (m)
*  rsh_min       minumum sheath size (m)
*  rsh_min2      2nd minumum sheath size (m)
*  epd           relative permittivity of insulation (unitless)
*  Cd            capacitance of dielectric (F)
*  Csh           capacitance of static sheath (F)
*  Csh2          2nd capacitance of static sheath (F)
*  C0            static capacitance (F/m)
*  C02           2nd static capacitance (F/m)
*  L0            static inductance (H/m)
*  L02           2nd static inductance (H/m)
*  Z0            static TL impedance (ohms/m)
*  Z02           2nd static TL impedance (ohms/m)
*  R0            measured resistance per unit length (ohms/m)
*  Rp            plasma resistance (ohms/m)
*  je_omlc       OML electron current denisty parameter
*  je_omlc2      2nd OML electron current denisty parameter
*  Csh_const     constant for Csh calculation (unitless)
*  Csh_const2    2nd constant for Csh calculation (unitless)
*
.param
+ r_a=0.00043
+ r_d=0.00127
+ rsh_min='2*lambdad'
+ rsh_min2='2*lambdad2'
```

```
+ epd=2.5
+ Cd='2*pi*epd*epsilon0/(log(r_d/r_a))'
+ Csh='2*pi*epsilon0/(log(rsh_min/r_d))'
+ Csh2='2*pi*epsilon0/(log(rsh_min2/r_d))'
+ C0='(Cd*Csh)/(Cd+Csh)'
+ C02='(Cd*Csh2)/(Cd+Csh2)'
+ L0='(mu0/(2*pi))*log(((dm+r_a)/2)/r_a)'
+ L02='(mu0/(2*pi))*log(((dm2+r_a)/2)/r_a)'
+ Z0='sqrt(L0/C0)'
+ Z02='sqrt(L02/C02)'
*  for lossless, set R0 and Rp to 1e-5
*+ R0=0.1026
+ R0=1e-5
*+ Rp=5e-4
+ Rp=1e-5
+ je_omlc='-2*sqrt(2)*r_d*elecden*
-->       echrg*vte*sqrt(echrg/(k_boltz*electempk))'
+ je_omlc2='-2*sqrt(2)*r_d*elecden2*
-->        echrg*vte*sqrt(echrg/(k_boltz*electempk))'
+ Csh_const='sqrt(3)*pwr((epsilon0/(echrg*elecden)),(5/12))*
-->         pwr(r_a,(1/6))'
+ Csh_const2='sqrt(3)*pwr((epsilon0/(echrg*elecden2)),(5/12))*
-->          pwr(r_a,(1/6))'
*************************************************


*************************************************
*  Variables controlling input risetimes,
*  frequencies, and amplitudes
*  Allows TL to be constructed of nperwl sections
*  per wavelength
*
*  fdrive      driving frequency (Hz)
*  trise       pulse risetime (s)
*  tplateau    pulse plateau length (s)
*  tfall       pulse falltime (s)
*  inclen      increment length (m)
*  numincs     number of increments (unitless)
*              note: numincs must match total increments
*  emftot      total emf along tether (V)
*  vsbias      voltage source bias voltage
*  vdrive      driving voltage amplitude (V)
*  vend        end (driving) point voltage (V)
*
.param
+ fdrive=500e3
+ trise=1e-6
*+ trise=1e-8
+ tfall='trise'
+ tplateau='trise'
*+ tplateau=1e-6
+ inclen=4
*+ numincs=2000
+ numincs=5000
+ emftot='numincs*incvolt*inclen'
+ vsbias='itether*(2*Z0+numincs*R0*inclen)+emftot'
+ vdrive=-500
+ vend=-500
*************************************************


*************************************************
*  assembled tether circuit
```

```
*
*xsource 1 0 sourceptr
xsource 1 0 sourcepul
*xsource 1 0 sourcesin
*xt 1 0 2 3 tether1000i
*xt 1 0 2 3 tether2000i
*xt 1 0 2 3 tether5000i
*xt 1 0 2 3 tether2000i2
xt 1 0 2 3 tether5000i2
rload 2 3 Z0
*rload 2 3 Z02
*rload 2 3 50
**************************************************


**************************************************
*  assembled static circuit
*
*xstatic 10 0 20 0 static10m
*xsourcestat 10 0 source1
*rloads 20 0 Z0
**************************************************


**************************************************
*  incremental static tether length (inclen m segment)
*  includes voltage sources
*
.subckt incstatic 1 2 3 4
rtether 5 6 'R0*inclen'
ltether 1 5 'L0*inclen'
ctether 3 4 'C0*inclen'
vtether 6 3 'incvolt*inclen'
rgnd 2 4 'Rp*inclen'
.ends incstatic
**************************************************


**************************************************
*  incremental plasma/cond tether length (inclen m segment)
*
.subckt inctether 1 2 3 4
rtether 5 6 'R0*inclen'
ltether 1 5 'L0*inclen'
* CTYPE must be set to 1 in order for HSPICE to calculate charge correctly
ctether 7 4 C='inclen*2.0*pi*epsilon0/(log(max((Csh_const*
-->              pwr(-min(v(7,4),0),(5/12))),rsh_min)/r_d))' CTYPE=1
cdielectric 3 7 'Cd*inclen'
*gjeoml 7 4 cur='inclen*je_omlc*sqrt(max(v(7,4),0))' min=-1e-9
rgjeomldc 7 4 100meg
vtether 6 3 'incvolt*inclen'
rgnd 2 4 'Rp*inclen'
.ends inctether
**************************************************


**************************************************
*  2nd incremental plasma/cond tether length (inclen m segment)
*
.subckt inctether2 1 2 3 4
rtether2 5 6 'R0*inclen'
ltether2 1 5 'L02*inclen'
* CTYPE must be set to 1 in order for HSPICE to calculate charge correctly
```

```
ctether2 7 4 C='inclen*2.0*pi*epsilon0/(log(max((Csh_const2*
-->              pwr(-min(v(7,4),0),(5/12))),rsh_min2)/r_d))' CTYPE=1
cdielectric2 3 7 'Cd*inclen'
*gjeoml2 7 4 cur='inclen*je_omlc2*sqrt(max(v(7,4),0))' min=-1e-9
rgjeomldc2 7 4 100meg
vtether2 6 3 'incvolt*inclen'
rgnd2 2 4 'Rp*inclen'
.ends inctether2
*************************************************


*************************************************
*  10 increment tether segments
*
.subckt tether10i 1 2 21 22
x1   1    2    3    4   inctether
x2   3    4    5    6   inctether
x3   5    6    7    8   inctether
x4   7    8    9    10  inctether
x5   9    10   11   12  inctether
x6   11   12   13   14  inctether
x7   13   14   15   16  inctether
x8   15   16   17   18  inctether
x9   17   18   19   20  inctether
x10  19   20   21   22  inctether
.ends tether10i
*************************************************


*************************************************
*  10 increment tether segments, 2nd
*
.subckt tether10i2 1 2 21 22
x1   1    2    3    4   inctether2
x2   3    4    5    6   inctether2
x3   5    6    7    8   inctether2
x4   7    8    9    10  inctether2
x5   9    10   11   12  inctether2
x6   11   12   13   14  inctether2
x7   13   14   15   16  inctether2
x8   15   16   17   18  inctether2
x9   17   18   19   20  inctether2
x10  19   20   21   22  inctether2
.ends tether10i2
*************************************************


*************************************************
*  100 increment tether segments
*
.subckt tether100i 1 2 21 22
x1   1    2    3    4   tether10i
x2   3    4    5    6   tether10i
x3   5    6    7    8   tether10i
x4   7    8    9    10  tether10i
x5   9    10   11   12  tether10i
x6   11   12   13   14  tether10i
x7   13   14   15   16  tether10i
x8   15   16   17   18  tether10i
x9   17   18   19   20  tether10i
x10  19   20   21   22  tether10i
.ends tether100i
*************************************************
```

```
*************************************************
*  100 increment tether segments, 2nd
*
.subckt tether100i2 1 2 21 22
x1   1   2   3   4   tether10i2
x2   3   4   5   6   tether10i2
x3   5   6   7   8   tether10i2
x4   7   8   9   10  tether10i2
x5   9   10  11  12  tether10i2
x6   11  12  13  14  tether10i2
x7   13  14  15  16  tether10i2
x8   15  16  17  18  tether10i2
x9   17  18  19  20  tether10i2
x10  19  20  21  22  tether10i2
.ends tether100i2
*************************************************

*************************************************
*  1000 increment tether segments
*
.subckt tether1000i 1 2 21 22
x1   1   2   3   4   tether100i
x2   3   4   5   6   tether100i
x3   5   6   7   8   tether100i
x4   7   8   9   10  tether100i
x5   9   10  11  12  tether100i
x6   11  12  13  14  tether100i
x7   13  14  15  16  tether100i
x8   15  16  17  18  tether100i
x9   17  18  19  20  tether100i
x10  19  20  21  22  tether100i
.ends tether1000i
*************************************************

*************************************************
*  1000 increment tether segments, 2nd
*
.subckt tether1000i2 1 2 21 22
x1   1   2   3   4   tether100i2
x2   3   4   5   6   tether100i2
x3   5   6   7   8   tether100i2
x4   7   8   9   10  tether100i2
x5   9   10  11  12  tether100i2
x6   11  12  13  14  tether100i2
x7   13  14  15  16  tether100i2
x8   15  16  17  18  tether100i2
x9   17  18  19  20  tether100i2
x10  19  20  21  22  tether100i2
.ends tether1000i2
*************************************************

*************************************************
*  2000 increment tether segments
*
.subckt tether2000i 1 2 5 6
x1   1   2   3   4   tether1000i
x2   3   4   5   6   tether1000i
.ends tether2000i
```

```
*************************************************

*************************************************
*  2000 increment tether segments, with 2nd den
*
.subckt tether2000i2 1 2 5 6
x1   1   2   3   4   tether1000i
x2   3   4   5   6   tether1000i2
.ends tether2000i2
*************************************************

*************************************************
*  5000 increment tether segments
*
.subckt tether5000i 1 2 11 12
x1   1   2   3   4   tether1000i
x2   3   4   5   6   tether1000i
x3   5   6   7   8   tether1000i
x4   7   8   9   10  tether1000i
x5   9   10  11  12  tether1000i
.ends tether5000i
*************************************************

*************************************************
*  5000 increment tether segments, with 2nd den
*
.subckt tether5000i2 1 2 11 12
x1   1   2   3   4   tether1000i
x2   3   4   5   6   tether1000i
x3   5   6   7   8   tether1000i
x4   7   8   9   10  tether1000i2
x5   9   10  11  12  tether1000i2
.ends tether5000i2
*************************************************

*************************************************
*  10 m static segments
*
.subckt static10m 1 2 21 22
x1   1   2   3   4   incstatic
x2   3   4   5   6   incstatic
x3   5   6   7   8   incstatic
x4   7   8   9   10  incstatic
x5   9   10  11  12  incstatic
x6   11  12  13  14  incstatic
x7   13  14  15  16  incstatic
x8   15  16  17  18  incstatic
x9   17  18  19  20  incstatic
x10  19  20  21  22  incstatic
.ends static10m
*************************************************

*************************************************
*  100 m tether segments
*
.subckt static100m 1 2 21 22
x1   1   2   3   4   static10m
x2   3   4   5   6   static10m
```

```
x3   5   6   7   8   static10m
x4   7   8   9   10  static10m
x5   9   10  11  12  static10m
x6   11  12  13  14  static10m
x7   13  14  15  16  static10m
x8   15  16  17  18  static10m
x9   17  18  19  20  static10m
x10  19  20  21  22  static10m
.ends static100m
************************************************


************************************************
*  voltage source: step model
*
.subckt sourcestp 2 4
rsource 2 3 Z0
vsource 3 4 pulse(-1000 -2000 0.0001ms 1us 1us 0.1s 1s)
.ends sourcestp
************************************************


************************************************
*  voltage source: pulser model
*
.subckt sourcepul 2 4
rsource 3 4 Z0
vsource 2 3 pulse(vsbias 'vsbias+
-->         2*vdrive' 0.0002ms trise tfall tplateau 1s)
.ends sourcepul
************************************************


************************************************
*  voltage source: pulse train model
*
.subckt sourceptr 2 4
rsource 3 4 Z0
vsource 2 3 pulse(vsbias 'vsbias+
-->         2*vdrive' 0.0002ms trise tfall tplateau 10.0us)
.ends sourceptr
************************************************


************************************************
* voltage source: sinusoidal source model
*
.subckt sourcesin 1 4
vendpt 1 2 vend
vsinbias 2 5 vsbias
* phase of -90 so it starts at max value
vsource 5 3 sin('2*vdrive' '2*vdrive' fdrive 0.0002ms 0 -90)
rsource 3 4 Z0
.ends sourcesin
************************************************


************************************************
*analysis parameters
*
.tran 100ns 0.3ms
.option ingold=1
.print tran xt.x1.x1.x1.x1.ctether:ceff
```

```
+ xt.x1.x10.x10.x10.ctether:ceff
+ xt.x2.x10.x10.x10.ctether:ceff
+ xt.x3.x10.x10.x10.ctether:ceff
+ xt.x4.x10.x10.x10.ctether:ceff
+ xt.x5.x10.x10.x10.ctether:ceff
+ xt.x1.x1.x1.x1.ctether:curr
+ xt.x1.x10.x10.x10.ctether:curr
+ xt.x2.x10.x10.x10.ctether:curr
+ xt.x3.x10.x10.x10.ctether:curr
+ xt.x4.x10.x10.x10.ctether:curr
+ xt.x5.x10.x10.x10.ctether:curr
+ xt.x1.x1.x1.x1.ctether:volt
+ xt.x1.x10.x10.x10.ctether:volt
+ xt.x2.x10.x10.x10.ctether:volt
+ xt.x3.x10.x10.x10.ctether:volt
+ xt.x4.x10.x10.x10.ctether:volt
+ xt.x5.x10.x10.x10.ctether:volt
+ xt.x1.x1.x1.x1.v(3,4)
+ xt.x1.x10.x10.x10.v(3,4)
+ xt.x2.x10.x10.x10.v(3,4)
+ xt.x3.x10.x10.x10.v(3,4)
+ xt.x4.x10.x10.x10.v(3,4)
+ xt.x5.x10.x10.x10.v(3,4)
+ xt.x1.x10.x10.x10.cdielectric:volt
+ xt.x1.x10.x10.x10.cdielectric:curr
.print tran v(1,0)  v(2,3)
.end
************************************************
```

E.1.2 TSS–1 Transient Model

This HSPICE input deck was utilized in the analyses of Section D.1 and the circuit diagram may be found in Figure D.7.

```
*  Modular TSS-1 circuit with satellite, tether, tether reel, SETS, and
*  Orbiter subcircuits
*

************************************************
*  status control options
*
.option post
*  if timestep problem, use this option
*.option method=gear
*  if convergence problem, use this option
.option converge=2
************************************************

************************************************
*  variable declarations
*  where:
*
*  itether      tether current (A)
*  vtether      tether voltage (V)
*  rete_den     RETE electron density measurement (per m^3)
*  rete_fact    RETE density correction factor
*  elecden      corrected electron density (per m^3)
*  lentether    tether length (m)
```

```
*  setsrval     SETS resistor value (ohms)
*  rtether      tether resistance (ohms)
*  electemp     electron temperature (eV)
*  satrad       satellite radius (m)
*  pi           pi value
*  epsilon0     permitivity of free space (F/m)
*  echrg        electronic charge (C)
*  corbiter     capacitance of orbiter (F)
*
.param
+  itether=21.260m
+  vtether=-48.38
+  rete_den=4.9184e11
+  rete_fact=1
+  elecden='rete_den*rete_fact'
+  lentether=224.15
+  setsrval=15
+  rtether=2258
+  electemp=0.1
+  satrad=0.800
+  pi=3.14159265359
+  epsilon0=8.852e-12
+  echrg=1.602e-19
+  corbiter=30u
***********************************************


***********************************************
*  compute Debye length for given plasma density
*
.param  lambdad='sqrt(epsilon0*electemp/(elecden*echrg))'
***********************************************


***********************************************
*  compute vorbiter, voltage of charged orbiter
*  if vorbiter > vtether set .param vorbiter = 0
*
.param vorbiter='vtether+itether*rtether'
.param vorbiter=0
***********************************************


***********************************************
*  compute tether reel values
*
.param
+  monreel='22000-lentether'
+  cwindval=5e-9
+  lreelval='pwr(monreel,2.2406)/439.178e6'
+  rreelval='monreel/9.74387'
+  rspinval=4000
+  cspinval=8.18963e-9
+  cflangeval='(monreel/8088.93+1.3)*1e-9'
***********************************************


***********************************************
*  Garrett source values
*  where:
*
*  ae_orb       Orbiter electron collection area (m^2)
*  thetae_orb   electron energy (eV)
```

```
*  ai_orb       Orbiter ion collection area (m^2)
*  thetaid_orb  ion temperature (O+ species) (eV)
*  velshut      relative shuttle velocity (m/s)
*  jir_orb      ion current density (A/m^2)
*  elecmass     mass of electron (kg)
*  k_orb        electron current density constant
*  jeo_orb      electron current density (A/m^2)
*  ae_sat       satellite electron collection area (m^2)
*  ai_sat       satellite ion collection area (m^2)
*  alpha_iorb   iorb ion shielding factor
*  alpha_isat   isat ion shielding factor
*
.param
+  ae_orb=25
+  thetae_orb=electemp
+  ai_orb=25
+  thetaid_orb=5
+  velshut=7.5e3
+  jir_orb='echrg*elecden*velshut'
+  elecmass=9.109e-31
+  k_orb='echrg/2*sqrt(2*echrg*thetae_orb/(pi*elecmass))'
+  jeo_orb='k_orb*elecden'
+  ae_sat='2*pi*pwr(satrad,2)'
+  ai_sat='pi*pwr(satrad,2)'
+  alpha_iorb=0.1
+  alpha_isat=0.08
*************************************************


*************************************************
* assembled circuit:  satellite, tether, reel, sets, and orbiter
*
xsatellite 0 1 satellite
xtether 0 1 2 tether
xreel 2 3 4 reel
xsets 3 4 sets
xorbiter 0 4 orbiter
*xcmm_lpf 3 5 4 cmm_lpf
*rmeasure 5 4 10meg
*************************************************


*************************************************
*  compute csatellite, capacitance between satellite and plasma
*  assume spherical capacitor with outer shell at constant*lambdad
*  only half due to satellite plasma wake
*
.param csatellite='0.5*epsilon0*4*pi/(1/satrad-1/(satrad+lambdad))'
.param csatellite='epsilon0*4*pi*satrad'
*.param csatellite=0e-9
*************************************************


*************************************************
*  satellite/ionosphere model
*
.subckt satellite 1 3
*csat 1 3 csatellite
*csat modeled using Crawford and Mlodnosky (1964)
.param csat0='2*pi*epsilon0*pwr(satrad,2)/lambdad'
csat 1 3 c='csat0*(1-exp(v(3,1)/thetae_orb))/
-->       sqrt(2*(exp(v(3,1)/thetae_orb)-(v(3,1)/thetae_orb)-1))'
gsat 1 3 cur='-ae_sat*jeo_orb*exp(v(3,1)/thetae_orb)
```

```
-->      +ai_sat*jir_orb*(1-alpha_isat*v(3,1)/thetaid_orb)'
rsat 1 3 100meg
.ends satellite
************************************************


************************************************
*  tether/ionosphere model
*
.subckt tether 1 2 3
ltether 4 5 '(346.23e-9)*lentether'
rtether 2 4 '0.1026*lentether'
ctether 5 1 '(20e-12)*lentether'
*ctether 5 1 '(112.475e-12)*lentether'
vteth 3 5 vtether
*rshunt 2 1 100meg
.ends tether
************************************************


************************************************
*  tether reel model
*
.subckt reel 1 5 10
lreel1 1 2 'lreelval/2'
rreel1 2 3 'rreelval/2'
cwind1 1 3 '2*cwindval'
cflange 3 10 'cflangeval/2'
rdamp1 1 3 0.8meg
*
lreel2 3 4 'lreelval/2'
rreel2 4 5 'rreelval/2'
cwind2 3 5 '2*cwindval'
rdamp2 3 5 0.8meg
cspin 5 10 'cspinval+cflangeval/2'
rspin 5 10 300k
*rspin 5 6 5k
*
*mutual inductance
k12 lreel1 lreel2 k=0.35
*
.ends reel
************************************************


************************************************
*  sets model
*
.subckt sets 2 4
gsetssw 2 4 vcr pwl(1) 16 10 delta=0.25 smooth=1 0.1v,10meg 0.9v,setsrval
vswitch 16 10 pulse(2 -1 0.01s 100ns 100ns 0.1s 1s)
csets 2 4 1nF
.ends sets
************************************************


************************************************
* cmm lpf model
*
.subckt cmm_lpf 6 2 3
xlpf_opamp 6 1 1 3 lpf_opamp
rlpf1 1 4 1.47k
rlpf2 4 5 1.47k
```

```
rlpf3 5 2 6.09k
clpf1 4 3 3300p
clpf2 5 3 3300p
.ends cmm_lpf
*
* ideal opamp with 100K gain and one-pole roll-off at 10 Hz
* non=4 inv=5 out=6 gnd=7
.subckt lpf_opamp 4 5 6 7
rin 4 5 1meg
egain_op 1 7 vcvs 4 5 100k
ropen_op 1 2 1k
copen_op 2 7 15.92u
eout_op 3 7 vcvs 2 7 1
rout_op 3 6 50
.ends lpf_opamp
************************************************


************************************************
*  orbiter/ionosphere model
*
.subckt orbiter 1 4
gorb 1 4 cur='-ae_orb*jeo_orb*exp(v(4,1)/thetae_orb)
-->      +ai_orb*jir_orb*(1-alpha_iorb*v(4,1)/thetaid_orb)'
corb 4 10 corbiter
gcorb 1 10 cur='0.001*(-3.33*exp(10*v(10,1))+0.395*(1-0.2*v(10,1)))'
*rorb 10 0 1
*  takes care of initial charge on the orbiter
*  this was necessary in ver 93a of HSPICE due to a bug
*  in the capacitor initial condition interpretation
vswitch 16 17 pulse(2 -1 0.01s 100ns 100ns 0.1s 1s)
vorb 15 10 vorbiter
rextra 15 1 1meg
gcapsw 15 4 vcr pwl(1) 16 17 delta=0 smooth=1 0.1v,10meg 0.9v,0.01
.ends orbiter
************************************************


************************************************
*analysis parameters
*
.tran 0.05ms 0.04s
.option ingold=1
.print V(3,4)
.print V(5,4)
.end
************************************************
```

E.1.3 TSS–1 Transient Model with FPEG

This HSPICE input deck was utilized in the analyses of Section D.2 and the circuit diagram may be found in Figure D.12.

```
*  Modular TSS-1 circuit, with satellite, tether, tether reel, SETS, and
*  orbiter subcircuits
*
*  FPEG model added (1 Sept 1995 SGB)
```

```
**************************************************
*  status control options
*
.option post
*  if timestep problem, use one of these options
*.option lvltim=1
.option method=gear
*.option gshunt=1e-9
*.option dvdt=4
*  if convergence problem, use one of these options
.option converge=2
*.option dcon=1
.option rmin=1.0e-15
*  since got numbers smaller than 1e-28
.option epsmin=1e-32
**************************************************


**************************************************
*  variable declarations
*  where:
*
*  itether       tether current (A)
*  vtether       tether voltage (V)
*  rete_den      RETE electron density measurement (per m^3)
*  rete_fact     RETE density correction factor
*  lentether     tether length (m)
*  vorbiter      Orbiter voltage (V)
*  elecden       corrected electron density (per m^3)
*  setsrval      SETS resistor value (ohms)
*  rtether       tether resistance (ohms)
*  electemp      electron temperature (eV)
*  satrad        satellite radius (m)
*  pi            pi value
*  epsilon0      permitivity of free space (F/m)
*  echrg         electronic charge (C)
*  k_boltz       Boltzmann's constant (J/K)
*  const_e       e value
*  corbiter      capacitance of orbiter (F)
*
.param
+  itether=1.54m
+  vtether=-4.0
+  rete_den=5.2e10
+  lentether=44.7
+  vorbiter=9.5
+  rete_fact=1
+  elecden='rete_den*rete_fact'
+  setsrval=15
+  rtether=2258
+  electemp=0.2
+  satrad=0.800
+  pi=3.14159265359
+  epsilon0=8.852e-12
+  echrg=1.602e-19
+  k_boltz=1.38e-23
+  const_e=2.71828182846
*+  corbiter=5u
+  corbiter=30u
**************************************************
```

```
**************************************************
*  compute Debye length for given plasma density
*
.param lambdad='sqrt(epsilon0*electemp/(elecden*echrg))'
**************************************************


**************************************************
*  compute tether reel values
*
.param
+  fullwoundlen=21700
+  monreel='fullwoundlen-lentether'
+  cwindval=5e-9
+  lreelval='pwr(monreel,2.2406)/439.178e6'
+  rreelval='monreel/9.74387'
+  rspinval=4000
+  cspinval=8.18963e-9
+  cflangeval='(monreel/8088.93+1.3)*1e-9'
**************************************************


**************************************************
*  Garrett source values
*  where:
*
*  ae_orb       Orbiter electron collection area (m^2)
*  thetae_orb   electron energy (ev)
*  ai_orb       Orbiter ion collection area (m^2)
*  thetaid_orb  ion temperature (O+ species) (eV)
*  velshut      relative shuttle velocity (m/s)
*  jir_orb      ion current density (A/m^2)
*  elecmass     mass of electron (kg)
*  k_orb        electron current density constant
*  jeo_orb      electron current density (A/m^2)
*  ae_sat       satellite electron collection area (m^2)
*                  from Garrett (4*pi*r^2)
*  ai_sat       satellite ion collection area (m^2)
*                  from Garrett (pi*r^2)
*  alpha_iorb   iorb ion shielding factor
*  alpha_isat   isat ion shielding factor
*  ae_corb      Orbiter capacitance electron collection area (m^2)
*  ai_corb      Orbiter capacitance ion collection area (m^2)
*  elec_sat     electron saturation current (A)
*  plas_pot     plasma potential (V)
*
.param
+  ae_orb=25
+  thetae_orb='electemp'
+  ai_orb='ae_orb'
+  thetaid_orb=5
+  velshut=7.5e3
+  jir_orb='echrg*elecden*velshut'
+  elecmass=9.109e-31
+  k_orb='echrg*sqrt((k_boltz*thetae_orb*11600)/(2*pi*elecmass))'
+  jeo_orb='k_orb*elecden'
+  ae_sat='2*pi*pwr(satrad,2)'
+  ai_sat='pi*pwr(satrad,2)'
+  alpha_iorb=0.1
+  alpha_isat=0.08
+  alpha_eorb=0.1
+  ae_corb=100
+  ai_corb=100
```

```
+  elec_sat='-ae_orb*jeo_orb'
+  plas_pot=0
*************************************************


*************************************************
*  assembled circuit:  satellite, tether, reel, sets, and orbiter
*
xsatellite 0 1 satellite
*rtemp2 0 1 0.1
xtether 0 1 2 tether
xreel 2 3 4 reel
xsets 3 4 sets2
xorbiter 0 4 orbiter2
*rorbshunt 0 4 1meg
*xcmm_lpf 3 5 4 cmm_lpf
*rmeasure 5 4 10meg
*************************************************


*************************************************
*  compute csatellite, capacitance between satellite and plasma
*  assume spherical capacitor with outer shell at constant*lambdad
*  only half due to satellite plasma wake
*
.param csatellite='0.5*epsilon0*4*pi/(1/satrad-1/(satrad+lambdad))'
.param csatellite='epsilon0*4*pi*satrad'
*.param csatellite=0e-9
*************************************************


*************************************************
*  satellite/ionosphere model
*
.subckt satellite 1 3
*csat 1 3 csatellite
*csat modeled using Crawford and Mlodnosky (1964)
.param csat0='2*pi*epsilon0*pwr(satrad,2)/lambdad'
csat 1 3 c='csat0*(1-exp(v(3,1)/thetae_orb))/
-->      sqrt(2*(exp(v(3,1)/thetae_orb)-(v(3,1)/thetae_orb)-1))'
gsat 1 3 cur='-ae_sat*jeo_orb*exp(v(3,1)/thetae_orb)
-->      +ai_sat*jir_orb*(1-alpha_isat*v(3,1)/thetaid_orb)'
rsat 1 3 100meg
.ends satellite
*************************************************


*************************************************
*  tether/ionosphere model
*
.subckt tether 1 2 3
ltether 4 5 '(346.23e-9)*lentether'
rtether 2 4 '0.1026*lentether'
ctether 5 1 '(20e-12)*lentether'
*ctether 5 1 '(112.475e-12)*lentether'
vteth 3 5 vtether
*rshunt 2 1 100meg
.ends tether
*************************************************


*************************************************
*  tether reel model
```

```
*
.subckt reel 1 5 10
lreel1 1 2 'lreelval/2'
rreel1 2 3 'rreelval/2'
cwind1 1 3 '2*cwindval'
cflange 3 10 'cflangeval/2'
rdamp1 1 3 0.8meg
*
lreel2 3 4 'lreelval/2'
rreel2 4 5 'rreelval/2'
cwind2 3 5 '2*cwindval'
rdamp2 3 5 0.8meg
cspin 5 10 'cspinval+cflangeval/2'
rspin 5 10 300k
*rspin 5 6 5k
*
*mutual inductance
k12 lreel1 lreel2 k=0.35
*
.ends reel
*************************************************


*************************************************
* sets model open circuited
*
.subckt sets2 2 4
rsets 2 4 35meg
csets 2 4 1nF
.ends sets2
*************************************************


*************************************************
* cmm lpf model
*
.subckt cmm_lpf 6 2 3
xlpf_opamp 6 1 1 3 lpf_opamp
rlpf1 1 4 1.47k
rlpf2 4 5 1.47k
rlpf3 5 2 6.09k
clpf1 4 3 3300p
clpf2 5 3 3300p
.ends cmm_lpf
*
* ideal opamp with 100K gain and one-pole roll-off at 10 Hz
* non=4 inv=5 out=6 gnd=7
.subckt lpf_opamp 4 5 6 7
rin 4 5 1meg
egain_op 1 7 vcvs 4 5 100k
ropen_op 1 2 1k
copen_op 2 7 15.92u
eout_op 3 7 vcvs 2 7 1
rout_op 3 6 50
.ends lpf_opamp
*************************************************


*************************************************
*  orbiter/ionosphere model
*
.subckt orbiter2 1 4
*  need two current sources to get complete characteristic
```

```
gorb 1 4 cur='-ae_orb*jeo_orb*exp((v(4,1)-plas_pot)/thetae_orb)
-->      +ai_orb*jir_orb*(1-alpha_iorb*v(4,1)/thetaid_orb)' min=elec_sat
gorb2 1 4 cur='-elec_sat-ae_orb*jeo_orb*(1+alpha_eorb*(v(4,1)
-->      +thetae_orb*const_e)/thetae_orb)' max=0
*  initial condition handled correctly in ver 95
corb 4 10 corbiter ic='vorbiter'
vcorb 4 10 vorbiter
rcorb 1 10 100meg
*  need two current sources to get complete characteristic
gcorb 1 10 cur='-ae_corb*jeo_orb*exp(v(10,1)/thetae_orb)
-->        +ai_corb*jir_orb*(1-alpha_iorb*v(10,1)/
-->        thetaid_orb)' min='-ae_corb*jeo_orb'
gcorb2 1 10 cur='ae_corb*jeo_orb-ae_corb*jeo_orb*(1+alpha_eorb*(v(10,1)
-->         +thetae_orb*const_e)/thetae_orb)' max=0
ifpeg 1 4 pulse(0 0.1 0.001 100e-9 100e-9 13.1e-3 26.2e-3)
.ends orbiter2
*************************************************


*************************************************
*analysis parameters
*
.tran 0.05ms 0.2s
*.tran 0.01ms 0.2s
.option ingold=1
.print V(3,4)
.end
*************************************************
```

E.2 XOOPIC Simulation Decks

XOOPIC Version 2.0 (with modifications) was used for these simulations.

E.2.1 Voltage Step ($\tau_{pe} \ll \tau_{ar} \ll \tau_{pi}$)

Other peak voltages are specified by setting the `PULSE_VOLT` parameter to desired voltage (*e.g.*, -500, -1000, -1500, -2000) in the `Variables{}` section of the input file.

```
cylper_unii_st500
{
     Cylindrical, periodic geometry for sheath expansion away
     from bare metal to which a negative HV step is applied, real ion
     mass used (approximately immobile ions)
}
Variables
{
     ELECMASS = 9.11E-31
     MASSRATIO = 100000
     OXIONMASS = MASSRATIO*ELECMASS
     PULSE_VOLT = -500
     Jmax = 8
     x1min = 0.0
     x1max = 0.02
     Kmax = 128
     Kmax_m  = 127
     x2min = 0.00065
```

```
     x2max = 1.0
     DENFACTOR = 1e6
}
Region
{
     Grid
     {
          J = Jmax
          x1s = x1min
          x1f = x1max
          K = Kmax
          x2s = x2min
          x2f = x2max
          Geometry=0
          PeriodicFlagX1=1
          PeriodicFlagX2=0
     }
     Species
     {
          name = electrons
          m = ELECMASS
          q = -1.6e-19
     }
     Species
     {
          name = oxygenions
          m = OXIONMASS
          q = 1.6e-19
          subcycle = 10
     }
     Control
     {
          dt = 5E-10
          ElectrostaticFlag = 4
          NonRelativisticFlag = 1
     }
     Load
     {
          units = EV
          speciesName = electrons
          x1MinMKS = x1min
          x1MaxMKS = x1max
          x2MinMKS = x2min
          x2MaxMKS = x2max
          temperature = 1.0
          density = 1e12
          np2c = DENFACTOR
     }
     Load
     {
          units = EV
          x1MinMKS = x1min
          x1MaxMKS = x1max
          x2MinMKS = x2min
          x2MaxMKS = x2max
          speciesName = oxygenions
          temperature = 1.0
          density = 1e12
          np2c = DENFACTOR
     }
     Conductor
     {
          QuseFlag = 0
```

```
          j1 = 0
          j2 = Jmax
          k1 = Kmax
          k2 = Kmax
          normal = -1
     }
     Dielectric
     {
          er = 1
          QuseFlag = 1
          j1 = 0
          k1 = Kmax_m
          j2 = Jmax
          k2 = Kmax_m
          normal = -1
          reflection = 1.0
     }
     Equipotential
     {
          j1 = 0
          k1 = 0
          j2 = Jmax
          k2 = 0
          a0 = 0
          tdelay = 5.0e-7
          trise = 1.0e-6
          a1 = PULSE_VOLT
          A = 0
          C = 1
     }
}
```

E.2.2 Voltage Drop ($\tau_{pe} \ll \tau_{af} \ll \tau_{pi}$)

(Note: the ellipsis in the code listing indicates the region is identical to the portion of the cylper_unii_st500 listing which is found in Section E.2.1.)

```
cylper_unii_pul500
{
     Cylindrical, periodic geometry for sheath expansion away
     from bare metal to which a negative HV pulse is applied, real ion
     mass used (approximately immobile ions)
}
Variables
{
     ELECMASS = 9.11E-31
     MASSRATIO = 100000
     OXIONMASS = MASSRATIO*ELECMASS
     PULSE_VOLT = -500
     Jmax = 8
     x1min = 0.0
     x1max = 0.02
     Kmax = 128
     Kmax_m  = 127
     x2min = 0.00065
     x2max = 1.0
     DENFACTOR = 1e6
}
Region
```

```
{

. . .

     Equipotential
     {
          j1 = 0
          k1 = 0
          j2 = Jmax
          k2 = 0
          a0 = 0
          tdelay = 5.0e-7
          trise = 1.0e-6
          tpulse = 1.0e-6
          tfall = 1.0e-6
          a1 = PULSE_VOLT
          A = 0
          C = 1
     }
}
```

E.2.3 Sinusoidal (RF) Input ($\omega_{pe} \gg \omega \gg \omega_{pi}$)

```
cylper_unii_sin500
{
     Cylindrical, periodic geometry for sheath expansion away
     from bare metal to which a negative HV full sinewave is applied,
     real ion mass used (approximately immobile ions)
}
Variables
{
     ELECMASS = 9.11E-31
     MASSRATIO = 100000
     OXIONMASS = MASSRATIO*ELECMASS
     PULSE_VOLT = -500
     Jmax = 8
     x1min = 0.0
     x1max = 0.02
     Kmax = 128
     Kmax_m  = 127
     x2min = 0.00065
     x2max = 1.0
     DENFACTOR = 1e6
     RF_FREQUENCY = 1e6
}
Region
{

. . .

     Equipotential
     {
          j1 = 0
          k1 = 0
          j2 = Jmax
          k2 = 0
          a0 = 0
          tdelay = 5.0e-7
          trise = 1.0e-8
          a1 = PULSE_VOLT
          phase = 1.5707963
```

```
          frequency = RF_FREQUENCY
          A = 0.5
          C = 0.5
     }
}
```

E.2.4 Fast Voltage Step ($\tau_{ar} < \tau_{pe}$)

```
cylper_unii_fp500
{
     Cylindrical, periodic geometry for sheath expansion away
     from bare metal to which a fast negative HV step is applied, real ion
     mass used (approximately immobile ions)
}
Variables
{
     ELECMASS = 9.11E-31
     MASSRATIO = 100000
     OXIONMASS = MASSRATIO*ELECMASS
     PULSE_VOLT = -500
     Jmax = 8
     x1min = 0.0
     x1max = 0.02
     Kmax = 128
     Kmax_m  = 127
     x2min = 0.00065
     x2max = 1.0
     DENFACTOR = 1e6
}
Region
{


. . .

     Equipotential
     {
          j1 = 0
          k1 = 0
          j2 = Jmax
          k2 = 0
          a0 = 0
          tdelay = 5.0e-7
          trise = 1.0e-8
          a1 = PULSE_VOLT
          A = 0
          C = 1
     }
}
```

APPENDIX F

Nomenclature

In this work, an attempt is made to combine the many varied nomenclatures found in the literature into one which is consistent. For anyone who has worked in the realm of plasma physics, you will no doubt appreciate the difficulty of such an undertaking. Throughout this work, mksA (meter–kilogram–second–Ampère) units are standard rather than cgs (centimeter–gram–second) and American/English units are converted wherever they are used.

F.1 Nomenclature

The following is a listing of the major symbols and variables used in this work, along with a brief description and the appropriate unit.

Nomenclature	Description, Unit
A	area, m^2
A_e	electron collection area, m^2
A_i	ion collection area, m^2
A_p	probe collection area, m^2

Nomenclature	Description, Unit
A_{sat}	satellite area, m^2
$\mathbf{B}$	magnetic–flux–density vector, $\mathrm{Wb/m}^2$ or T
$\mathbf{B}_0$	background magnetic–flux–density vector, $\mathrm{Wb/m}^2$ or T
B_0	background magnetic–flux density, $\mathrm{Wb/m}^2$ or T
$\mathbf{B}_{\mathrm{AMAG}}$	magnetic–flux density measured by AMAG, $\mathrm{Wb/m}^2$ or T
$\mathbf{B}_{\mathrm{chamber}}$	magnetic–flux density in plasma chamber, $\mathrm{Wb/m}^2$ or T
$\mathbf{B}_E$	geomagnetic flux–density vector, $\mathrm{Wb/m}^2$ or T (also G)
B_E	geomagnetic flux–density, $\mathrm{Wb/m}^2$ or T (also G)
$\mathbf{B}_{\mathrm{IGRF}}$	magnetic–flux density from IGRF–90 model, $\mathrm{Wb/m}^2$ or T
B_{plas}	magnetic–flux density in plasma, $\mathrm{Wb/m}^2$ or T
B_{vac}	magnetic–flux density in vacuum, $\mathrm{Wb/m}^2$ or T
B_w	magnetic–flux density from wire current, $\mathrm{Wb/m}^2$ or T
C	capacitance, F
C	transmission–line capacitance per unit length, F/m
c	speed of light in a vacuum, 2.998×10^8 m/s
C_d	dielectric capacitance per unit length, F/m
C_{flange}	tether–reel flange capacitance, F
C_{orb}	Orbiter capacitance, F
C_s	sheath capacitance per unit area, $\mathrm{F/m}^2$
C_{sat}	satellite sheath capacitance, F
C_{sh}	voltage–dependent–sheath capacitance per unit length, F/m
C_{spin}	tether–reel spindle capacitance, F
C_{tot}	total tether capacitance per unit length, F/m

Nomenclature	Description, Unit
C_{wind}	tether–reel interwinding capacitance, F
$\mathbf{D}$	electric–flux–density vector, C/m^2
$\mathbf{E}$	electric–field–strength vector, V/m
E	electric–field, V/m
E	tether transmission–line *emf* per unit length, V/m
E_a	electric–field at conductor surface, V/m
E_{edge}	E–field of oscillating sheath edge, V/m
$\mathbf{E}_{\text{tot}}$	total electric–field vector, V/m
$\mathbf{F}$	force vector, N
f	excitation frequency, Hz
f_{ce}	electron cyclotron frequency, Hz
f_{ci}	ion cyclotron frequency, Hz
f_{lh}	lower hybrid frequency, Hz
f_{max}	highest frequency component of interest, Hz
$\mathbf{F}_P$	ponderomotive force vector, N
f_p	plasma frequency, Hz
f_{pe}	electron plasma frequency, Hz
f_{pi}	ion plasma frequency, Hz
f_{ring}	sheath–edge oscillation frequency, Hz
f_{uh}	upper hybrid frequency, Hz
G	transmission–line conductance per unit length, S/m
$\mathbf{H}$	magnetic–field–strength vector, A/m
I_{bp}	biased–probe collected current, A

Nomenclature	Description, Unit
I_{CS}	Orbiter–capacitance discharge current, A
I_e	incident electron current, A
I_{eng}	current to engine bells, A
i_{ep}	electron probe current, A
I_{FPEG}	SETS FPEG discharge current, A
I_i	incident ion current, A
i_{ip}	ion probe current, A
I_{ram}	ion ram current, A
I_{sat}	current to satellite, A
I_{tether}	tether current, A
I_w	wire current, A
$\mathbf{J}$	current–density vector, A/m^2
$\mathbf{j}$	current–density vector, A/m^2
j	imaginary number, defined as $j^2 = -1$
$\mathbf{J}_c$	conduction–current–density vector, A/m^2
j_{CL}	Child–Langmuir current density, A/m^2
j_d	displacement current density, A/m^2
j_e	electron current density, A/m^2
j_{ir}	ion ram current density, A/m^2
j_{LB}	Langmuir–Blodgett current density, A/m^2
j_{oml}	orbital–motion–limited current density, A/m^2
j_{sh}	sheath current density, A/m^2
k	wave number, m^1

Nomenclature	Description, Unit
k	Boltzmann's constant, 1.38×10^{-23} J/K
k	(subscript) particle species, generally e or i
L	transmission–line inductance per unit length, H/m
l	length, m
L_a	antenna length, m
L_{approx}	approximate tether inductance per unit length, H/m
L_B	scale length of B–field spatial variation, m
L_c	return–current–shell inductance per unit length, H/m
L_o	characteristic object length, m
L_p	scale length of plasma, m
L_{reel}	tether reel inductance, H
L_s	spatial scale length, m
L_{sh}	sheath inductance per unit length, H/m
L_{tot}	total tether inductance per unit length, H/m
m_e	electron mass, 9.109×10^{-31} kg
m_i	ion mass, kg
N	integer, unitless
N_D	number of electrons in Debye sphere, unitless
n_e	electron plasma density (or simply, plasma density), m^{-3}
n_i	ion density, m^{-3}
n_0	undisturbed plasma density, m^{-3}
$\mathbf{p}$	momentum vector, N·s
Q	total charge, C

Nomenclature	Description, Unit
q	elementary charge magnitude, 1.602×10^{-19} C
Q_a	total charge on conductor, C
q_e	electron charge, -1.602×10^{-19} C
q_i	ion charge (singly ionized), $+1.602 \times 10^{-19}$ C
R	transmission–line resistance per unit length, Ω/m
$\mathbf{r}$	position vector, m
r	radial distance, m
$\tilde{r}$	normalized radial distance, dimensionless
r_a	conductor radius, m
$\tilde{r}_a$	normalized conductor radius, dimensionless
R_{bp}	biased–probe measurement resistance, Ω
R_c	distance from Earth's center, m
r_c	return–current–shell radius, m
r_{ce}	electron gyroradius, m
r_{ch}	equal charge radius, m
r_{ci}	ion gyroradius, m
r_{CL}	Child–Langmuir sheath radius, m
r_d	radius of dielectric–coated conductor, m
R_{damp}	tether reel damping resistance, Ω
R_E	Earth's radius, 6371 km
r_{edge}	oscillating sheath–edge radius, m
$\tilde{r}_{\mathrm{edge}}$	normalized oscillating sheath–edge radius, dimensionless
R_{load}	TSS (*i.e.*, SETS) load resistance, Ω

Nomenclature	Description, Unit
R_{loss}	tether–reel loss resistance, Ω
r_m	impact radius, m
R_{open}	TSS open–circuit load impedance, Ω
R_p	plasma resistance per unit length, Ω/m
R_r	radiation resistance, Ω
R_{reel}	tether–reel series resistance, Ω
r_s	general sheath distance, m
r_{sat}	satellite radius, m
r_{sh}	ion–matrix–sheath distance, m
$\tilde{r}_{\text{sh}}$	normalized ion–matrix sheath distance, dimensionless
$r_{\text{sh,min}}$	minimum ion–matrix–sheath distance, m
R_{SHUNT}	SETS SHUNT load resistance, $\approx 15\ \Omega$
R_{tether}	total tether resistance, Ω
t	time, s
T_e	electron temperature, K
T_i	ion temperature, K
u_0	characteristic ion speed, m/s
u_B	Bohm (ion–sound) speed, m/s
U_c	magnetic energy in return–current shell per unit length, J/m
U_H	magnetic energy per unit length, J/m
U_{sh}	magnetic energy in sheath per unit length, J/m
V	voltage, V
$\tilde{V}$	normalized voltage, dimensionless

Nomenclature	Description, Unit
$\mathbf{v}$	velocity vector, m/s
V_a	applied potential, V
$\tilde{V}_a$	normalized applied potential, dimensionless
V_{ap}	probe potential with respect to plasma potential, V
V_{bp}	biased–probe voltage, V
V_{CS}	voltage on Orbiter–capacitance discharge–current source, V
v_d	drift velocity, m/s
V_e	sheath–edge potential, V
V_{eng}	voltage on engine bells, V
V_f	floating potential, V
v_g	group velocity, m/s
V_{load}	voltage across load resistance, V
V_m	minimum sheath potential, V
v_{max}	maximum wave phase velocity, m/s
V_{orb}	Orbiter voltage, V
v_{orb}	orbital velocity, m/s
V_p	plasma potential, V
v_p	propagation (phase) velocity, m/s
v_{part}	particle velocity, m/s
V_{peak}	normalized peak tether voltage transient, V/mA
v_{prop}	propagation velocity, m/s
V_{ring}	oscillating conductor voltage, V
v_{rot}	rotational velocity of Earth, m/s

Nomenclature	Description, Unit
V_s	potential across sheath, V
$\mathbf{v}_s$	spacecraft velocity vector (relative to rotating Earth), m/s
v_s	spacecraft velocity (relative to rotating Earth), m/s
V_{sat}	satellite voltage, V
V_{sh}	potential across voltage–dependent sheath, V
V_{source}	source voltage, V
v_{te}	electron thermal velocity, m/s
V_{tether}	total voltage along tether, V
v_{ti}	ion thermal velocity, m/s
Z_0	transmission–line characteristic impedance, Ω
Z_i	ionization level, integer
Z_{iono}	ionospheric effective impedance, Ω
Z_{load}	load impedance, Ω
Z_{source}	source impedance, Ω
α_e	electron sheath factor, dimensionless
α_i	ion sheath factor, dimensionless
α_{LB}	Langmuir–Blodgett modified sheath factor, dimensionless
α_P	factor in Poisson's equation, $\alpha_P \in [0, 1, 2]$
Δz	incremental length, m
δ_m	magnetic skin depth, m
ε	permittivity, F/m
$\overline{\overline{\varepsilon}}$	permittivity tensor, F/m
ε_0	free space permittivity, 8.85×10^{-12} F/m

Nomenclature	Description, Unit
ε_d	relative permittivity of dielectric, dimensionless
ε_{eff}	effective relative permittivity, dimensionless
ε_r	relative permittivity, dimensionless
η_p	plasma resistivity, $\Omega{\cdot}$m
$\eta_\parallel$	parallel plasma resistivity, $\Omega{\cdot}$m
θ_0	initial particle energy, eV
θ_i	ion temperature, eV
θ_{ir}	ion ram energy, eV
θ_m	magnetic latitude, degrees
κ	tether–reel inductance coupling coefficient
Λ	plasma parameter, dimensionless
λ	wavelength, m
λ_D	Debye length, m
λ_{min}	minimum wavelength of interest, m
μ	permeability, H/m
μ_0	free–space permeability, $4\pi \times 10^{-7}$ H/m
ν	collision frequency, Hz
ν_{ei}	electron–ion collision frequency, Hz
ρ_s	surface charge density, C/m^2
ρ_{sa}	surface charge density on conductor, C/m^2
ρ_v	volume charge density, C/m^3
σ	conductivity, S/m
σ_p	plasma conductivity, S/m

Nomenclature	Description, Unit
$\sigma_{\parallel}$	parallel plasma conductivity, S/m
τ	timescale, s
τ_a	applied-voltage overall pulse length, s
τ_{af}	applied-voltage falltime, s
τ_{ap}	applied-voltage plateau, s
τ_{ar}	applied-voltage risetime, s
τ_{bp}	biased-probe risetime, s
τ_{CL}	timescale to establish CL-Law sheath, s
τ_d	magnetic diffusion time, s
τ_{pe}	electron plasma period, s
τ_{pi}	ion plasma period, s
$\varphi_{\mathrm{tether}}$	total *emf* generated along tether, V
ω	angular excitation frequency, rad/s
ω_{ce}	angular electron-cyclotron frequency, rad/s
ω_{ci}	angular ion-cyclotron frequency, rad/s
ω_{lh}	angular lower-hybrid frequency, rad/s
ω_p	angular plasma frequency, rad/s
ω_{pe}	angular electron-plasma frequency, rad/s
ω_{pi}	angular ion-plasma frequency, rad/s
ω_{ring}	oscillating sheath-edge angular frequency, rad/s
ω_{uh}	angular upper-hybrid frequency, rad/s

F.2 Chen–To Tai's Novel Vector Notation

In the Winter of 1998, I had the pleasure of attending a Radiation Laboratory lecture given by Chen–To Tai, Professor Emeritus at the University of Michigan. In the lecture, Prof. Tai presented a new notation for vector analysis which he had developed. This notation is outlined and utilized in his book *Generalized Vector and Dyadic Analysis: Applied Mathematics in Field Theory, 2nd Edition* [*Tai*, 1997] and in a recent Letter to the *IEEE AP Magazine* [*Tai*, 1998].

Prof. Tai presents a compelling argument for adopting his notation, not the least of which are remarks made by E. B. Wilson himself (the author of the first book on vector analysis based on the lectures of his professor, J. W. Gibbs). Those remarks, made in 1909, state that Gibb's notation must eventually be changed to meet the following lacking requirements: 1) correct ideas relative to vector fields and, 2) analytical suggestions of notations.

Prof. Tai has developed three *independent differential operators* which meet the above requirements. These operators are denoted by ∇ (gradient), $\nabla\!\!\!\!\cdot\;\,$ (divergence), and $\nabla\!\!\!\!\times$ (curl) and defined by

$$
\begin{aligned}
\nabla &= \sum_i \frac{\hat{u}_i}{h_i}\frac{\partial}{\partial v_i}, && \text{(F.1)}\\
\nabla\!\!\!\!\cdot\;\, &= \sum_i \frac{\hat{u}_i}{h_i}\cdot\frac{\partial}{\partial v_i}, && \text{(F.2)}\\
\nabla\!\!\!\!\times &= \sum_i \frac{\hat{u}_i}{h_i}\times\frac{\partial}{\partial v_i}, && \text{(F.3)}
\end{aligned}
$$

where $\hat{u}_i$ denotes the unit vectors, h_i denotes the metric coefficients, and v_i denotes the coordinate variables, with $i = 1, 2, 3$ (see Table F.1). These operators are truly differential operators, as shown by *Tai* [1997]. This notation clears up the confusion which results from using Gibb's notation for divergence and curl, *i.e.*, $\nabla \cdot \mathbf{A}$ and

$\nabla \times \mathbf{A}$. Gibb's notation can lead to the commonly committed mistake of treating, for example, $\nabla \cdot \mathbf{A}$ as the scalar product between ∇ and $\mathbf{A}$ in Cartesian coordinates. This treatment is obviously incorrect since it does not hold true in other coordinate systems. Tai's operators are invariant in any curvilinear system.

Table F.1: Table listing the three most common orthogonal curvilinear systems (OCS) and their respective coordinate variables and metric coefficients. Other OCS's are listed in §2.2 of *Tai* [1997].

Orthogonal Curvilinear System	Coordinate Variables v_1, v_2, v_3	Metric Coefficients h_1, h_2, h_3
Cartesian	x, y, z	1, 1, 1
Cylindrical	r, φ, z	1, r, 1
Spherical	r, θ, φ	1, r, $r \sin\theta$

Tai's notation is used in this work.

BIBLIOGRAPHY

BIBLIOGRAPHY

Adachi, S., "Transmission line theory of antenna impedance in a magnetosphere," *Radio Science*, **12**(1), 23–31, 1977.

Agüero, V., P. M. Banks, B. Gilchrist, I. Linscott, W. J. Raitt, D. Thompson, V. Tolat, A. B. White, S. Williams, and P. R. Williamson, "The Shuttle Electrodynamic Tether System (SETS) on TSS–1," *Il Nuovo Cimento*, **17C**(1), 49–65, 1994.

Agüero, V. M., *A Study of Electrical Charging on Large LEO Spacecraft Using a Tethered Satellite as a Remote Plasma Reference*, Ph.D. Thesis, Stanford Univ., Stanford, CA, June 1996.

Allen, J. E., "Probe theory—The orbital motion approach," *Physica Scripta*, **45**, 497–503, 1992.

Allred, D. B., J. D. Benson, H. A. Cohen, W. J. Raitt, D. A. Burt, I. Katz, G. A. Jongeward, J. Antoniades, M. Alport, D. Boyd, W. C. Nunnally, W. Dillon, J. Pickett, and R. B. Torbert, "The SPEAR–1 experiment: High voltage effects on space charging in the ionosphere," *IEEE Transactions on Nuclear Science*, **NS–35**(6), 1386–1393, 1988.

Ament, W. S., J. C. Katzon, M. Katzin, and B. Y.-C. Koo, "Impedance of a cylindrical dipole having a sinusoidal current distribution in a homogeneous anisotropic ionosphere," *Journal of Research, NBS/USNC–URSI (Radio Science)*, **68D**(4), 379–405, 1964.

Andrews, J. G., "The sheath criterion for a growing sheath," *Journal of Plasma Physics*, **4**(3), 603–606, 1970.

Andrews, J. G., and R. H. Varey, "Sheath growth in a low pressure plasma," *Physics of Fluids*, **14**(2), 339–343, 1971.

Arnold, D. A., and M. Dobrowolny, "Transmission line model of the interaction of a long metal wire with the ionosphere," *Radio Science*, **15**(6), 1149–1161, 1980.

Baker, D. A., *Transverse Sheath Wave Propagation in a Magnetoplasma*, M.S. Thesis, Univ. of Toronto, Toronto, Ontario, Canada, 1988.

Balanis, Constantine A., *Advanced Engineering Electromagnetics*, John Wiley & Sons, New York, NY, 1989.

Balmain, K. G., "The impedance of a short dipole in a magnetoplasma," *IEEE Transactions on Antennas and Propagation*, **AP–12**(9), 605–617, 1964.

Balmain, K. G., H. G. James, and C. C. Bantin, "Magnetoplasma sheath waves on a conducting tether in the ionosphere, with applications to EMI propagation on large space structures," paper presented at Fourth Annual Workshop on Space Operations Applications and Research (SOAR '90), Albuquerque, New Mexico, 1990.

Banks, P. M., P. R. Williamson, and K. L. Oyama, "Electrical behavior of a shuttle electrodynamic tether system (SETS)," *Planetary and Space Science (GB)*, **29**(2), 139–47, 1981.

Banks, P. M., W. J. Raitt, A. B. White, R. I. Bush, and P. R. Williamson, "Results from the Vehicle Charging and Potential Experiment on STS–3," *Journal of Spacecraft and Rockets*, **24**(2), 138–149, 1987.

Banks, P. M., "Review of electrodynamic tethers for space plasma science," *Journal Spacecraft and Rockets*, **26**(4), 234–239, 1989.

Basu, J., and J. N. Maiti, "Propagation along a dielectric-coated cylinder immersed in plasma," *Journal of Applied Physics*, **45**(11), 4795–4796, 1974.

Baum, C. E., "Properties of lightning–leader pulses," in *Lightning Electromagnetics*, Robert L. Gardner, Editor, Hemisphere Publishing, New York, NY, 3–16, 1990.

Baum, C. E., and L. Baker "Analytic return–stroke transmission–line model," in *Lightning Electromagnetics*, Robert L. Gardner, Editor, Hemisphere Publishing, New York, NY, 17–40, 1990.

Benson, F. A., and J. D. Last, "Nonlinear–transmission–line harmonic generator," *Proceedings of the I.E.E.*, **112**(4), 635–643, 1965.

Bilén, S. G., D. S. Lauben, P. R. Williamson, S. D. Williams, V. M. Agüero, and B. E. Gilchrist, "Electrical characterization of the TSS–1 and TSS–1R tether deployer system," *Rep. SETS-057-0199*, Space Physics Research Laboratory, Univ. of Michigan, Ann Arbor, MI, 1994.

Bilén, S. G., B. E. Gilchrist, C. Bonifazi, and E. Melchioni, "Transient response of an electrodynamic tether system in the ionosphere: TSS–1 first results," *Radio Science*, **30**(5), 1519–1535, 1995.

Bilén, S. G., V. M. Agüero, B. E. Gilchrist, and W. J. Raitt, "Transient potential modification of large spacecraft due to electron emissions," *Journal of Spacecraft and Rockets*, **34**(5), 655–661, 1997.

Birdsall, C. K., and A. B. Langdon, *Plasma Physics via Computer Simulation*, McGraw–Hill, New York, NY, 1985.

Biswas, S., and J. Basu, "Propagation along a dielectric–coated cylinder immersed in a magnetoplasma," *Journal of Applied Physics*, **68**(4), 1931–1933, 1990.

Bonifazi, C., G. Manarini, J. Sabbagh, F. Svelto, D. C. Thompson, B. E. Gilchrist, P. M. Banks, and M. Dobrowolny, "Tethered-Satellite System (TSS): Preliminary results on the active experiment core equipment," *Il Nuovo Cimento*, **16C**(5), 515–538, 1993.

Bonifazi, C., F. Svelto, and J. Sabbagh, "TSS Core equipment: I—Electrodynamic package and rationale for system electrodynamic analysis," *Il Nuovo Cimento*, **17C**(1), 13–47, 1994.

Borovsky, J. E., "The dynamic sheath: Objects coupling to plasmas on electron–plasma–frequency time scales," *Physics of Fluids*, **31**(5), 1074–1100, 1988.

Borovsky, J. E., "An electrodynamic description of lightning return strokes and dart leaders: Guided wave propagation along conducting cylindrical channels," *Journal of Geophysical Research*, **100**(D2), 2697–2676, 1995.

Bozorth, Richard M., *Ferromagnetism*, D. Van Nostrand Company, New York, NY, 1951.

Brundin, C. L., "Effects of charged particles on the motion of an Earth satellite," *AIAA Journal*, **1**(11), 2529–2538, 1963.

Brutscher, J., R. Günzel, and W. Müller, "Sheath dynamics in plasma immersion ion implantation," *Plasma Sources, Science and Technology*, **5**, 54–60, 1996.

Butler, A., M. Dobrowolny, S. Ekholm, U. Guidoni, C. Harvey, L. Iess, J.–P. Lebreton, M. Maggi, E. Melchioni, and G. Vannaroni, "RETE experiment Langmuir probe data analysis for the TSS–1 mission," *Rep. IFSI–94–2*, Inst. di Fis. dello Spazio Interplanet., Consiglio Nazionale delle Ricerche, Frascati, Italy, 1994.

Calder, A. C., G. W. Hulbert, and J. G. Laframboise, "Sheath dynamics of electrodes stepped to large negative potentials," *Physics of Fluids B*, **5**(3), 674–690, 1993.

Carroll, J. A., "SEDS deployer design and flight performance," *AIAA Paper 93–4764*, 1993.

Carter, B. L., D. R. Harken, J. H. Parry, S. A. Samson, Holly S. Snyder, E. C. Sutton, E.–W. Bai, and K. E. Lonngren, "Simulation of linear and nonlinear wave propagation on transmission lines," *Electromagnetics*, **15**, 665–677, 1995.

Chen, K.–M., "Interaction of a radiating source with a plasma," *Proceedings of the IEE*, **111**(10), 1668–1678, 1964.

Chen, Francis F., *Introduction to Plasma Physics and Controlled Fusion, Volume 1: Plasma Physics*, 2nd edition, Plenum Press, New York, NY, 1984.

Chester, J. K., "Effects of expanding sheaths on the operation of mercury–arc rectifiers," *Journal of Science and Technology*, **37**(1), 2–10, 1970.

Child, C. D., "Discharge from hot CaO," *Physical Review*, **32**, 492, 1911.

Chu, P. K., S. Qin, C. Chan, N. W. Cheung, and L. A. Larson, "Plasma immersion ion implantation—a fledgling technique for semiconductor processing," *Materials Science and Engineering*, **R17**, 207–280, 1996.

Collins, G. A., and J. Tendys, "Sheath development around a high–voltage cathode," *Plasma Sources, Science and Technology*, **3**(1), 10–18, 1994.

Conde, Luis, Luis León, and Luis F. Ibáñez, "Electron transport properties of stationary plasma clouds generated with hollow cathode discharges," *IEEE Transactions on Plasma Science*, **PS–25**(4), 548–552, 1997.

Conrad, J. R., "Sheath thickness and potential profiles of ion–matrix sheaths for cylindrical and spherical electrodes," *Journal of Applied Physics*, **62**(3), 777–779, 1987.

Cooper Industries, *Belden Master Catalog*, 1989.

Courant, R., K. Friedrichs, and H. Lewy, "Über die partiellen Differenzengleichungen der mathematischen Physik," ("On partial differential equations in mathematical physics"), *Mathematische Annalen*, **100**, 32–74, 1928.

Crawford, F. W., and R. F. Mlodnosky, "Langmuir probe response to periodic waveforms," *Journal of Geophysical Research*, **69**(13), 2765–2773, 1964.

Crouch, D. S., A. C. Park, G. M. Kyrias, B. Strim, S. Lioy, G. Compton, A. Lorenzini, C. Conley, "An update to proposed space tether applications for international space station *Alpha*," paper presented at 4th Intl. Conf. on Tethers in Space, Washington, D.C., 10–14 April, 1995.

Dascher, D. J., "Measuring parasitic capacitance and inductance using TDR," *Hewlett–Packard Journal*, **47**(2), 83–96, 1996.

Dawson, John M., "Particle simulation of plasmas," *Reviews of Modern Physics*, **55**(2), 403–447, 1983.

Denisov, V. P., V. A. Isaev, V. N. Kruglov, and G. V. Permitin, "Impedance of a high–frequency inductor in a dense collisionless plasma," *Soviet Journal of Plasma Physics*, **10**(4), 486–490, 1984.

Dobrowolny, M., "The TSS project: Electrodynamics of long metallic tethers in the ionosphere," *Rivista del Nuovo Cimento*, **10**(3), 1–83, 1987.

Dobrowolny, M., and E. Melchioni, "Electrodynamic aspects of the First Tethered Satellite System," *Journal of Geophysical Research*, **98**(A8), 13,761–13,778, 1993.

Dobrowolny, M., E. Melchioni, U. Guidoni, L. Iess, M. Maggi, R. Orfei, Y. de Conchy, C. C. Harvey, R. M. Manning, F. Wouters, J.–P. Lebreton, S. Ekholm, and A. Butler, "The RETE experiment for the TSS–1 mission," *Il Nuovo Cimento*, **17C**(1), 101–121, 1994a.

Dobrowolny, M., and N. H. Stone, "A technical overview of TSS–1: The First Tethered Satellite System Mission," *Il Nuovo Cimento*, **17C**(1), 1–12, 1994b.

Donohue, Dennis J., *Plasma Wave Radiation Induced by a Conducting Tethered Satellite System*, Ph.D. Thesis, Stanford University, Stanford, CA, June 1991.

DuPont, *Data Manual for Kevlar®49 Aramid*, May 1986.

DuPont, *Nomex® M Aramid and Mica Paper Types 418 and 419 Typical Properties*, Doc. No. H–22371, 1992.

DuPont, *DuPont—On the Forefront of Fluoropolymer Technology*, Doc. No. E–96678-5, 1996.

Emmert, G. A., and M. A. Henry, "Numerical simulation of plasma sheath expansion, with applications to plasma–source ion implantation," *Journal of Applied Physics*, **71**(1), 113–117, 1992.

Emmert, G. A., "Model of expanding sheaths and surface charging at dielectric surfaces during plasma source ion implantation," *Journal of Vacuum Science Technology B*, **12**(2), 880–883, 1994.

En, W., and N. W. Cheung, "Analytical modeling of plasma immersion ion implantation target current using the SPICE circuit simulator," *Journal of Vacuum Science Technology B*, **12**(2), 833–837, 1994.

En, W., M. A. Lieberman, and N. W. Cheung, "Comparison of experimental currents with analytical model results for plasma immersion ion implantation," *IEEE Transactions on Plasma Science*, **PS–23**(5), 415–421, 1995.

En, W., B. P. Linder, and N. W. Cheung, "Modeling of oxide charging effects in plasma processing," *Journal of Vacuum Science and Technology B*, **14**(1), 552–559, 1996.

Faehl, R., B. De Volder, and B. Wood, "Application of particle–in–cell simulation to plasma source ion implantation," *Journal of Vacuum Science Technology B*, **12**(2), 884–888, 1994.

Galejs, J., "Impedance of a finite insulated cylindrical antenna in a cold plasma with a longitudinal magnetic field," *IEEE Transactions on Antennas and Propagation*, **AP–14**(6), 727–736, 1966a.

Galejs, J., "Impedance of a finite insulated cylindrical antenna in a cold plasma with a perpendicular magnetic field," *IEEE Transactions on Antennas and Propagation*, **AP–14**(6), 737–748, 1966b.

Gallagher, D. L., L. Johnson, J. Moore, and F. Bagenal, "Electrodynamic tether propulsion and power generation at Jupiter," NASA Technical Publication, *NASA/TP-1998-208475*, Marshall Space Flight Center, June, 1998.

Garrett, H. B., "The charging of spacecraft surfaces," *Journal of Geophysics and Space Physics*, **19**(4), 577–616, 1981.

Garrett, H. B., and A. C. Whittlesey, "Spacecraft charging, an update," *AIAA Paper 96–0143*, Jan. 1996.

Gear, C. William, *Numerical Initial Value Problems in Ordinary Differential Equations*, Prentice–Hall, Englewood Cliffs, NJ, 1971a.

Gear, Charles W., "Simultaneous numerical solution of differential–algebraic equations," *IEEE Transactions on Circuit Theory*, **CT–18**(1), 89–95, 1971b.

Gerver, M. J., D. E. Hastings, and M. R. Oberhardt, "Theory of plasma contactors in ground–based experiments and low Earth orbit," *Journal of Spacecraft and Rockets*, **27**(4), 391-402, 1990.

Gilchrist, B. E., P. M. Banks, T. Neubert, V. M. Agüero, S. G. Bilén, S. D. Williams, I. R. Linscott, D. C. Thompson and W. J. Raitt, "Measurements of TSS–1 voltage–current characteristics using the SETS experiment," paper presented at American Geophysical Union, 1992 Fall Meeting, San Fransisco, 1992.

Gilchrist, B. E., V. M. Agüero, P. M. Banks, T. Neubert, C. Bonifazi, D. C. Thompson, W. J. Raitt, and S. D. Williams, "Modification of the TSS-1 electrodynamic tether current–voltage characteristics due to orbiter thruster firings" (abstract), *EOS, Transactions, American Geophysical Union*, **74**(43), Fall Meeting suppl., 466, 1993.

Gilchrist, B. E., S. D. Williams, N. Voronka, W. J. Raitt, D. C. Thompson, S. G. Bilén, and V. M. Agüero, "Electrodynamic tethers for double probe potential measurements in the ionosphere and magnetosphere," paper presented at Measurement Techniques for Space Plasmas, Santa Fe, NM, 3–7 April, 1995.

Godard, R., *A Symmetrical Model for Cylindrical and Spherical Collectors in a Flowing Collisionless Plasma*, Ph.D. Thesis, York Univ., Toronto, Ontario, Canada, 1975.

Godard, R., and J. G. Laframboise, "Total current to cylindrical collectors in collisionless plasma flow," *Planetary and Space Science*, **31**(3), 275–283, 1983.

Godard, R., and J. G. Laframboise, "Low–frequency sheath admittance of a sphere in a collisionless plasma," *Radio Science*, **21**(3), 421–428, 1986.

Godard, R., H. G. James, J. G. Laframboise, B. Macintosh, A. G. McNamara, S. Wantanabe, and B. A. Whalen, "The OEDIPUS experiment: Analysis of the current/voltage data," *Journal of Geophysical Research*, **96**(A10), 17,879–17,890, 1991.

Godyak, V. A., "Statistical heating of electrons at an oscillating plasma boundary," *Soviet Physics—Technical Physics*, **16**(7), 1073–1076, 1972.

Goubau, G., "Surface waves and their application to transmission lines," *Journal of Applied Physics*, **21**, 1119–1128, 1950.

Goubau, G., "Single–conductor surface–wave transmission lines," *Proceedings of the IRE*, **39**, 619–624, 1951.

Grard, Réjean Jules Léon, *Interpretation of Impedance Probe Measurements in the Ionosphere*, Ph.D. Thesis, Stanford University, Stanford, CA, March 1966.

Greene, M., D. Wheelock, and M. Baginski, "Electrodynamics of the getaway tether experiment," *Journal of Spacecraft and Rockets*, **26**(6), 452–459, 1989.

Grossi, M. D., "Spaceborne long vertical wire as a self–powered ULF/ELF radiator," *IEEE Journal of Oceanic Engineering*, **OE–9**(3), 211–213, 1984.

Grossner, N. R., *Transformers for Electric Circuits*, 2nd edition, McGraw–Hill, New York, NY, 362–419, 1983.

Hackbusch, Wolfgang, *Multi–Grid Methods and Applications*, Springer–Verlag, New York, NY, 1985.

Hahn, S. J., and J. K. Lee, "Kinetic simulation of the transient sheath in plasma ion implantation," *Japanese Journal of Applied Physics*, **31**(8), 2570–2579, 1992.

Hastings, D. E., "Theory of plasma contactors used in the ionosphere," *Journal of Spacecraft and Rockets*, **24**(3), 250–256, 1987.

Hastings, D. E., "A review of plasma interactions with spacecraft in Low Earth Orbit," *Journal of Geophysical Research*, **100**(A8), 14,457–14,483, 1995.

Hawkins, J. G., *Vehicle Charging and Return Current Measurements During Electron Beam Emission Experiments from the Shuttle Orbiter*, Ph.D. Thesis, Stanford Univ., Stanford, CA, April 1988.

He, J., M. A. Elnaby, and A. Elshabini–Riad, "Time domain modeling of a microwave Schottky diode," *Solid-State Electronics*, **37**(10), 1753–1758, 1994.

Hilbish, Robert Thomas, *Harmonic Generation using the Varactor Capabilities of the Plasma Sheath*, Ph.D. Thesis, Purdue Univ., West Lafayette, IN, June 1967.

Hockney, R. W., and J. W. Eastwood, *Computer Simulation Using Particles*, Adam Hilger, New York, NY, 1988.

Holt, E. H., and R. E. Haskell, *Foundations of Plasma Physics*, Macmillan Company, New York, NY, 1965.

Hong, M., and G. A. Emmert, "Two–dimensional fluid modeling of time–dependent plasma sheath," *Journal of Vacuum Science Technology B*, **12**(2), 889–896, 1994.

Hong, M., and G. A. Emmert, "Two–dimensional fluid simulation of expanding plasma sheaths," *Journal of Applied Physics*, **78**(12), 6967–6973, 1995.

Hsue, C.-W., and T.-W. Pan, "Reconstruction of nonuniform transmission lines from time–domain reflectometry," *IEEE Transactions on Microwave Theory and Techniques*, **45**(1), 32–38, 1997.

Humphries, Stanley, Jr., *Charged Particle Beams*, John Wiley and Sons, New York, NY, 1990.

Hutchinson, I. H., *Principles of Plasma Diagnostics*, Cambridge University Press, Cambridge, U. K., 1987.

Iess, L., and M. Dobrowolny, "The interaction of a hollow cathode with the ionosphere," *Physics of Fluids B*, **1**(9), 1880–1889, 1989.

Ishizone, T., K. Taira, S. Adachi, and Y. Mushiake, "Sheath effects on the current distribution along an antenna in a plasma," *IEEE Transactions on Antennas and Propagation*, **AP–17**(5), 398–400, 1969a.

Ishizone, T., S. Adachi, K. Taira, Y. Mushiake, and K. Miyazaki, "Measurement of antenna current distribution in an anisotropic plasma," *IEEE Transactions on Antennas and Propagation*, **AP–17**(9), 678–679, 1969b.

Ishizone, T., S. Adachi, and Y. Mushiake, "Electromagnetic wave propagation along a conducting wire in a general magnetoplasma," *Proceedings of the IEEE*, **58**(11), 1843–1844, 1970a.

Ishizone, T., S. Adachi, and Y. Mushiake, "Measurement of the phase constant along a conducting wire in a magnetoplasma," *Proceedings of the IEEE*, **58**(11), 1852–1854, 1970b.

Jäger, D., "Characteristics of travelling waves along the non–linear transmission lines for monolithic integrated circuits: A review," *International Journal of Electronics*, **58**(4), 649–669, 1985.

James, H. G., and B. A. Whalen, "OEDIPUS–A: Space research with a new tether," *EOS, Transactions, American Geophysical Union*, **72**(12), 137, 139, 140, 144, 1991.

James, H. G., "Tether phenomena observed in the OEDIPUS–A Experiment," in *The Behavior of Space Systems in the Space Environment*, R. N. DeWitt *et al.*, Editors, *NATO ASI Series, Series E, Applied Sciences, no. 245*, Kluwer Academic, Norwell, MA, 581-603, 1993.

James, H. G., K. G. Balmain, C. C. Bantin, and G. W. Hulbert, "Sheath waves observed on OEDIPUS A," *Radio Science*, **30**(1), 57–73, 1995.

Johnson, C. Y., "Ion and neutral composition of the ionosphere," *Ann. IQSY*, **5**, 1969.

Johnson, L., and J. Ballance, "Propulsive Small Expendable Deployer System (ProSEDS) space demonstration," Tether Technology Interchange Meeting, NASA MSFC, 9–10 Sept. 1997, *NASA/CP–1998–206900*, 103–108, 1997.

Johnson, L., and M. Herrmann, "*International Space Station* electrodynamic tether reboost study," NASA Technical Memorandum, *NASA/TM–1998–208538*, Marshall Space Flight Center, July 1998.

Katz, I., G. A. Jongeward, V. A. Davis, M. J. Mandell, R. A. Kuharski, J. R. Lilley Jr., W. J. Raitt, D. L. Cooke, R. B. Torbert, G. Larson, and D. Rau, "Structure of the bipolar plasma sheath generated by SPEAR–1," *Journal of Geophysical Research*, **94**(A2), 1450–1458, 1989.

Katz, I., E. Melchioni, M. Mandell, M. Oberhardt, D. Thompson, T. Neubert, B. Gilchrist, and C. Bonifazi, "Observations of ionosphere heating in the TSS–1 subsatellite presheath," *Journal of Geophysical Research*, **99**(A5), 8961–8969, 1993.

Kawashima, N., S. Sasaki, K.–I. Oyama, K. Hirao, T. Obayashi, W. J. Raitt, A. B. White, P. R. Williamson, P. M. Banks, and W. F. Sharp, "Results from a tethered rocket experiment (CHARGE–2)," *Advances in Space Research*, **8**(1), 197–201, 1988.

Kelly, Michael C., *The Earth's Ionosphere—Plasma Physics and Electrodynamics*, Academic Press, San Diego, CA, 1989.

Kielkowski, Ron M., *Inside SPICE: Overcoming the Obstacles of Circuit Simulation*, McGraw–Hill, New York, NY, 1994.

Kingsep, A. S., K. V. Chukbar, and V. V. Yan'kov, "Electron magnetohydrodynamics," in *Reviews of Plasma Physics*, B. B. Kadomtsev, Editor, Consultants Bureau, New York, NY, 243–291, 1990.

Krall, Nicholas A., and Alvin W. Trivelpiece, *Principles of Plasma Physics*, San Francisco Press, San Francisco, CA, 1986.

Krehbiel, J. P., L. H. Brace, R. F. Theis, W. H. Pinkus, and R. B. Kaplan, "The Dynamics Explorer Langmuir probe instrument," *Space Science Instrumentation*, **5**, 493–502, 1981.

Kunz, Karl S., and Raymond J. Luebbers, *The Finite Difference Time Domain Method for Electromagnetics*, CRC Press, Boca Raton, FL, 1993.

Kushner, Mark J., "Mechanisms for power deposition in Ar/SiH_4 capacitively coupled RF discharges," *IEEE Transactions on Plasma Science*, **PS–14**(2), 188–196, 1986.

Kuusela, T., "Soliton experiments in transmission lines," *Chaos, Solitons, and Fractals*, **5**(12), 2419–2462, 1995.

Kuźniar, Władysław, "Electrical waves in long transmission lines with parameters varying in time," *Archiwum Elektrotechnika*, **26**, 19–27, 1987.

Laframboise, J. G., "Theory of spherical and cylindrical Langmuir probes in a collisionless, Maxwellian plasma at rest," *UTIAS Report No. 100*, Institute for Aerospace Studies, Univ. of Toronto, Toronto, Ontario, Canada, June 1966.

Laframboise, J. G., J. Rubinstein, and F. H. Palmer, "Theory of topside sounder transmission effects on antenna quasistatic sheath impedance," *Radio Science*, **10**(8,9), 773–784, 1975.

Laframboise, J. G., and L. J. Sonmor, "Current collection by probes and electrodes in space magnetoplasmas: A review," *Journal of Geophysical Research*, **98**(A1), 337–357, 1993.

Landauer, R., "Shock waves in nonlinear transmission lines and their effect on parametric amplification," *IBM Journal of Research and Development*, **4**(4), 391–401, 1960.

Langmuir, I., "The effect of space charge and residual gases on thermionic currents in high vacuum," *Physical Review*, **2**, 450–486, 1913.

Langmuir, I., and K. B. Blodgett, "Current limited by space charge flow between concentric spheres," *Physical Review*, **24**, 49–59, 1924.

Lassudrie–Duchesne, P., G. Dubost, and C. Terret, "Mesure de la distribution de courant à la surface d'un doublet immergé dans un plasma chaud isotrope," ("Measurement of the current distribution on the surface of a dipole immersed in an isotropic hot plasma"), *C. R. Acad. Sc. Paris, Series B*, **276**(5 February), 207–210, 1973.

Laurin, J.–J., G. A. Morin, and K. G. Balmain, "Sheath wave propagation in a magnetoplasma," *Radio Science*, **24**(3), 289–300, 1989.

Lawson, W. S., "Coaxial and surface modes in tokamaks in the complete cold–plasma limit," *Plasma Physics and Controlled Fusion*, **34**(2), 175–189, 1992.

Lieberman, M. A., "Analytical solution for capacitive RF sheaths," *IEEE Transactions on Plasma Science*, **PS-16**(6), 638–644, 1988.

Lieberman, M. A., "Model of plasma immersion ion implantation," *Journal of Applied Physics*, **66**(7), 2926–2929, 1989.

Liemohn, H. B., "Electrical charging of shuttle orbiter," *IEEE Transactions on Plasma Science*, **PS–4**(4), 229–240, 1976.

Linder, B. P., and N. W. Cheung, "Plasma immersion ion implantation with dielectric substrates," *IEEE Transactions on Plasma Science*, **PS–24**(6), 1383–1388, 1996.

Linh, N. P., and M. Nachman, "Excitation of the half-frequency of the input signal in the response of an antenna immersed in a plasma," *IEEE Transactions on Plasma Science*, **PS–18**(4), 717–724, 1990.

Linscott, I., "Tether aperture synthesis: Use of the TSS–1 tether to synthesize aperture for VLF radio signals," Center for Radar Astronomy Report, Stanford Univ., Stanford, CA, 1992.

Lonngren, K. E., "Observations of solitons on nonlinear dispersive transmission lines," in *Solitons in Action*, K. E. Lonngren and A. Scott, Editors, Academic Press, New York, NY, 127–152, 1978.

Lorenzini, E. C., and J. A. Carroll, "In–orbit experimentation with the Small Expendable–tether Deployment System," *ESA Journal*, **15**(1), 27–33, 1991.

Lorenzini, E., C. J. Dyer, and M. D. Grossi, "Orbiting transmitter and antenna for spaceborne communications at ELF/VLF to submerged submarines," paper presented at ELF/VLF/LF Radio Propagation and Systems Aspects, Brussels, Belgium, 1992.

Lu, H. S., and K. K. Mei, "Cylindrical antennas in gyrotropic media," *IEEE Transactions on Antennas and Propagation*, **AP–19**(5), 669–674, 1971.

Lüttgen, A. A. E., and K. G. Balmain, "Nonreciprocal magnetoplasma sheath waves on structures in space," paper presented at Fourth International Conference on Tethers in Space, Washington, DC, 1995.

Lüttgen, A. A. E., and K. G. Balmain, "Nonreciprocal magnetoplasma sheath waves," *Radio Science*, **31**(6), 1599–1613, 1996.

Ma, T.–Z., and R. W. Schunk, "High negative voltage spheres in an unmagnetized plasma: Fluid simulations," *Plasma Physics and Controlled Fusion*, **34**(5), 783–799, 1992.

Marec, J., and G. Mourier, "Sur la propogation des ondes de surface et la nature des résonances électrostatiques de gaines," ("On the propagation of surface waves and the nature of electrostatic resonances of sheaths"), *C. R. Acad. Sc. Paris, Series B*, **271**(10 August), 367–370, 1970.

Martin Marietta, *TSS System and Subsystem Analysis: System Design, Vol. 1, TSS–SSA–01*, Astronautics Group, Denver, CO, 1990.

Martin Marietta, *Tethered Satellite System (TSS) Data Reference Book*, Civil and Space Communications, Denver, CO, 44–54, 1992.

Martínez–Sanchez, M., and D. E. Hastings, "A systems study of a 100 kW electrodynamic tether," *The Journal of the Astronautical Sciences*, **35**(1), 75–96, 1987.

Martínez–Sanchez, M., and J. R. Sanmartin, "Artificial auroral effects from a bare conducting tether," *Journal of Geophysical Research*, **102**(A12), 27,257–27,263, 1997.

Matsumoto, H., and Y. Omura, *Computer Space Plasma Physics: Simulation Techniques and Software*, Terra Scientific Publishing, Tokyo, Japan, 1993.

Mattos, Marcos André da Frota, and Christos Christopoulos, "A nonlinear transmission line model of the lightning return stroke," *IEEE Transactions on Electromagnetic Compatibility*, **EMC–30**(3), 401–406, 1988.

Mavrodineanu, R., "Hollow cathode discharges," *Journal of Research of the National Bureau of Standards*, **89**(2), 143–185, 1984.

McCoy, J. E., I. Katz, J. R. Lilley, A. Greb, V. A. Davis, and D. C. Ferguson, "Physics of current flow between the ionosphere and the Plasma Motor Generator (PMG) plasma contactors" (abstract), *EOS, Transactions, American Geophysical Union*, **74**(43), Fall Meeting supplement, 466, 1993.

McNutt, W. J., T. J. Blalock, and R. A. Hinton, "Response of transformer windings to system transient voltages," *IEEE Transactions on Power Applications and Systems*, **PAS–93**(2), 457–467, 1974.

Meta–Software, Inc., *HSPICE User's Manual: Volume I, Simulation and Analysis, Version 96.1, February 1996*, Campbell, CA, 1996a.

Meta–Software, Inc., *HSPICE User's Manual: Volume II, Elements and Device Models, Version 96.1, February 1996*, Campbell, CA, 1996b.

Meta–Software, Inc., *HSPICE User's Manual: Volume III, Applications and Examples, Version 96.1, February 1996*, Campbell, CA, 1996c.

Mittra, R., "Radiation resistance of antennas in anisotropic media," *Electronics Letters*, **1**(9), 258–259, 1965.

Morin, G. A., and K. G. Balmain, "Hydrodynamic radio–frequency model of an ion sheath near a conductor in a plasma," *Radio Science*, **26**(2), 459–467, 1991.

Morin, G. A., and K. G. Balmain, "Plasma sheath and presheath waves: Theory and experiment," *Radio Science*, **28**(2), 151–167, 1993.

Morrison, P. J., W. B. Thompson, and P. R. Williamson, "Current collection by a long wire in near–earth orbit," *IEEE Transactions on Plasma Science*, **PS–6**(4), 435–441, 1978.

Nachman, M., M. Le Blanc, and N. P. Linh, "Sheath-wave-related resonances in the frequency response of a cylindrical monopole in a plasma," *IEEE Transactions on Plasma Science*, **PS–16**(3), 333–341, 1988.

Nagashima, H., and Y. Amagishi, "Experiment on the Toda lattice using nonlinear transmission lines," *Journal of the Physical Society of Japan*, **45**(2), 680–688, 1978.

Neubert, T., M. J. Mandell, S. Sasaki, B. E. Gilchrist, P. M. Banks, P. R. Williamson, W. J. Raitt, N. B. Myers, K.–I. Oyama, and I. Katz, "The sheath structure around a negatively charged rocket payload," *Journal of Geophysical Research*, **95**(A5), 6155–6165, 1990.

Oberhardt, M. R., D. Hardy, D. C. Thompson, W. J. Raitt, E. Melchioni, C. Bonifazi, and M. P. Gough, "Positive spacecraft charging as measured by the Shuttle Potential and Return Electron Experiment," *IEEE Transactions on Nuclear Science*, **40**(6), 1532–1541, 1993.

Oberhardt, M. R., D. A. Hardy, W. E. Slutter, J. O. McGarity, D. J. Sperry, A. W. Everest III, A. C. Huber, J. A. Pantazis, and M. P. Gough, "The Shuttle Potential and Return Electron Experiment (SPREE)," *Il Nuovo Cimento*, **17C**(1), 1994, 67–83, 1994.

Okuda, T., "Dynamic properties of a probe in gas–discharge plasma," *Electrical Engineering in Japan*, **83**(Nov.), 28–38, 1963a.

Okuda, T., "Transient space charge in gas–discharge plasma," *Electrical Engineering in Japan*, **83**(Nov.), 39–49, 1963b.

Okuda, T., "Recovery of space–charge layers in gas–discharge plasmas," *Electrical Engineering in Japan*, **83**(Nov.), 49–58, 1963c.

Osbourne, F. J. F., F. H. C. Smith, R. E. Barrington, and W. E. Mather, "Plasma–induced interference in satellite v.l.f. receivers," *Canadian Journal of Physics*, **45**(1), 47-56, 1967.

Osmolovsky, I. K., K.–I. Oyama, S. Sasaki, and N. A. Savich, "Electric oscillations in the electrodynamic tethered space systems," *ISAS Research Note 519*, Institute of Space and Astronautical Science, Sagamihara, Japan, October 1992.

Parks, D. E., M. J. Mandell, and I. Katz, "Fluid model of plasma outside a hollow cathode neutralizer," *Journal of Spacecraft and Rockets*, **19**(4), 354–357, 1982.

Parks, D. E., and I. Katz, "Theory of plasma contactors for electrodynamic tethered satellite systems," *Journal of Spacecraft and Rockets*, **24**(3), 245–249, 1987.

Parks, D. E., I. Katz, B. Buchholtz, and P. Wilbur, "Expansion and electron emission characteristics of a hollow–cathode plasma contactor," *Journal of Applied Physics*, **74**(12), 7094–7100, 1993.

Penzo, P. A., and P. W. Ammann, *Tethers in Space Handbook*, 2nd edition, NASA, Washington, DC, 1989.

Perkins, F.W., "Radiofrequency sheaths and impurity generation by ICRF antennas," *Nuclear Fusion*, **29**(4), 583–592, 1989.

Pozar, David M., *Microwave Engineering*, Addison–Wesley, New York, NY, 1990.

Qin, S., J. D. Berstein, Z. Zhao, W. Liu, C. Chan, J. Shao, and S. Denholm, "Charging effects in plasma immersion ion implantation for microelectronics," *Journal of Vacuum Science and Technology B*, **13**(5), 1994-1998, 1995.

Raitt, W. J., N. Myers, J. Roberts, D. Thompson, B. Gilchrist, and S. Sasaki, "Recent observations of high voltage spacecraft–environment interaction at LEO altitudes using sounding rockets," *AIAA–90–0635*, paper presented at AIAA 28th Aerospace Sciences Meeting, Reno, NV, Jan. 8–11, 1990.

Raizer, Yuri P., Mikhail N. Shneider, and Nikolai A. Yatsenko, *Radio–Frequency Capacitive Discharges*, CRC Press, Boca Raton, FL, 1995.

Rubinstein, J., and J. G. Laframboise, "Plasma sheath around a floating cylindrical antenna at high power," *Canadian Journal of Physics*, **48**, 1882–1893, 1970.

Sasaki, S., K.-I. Oyama, N. Kawashima, T. Obayashi, K. Hirao, W. J. Raitt, N. B. Meyers, P. R. Williamson, P. M. Banks, and W. F. Sharp, "Tethered rocket experiment (CHARGE–2): Initial results on electrodynamics," *Radio Science*, **23**(6), 975–988, 1988.

Savas, Stephen E., and Richard W. Plavidal, "Spatial variations in the electrode potential of capacitive radio–frequency plasmas due to transverse electromagnetic modes (summary abstract)," *Journal of Vacuum Science and Technology A*, **6**(3), 1775–1777, 1988.

Savas, S. E., and K. G. Donohoe, "Capacitive probes for RF process plasmas," *Review of Scientific Instruments*, **60**(11), 3391–3395, 1989a.

Savas, S. E., "Electrode surface rf harmonics generated by the nonlinear sheath in a coaxial capacitive rf discharge," in *Radio-Frequency Power in Plasmas: Eighth Topical Conference*, R. McWilliams, Editor, AIP Conference Proceedings **190**, American Institute of Physics, New York, NY, 470–473, 1989b.

Savich, N. A., "Problems and prospects of fundamental studies of electrodynamic properties of tethered satellite systems," Report, Academy of Sciences of the USSR Institute of Radio Engineering and Electronics, 1988.

Savich, N. A., "Electrodynamics of tethered satellite systems: Two concepts," *IAF–89–013*, paper presented at 40th Congress of the International Astronautical Federation, Málaga, Spain, Oct. 7–12, 1989.

Sawaya, K., T. Ishizone, and Y. Mushiake, "Measurement of the impedance of a linear antenna in a magnetoplasma," *Radio Science*, **13**(1), 21–29, 1978.

Scheuer, J. T., M. Shamim, and J. R. Conrad, "Model of plasma source ion implantation in planar, cylindrical, and spherical geometries," *Journal of Applied Physics*, **67**(3), 1241-1245, 1990.

Schott, L., "Electrical probes," in *Plasma Diagnostics*, W. Lochte–Holtgreven, editor, AIP Press, New York, NY, 668–731, 1995.

Scott, A. C., F. Y. F. Chu, and D. W. McLaughlin, "The soliton: A new concept in applied science," *Proceedings of the IEEE*, **61**(10), 1443–1483, 1973.

Shamim, M., J. T. Scheuer, and J. R. Conrad, "Measurements of spatial and temporal sheath evolution for spherical and cylindrical geometries in plasma source ion implantation," *Journal of Applied Physics*, **69**(5), 2904–2908, 1991.

Sheridan, T. E., and M. J. Alport, "Ion-matrix sheath around a square bar," *Journal of Vacuum Science and Technology B*, **12**(2), 897–900, 1994.

Sheridan, T. E., "Particle–in–cell simulation of the pulsed sheath in a trench," *IEEE Transactions on Plasma Science*, **24**(1), 57–58, 1996.

Sheridan, T. E., "Analytic solution for plasma dynamics in a small, pulsed bore," *Physics of Plasmas*, **4**(9), 3442–3444, 1997.

Shirakawa, Teruyuki, Hirotaka Toyoda, and Hideo Sugai, "RF plasma production at ultralow pressures with surface magnetic confinement," *Japanese Journal of Applied Physics*, **29**(6), L1015–L1018, 1990.

Shkarofsky, I. P., "Nonlinear sheath admittance, currents, and charges associated with high peak voltage drive on a VLF/ELF dipole antenna moving in the ionosphere," *Radio Science*, **7**(4), 503–523, 1972.

Shugg, W. Tillar, *Handbook of Electrical and Electronic Insulating Materials*, 2nd edition, IEEE Press, New York, NY, 1995.

Smy, P. R., and J. R. Greig, "Transient response of the Langmuir probe at low pressures," *Journal of Physics D*, **1**(1), 351–359, 1968.

Sommerfeld, A., "Über die Fortpflanzung elektrodynamischer Wellen Langs eines Drahtes," ("On the propagation of electrodynamic waves along single wires"), *Annalen der Physik und Chemie*, **67**, 233, 1899.

Stenzel, R., and J. Urrutia, "Currents between tethered electrodes in a magnetized laboratory plasma," *Journal of Geophysical Research*, **95**(A5), 6209–6226, 1990.

Stenzel, R. L., J. M. Urrutia and C. L. Rousculp, "Transport of time–varying plasma currents by whistler wave packets," *IEEE Transactions on Plasma Science*, **PS–20**(6), 787-796, 1992.

Stenzel, R. L., J. M. Urrutia and C. L. Rousculp, "Pulsed currents carried by whistlers. Part I: Excitation by magnetic antennas," *Physics of Fluids B*, **5**(2), 325–338, 1993.

Stevens, J. E., M. J. Sowa, and J. L. Cecchi, "Uniformity of radio frequency bias voltages along conducting surfaces in a plasma," *Journal of Vacuum Science and Technology A*, **14**(1), 139–143, 1996.

Stewart, R. A., and M. A. Lieberman, "Model of plasma immersion ion implantation for voltage pulses with finite rise and fall times," *Journal of Applied Physics*, **70**(7), 3481–3487, 1991.

Stix, T. H., *Waves in Plasmas*, American Institute of Physics, New York, NY, 1992.

Stratton, J. A., *Electromagnetic Theory*, McGraw–Hill, New York, NY, 1941.

Sugai, H., K. Nakamura, and K. Suzuki, "Electrostatic coupling of antenna and the shielding effect in inductive RF plasmas," *Japanese Journal of Applied Physics*, **33**, 2189–2193, 1994.

Swift, J. D., and M. J. R. Schwar, *Electrical Probes for Plasma Diagnostics*, American Elsevier Publishing Company, New York, NY, 1969.

Tai, Chen–To, *Generalized Vector and Dyadic Analysis: Applied Mathematics in Field Theory*, 2nd edition, IEEE Press, New York, NY, 1997.

Tai, Chen–To, "Notation in vector analysis," *IEEE Antennas and Propagation Magazine*, **AP–40**(2), 65–66, 1998.

Tanenbaum, B. Samuel, *Plasma Physics*, McGraw–Hill, New York, NY, 1967.

Tascione, Thomas F., *Introduction to the Space Environment*, Orbit Book Company, Malabar, FL, 1988.

Thompson, D. C., W. J. Raitt, M. R. Oberhardt, D. A. Hardy, V. M. Aguero, I. R. Linscott, T. N. Neubert, B. E. Gilchrist, and P. M. Banks, "Global survey of TSS–1 current collection as measured by the SETS experiment," paper presented at 1992 AGU Fall Meeting, San Fransisco, CA, 1992.

Thompson, D. C., W. J. Raitt, C. Bonifazi, S. D. Williams, V. M. Agüero, B. E. Gilchrist, and P. M. Banks, "TSS–1: Orbiter current and voltage experiments," paper presented at 31st Aerospace Sciences Meeting and Exhibit, Reno, NV, 1993.

Trivelpiece, A. W., and R. W. Gould, "Space charge waves in cylindrical plasma columns," *Journal of Applied Physics*, **30**(11), 1784–1793, 1959.

Tuinenga, Paul W., *SPICE: A guide to Circuit Simulation & Analysis Using PSpice*, Prentice Hall, Englewood Cliffs, NJ, 1988.

Urrutia, J. M., R. L. Stenzel, and C. L. Rousculp, "Pulsed currents carried by whistlers. Part II: Excitation by biased electrodes," *Physics of Plasmas*, **1**(5), 1432–1438, 1994.

Vahedi, V., M. A. Lieberman, M. V. Alves, J. P. Verboncoeur, and C. K. Birdsall, "A one-dimensional collisional model for plasma-immersion ion implantation," *Journal of Applied Physics*, **69**(4), 2008–2014, 1991.

Vannaroni, G., M. Dobrowolny, E. Melchioni, F. D. Venuto, and R. Giovi, "Characterization of the interaction between a hollow cathode source and an ambient plasma," *Journal of Applied Physics*, **71**(10), 4709–4717, 1992.

Verboncoeur, J. P., A. B. Langdon, and N. T. Gladd, "An object-oriented electromagnetic PIC code," *Computer Physics Communications*, **87**, 199–211, 1995. Codes available from `http://ptsg.eecs.berkeley.edu`.

Vesuvius McDanel, *Catalog of Standard Products*, 1993.

Walter, C. H., *Traveling Wave Antennas*, McGraw–Hill, New York, NY, 1965.

Whipple, E. C. "Current collection from an unmagnetized plasma: A tutorial," in *Current Collection from Space Plasmas, NASA CP-3039*, Singh *et al.*, editors, 1–12, 1990.

Williams, S. D., B. E. Gilchrist, V. M. Agüero, R. S. Indiresan, D. C. Thompson, and W. J. Raitt, "TSS–1R vertical electric fields: Long baseline measurements using an electrodynamic tether as a double probe," *Geophysical Research Letters*, **25**(4), 445–448, 1998.

Wood, B.P., "Displacement current and multiple pulse effects in plasma source ion implantation," *Journal of Applied Physics*, **73**(10), 4770–4778, 1993.

IMAGE EVALUATION
TEST TARGET (QA-3)

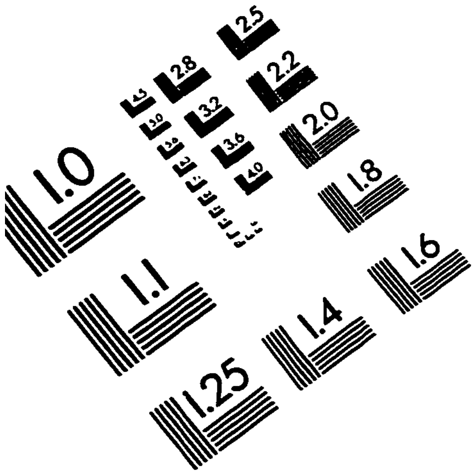

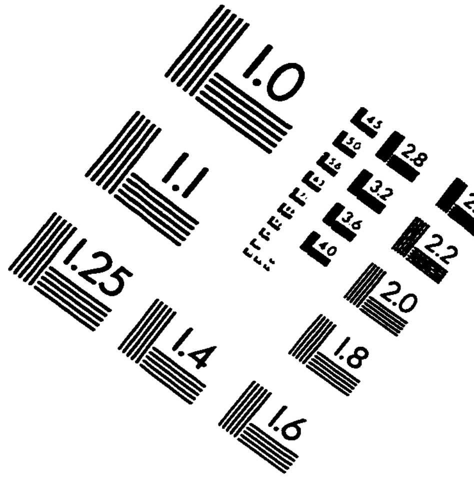

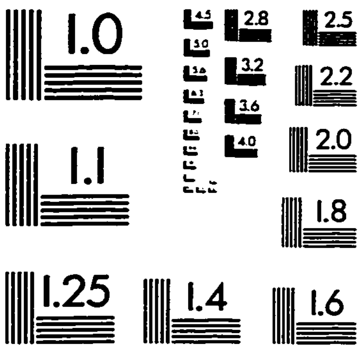

150mm

6″

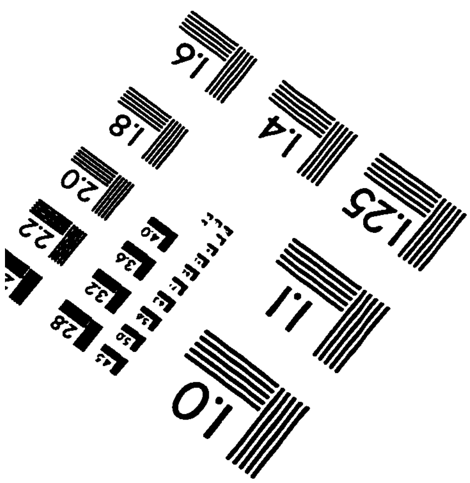

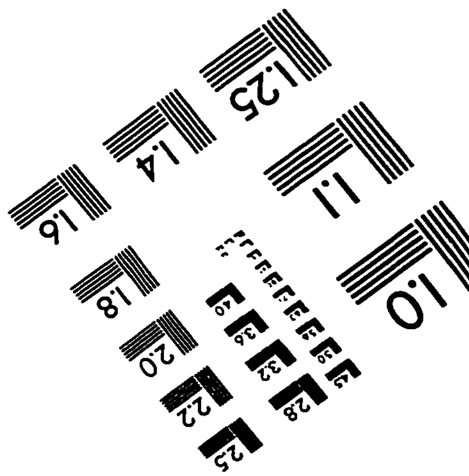

APPLIED IMAGE, Inc
1653 East Main Street
Rochester, NY 14609 USA
Phone: 716/482-0300
Fax: 716/288-5989